Design, Synthesis and Structural Characterization of Carrier Platforms for Therapeutics Delivery

Kumulative Dissertation

zur Erlangung des Doktorgrades der Naturwissenschaften

Doctor rerum naturalium (Dr. rer. nat.)

der

Naturwissenschaftlichen Fakultät II
Chemie, Physik und Mathematik

der Martin-Luther-Universität
Halle-Wittenberg

vorgelegt von

Herrn Rana Hore

Gutachter:

1. Prof. Dr. Jörg Kreßler

2. Prof. Dr. Markus Pietzsch

3. Prof. Dr. Jörg C. Tiller

Tag der öffentlichen Verteidigung: 26.08.2025

Dedication

To the moments of doubt and the triumphs of belief

To my family, the heart of my accomplishments

Anybody who has been seriously engaged in scientific work of any kind realizes that over the entrance to the gates of the temple of science are written the words: Ye must have faith. It is a quality which the scientist cannot dispense with.

— Max Planck

April 23, 1858 - October 4, 1947

In Max Planck and James Vincent Murphy (trans.), Where Is Science Going? (1932)

Preliminary remark

The present dissertation is written in a cumulative format, integrating research findings that have been previously published in peer-reviewed journals. These publications contain comprehensive experimental procedures and a thorough discussion of the relevant results presented herein.

This dissertation is based on the following publications:

Paper I: Enzymatic HES conjugation with recombinant human erythropoietin *via* variant microbial transglutaminase TG[16]

Rana Hore, Razan Alaneed, Markus Pietzsch, and Jörg Kressler
Starch-Stärke 2022, 74 (9-10), 2200034,
https://doi.org/10.1002/star.202200034

Paper II: Synthesis and characterization of self-assembled highly stearate grafted hydroxyethyl starch conjugates

Rana Hore, Haroon Rashid, Frank Syrowatka, and Jörg Kressler
Polysaccharides 2024, 5 (2), 142-157,
https://doi.org/10.3390/polysaccharides5020011

Paper III: Synthesis and characterization of dimeric artesunate glycerol monocaprylate conjugate and formulation of nanoemulsion preconcentrate

Rana Hore, Nazmul Hasan, Karsten Mäder, and Jörg Kressler
Molecules 2023, 28 (13), 5208,
https://doi.org/10.3390/molecules28135208

Table of Contents

List of abbreviations

10-HCPT	10-hydroxy camptothecin
10-HCPT-HES	10-hydroxy camptothecin-hydroxyethyl starch conjugate
^{13}C NMR	Carbon-13 nuclear magnetic resonance spectroscopy
^{1}H NMR	Proton nuclear magnetic resonance spectroscopy
2D NMR	Two-dimensional nuclear magnetic resonance spectroscopy
Å	Angstrom
ACV	Acyclovir
AFM	Atomic force microscopy
AGEM400	Dimeric erythropoietin mimetic peptide
AGU	Anhydrous glucose subunit
APT	Attached proton test
ARTP	Atmospheric and room temperature plasma
AS	Artesunate
Asp	Aspartic acid
BSA	Bovine serum albumin
C18	1-octadecanethiol
CalTech	California Institute of Technology
CDI	1,1′-carbonyldiimidazole
CMC	Critical micelle concentration
COSY	Homonuclear correlation spectroscopy
CQ-HES	Chloroquine-hydroxyethyl starch conjugate
cRGD	Cyclic arginyl-glycyl-aspartic acid peptide
CuAAC	Cu-catalyzed azide-alkyne 1,3-dipolar cycloaddition
Cys	Cysteine
D-AS-GC	Dimeric artesunate glycerol monocaprylate conjugates
DCC	*N,N′*-dicyclohexylcarbodiimide
D_h	Hydrodynamic diameter
DIC	*N,N′*-diisopropylcarbodiimide
DLS	Dynamic light scattering
DMAP	4-dimethylaminopyridine
DMC	Dimethylcasein
DNA	Deoxyribonucleic acid

DOSY NMR	Diffusion-ordered nuclear magnetic resonance spectroscopy
DOX	Doxorubicin
DSC	Differential scanning calorimetry
E. coli	Escherichia coli
EDC·HCl	1-ethyl-3-(3-dimethylaminopropyl)carbodiimide hydrochloride
EPO	Erythropoietin
epPCR	Error-prone polymerase chain reaction
ESF	European science foundation
ESI-TOF MS	Electrospray ionization time-of-flight mass spectroscopy
FA	Folic acid
FDA	Food and Drug Administration
FRa	Folate acid receptor
FTIR	Fourier transform infrared
GC	Glycerol monocaprylate
GCSF	Granulocyte-colony stimulating factor
Gln	Glutamine
GRAS	Generally recognized as safe
GSH	Glutathione
HEMA	Hydroxyethyl methacrylate
HES	Hydroxyethyl starch
HES-DOX/cRGD	Hydroxyethyl starch-doxorubicin-cyclic arginyl-glycyl-aspartic acid peptide conjugate
HES-DOX/LHRH	Hydroxyethyl starch-doxorubicin-luteinizing hormone-releasing hormone conjugate
HES–EPO	Hydroxyethyl starch-erythropoietin conjugate
HES-FA	Hydroxyethyl starch-folic acid conjugate
HES-*g*-NH_2	Hydroxyethyl starch-*g*-hexamethylenediamine conjugate
HES-*g*-NH_2-R	Hydroxyethyl starch-*g*-hexamethylenediamine-rhodamine B-isothiocyanate conjugate
HES-Hyd-DOX	Hydroxyethyl starch-doxorubicin conjugate through hydrazine bond
HES-OA	Hydroxyethyl starch-oleic acid conjugate
HES-SS-DOX	Hydroxyethyl starch-doxorubicin conjugate through disulfide linkage
hGH	Human growth hormone
His	Histidine

HIV	Human immunodeficiency virus
HLE	Half-life extension
HMBC	Heteronuclear multiple bond correlation spectroscopy
HMDA	Hexamethylenediamine
HPMA	*N*-(2-hydroxypropyl)methacrylamide
h	Hour
HSQC	Heteronuclear single-quantum coherence
Hyd	Hydrazine
ICG	Indocyanine green
ICG@HES-OA	Indocyanine green-loaded hydroxyethyl starch-oleic acid nanoparticles
iRGD	Internalizing RGD (CRGDK/RGPD/EC, 9-amino acid cyclic peptide)
iRGD-HES-SS-C18	Hydroxyethyl starch-octadecanethiol-internalizing 9-amino acid cyclic peptide conjugate
kDa	Kilodalton
LDC(s)	Lipid drug conjugate(s)
LHRH	Luteinizing hormone-releasing hormone
LIPID MAPS	Lipid metabolites and pathways strategy
LPH	Lipid-polymer hybrid
Lys	Lysine
m/z	Mass-to-charge ratio
MCT	Medium-chain triglycerides
MDC	Monodansyl cadaverine
MLP	Mitomycin C lipid-based prodrug
MLV	Multilamellar vesicles
MMC	Mitomycin C
mRNA	Messenger ribonucleic acid
mTGase(s)	Microbial transglutaminase(s)
MTX	Methotrexate
MTX-HES	Methotrexate-hydroxyethyl starch conjugate
$NaBH(OAc)_3$	Sodium triacetoxyborohydride
$NaBH_3CN$	Sodium cyanoborohydride
nanoDSF	Nano differential scanning fluorimetry
NHS	*N*-hydroxysuccinimide
NLC(s)	Nanostructured lipid carrier(s)

nm	Nanometer
NMR	Nuclear magnetic resonance spectroscopy
NNI	National nanotechnology initiative
NST	Nanoscience and nanotechnology
O/W	Oil-in-water
OA	Oleic acid
PCL	Poly(ε-caprolactone)
PDI	Polydispersity index
PDSA	Poly(D-sorbitol adipate)
PEG	Poly(ethylene glycol)
PGA(M)	Poly(glycerol adipate), (M) refers to dimethyl adipate
PGA	Poly(glycolic acid)
PLA	Poly(lactic acid)
PLGA	Lactic and glycolic acid copolymers
PL-MLP	Pegylated liposomal formulation of mitomycin C lipid-based prodrug
PNGase F	Peptide-*N*-glycosidase F
PPh_3	Triphenylphosphine
PVE	Plasma volume expander
PVP	Poly(vinyl pyrrolidone)
rHuEPO	Recombinant human erythropoietin
rHuEPO-HES	Recombinant human erythropoietin-hydroxyethyl starch conjugate
SA	Stearic acid
SARS-CoV-2	Severe acute respiratory syndrome coronavirus 2
SDS-PAGE	Sodium dodecyl sulphate-polyacrylamide gel electrophoresis
SEM	Scanning electron microscopy
SEM	Scanning electron microscopy
SLN(s)	Solid lipid nanoparticle(s)
SQ	Squalene
SQACV	Squalene-acyclovir conjugate
SQgem	Squalene-gemcitabine conjugate
St-HES	Stearate-hydroxyethyl starch conjugate
STM	Scanning tunneling microscope
$t_{1/2}$	Half-life time
TEM	Transmission electron microscopy

TGase(s)	Transglutaminase(s)
T_m	Transition temperature
UV	Ultraviolet
W/O	Water-in-oil
W/O/W	Water-in-oil-in-water
WAXS	Wide-angle X-ray scattering

1. Introduction

1.1. Nanotechnology and nanomedicine

Nanoscience and nanotechnology (NST) are the emerging and interdisciplinary field of scientific research that focuses on the study of structural properties, design, development, and application of materials at the nanoscale range [1]. The National Nanotechnology Initiative (NNI) in the United States defines nanotechnology as the science involved in understanding and manipulation of materials at the atomic or molecular levels to generate structures with outstanding characteristics in terms of sizes and shapes at this scale, enabling innovative applications in various fields [2]. Simply, the study of nanostructure formation along with the development of the theoretical models and simulations that describe these nanoscale phenomena form the core of nanoscience, whereas nanotechnology harnesses these properties to create innovative solutions to longstanding challenges and develop novel technologies with unprecedented precision and functionality [3]. These nanoscale materials often exhibit unique physical, chemical, and biological properties that differ significantly from those observed at their larger-scale counterparts [4–6]. These properties open up a plethora of applications in areas like medicine, where nanoparticles can be engineered to targeted drug delivery, enhancing treatment efficacy and reducing side effects [7]; electronics, through the development of small and efficient semiconductors, improve solar cells performance, batteries, and other electronic devices by optimizing conductivity, development of more efficient energy storage devices and conversion technologies [8,9]; and environmental science, with the design of more effective catalysts and sensors [10–12].

Nanotechnology is considered a relatively modern innovation and a fairly new advancement in scientific research, its fundamental concepts indeed have a rich history that traces back to ancient civilizations often surprising how far back their applications extend. In the 4th century, the “Lycurgus cup” showcased an example of ancient Roman glassware exhibiting dichroic properties utilizing colloidal gold and silver that change color under different lighting sources. This phenomenon is attributed to the unique interaction of nanoparticles with light, demonstrating an early understanding of nanoscale materials [13,14]. By the medieval period between the 6th and 15th centuries, European cathedrals featured vibrant stained glass windows utilizing gold and other metal compound nanoparticles, highlighting the application

in art for creating rich coloration [15,16]. During the Italian Renaissance (15^{th}–16^{th} centuries), the production of lustered glazed majolica pottery by incorporating nanoparticle components further showcased the historical use of nanoscale materials [17]. The field of nanotechnology gained significant momentum in the 19^{th} and 20^{th} centuries. In 1857, Michael Faraday demonstrated the ability of colloidal gold to produce different colors under specific lighting, leading to various applications in optics and medicine [18]. Further advancements included the invention of transmission electron microscopy (TEM) in 1931 by Max Knoll and Ernest Ruska [19], scanning electron microscopy (SEM) in 1937 by Manfred von Ardenne [20], scanning tunneling microscope (STM) in 1981 by Gerd Binning and Heinrich Rohrer [21,22] and the discovery of atomic force microscopy (AFM) in 1986 by IBM scientists Gerd Binnig, Calvin Quate, and Christoph Gerber [23,24]. This enabled detailed imaging of materials at the nanoscale and laid crucial groundwork for nanotechnology research and applications.

The conceptual idea behind the nanoscale technology was first introduced by the renowned physicist Richard Feynman in his speech entitled “There’s Plenty of Room at the Bottom” at the California Institute of Technology (CalTech) on December 29, 1959 [25]. He envisioned the possibility of manipulating individual matters at atomic and molecular levels, which has often been credited as a key inspiration and foundation in the field of nanotechnology. More than a decade later, Norio Taniguchi in a 1974 conference, coined the term “nano-technology” [26]. Motivated by Feynman's ideas, K. Eric Drexler used the term “nanotechnology” independently in his 1986 published book “Engines of Creation: The Coming Era of Nanotechnology”, which has later been known as “molecular nanotechnology” [27]. He was known as the “founding father of nanotechnology” for establishing the core principles of molecular engineering and outlining the application of advanced nanotechnologies [28].

Nanotechnology has emerged as a promising area of innovation with wide-ranging applications, impacting nearly every facet of contemporary life. In particular, its integration with medicine has given rise to the development of a new scientific discipline known as nanomedicine. The origin of nanomedicine indeed has early roots in ancient civilizations in the context of traditional medicine and materials science. Ayurvedic Bhasma referred to as “Swarna Bhasma” represents an excellent example of ancient nanomedicine [29]. This Ayurvedic preparation was the colloidal form of gold which was used in traditional Ayurvedic medicine for various purposes, including rejuvenation and the treatment of various diseases [30]. However, the modern field of nanomedicine began to take place in the 20^{th}

century, particularly with the contributions of pioneering scientists Elie Metchnikoff and Paul Ehrlich. Metchnikoff's work focused on phagocytosis and the immune system [31], while Ehrlich is renowned for his development of the “Zauberkugel” or “magic bullet” concept— a targeted drug therapy without affecting healthy tissues [32]. The term "nanomedicine" was first introduced in 1991 in “Unbounding the Future. The Nanotechnology Revolution” [33] and became widely established after the book “Nanomedicine” published by Robert A. Freitas in 1999 [34]. The European Science Foundation (ESF) defined nanomedicine as follows: “*Nanomedicine uses nano-sized tools for the diagnosis, prevention, and treatment of disease and to gain an increased understanding of the complex underlying pathophysiology of disease. The ultimate goal is to improve quality of life*” [35].

Nowadays, nanomedicine covers a diverse range of fields, significantly improving healthcare through innovative applications in drug delivery, vaccine development, biosensors, microfluidics, medical implants, and microarray tests to tissue engineering using nanoscale materials [36–38]. Nanomedicine-associated drug delivery investigations started drastically when Bangham for the first time prepared lipid vesicles (liposomes) around 1965 [39], and in the mid of the 1970s, when Ringsdorf investigated the attachment of pharmacologically active ingredients to water-soluble polymers [40]. From this point onward, an incredible extent of studies has been conducted to design and develop nanocarrier-based drug delivery systems to ensure better safety, efficacy, and specificity [41]. Recently, nanocarriers for therapeutic delivery have gained significant attention in the field of advanced medicine after the most successful development of the SARS-CoV-2 mRNA vaccines [42]. The Pfizer-BioNTech and Moderna vaccines used lipid nanoparticles (a type of nanocarrier) to encapsulate and protect the fragile mRNA molecules, to deliver therapeutic agents specifically to target cells, and to release their payload in a controlled manner [43].

The development of therapeutic agents involves the integration of drug design and delivery to enhance the efficacy and safety of treatments. To leverage the advantages of current scientific advances, modern technology requires combining newer or existing therapeutic agents with nanotechnology platforms to alter their properties for effective drug delivery systems. Among the various nanomaterials used in biomedical and pharmaceutical applications, polymers such as polysaccharides and lipids have been extensively investigated as carriers for therapeutic delivery due to their versatility, biocompatibility, biodegradability, diverse functionality, and regulatory status.

1.2. Polysaccharides as therapeutic carriers

The fundamental properties of polymers utilized as biomaterials for the fabrication of therapeutic carriers include stability, biodegradability, and biocompatibility. Natural polymers inherently fulfill these criteria and are also recognized as being safe and non-toxic. These characteristics led to the extensive investigation of various natural polymers for their potential use as carriers for therapeutic delivery and other biomedical applications [44]. Among the natural polymers, polysaccharides are the most diverse and abundant macromolecules which are isolated from a wide range of renewable sources such as starch and cellulose from plants, agar and alginate from algae, chitin and hyaluronic acid from animals, dextran and xanthan from bacteria, pullulan and galactan from fungi [45] (Figure 1).

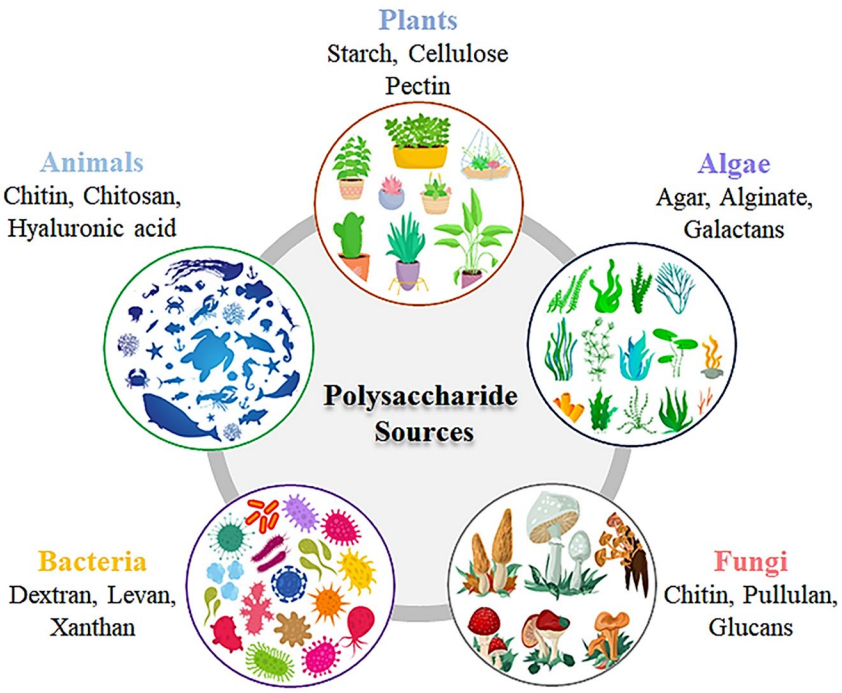

Figure 1. Sources of polysaccharides with examples [45].

Polysaccharides are long-chain linear or branched polymeric carbohydrates composed of monosaccharide repeating units linked by O-glycosidic bonds. The common repeating units of polysaccharides are d-glucose, d-fructose, d-galactose, l-galactose, d-mannose, l-arabinose, and d-xylose. Additionally, polysaccharides may contain various monosaccharide derivatives like amino sugars, such as d-glucosamine and d-galactosamine, along with their derivatives, N-acetylneuraminic acid and N-acetylmuramic acid [46]. Due to the varying chemical compositions, a wide range of molar masses, and the presence of various functional groups on

molecular chains such as hydroxyl, carboxyl, aldehyde, and amine groups, polysaccharides possess significant diverse structural properties and functional versatility [47]. Furthermore, the large number of reactive functional groups contribute to their hydrophilicity, allowing for aqueous solubility and facilitating interactions with biological tissues through non-covalent bonds as well as enabling chemical and biochemical modifications to conjugate drugs or therapeutic agents according to the desired properties. These characteristics along with the available sources and low processing cost convert polysaccharides the key biomaterials for pharmaceutical applications and are classified as "generally recognized as safe" (GRAS) by the U.S. Food and Drug Administration (FDA) under the Federal Food, Drug, and Cosmetic Act [48]. The key attributes of polysaccharides are [49,50] :

Biocompatibility: Polysaccharides are biological macromolecules of natural origin that closely resemble components of the extracellular matrix, enabling to minimization of or avoiding immunological responses and providing high biocompatibility.

Biodegradability: Most polysaccharides are degraded in the body by enzymatic catalysis, leading to the formation of their monomeric or oligomeric units that can easily be eliminated from the body. Many enzymes such as glycosidases, hyaluronidases, esterases, proteases, and various other lysosomal enzymes facilitate polysaccharide degradation which in turn reduces side effects.

Diverse sources: Polysaccharides found abundantly in nature and their simple isolation and purification methods, make these polymers available at low cost for further applications.

Bioactivity: Many polysaccharides naturally exhibit bioactive properties and interact with tissue and mucous membranes which can be used to design carriers for target-specific drug delivery. Some polysaccharides have antimicrobial and anti-inflammatory effects such as chitosan and heparin.

Solubility: Several polysaccharides have very high aqueous solubility due to the large number of functional groups. This solubility can be altered through simple modification, for example, the solubility of chitin in an acidic medium can be tuned by modifying the degree of deacetylation.

Ease of modifications: Due to the presence of numerous functional groups on the backbone, polysaccharides give easy access for modifications through cross-linking, grafting,

esterification, etherification, and various other physical and chemical methods to produce novel semi-synthetic polysaccharide derivatives with extended functionality.

These characteristics make polysaccharides an ideal choice to develop potential carriers for advanced therapeutic delivery by combining the essential features from the nanoparticulate platform. Common examples of polysaccharides that have been extensively studied and utilized as drug-delivery vehicles are chitosan, alginate, hyaluronic acid, dextran, cellulose, starch, and pullulan [51] (Figure 2). Polysaccharides have been widely used as excipients in the pharmaceutical industry. However, they became increasingly popular in the field of drug delivery to conjugate drugs, proteins, DNA, and targeting antibodies and to develop nanocarrier-based polyelectrolyte matrix, hydrogels, films, and nanoparticles [52].

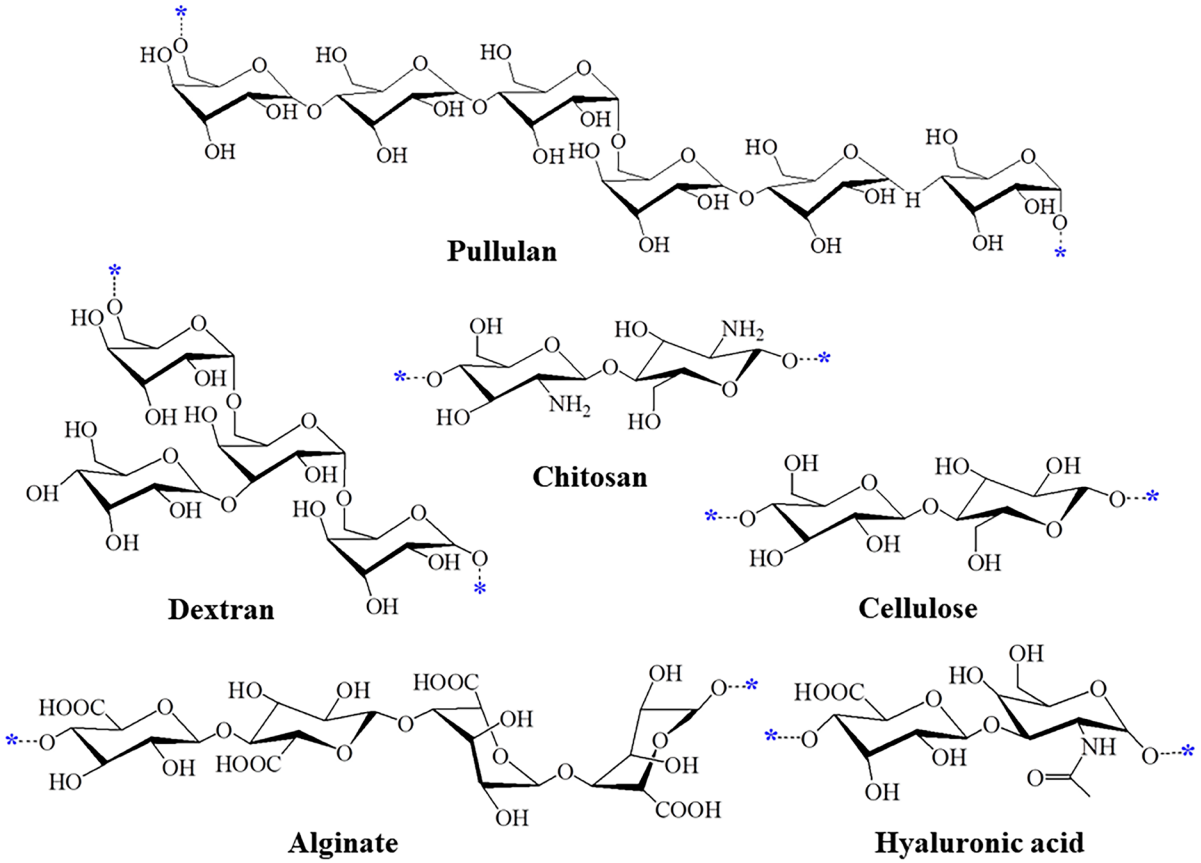

Figure 2. Common examples of polysaccharides used in drug delivery.

Despite their outstanding properties, the use of polysaccharides in drug delivery systems presents several potential challenges. One major issue is the variability of the molar masses which can differ significantly between batches of naturally sourced polymers, making it difficult to establish a precise delivery vehicle and a consistent drug delivery performance. Another significant challenge is that many polysaccharides are poorly soluble in organic

solvents, which limits their extent of possible modifications. Organic solvents are frequently employed in drug delivery system fabrication processes for functionalization or cross-linking. This poor solubility issue can hinder the development of polysaccharide-based drug delivery platforms and restrict the ability to tailor their properties for specific applications [53]. To address these challenges, improvements are necessary for quantifying and standardizing the physicochemical properties of polysaccharides. Such improvements are crucial for developing consistent drug delivery systems with well-defined characteristics that can advance to clinical trials [54]. Dextran-doxorubicin drug conjugate (AD-70, Phase I, 1993) was the first polysaccharide entering the clinical phase. Dextran-based formulations such as DE-310 (Phase I, 2005) and Delimotecan (Phase I, 2008) have also reached clinical trials over the years. Moreover, other polysaccharides that have entered the clinical phase including chitosan (Milican, Phase II, 2006); hyaluronic acid (RadiaPlex, Phase III, 2007), ONCOFID-P-B (Phases I and II, 2011); cyclodextrin (CALAA-01, Phase I, 2008), CRLX101/IT-101 (Phases I and II, 2012); alginate (DIABECELL, Phases I, II and III, 2009), IK-5001 (Phase I, 2010) and OligoG CF-5/20 (Phases I and II, 2014) [48].

1.2.1. Hydroxyethyl starch (HES)

Hydroxyethyl starch (HES) is a semi-synthetic derivative of the natural polysaccharide, starch, formerly utilized as a colloidal plasma volume expander (PVE) [55]. Starch is composed of two complex macromolecular components: amylose and amylopectin. Amylose is a flexible and linear chain polymer made of glucopyranose units connected by α-(1,4) glycosidic linkages. Though amylose is taken as a linear chain polymer, branched amylose has also been reported which contains few branches. Both types of amylose are long-chain polymers containing hundreds to thousands of glucosyl units. Amylopectin is a branched polymer with short α-(1,4) segments linked by α-(1,6) glycosidic branching points in every 25–30 glucose units. The extent of amylose and amylopectin in starch differs from plant to plant sources [56]. Hydroxyethyl starch is mainly composed of amylopectin, originated from waxy maize and less frequently from potatoes which is further modified by hydroxyethyl groups. The most preferred method to synthesize HES is, at first, the partial acid or enzymatic hydrolysis of starch-rich in amylopectin and then the etherification reaction with ethylene oxide in an alkaline medium followed by purification/fractionation of HES to adjust the polydispersity [57]. HES closely resembles the structure of glycogen, a branched polysaccharide that acts as energy storage in the human body. The structural interrelation of

HES to glycogen is possibly one of the most comprehensive reasons for its reduced immunogenicity and low hypersensitivity [58]. The structure of HES is shown in Figure 3.

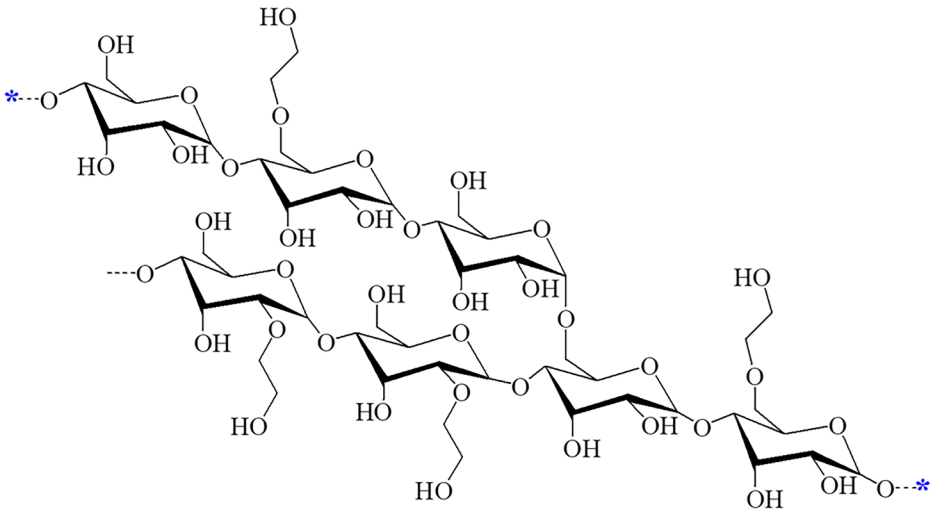

Figure 3. Structure of hydroxyethyl starch (HES).

Besides, hydroxyethylation conveys many new characteristics in starch, it increases mainly the solubility in water compared to starch and shows higher stability to hydrolysis. Most notably, an increase in *in vivo* half-life is observed after hydroxyethylation [59]. The half-life time of starch is a few minutes because of its rapid degradation by an intracellular enzyme called plasma α-amylase [60], however, it significantly increases for HES due to steric hindrance of the hydroxyethyl side chains. Moreover, it is possible to control the biodegradability of HES because the rate and extent of biodegradation can be modulated by altering the molar mass and the degree of hydroxyethylation [61]. Hydroxyethylation occurs at the hydroxyl functional group of the anhydrous glucose subunit (AGU) of the starch molecule or to that of an already attached hydroxyethyl group [62]. This etherification reaction takes place mainly at the C-2 and sequentially at C-6 and to a very lesser extent at the C-3 carbon atom [63]. The C-2 position of starch is clinically very important since an enzymatic breakdown by serum α-amylase happens more slowly when the substitution occurs predominantly at the C-2 position of HES rather than substitution at C-6 or C-3 positions and increases the blood circulation time. The degree of substitution of starch is finely tuned in such a way that the solubility of the starch is ensured and degradation by serum amylase is not prevented too extremely [64].

However, HES can present some limitations due to its variable properties. For instance, the branching patterns of amylopectin can vary depending on the source of starch and the pathway of synthesis. Furthermore, source-dependent molar mass variations, inconsistent and

random distribution of hydroxyethyl moiety on HES backbones, and polydispersity can influence the *in vivo* efficacy and potential side effects of HES [65]. Besides, some adverse effects have been reported for HES macromolecules. Some studies showed that a high dose of slowly metabolizing HES could interact with platelets and blood coagulation factors, for example, factor VIII and von Willebrand factor, which lead to coagulation impairment and decrease the plasma level of these factors [66–68]. Other studies claimed that HES administration could cause renal dysfunction or kidney injury [69,70]. On the other hand, some studies also reported no adverse effects on kidney functions after HES administration [71,72].

1.2.2. Applications of HES

HES is primarily used as a fluid replacement therapy under the trade name of VitaHES, Infukoll, Voluven®, and Hespan® to increase or maintain intravascular volume for critically ill patients in intensive care units [73]. It exhibits several distinct pharmacological properties such as improving serum colloid osmotic pressure and hemodynamics, reducing blood viscosity, reducing the systemic inflammatory response, inhibitory effect on blood coagulation functions, and minimizing colorectal cancer metastasis. Besides PVE, HES is also used as a cryopreservative agent and organ preservation solution [74].

Another applied field of HES is the development of designed carriers and nanoconjugates for the delivery of diagnostic and therapeutic drugs. The large number of free hydroxyl groups available for modification in designed manners, solubility, low immunogenicity, and prolonged *in vivo* half-life make HES an ideal choice as a carrier for developing HES-based drug delivery systems. Although some adverse effects have been reported using HES as PVE, however, for nanocarrier drug delivery experiments minimal concentrations are used compared to PVE, therefore, safety issues associated with HES are significantly reduced. To date, a wide range of therapeutic drug conjugation with HES has been investigated to develop HES-based drug delivery systems such as HES-drug conjugates, HES-protein conjugates, micelles, vesicles, nanocapsules, and hydrogels. For instance, Methotrexate (MTX) is an antifolate drug used for treating certain cancers and rheumatoid arthritis, but its clinical use is limited by dose-dependent liver toxicity. To address this, MTX was conjugated with HES through esterification to develop MTX-HES conjugates. The *in vivo* experiments demonstrated a significantly higher antitumor efficacy of HES-MTX conjugates than unconjugated MTX in MV-4-11 human leukemia cells and with CDF1 mice intraperitoneally

inoculated with murine leukemia cells of NOD/SCID mice. Another anti-cancer agent, 10-hydroxy camptothecin (10-HCPT) exhibits very low aqueous solubility and a short plasma half-life, limiting its clinical use. 10-HCPT was modified through the conjugation reaction with HES *via* ester bond formation to form 10-HCPT-HES conjugates. The modified 10-HCPT-HES conjugates showed increased water solubility of approximately 100 times, a half-life extension of 4.38 h from 10 min (free 10-HCPT), and a sustained release of the drug till 48 h [75]. Sleightholm et al. developed chloroquine-modified HES (CQ-HES) which revealed an improved ability of the conjugates to inhibit the migration and invasion of pancreatic cancer cells [76].

HES has also been used to develop stimuli-responsive nanoparticulate drug delivery systems. For example, doxorubicin-HES conjugates (HES-SS-DOX) were synthesized by conjugating DOX onto HES through a redox-sensitive disulfide bond and revealed the formation of a nano-assembly with a diameter of 19.9 ± 0.4 nm and glutathione (GSH)-mediated DOX delivery to the tumor microenvironment [77]. Consequently, Li et al. synthesized HES-DOX conjugates *via* pH-sensitive hydrazine (Hyd) bond to develop HES-Hyd-DOX conjugates and *via* acid-sensitive linkage to synthesize HES-DOX, cyclic Arg-Gly-Asp peptides (cRGD) conjugated HES-DOX/cRGD and luteinizing hormone-releasing hormone (LHRH)-conjugated HES–DOX/LHRH. Results showed that all the conjugates self-assemble to form nanoparticles and stimuli-responsive drug release in tumor cells with high efficacy and specificity [74].

Apart from that, HES was modified with particular hydrophobic moieties for the development of self-assembled nanocarriers to encapsulate different drugs and enhance their delivery. Hu et al. synthesized 1-octadecanethiol (C18) conjugated hydrophobic HES derivative *via* a redox-sensitive disulfide bond and further decorated with tumor blood vessels and tumor cells specific iRGD molecules to develop iRGD-HES-SS-C18 conjugates. In this study, DOX was encapsulated as a model drug. Results demonstrated the formation of nanoclusters which enhance iRGD targeted DOX delivery to the tumors and improved tumor cell internalization and permeability of the conjugates. In a separate investigation, oleic acid (OA) grafted HES conjugates (HES-OA) were synthesized and self-assembled into ICG-loaded nanoparticles. Combined with β-phenylethyl isothiocyanate, ICG@HES-OA nanoparticles showed enhanced synergistic tumor inhibition effects [75]. Lauric acid-modified HES displayed the formation of stable micelles or vesicles with a very low degree of grafting [78]. Recently, highly stearate-grafted HES conjugates (St-HES) were synthesized, and detailed

characterization was performed for both native HES and St-HES conjugates. Interestingly, the results showed a transition from amorphous HES to a semicrystalline character with increasing the degree of grafting and the conjugates were able to form self-assembled micelles. The increased hydrophobic segments in the core of the micelles may facilitate encapsulating water-insoluble drugs with high loading capacity and prolong the circulation time [79]. Additionally, HES has been employed to develop nanocapsules and hydrogels as effective therapeutic delivery systems [80]. Baier et al. developed HES-based nanocapsules using an inverse miniemulsion method through interfacial polyaddition reaction with diisocyanate followed by carboxymethylation and conjugation with folic acid (FA) as a model targeting agent. The HES-FA nanocapsule confirmed the potential of folate acid receptor (FRa) mediated capability towards HeLa cells. A HES-based hydrogel microsphere was prepared by introducing a polymerizable group, hydroxyethyl methacrylate (HEMA), which was then crosslinked *via* photopolymerization in a water-in-water (w/w) emulsion system. The hydrogel loaded with a model protein showed an initial burst release followed by a slower release rate which was extended till 4 months *in vitro* [80].

HESylation (coupling of HES with a desired moiety) has been widely used in the field of therapeutic protein polymer conjugation. Several investigations have been carried out after the first introduction of HES albumin conjugates by Richter and de Belder in the 1970s [55]. For instance, erythropoietin (EPO) was chemically conjugated with HES using two different strategies: targeting the glycosylation sites of the protein to introduce polymer and reductive amination of HES which allows for modification of the N-terminal α-amino group of the protein. Both HES-EPO conjugates exhibited significant *in vitro* and *in vivo* activities that are comparable to PEGylated (covalent coupling of poly(ethylene glycol) with desired molecules) EPO (Mircera®) [55]. Similarly, a dimeric erythropoietin mimetic peptide AGEM400 was covalently coupled with HES by Kessler et al. The study found that the AGEM400 (HES) conjugates efficiently increase the plasma half-life of AGEM400 and also activate *in vitro* erythropoiesis and stimulate survival of EPO-dependent UT7/EPO cell line [81]. Site-specific HESylation was applied by reductive amination using a HES derivative carrying an aldehyde linker to conjugate anakinra. HESylated anakinra increased the plasma half-life by around 6.5 times and bioavailability by around 45 times compared to native anakinra [82]. Recently, a site-selective enzymatic conjugation of HES with recombinant human erythropoietin (rHuEPO) was reported. The conjugation reaction was carried out between an amine-functionalized HES (HES-*g*-NH_2) and rHuEPO catalyzed by

thermoresistant variant mTGase TG[16]. The SDS-PAGE analysis revealed high molar mass conjugates as well as cross-linked aggregates. This demonstrated the site-specific HESylated rHuEPO conjugation using an enzymatic method under mild reaction conditions which may potentially lead to an increase in the half-life of rHuEPO [83].

1.3. Lipids as therapeutic carriers

The term lipids refers to a group of compounds that are structurally and functionally diverse, composed of fatty acids and their derivatives. These molecules are insoluble in water but readily soluble in organic solvents [84]. Lipids are the most essential structural constituents of cellular membranes and plasma and are responsible for many biological functions to regulate cell homeostasis. According to the Lipid Metabolites and Pathways Strategy (LIPID MAPS) consortium, lipids can be classified as fatty acids, glycerolipids, glycerophospholipids, sphingolipids, sterol lipids, prenol lipids, saccharolipids, and polyketides [85]. By varying the chain lengths and incorporating multiple functional groups, the diversity and physicochemical properties of these structures can be further expanded and modulated. The wide range of structural and functional variations opened up the possibilities of applying lipids as an essential alternative to synthetic polymers for the development of lipid-based nanocarrier drug delivery systems. By harnessing the distinctive properties, lipids play an essential role in fabricating designed nanocarriers for the efficient delivery of active substances. Lipid-based carriers offer a versatile platform to encapsulate and protect drugs as well as other active substances, allowing control and sustain release of the encapsulated substances while enhancing their stability and bioavailability to improve therapeutic efficacy [50].

Recent progress in lipid-based nanoparticles has revolutionized advanced drug delivery systems, particularly in pharmaceutical sciences, by providing enhanced solutions for addressing and combating various diseases. Consequently, researchers have exhibited significant interest in lipid-based nanocarriers due to their biodegradability, biocompatibility, non-toxicity, safe and non-immunogenic characteristics, making lipids a suitable candidate as carriers for delivering drugs through different routes of administration. A wide variety of lipid-based nanoparticles have been developed for drug delivery applications over the years including solid lipid nanoparticles (SLNs), nanostructured lipid carriers (NLCs), lipid drug conjugates (LDCs), liposomes, nanoemulsions, lipid extrudates and implants and lipid-polymer hybrid (LPH). The most extensively studied lipid-based nanocarriers are SLNs and

NLCs, however, the major drawback of these nanoparticulate systems is the limited loading capacity of the hydrophilic drugs due to the partitioning effect. To address this challenge, one of the strategic pathways that have been employed is the designing of lipid drug conjugates (LDCs). Moreover, LDCs gained particular attention for their potential in medical and drug development applications [86].

LDCs are modified chemical entities in which the active substances are linked with lipids *via* covalent or non-covalent interactions. Different lipids such as fatty acids, glycerides, steroids, and phospholipids (Figure 4) have been utilized to synthesize LDCs which enhance the lipophilicity of parent drugs and alter the other drug characteristics.

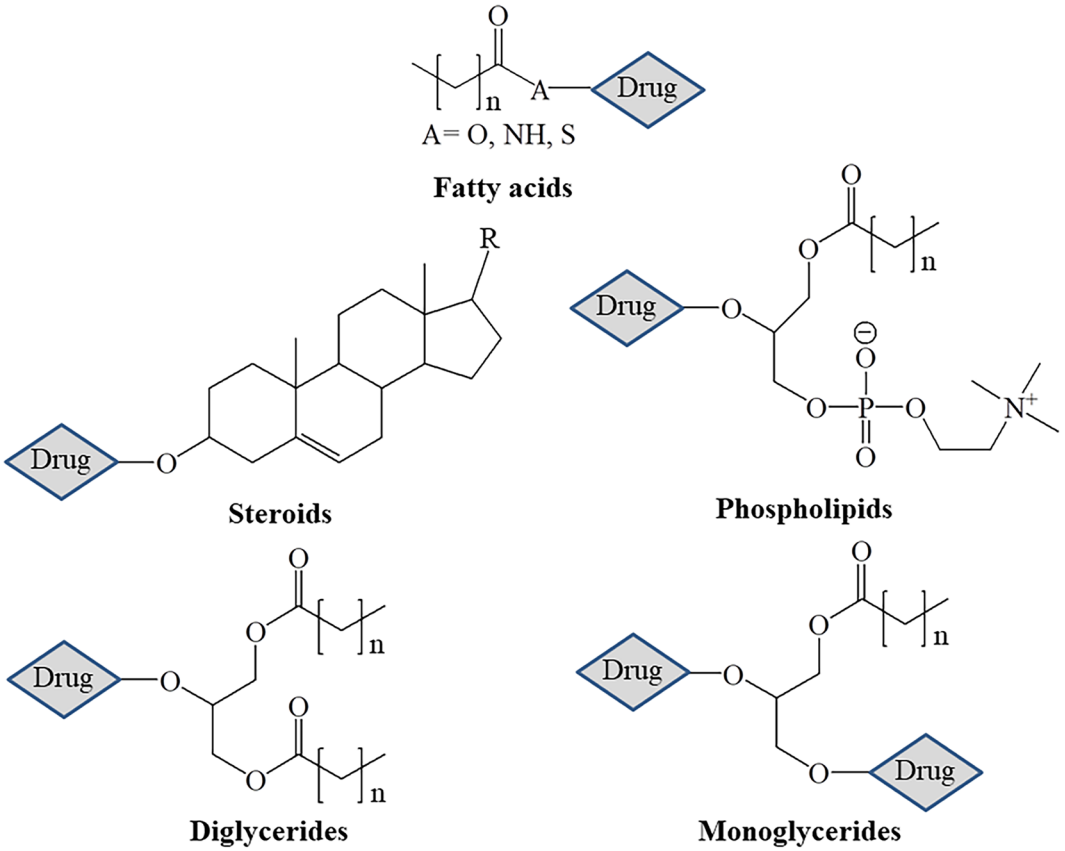

Figure 4. General structures of lipids used for lipid drug conjugates (LDCs).

Moreover, LDCs exhibit several advantages including increased systemic bioavailability, improved targeted drug delivery, extended drug release, enhanced drug diffusivity, increased drug loading capacity and stability, overcome drug resistance, and decreased toxicity [87]. LDCs can be administered without further requirements of delivery carriers because the conjugation of a lipid with a drug may produce an amphiphilic molecule that can form self-assembled nanoparticles. Several studies have been performed to deliver LDCs effectively without a delivery carrier. For instance, squalene, a most commonly used lipid for LDCs, has

the ability to self-assemble into nanoparticles in aqueous solutions. Couvreur et al. synthesized squalene-gemcitabine conjugate (SQgem) which formed nanoassemblies by simple precipitation in water [88]. The cryogenic transmission electron microscopy revealed hexagonal or multifaceted shape nanoassemblies with an average particle size of 104 nm in which water and gemcitabine were at the core surrounded by squalene molecules, showing improved anticancer effects in different tumor cell lines. The self-assembled SQgem conjugates exhibit greater anticancer activity in the P388 subcutaneous-tumor-bearing mice. Similarly, the antiviral drug acyclovir (ACV) has been conjugated with squalene (SQ) molecules to develop amphiphilic SQACV conjugates and found that the self-assembled SQACV enhances ocular bioavailability of ACV [89]. Although carrier-free self-assembled LDCs showed promising outcomes for drug delivery, most LDCs are usually integrated into various delivery platforms like lipid nanoparticles, liposomes, micelles, nanoemulsions, and others to improve targeted drug delivery, protect from degradation, and prevent dose dumping. The release of drugs from LDC-loaded formulations involves two crucial steps that could positively impact the pharmacokinetic profile of drugs. Initially, the LDC is released from the formulation through diffusion or erosion. Next, the released LDC is converted into the parent drug by gastrointestinal or other physiological enzymes [90]. In general, LDC-loaded formulations provide the kinetic stability of the dispersed particles by reducing the interfacial tension between the dispersed phase and dispersion medium by increasing the surface-to-volume ratio [91]. LDC-loaded formulations have been widely investigated by utilizing different delivery platforms. Gabizon and coworkers reported the synthesis of mitomycin C lipid-based prodrug (MLP) where mitomycin C (MMC) conjugated with a glyceride lipid moiety, di-stearic acyl glycerol, through a dithiobenzyl bridge. The PEGylated liposomal formulation (PL-MLP) of MLP showed an extended plasma half-life of MLP (10–15 h), high *in vitro* stability, and no drug leakage in mouse tumor models. PL-MLP also observed delayed tumor growth, higher tumor regression and reduced toxicity in human gastroentero-pancreatic tumor models of mice [92]. In another study, a highly lipophilic squalenoyl-paclitaxel prodrug was obtained by using paclitaxel and 1,1′,2-*tris*norsqualenoic acid *via* carbodiimide reaction, aiming to enhance the incorporation efficiency in phospholipid multilamellar vesicles (MLV) formulation. The authors found that the incorporated lipophilic squalenoyl–paclitaxel prodrug was retained in the MLV and the encapsulation efficiency was increased compared to parent paclitaxel [93]. Recently, a nanoemulsion preconcentrate formulation containing dimeric artesunate glycerol monocaprylate conjugates (D-AS-GC) was reported. D-AS-GC was synthesized by applying

the dimerization concept using antimalarial drug artesunate (AS) and a dimeric moiety glycerol monocaprylate (GC). Subsequently, a lipid-based nanoemulsion formulation was developed as a carrier for lipophilic D-AS-GC. The results demonstrated the successful synthesis of D-AS-GC and a transparent D-AS-GC containing nanoemulsion formulation upon dilution in an aqueous phase. Moreover, AFM investigations revealed the evaporation-induced coalescence of the droplets which clearly visualized the formation of a core shell-like structure containing the lipophilic D-AS-GC in the inner cavity of the droplets composed of oil phase with an outer layer of surfactant/cosurfactant [94].

1.4. Conjugation strategies

1.4.1. Chemical conjugation

Several chemical strategies have been developed to achieve an effective conjugation reaction between therapeutic agents with the carriers. Figure 5 represents a summary of the most common chemical reactions used in organic synthesis and pharmaceutical drug delivery.

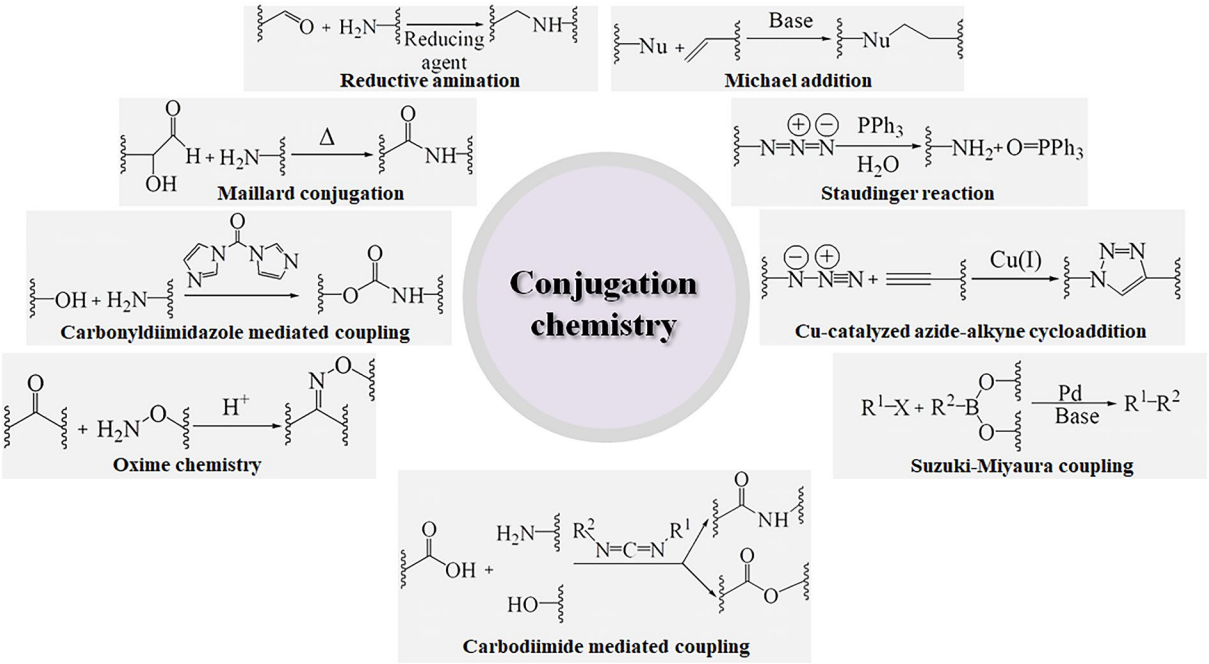

Figure 5. Some common chemical strategies used for conjugation reactions.

Reductive amination

Reductive amination is a well-established and popular method in pharmaceutical and organic chemistry for the efficient and rapid formation of C–N bonds, facilitating the attachment of amines to carbonyl-containing compounds, such as aldehydes and ketones [95]. This process involves an initial reaction of the carbonyl group with a primary amine under acidic

conditions to form a hemiaminal intermediate, which then undergoes dehydration to produce an unstable reversible imine or iminium ion intermediate (Schiff base) [96]. Subsequently, the imine intermediate is irreversibly reduced using a mild reducing agent at room temperature to yield the desired amine bond between the substrate of interest. Hydrogenation using various catalysts and borohydrides such as sodium cyanoborohydride ($NaBH_3CN$) and sodium triacetoxyborohydride ($NaBH(OAc)_3$) are commonly used as reducing agents due to their high selectivity for imines and minimal reactivity with other oxo groups [97–101]. Reductive amination has been applied across different fields particularly in organic synthesis [102,103], pharmaceuticals and therapeutic delivery [96,104,105], materials sciences [106], and agrochemicals [107,108].

Maillard conjugation

The Maillard reaction is a rapid, non-enzymatically catalyzed reaction which occurs between amino acids and reducing sugars when heated [109,110]. The French chemist Louis-Camille Maillard first described the Maillard reaction in 1912 and the mechanism was explained by an African-American chemist John E. Hodge in 1953 [111–114]. The Maillard reaction is initiated by the condensation between the amino groups and the reducing sugars to produce a Schiff base [115]. The reaction is followed by a series of complex reactions and goes through Amadori rearrangement to give a more stable Amadori product [116]. The final stage results in the formation of various products such as *n*-formylated drugs and melanoidins which are brown nitrogen-containing polymers and co-polymers [109,117,118]. As the Maillard reaction is a natural, nontoxic, and effective method [119], it has been widely applied in the food industry for protein modification with diverse flavors, aromas, and textures [116,120–123]. Moreover, the Maillard reaction attracted scientific interest in the fields of pharmaceutical drug delivery to develop polysaccharide-protein Maillard conjugate-based nanoparticles [124–130].

Copper (Cu)-catalyzed azide-alkyne cycloaddition

Click chemistry has received tremendous interest as an emerging technique in the fields of biomedical science, material science, and chemistry due to its biocompatibility and bioorthogonality [131,132]. The term “click chemistry” was introduced by K. Barry Sharpless and coworkers in 2001 in the field of drug discovery [133,134]. The Cu-catalyzed azide-alkyne 1,3-dipolar cycloaddition (CuAAC) is a prominent example of click reaction and is exploited widely in various fields such as polymer functionalization, bioconjugation, liposomes, metal and silica nanoparticles and dendrimers [135–140]. The reaction involves

cycloaddition between an azide and a terminal alkyne catalyzed by Cu(I) at room temperature, both in aqueous media and organic solvents, and applied for various applications [141,142].

Oxime chemistry

Oxime chemistry has become increasingly popular in recent years due to its ease of synthesis and is now being utilized in a wide range of applications. Oximes are synthesized by condensation reaction between aldehydes or ketones and aminooxy groups in a slightly acidic medium, resulting in the formation of ketoximes or aldoximes [143]. As members of the imine family, oximes are also known as Schiff's bases when all R groups are alkyl or aryl [144,145]. Although imines are typically unstable, the presence of an oxygen atom near the amine in the aminooxy group (known as the α-effect) enhances the oxime bond's stability under physiological conditions, making it suitable for conjugation [146,147]. Oxime ligations have been applied for numerous applications, mainly in the field of bioconjugation and in industry for the production of caprolactam [148–153].

Michael addition

The Michael addition discovered by Arthur Michael, is a versatile synthetic methodology for the coupling reaction between nucleophiles with activated olefins or alkynes, resulting in the nucleophile adding across a carbon-carbon multiple bond [154]. The Michael addition is a special type of 1,4-conjugate addition reaction that refers to the addition of an enolate-type nucleophile known as ‘Michael donor’, in the presence of a catalyst to an activated α,β-unsaturated carbonyl-containing compound, known as ‘Michael acceptor’. This reaction is further proceeded by generating a negatively charged enolate intermediate that upon protonation forms the Michael adduct [155–159]. The Michael addition yields highly selective products with high conversions and favorable reaction rates under mild reaction conditions [160,161]. Michael addition reactions are widely applied in organic synthesis, materials chemistry, surface modification, bioconjugation, and polymer synthesis and modifications [162–165].

Staudinger reaction

The Staudinger reaction is an important method in organic chemistry for its utility in synthesizing amines from azides and was first described by Hermann Staudinger in 1919 [166]. It involves the reaction between an azide and a phosphine using triphenylphosphine (PPh_3) as the reducing agent. The reaction proceeds through the formation of an

iminophosphorane or aza-ylide intermediate and nitrogen gas, which then hydrolyzes in the presence of water to produce the desired amine and triphenylphosphine oxide as a by-product [167,168]. The reaction is considered to be a mild, stable, and highly selective process under physiological conditions [169]. The Staudinger reaction was first introduced by Saxon and Bertozzi in the field of glycobiology and till then it is a well-established chemical method for bioconjugation [170,171]. This method has been commonly used for the labeling of chemical probes to biomolecules such as glycans [172–174], lipids [175–177], proteins [178–180], and DNA [181–183]. Furthermore, the Staudinger method is also utilized as a useful synthetic method for the synthesis and modification of various peptides/proteins [184–186], construction of microarrays [187–189], cell surface engineering [190–192], and drug delivery [193,194].

Suzuki-Miyaura coupling

The Suzuki–Miyaura coupling reaction is a suitable and highly effective technique for the formation of new carbon-carbon bonds [195]. Suzuki and Miyaura first introduced the synthesis of arylated-alkenes using palladium as a catalyst in 1979, since then the Suzuki-Miyaura coupling has become widely applied in the synthesis of various organic compounds and complex molecules, both in industry and academic research [196]. In the Suzuki–Miyaura coupling reaction, an organoboron compound (boronic acid or boronic ester) and an organohalide are cross-coupled using a palladium catalyst in the presence of a base in a suitable organic solvent [197–200]. This reaction has been widely used for the of amino acids and peptides/proteins functionalization [201–205], polymer synthesis [206], polymer-protein conjugation [207], and drug discovery and development [208].

Carbodiimide and carbonyldiimidazole-mediated coupling

Carbodiimide and carbonyldiimidazole-mediated coupling are the most universal methods for the labeling and conjugation of small molecules and biomolecules with the targeted moiety. Carbodiimide-based coupling is the most common method for the activated esters preparation using 1-ethyl-3-(3-dimethylaminopropyl)carbodiimide hydrochloride (EDC·HCl), *N,N′*-di cyclohexylcarbodiimide (DCC), and *N,N′*-diisopropylcarbodiimide (DIC) as activating agents [209]. Among them, the EDC-based coupling strategy has been widely investigated. It is considered a zero-length cross-linking agent employed to couple carboxyl groups with amines or alcohol, thereby forming stable covalent amide or ester bonds, respectively [210]. EDC is a water-soluble crosslinker which activates carboxylic acid groups suitable for coupling primary amines and hydroxyl groups and subsequently forms reactive O-acylisourea

intermediates. The O-acylisourea intermediate can readily rearrange to water-soluble by-product N-acylurea that can easily be removed by simple dialysis or gel filtration [211,212]. *N*-hydroxysuccinimide (NHS) or sulfo-NHS and DMAP (4-dimethylaminopyridine) are often used in combination with EDC as the catalyst to enhance the coupling efficiency and to produce a stable intermediate [213,214]. This coupling strategy has been extensively applied in the field of peptide/protein crosslinking [215,216], immobilization of macromolecules [217], therapeutic delivery [79,218–220], nanoparticle functionalization [221,222], and surface modification [223,224].

Another commonly used and safe coupling agent is 1,1′-carbonyldiimidazole (CDI) [225], useful for the preparation of carbonates, ureas, amides, carbamates, urethanes, and esters [226–229]. The CDI-mediated coupling reaction proceeds with the formation of a reactive intermediate N-acylimidazole, which subsequently reacts with amines or alcohols to form stable covalent bonds with the liberation of imidazole and carbon dioxide as byproducts [230]. The CDI coupling reaction has been applied for various applications such as peptide synthesis [231–235], synthetic chemistry [236,237], enzyme and ligand immobilization [238,239], therapeutic delivery [83,240,241], and in the pharmaceutical industry [242,243].

1.4.2. Enzymatic conjugation

The increasing demand for proteins, peptides, and enzymes in commercial uses has driven the importance of advanced tools to modify these molecules [244]. Functionalizing proteins with small molecules and other macromolecules facilitates the protein-based products to enhance stability, target drug delivery, create novel materials, and improve robustness [245–249]. Different chemical conjugation strategies have been utilized in protein functionalization due to robustness and high conversion rates. However, these approaches have several shortcomings such as lack of site specificity, selectivity, and instability of proteins under harsh reaction conditions. Moreover, the conjugation reactions with lysine (Lys), the most abundant surface residue in proteins, produce a heterogeneous mixture of the resulting conjugates which in turn decrease the bioactivity of the protein [250,251]. For example, lysine was modified *via* *N*-hydroxysuccinimide (NHS) chemistry, leading to heterogeneous conjugates with altered pharmacokinetic and therapeutic properties [252]. The less abundant cysteine residue has also been modified through maleimide coupling, resulting in the formation of unstable thiosuccinimide [253,254]. Apart from chemical coupling, enzyme-mediated bioconjugation has been employed as an alternative approach for protein conjugation in the chemical and pharmaceutical industry due to high reactivity, site

specificity, regioselectivity, and efficiency under mild reaction conditions [255]. Different enzymes have been widely used for protein modification such as peptidases (subset of the hydrolase family) class including sortase A and subtiligase; transferases class including transglutaminase, farnesyltransferase, *n*-myristoyl transferase and phosphopantetheinyl transferases; ligase class including tyrosine ligase, lipoic acid ligase and biotin ligase; and oxidoreductases class including formylglycine generating enzyme, laccases, peroxidases and tyrosinases [256,257]. Among those enzymes, transglutaminases are one of the most comprehensively studied transferase classes for site-specific protein modification.

1.4.2.1. Transglutaminases

Transglutaminases (TGases, EC 2.3.2.13) are the most studied and well-established enzyme in the field of enzymatically catalyzed protein modification. For protein conjugation, TGases are specifically selective for one or few glutamine (Gln) residues (act as acyl donors) of the targeted protein, while flexible regarding the amine-containing acyl acceptors, allowing various possibilities for modification [258]. TGases are protein-glutamine γ-glutamyltransferases that catalyze acyl-transfer reactions by transferring the acyl group from the γ-carboxamide of a protein-bound Gln residue to various linear primary amines including the ε-amino group of lysine residues, forming an isopeptide bond with formation of ammonia as a by-product (Figure 6). Depending on the acyl acceptor substrate, TGases can modify proteins by incorporating primary amines such as alkylamine or an oligoamine, intra- and inter-molecular protein crosslinking *via* lysine residues, and water (act as acyl acceptor) assisted deamidation of Gln residues [259]. TGases are mostly distributed in mammalian tissues and body fluids, plants, and microorganisms [260,261]. TGases are widely used in the food industry, biomedical engineering, textiles, and leather processing [262]. TGase was first isolated and purified from guinea pigs and until the late 1980s, was the only primary source of this enzyme for commercial use [263]. However, the widespread industrial use of this TGase has been constrained by its calcium-dependent transamidation activity, limited availability of the sources, and high production costs [264]. To optimize these limitations, extensive investigations have been conducted to screen TGases by genetic engineering and from microbial origins that are typically economical and can be produced in large quantities with high purity [265].

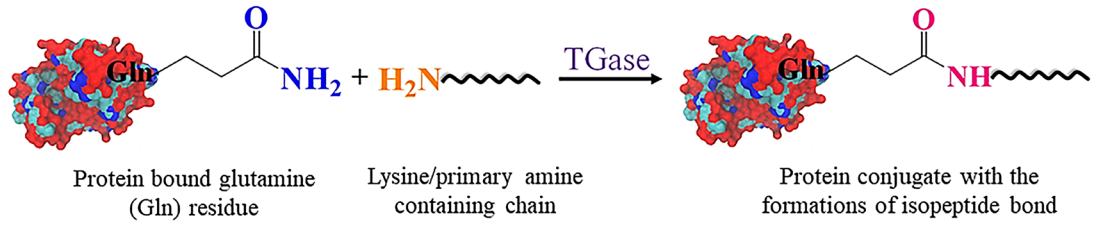

Figure 6. Schematic representation of TGase-catalyzed coupling reaction.

1.4.2.2. Microbial transglutaminases

Genetic engineering using host microorganisms is an important strategy to obtain TGases in large amounts at low prices for industrial, medical, or research applications. Several researchers have tried to produce genetically modified TGases, such as expressing guinea pig liver TGase in E. coli, *Streptoverticillium* TGase in E. coli, human factor XIIIa in yeast and *Streptomyces* species, but due to regulatory and consumer issues, none have been accepted for commercial uses [266–269]. Afterwards, screening of TGase from microbial sources was conducted in collaboration with Amano Pharmaceutical Co. using the hydroxamate assay and found a microorganism with calcium-independent TGase activities [270]. The enzyme known as microbial TGase (mTGase), a variant *Streptoverticillium mobaraense* (later classified as *Streptomyces mobaraensis*), facilitates the large-scale production of TGase using conventional fermentation technology [269,271]. The enzyme has been approved by the FDA as a generally recognized as safe (GRAS) substance for human consumption [272].

mTGase is a simple monomeric protein composed of a single polypeptide chain of 331 amino acids, a molecular mass of 37.9 kDa, and an isoelectric point of 8.9. It has a tertiary disk-like structural domain with an α/β fold determined by eight β-strands surrounded by 11 α-helices and overall dimensions of 65 × 59 × 41 Å. The active center of mTGase is composed of a catalytic Cys-Asp-His triad (cysteine 64, aspartic acid 255, and histidine 274 residues) where the thiol group of Cys64 is the key residue for catalytic cross-linking activity [273].

The catalytic mechanism of mTGase begins with a nucleophilic attack by the thiol group of Cys64 on an acyl donor Gln residue of protein (step 1). Asp255 then donates a proton, forming a thioester **Intermediate I** and releasing ammonia (steps 2 and 3). An amine substrate (acyl acceptor) proceeds towards the active carbonyl group of the thioester **Intermediate I** and subsequently the nucleophilic attack by negatively charged Asp255 to a proton of the amine leads to a thioester **Intermediate II** formation (step 4). Finally, the cross-

linked product is released from the thioester **Intermediate II**, regenerating the free enzyme (steps 5 and 6) [273]. The mTGase-mediated catalytic mechanism is shown in Figure 7.

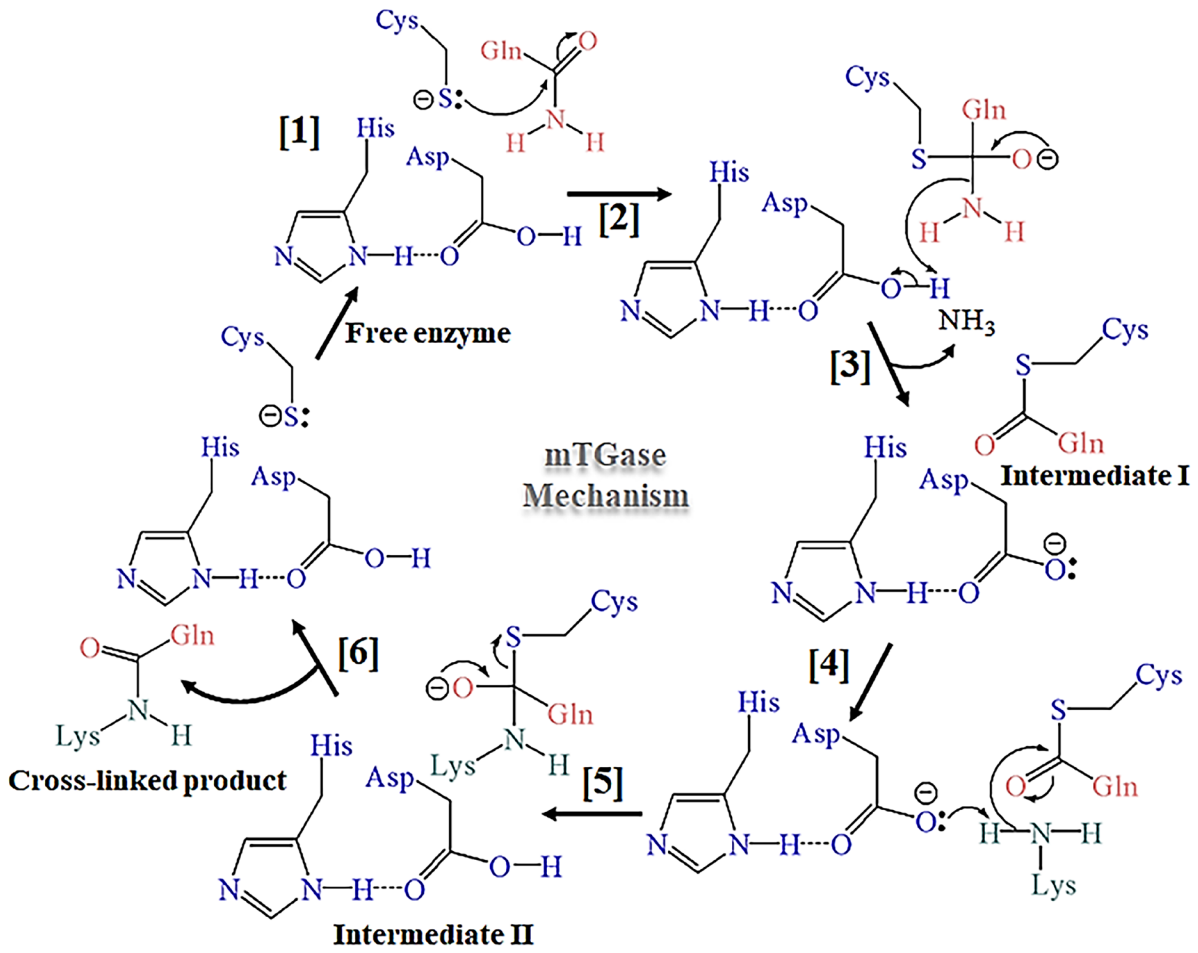

Figure 7. mTGases-catalyzed reaction mechanism. His, Histidine; Cys, Cysteine; Asp, Aspartic acid; Lys, Lysine and Gln, Glutamine [273].

The catalytic activity of mTGases highly depends on the reaction condition and the presence of metal ions. For example, mTGase from *Streptomyces mobaraensis* shows maximum activity at 55 °C while losing its activity at 70 °C within in few minutes. For a range of mTGase species, the temperature between 45–55 °C and pH around 5 to 8 are considered as optimal for mTGases activity and stability. In addition, metal cations such as Li^{+}, Cu^{2+}, Zn^{2+}, and Pb^{2+} inhibit the mTGases activity by binding with and blocking the thiol group of the single cysteine residue [274,275]. mTGase is Ca^{2+} independent which is a very useful property for food protein modification such as myosins, milk caseins, and soybean globulins. These are sensitive to Ca^{2+}, readily precipitate, and show less sensitivity to mTGases [276]. Moreover, the catalytic activity of mTGase depends on the flanking amino acids near to Gln

and Lys residues. Investigation on recombinant *Streptomyces mobaraensis* mTGase shows that hydrophobic and basic residues, particularly arginine, tyrosine, and leucine, favorably enhance the mTGase activity at Gln+1 and Gln-1 positions, while negatively charged amino acids at Gln-1 inhibit it. On the other hand, Proline is only accepted at Gln-1 but not at Gln+1, and peptides with Lys at Gln+1 or Gln-1 are not recognized due to potential cross-linking. For acyl acceptor substrates, peptides with aromatic amino acids near Lys or those containing two Lys residues exhibit higher activity, while those with negatively charged residues at Lys+1 or Lys-1 are not accepted by mTGase [277]. Additionally, mTGase prefers flexible and unfolded protein regions, as shown by Spolaore et al., who found that mTGase recognized the amino acids Lys127, Lys164, and Gln101 located in such regions for site-specific modifications [278,279].

Many efforts have focused on developing mTGase variants with enhanced activity and thermal stability since some cross-linking reactions catalyzed by mTGase require high temperatures to maintain enzyme bioactivity. A screening method was first introduced by Marx et al. for the development of thermostable and heat-sensitive mTGase variants by random mutagenesis. Seven mutants namely S2P, S23 L, Y24 N, G257S, K269E, H289Y, and L294 M were produced using error-prone polymerase chain reaction (epPCR) and demonstrated significantly enhanced thermostability at 60 °C. The S2P mutant which involved the substitution of a single amino acid (Serine with Proline) near the N-terminus, particularly exhibited a 270% increase in $t_{1/2}$ at 60 °C and higher specific activity at 37 °C [280]. In another study, atmospheric and room temperature plasma (ARTP) mutagenesis was utilized to enhance the fermentation production of TGase from *Streptomyces mobaraensis* for food industry applications [281]. Recently, a new thermoresistant variant of mTGase, TG^{16}, was developed using recombinant engineering on E. coli BL21Gold (DE3) cells and a combination of a series of amino acid substitutions, particularly S2P, S23Y-Y24 N, H289Y, and K294L. The mTGase-TG^{16} variant shows a 19-fold improved $t_{1/2}$ at 60 °C within 38 min compared to the wild-type mTGase [282]. mTGase is widely used in the food industry for restructured meat products, dairy products like cheese curd and yogurts, wheat products, baking, edible films, textiles, and leather manufacturing. Besides, mTGase is also potentially applied in the biomedical and pharmaceutical fields for site-specific antibody-drug conjugations, protein-protein conjugations, and polymer-protein conjugations and for immobilization of target molecules on solid supports [257]. Many studies have reported the mTGase-catalyzed PEG conjugation (PEGylation) to human GCSF, human growth hormone

(hGH), and recombinant human interleukin-2 with an improved pharmacokinetic profile of the therapeutic proteins [283–285]. Additionally, PGA(M) (poly(glycerol adipate)) and HES conjugation with a model protein, dimethylcasein (DMC), *via* mTGase-mediated coupling has also been reported [286,287]. Recently, a sugar-based amine grafted poly(D-sorbitol adipate) (PDSA) has been conjugated with recombinant human erythropoietin (rHuEPO) using a thermoresistant variant of mTGase TG^{16} at the transition temperature T_m of rHuEPO (54.3 °C) [288]. This new polyester-based rHuEPO-PDSA conjugates opened up new possibilities for utilizing this enzymatic method for therapeutic protein conjugation with potential applications. Accordingly, amine-functionalized HES conjugated with rHuEPO using the same TG^{16} variant to develop biodegradable and water-soluble rHuEPO-HES conjugates could potentially enhance the pharmacokinetics properties of rHuEPO [83].

1.5. Formulation strategies

To achieve efficient delivery of the therapeutic agents, several formulation strategies have been established to develop nanocarrier platforms in the field of nanomedicine. Some of these nanocarrier systems are briefly described below and illustrated in Figure 8.

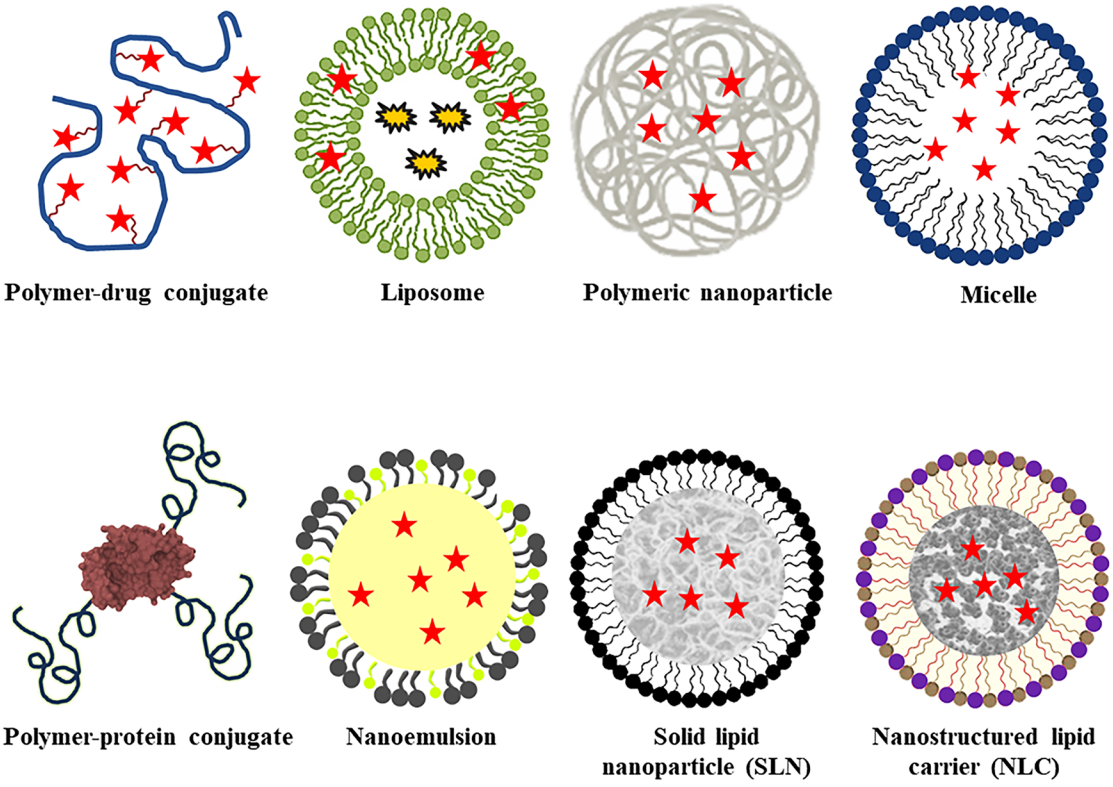

Figure 8. Different nanocarrier systems for therapeutic delivery.

Polymer-drug conjugates

Polymer-drug conjugates can be defined as a system in which the pharmacologically active drug molecules are covalently attached to the polymer backbones commonly through a biodegradable linker with or without additional attachment of solubilizer, targeting moieties or diagnostic agents. Polymer-drug conjugates offer several advantages such as better drug solubility, extended plasma half-life, increased bioavailability, enhanced therapeutic effectiveness, controlled drug release, protection from degradation, reduced drug toxicity and side effects, and improved overall pharmacokinetic profiles and patient compliances. The most important factors that influence polymer-drug conjugations are the selection of polymers, selectivity of functional groups, and biodegradable bond formation to release the drugs in their active form to their target sites [214]. The polymer-drug conjugate was first reported by von Horst Jatzkewitz who conjugated poly(vinyl pyrrolidone) (PVP) with a psychedelic alkaloid mescaline through a glycylglycine spacer. Consequently, numerous synthetic polymers have been extensively studied to achieve an efficient delivery of drugs. Among synthetic polymers, PEG is widely used as a gold standard for polymer-drug conjugations and many PEG-based drug products are already in the clinical trial or approved by the Food and Drug Administration (FDA) for the treatment of various diseases. Besides, various natural biopolymers have also been explored as substitutes to commonly used synthetic polymers for the development of polymer-drug conjugates [289].

Polymer-protein conjugates

Proteins are widely used for the treatment of various diseases such as cancer, autoimmune diseases, diabetes, and others. While proteins provide high therapeutic activity and specificity, these therapeutic agents face challenges like short plasma half-life, poor stability, low solubility, immunogenicity, and rapid renal clearance which limit their effectiveness. Thus, there have been ongoing efforts to find better alternatives for protein delivery. Polymer conjugation with therapeutic proteins has been proven as an effective method to address the aforementioned issues. Covalent coupling of PEG with bovine serum albumin (BSA) was the first developed polymer-protein conjugate reported by Abuchowski et al. The PEG-BSA conjugates showed a prolonged plasma half-life, low immunogenicity, and better solubility compared to native BSA [290]. Subsequently, many PEGylated proteins have been investigated and approved for the treatment of various diseases. To date, PEG is the most widely used and accepted polymer for clinical applications due to its water solubility, flexibility, and biocompatibility. Besides, PEG provides a “stealth effect” that reduces

interactions between proteins and the reticuloendothelial system, thereby preventing rapid clearance [291]. Additionally, highly functional water-soluble, biocompatible, and biodegradable polymer alternatives, including polyester and polysaccharides-based protein conjugates have also been synthesized and evaluated for expanding the field of polymer–protein conjugations. For example, PDSA and HES have been enzymatically conjugated with rHuEPO *via* mTGase-mediated coupling reaction under mild conditions which could positively impact the pharmacokinetics profile of rHuEPO [83,288].

Liposomes

Liposomes are spherical-shaped vascular structures composed of self-assembled lipid bilayers made up of one or more hydrated phospholipids. Liposomes form a core shell-like structure in which the inner core consists of hydrophilic domains surrounded by a hydrophobic bilayer phospholipids shell. The inner aqueous core facilitates encapsulating the hydrophilic entities, while the hydrophobic shell in the lipid bilayers can encapsulate hydrophobic substances. Being structurally similar to biomembranes, allows liposomes to interact easily with cell membranes, resulting in excellent biocompatibility. Besides, the available possibility of modifying liposomal surfaces by conjugating with polymers (e.g. PEGylated stealth liposomes) and targeting moieties (e.g. monoclonal antibodies or receptor ligands) to alter the pharmacokinetic properties, makes them an ideal choice for designing carriers of various therapeutic drugs [292]. Liposomes were initially discovered by Bengham in the 1960s, and have since become the most commonly used carrier system of drugs and therapeutics for many diseases. Liposomal drug delivery systems offer several benefits such as improved drug delivery by targeting the site of action, prolonged systemic circulation time, encapsulation of both hydrophilic and lipophilic drugs in the same cargo, preventing degradation, and reduced drug-related toxicity and side effects. Various types of liposomes have been developed including unilamellar liposomes, multilamellar liposomes, and long-circulating liposomes as carriers for therapeutic agents, including drugs, proteins, enzymes, nucleic acids, and theranostics. Moreover, liposomes are often used as a model for biological cell membranes. The first liposome-based formulation "Doxil®", a liposome-encapsulated doxorubicin, was approved by the FDA in 1995 for treating HIV. Since then many liposomal formulations have been developed and are at various stages of preclinical and clinical development [293].

Polymeric nanoparticles

Polymeric nanoparticles are self-assembled colloidal systems composed of different polymeric materials with dimensions on the nanoscale range. Extensive research has been conducted on polymeric nanoparticles as nanocarriers for the delivery of various therapeutic agents. These nanoparticles can be categorized as matrix-type nanospheres or reservoir-type nanocapsules. Nanospheres are networks of polymer in which the drugs are dispersed or embedded in the polymeric matrix, whereas nanocapsules have core shell-like architectures in which the drugs are dissolved or encapsulated in the core surrounded by a polymer membrane [294]. Like other nanocarrier drug delivery systems, polymeric nanoparticles impart multiple advantages, such as prolonged circulation time, high drug loading capacity, enhanced stability, and controlled and sustained drug release. The principal advantage of polymeric carriers is their tunable characteristics which means it has the ability to modulate the physical, chemical, and biological properties of the nanoparticles by designedly modifying the core and the surface components, leading to control the degradation of nanoparticle and hence the drug release. In addition, the biocompatibility and biodegradability of the polymeric nanoparticles further improve their effectiveness in drug delivery [295]. Several polymers, both natural and synthetic, have been widely employed as drug delivery vehicles due to their versatile and attractive features. The most commonly used synthetic polymers are *N*-(2-hydroxypropyl)methacrylamide (HPMA) copolymer, poly(lactic acid) (PLA), poly(glycolic acid) (PGA), lactic and glycolic acid copolymers (PLGA), and poly(ε-caprolactone) (PCL). Besides natural polymers such as dextran, alginate, chitosan, and heparin have been widely investigated as nanoparticulate carriers [296].

Micelles

Micelles are monolayer colloidal systems formed spontaneously *via* self-assembly of the amphiphilic macromolecules above certain specific concentrations. This particular concentration at which micelles formation occurs is known as the critical micelle concentration (CMC) [297]. Amphiphilic molecules are composed of both hydrophilic head groups and lipophilic segments. Significant solubility differences between the hydrophilic and lipophilic parts of the amphiphiles, enabling them to form core shell-like nanostructured micelles in a suitable medium. Generally, micelles are composed of a lipophilic core surrounded by a hydrophilic shell in an aqueous medium. However, in non-polar solvents, the composition of micelles is reversed, leading to the formation of reverse micelles with a hydrophilic inner core and a lipophilic outer block. In common micellar system, the

hydrophilic polar head groups usually interact with the outer bulk aqueous phase providing the steric stability of the system, while the lipophilic segments tend to aggregate in the core of the micelles to avoid contact with the surrounding aqueous medium. The versatile characteristics allow micelles to serve as a suitable nanocarrier for both hydrophilic and hydrophobic drugs. The drugs can be loaded in the micelles either by physical encapsulation through noncovalent interactions or by covalent attachment of drugs with suitable entities like polymers or lipids before micellization [298]. For example, highly stearate grafted HES (St-HES) conjugates were synthesized, capable of producing self-assembled micelles in an aqueous medium with a more hydrophobic inner core that could effectively encapsulate highly hydrophobic drugs with a high encapsulation efficiency [79]. Typically, dissolution in an aqueous medium is a crucial factor for drug absorption and biodistribution. These amphiphilic polymeric micelles have been extensively investigated due to the enhanced solubility of poorly soluble drugs and improved *in vivo* pharmacokinetics.

Nanoemulsions

Nanoemulsion is another important approach to nanocarrier platforms for drug delivery. Nanoemulsion is a biphasic liquid dispersion of oil and aqueous phase stabilized by an emulsifying agent. The droplet size of nanoemulsion is in the nanometer range with a very low polydispersity index. Depending on the dispersed and continuous phase, nanoemulsions can be classified as oil-in-water (O/W), water-in-oil (W/O), or multiple emulsion systems such as W/O/W. Among them, O/W nanoemulsions have been frequently used for the delivery of poorly water-soluble or lipid drug conjugates. The O/W nanoemulsions are usually composed of an oil core surrounded by surfactants dispersed in aqueous phase. Sometimes a co-surfactant is used in combination with surfactants to facilitate the nanoemulsion stabilization process. Nanoemulsions are biocompatible and kinetically stable due to small droplet size which gives rise to an isotropic, clear, or translucent formulation. Due to the composition of the oil core, it provides high encapsulation efficiency of hydrophobic drugs or lipid drug conjugates [299]. Recently, a nanoemulsion formulation was developed using medium-chain triglycerides (MCT), Kolliphor HS15, and propylene glycol as oil, surfactant, and cosurfactant, loaded with dimeric artesunate glycerol monocaprylate conjugates (D-AS-GC) in the oil core demonstrated a clear, stable nanoemulsion formulation when dispersed in the aqueous phase (water). The authors concluded that the dimeric lipid drug conjugates in combination with nanoemulsion formulation could efficiently increase the

in vivo half-life, prolong circulation time, protect from degradation, and overcome drug resistance of the antimalarial drug, artesunate [94].

Solid lipid nanoparticles (SLNs)

Solid lipid nanoparticles (SLNs) are lipid-based colloidal drug delivery carriers developed in the early 1990s. SLNs are structurally similar to nanoemulsion formulations except the liquid lipid (oil) core of an emulsion is replaced with solid lipids. A standard model of SLNs consists of a solid lipid core encased by an emulsifier interface. The process of formulating SLNs usually involves melting the solid lipids and then dispersing them in an aqueous phase to form nanoparticles typically with the help of emulsifiers [300]. This solid lipid core can be made from various biocompatible and biodegradable lipids such as triglycerides, fatty acids and fatty alcohols, waxes, and steroids that are solid at room and body temperature. The outer shell of SLNs is typically stabilized by emulsifying agents to maintain homogenous dispersion and prevent aggregation. The distribution of the drug within SLNs can be achieved by following three different models, homogeneous matrix model (uniformly distributed within the lipid matrix), drug-enriched shell model (entrapped into the shell around the lipid core), or drug-enriched core model (embedded in the core with an encased lipid shell) [301]. Thus, SLNs could effectively load both hydrophilic and hydrophobic therapeutic agents, making it one of the most versatile options for drug administration through various routes.

Nanostructured lipid carriers (NLCs)

Nanostructured lipid carriers (NLCs) are the second-generation lipid-based nanocarriers for drug delivery. NLCs consist of a mixture of solid lipids and liquid lipids, which help to release the drugs in a controlled manner by increasing drug loading and reducing the initial burst release [302]. NLCs are produced by melting the blend of solid and liquid lipids, dispersed in a hot aqueous solution of emulsifying agents (stabilizer) followed by cooling to form lipid matrixes. The blending of solid and liquid lipids exhibits melting point depression compared to the original lipids, while the matrix remains solid at body temperature. The basic concept of NLC is to disrupt the perfect crystal formation by using a lipid mixture with varied crystal structures and sizes. This results in a lipid matrix with numerous imperfections, creating enough space for drug incorporation with high loading capacity and efficiency. The preparation of an imperfect crystal structure is the perfectness of NLCs [303].

2. Aim and objectives

Drug delivery systems are an advanced field of research that intricately weaves together the drug design and delivery mechanisms to optimize therapeutic outcomes. This approach capitalizes on cutting-edge scientific progress, where modern technology increasingly incorporates nanotechnology platforms to improve drug delivery systems. Nanotechnology enables the development of precise drug delivery systems with controlled release rates, improved solubility and bioavailability, and enhanced absorption of therapeutic agents. By combining modified or existing therapeutic agents with nanotechnology, researchers can finely tune the physical and chemical properties of these drugs. Drug design involves synthesizing and modifying the active substances to achieve the desired pharmacokinetic and pharmacodynamic properties of the therapeutic agents. Concurrently, the delivery aspect focuses on devising innovative systems to optimize drug formulations and tailored drug carriers to alter bioavailability and release kinetics. Combining the drug design with delivery technologies leads to the development of potent therapeutic agents while minimizing side effects and improving effective and safer treatments. Several natural polymers such as polysaccharides and lipids have been extensively investigated as carriers for therapeutic delivery for the development of polymer-drug conjugates, polymer-protein conjugates, nanoparticle, and lipid-based nano-formulations to improve stability, solubility, plasma half-life and protection of the therapeutic agents from degradation.

Proteins have been extensively utilized as alternative therapeutics for the treatment of numerous diseases with high efficiency and specificity. However, despite their potential advantages, protein therapeutics face some challenges such as instability, short plasma half-life, immunogenicity, and fast renal clearance. Therefore, continuous efforts have been made to develop improved methods for protein delivery. One of the most effective ways to overcome these issues is conjugating polymers with proteins. Several chemical conjugation methods have been employed for protein modifications. Nonetheless, these methods often suffer from issues like poor selectivity, instability, and deteriorating effects on protein functions. To address these problems, the first objective of this work is to develop enzyme-catalyzed polymer-based polymer-protein conjugates using a semisynthetic starch derivative HES under mild reaction conditions. To achieve this, a therapeutic protein, recombinant

human erythropoietin (rHuEPO), is used to conjugate with an amine-modified HES enzymatically catalyzed by a thermoresistant variant mTGase, TG[16]. First, an amine-modified HES (HES-*g*-NH_2) is synthesized through a one-step carbonyldiimidazole (CDI) mediated reaction between HES and hexamethylenediamine (HMDA) which can act as a potential substrate for mTGase. Characterization of HES and HES-*g*-NH_2 is performed using ^{1}H NMR, 2D ^{1}H–^{1}H homonuclear correlation spectroscopy (COSY), ^{13}C–^{1}H heteronuclear single quantum coherence (HSQC) spectroscopy, and Fourier transform infrared (FTIR) spectroscopy. The free amine groups of HES-*g*-NH_2 are then partially labeled with a fluorescent dye, rhodamine-B-isothiocyanate to prepare rhodamine B-labeled HES-*g*-NH_2 (HES-*g*-NH_2-R) and characterized by ^{1}H NMR spectroscopy. Afterward, both HES-*g*-NH_2 and HES-*g*-NH_2-R are used in conjugation reactions with recombinant human erythropoietin (rHuEPO) at its transition temperature, catalyzed by the thermoresistant variant mTGase TG[16]. N-deglycosylated rHuEPO is also prepared after treatment with peptide-*N*-glycosidase F (PNGase F) which ensures that conjugation occurs with the polypeptide backbone rather than the glycan moieties of rHuEPO and applied for conjugation with HES-*g*-NH_2 and HES-*g*-NH_2-R using the same recation conditions. All conjugates are analyzed by SDS-PAGE and examined using fluorescence analysis and silver staining.

The second objective of this work is to further apply HES to develop a design polymeric nanocarrier that can be used to encapsulate hydrophobic and poorly water-soluble drugs with high encapsulation efficiency and provide sustained release of therapeutics agents. To achieve this, amphiphilic HES conjugates are synthesized *via* the Steglich esterification reaction by varying the grafting ratio of stearic acid (SA) to HES. Two different stearate grafted HES (St-HES) conjugates are prepared. HES and the synthesized St-HES conjugates are thoroughly investigated using ^{1}H, 2D HSQC, and HMBC (heteronuclear multiple bond correlation) NMR spectroscopy to get precise structural information which can further facilitate the determination of the grafting ratio. The degree of grafting for the St-HES conjugates is quantified using ^{1}H NMR spectroscopy. The thermal behavior and crystallization properties of native HES and St-HES conjugates are examined using differential scanning calorimetry (DSC) and wide-angle X-ray scattering (WAXS). Finally, the St-HES conjugates are subjected to prepare self-assembled micelles in an aqueous phase. To analyze the particle size and morphology of the micelles, dynamic light scattering (DLS) and scanning electron microscopy (SEM) experiments are conducted.

The final aim of this work is to explore a possible alternative to polymer-based drug delivery systems. To accomplish this, a lipid-based formulation is developed by combining two established strategies. The first strategy involves synthesizing a new dimeric lipidic drug conjugate by utilizing the dimerization technique and the second strategy is to formulate a nanoemulsion preconcentrate for the delivery of this novel conjugate. Accordingly, a dimeric artesunate glycerol monocaprylate conjugate (D-AS-GC) is synthesized using the antimalarial drug artesunate (AS) and a dimeric linker molecule glycerol monocaprylate (GC) through carbodiimide mediated esterification reaction to obtain lipidic D-AS-GC conjugates. Artesunate is chosen for this work due to its potential therapeutic efficacy and rapid action while suffering from short plasma half-life and spread of resistance among malaria parasites, which limits its optimal therapeutic efficacy. The detailed structural characterization of AS, GC, and the D-AS-GC conjugate is conducted using ^{1}H, attached proton test (APT) ^{13}C, 2D HSQC, and HMBC NMR spectroscopy. To confirm the molar mass of the conjugate, an electrospray ionization time-of-flight mass spectroscopy (ESI-TOF MS) experiment is performed. Additionally, various formulations of D-AS-GC loaded nanoemulsion preconcentrates are developed and diluted with an aqueous phase. The particle size of each formulation is assessed using DLS. The particle size of the optimized nanoformulation is then further analyzed with diffusion-ordered NMR spectroscopy (DOSY). Atomic force microscopy (AFM) is employed to examine the final morphology of dried emulsion droplets on different substrates.

3. Results

The main aim of this research was the design, synthesis, and structural characterization of polysaccharide and lipid-based carriers for the delivery of therapeutics. Due to the diversity of the topics investigated, this doctoral thesis covers two different subject areas that have been published in three peer-reviewed research articles. The published results are presented in this section. This section has been subdivided into two parts: part A addresses the development of macromolecular carriers based on hydroxyethyl starch (HES), comprising two subsections 3.1.1 (Paper I) and 3.1.2 (Paper II). Part B focuses on the development of lipid-based drug conjugates and formulation of a nanoparticulate drug delivery system, presented in subsection 3.2.1 (Paper III). Paper I describes the enzymatic approach for the conjugation of recombinant human erythropoietin (rHuEPO) with the semisynthetic polysaccharide derivative HES using a highly thremoresistant variant of microbial transglutaminase mTGase TG[16]. Therefore, amine-modified HES (HES-*g*-NH_2) conjugates are synthesized *via* CDI-mediated coupling reaction to introduce primary amine groups that can act as an acyl acceptor substrate for mTGase TG[16]. The HES-*g*-NH_2 and the dye-labeled HES-*g*-NH_2-R are subsequently applied for the enzymatic conjugation with rHuEPO catalyzed by mTGase TG[16]. The published results based on introducing primary amine groups on the HES backbone and its mTGase TG[16]-mediated conjugation reaction with rHuEPO are presented in subsection 3.1.1. The starch derivative HES is further used for the synthesis of highly hydrophobized stearic acid-HES conjugates (St-HES). Furthermore, these conjugates have been investigated to design a self-assembled carrier for drug delivery. The published results of the synthesis of highly grafted St-HES conjugates and the self-assembly of these conjugates are presented in subsection 3.1.2. Furthermore, a different approach has also been investigated as a potential alternative to polymer-based delivery systems. A lipid-based drug conjugate has been obtained by utilizing the dimerization technique and a nanoemulsion preconcentrate formulation has been developed as a substitute carrier for the delivery of drugs specifically antimalarial artesunate. The synthesis of dimeric artesunate glycerol monocaprylate conjugate (D-AS-GC) and the formulation of nanoemulsion preconcentrate are presented in subsection 3.2.1.

3.1. Part A – Hydroxyethyl starch (HES) based conjugates

3.1.1. Paper I: Enzymatic HES conjugation with recombinant human erythropoietin *via* variant microbial transglutaminase TG[16]

Protein therapeutics have been widely used as promising drug candidates for the treatment of numerous pathophysiological conditions. Most of the therapeutic proteins, e.g. recombinant human erythropoietin (rHuEPO), exhibit relatively shorter plasma half-life. Covalent coupling of proteins with polymers is the most efficient approach to extend the protein half-life *in vivo*. Among several approaches, HESylation represents an effective alternative half-life extension (HLE) strategy based on protein conjugation with the HES to improve the pharmacokinetic and pharmacodynamic profiles of the therapeutic proteins. Various enzymatic methods have been increasingly investigated as alternatives to the chemical approaches for the conjugation of protein to polymers.

To this aim, the following paper investigates the enzymatic conjugation of rHuEPO with HES using a thermoresistant variant of microbial transglutaminase (mTGase), TG[16]. Initially, an amine-functionalized HES (HES-*g*-NH_2) was designed to obtain an acyl acceptor substrate for the mTGase-catalyzed reaction with rHuEPO and thoroughly characterized by ^{1}H NMR, 2D NMR, and FTIR spectroscopy. Subsequently, HES-*g*-NH_2 conjugates are partially labeled with rhodamine-B-isothiocyanate to form rhodamine B-labeled HES-*g*-NH_2 (HES-*g*-NH_2-R). The conjugation reaction of rHuEPO with HES-*g*-NH_2 and HES-*g*-NH_2-R was catalyzed by mTGase TG[16] at 54 °C, analyzed by SDS-PAGE, and observed using fluorescence and silver staining. SDS-PAGE analysis revealed the formation of high molecular mass rHuEPO-HES conjugates and aggregates, thus demonstrating the efficiency of the TG[16]-mediated enzymatic approach for preparing rHuEPO-HES conjugates. Overall, this study highlights the potential of using the enzymatic approach for developing rHuEPO-HES conjugates under mild reaction conditions which could potentially enhance the pharmacokinetics of rHuEPO, making it suitable for therapeutic applications.

The author's contributions to the following article are: R. Hore designed the research, conceptualized the work, performed the experiments and analyzed the data, wrote the original draft, and made the finalization of the manuscript. R. Alaneed carried out the SDS-PAGE experiments and analyzed the data. J. Kressler and M. Pietzsch conceptualized the work, and supervised, discussed the results, reviewed them, and finalized the manuscript.

Title

Enzymatic HES Conjugation with Recombinant Human Erythropoietin *via* Variant Microbial Transglutaminase TG[16]

Authors

Rana Hore, Razan Alaneed, Markus Pietzsch, and Jörg Kressler*

Bibliographic Details

Starch-Stärke
Volume 74, Issue 9-10, Pages 2200034
Published 30 June 2022
DOI: 10.1002/star.202200034

∗: Corresponding Author

Source (Starch-Stärke; https://doi.org/10.1002/star.202200034). The link to the article on the publisher's website is: https://onlinelibrary.wiley.com/doi/full/10.1002/star.202200034. Supporting information can be found at: https://onlinelibrary.wiley.com/action/downloadSupplement?doi=10.1002%2Fstar.202200034&file=star202200034-sup-0001-SuppMat.pdf.

RESEARCH ARTICLE

Starch
www.starch-journal.com

Enzymatic HES Conjugation with Recombinant Human Erythropoietin via Variant Microbial Transglutaminase TG^{16}

Rana Hore, Razan Alaneed, Markus Pietzsch, and Jörg Kressler**

Microbial transglutaminases (mTGases) or protein-glutamine γ-glutamyltransferases are a family of enzymes that catalyze the transamidation of glutamine (Gln) residues of proteins or peptides with various primary amines. mTGase is suitable for site-specific enzymatic modification of therapeutic proteins. Here, the enzymatic conjugation of recombinant human erythropoietin (rHuEPO) with the semisynthetic starch derivative, hydroxyethyl starch (HES), is studied, using a thermoresistant variant mTGase TG^{16}. An amine-modified HES (HES-*g*-NH$_2$) is synthesized to act as an acyl acceptor substrate for TG^{16} and characterized by ^{1}H NMR, 2D NMR, and Fourier transform infrared (FTIR) spectroscopy. Subsequently, HES-*g*-NH$_2$ is labeled with rhodamine B-isothiocyanate resulting in rhodamine B-labeled HES-*g*-NH$_2$ (HES-*g*-NH$_2$-R). Finally, amine-modified HES before and after labeling is applied for the conjugation reaction with rHuEPO at its transition temperature T_m. Using SDS-PAGE, high molar mass conjugates as well as aggregates are observed, thus, demonstrating the efficient conjugation of HES with the acyl donor rHuEPO. Importantly, it is shown that this enzymatic method gives easy access to the preparation of rHuEPO-HES conjugates.

1. Introduction

Transglutaminases (TGases, EC 2.3.2.13) comprise a diverse group of enzymes found in several organisms including mammalians, vertebrates, invertebrates, plants, and microorganisms, which catalyze the formation of a protease resistant isopeptide bond between the γ-carboxamide group of protein-bound glutamine (Gln) residues (acyl donor) and various primary amines (acyl acceptors).[1–3] TGases have been widely used in food processing, textile, and leather industries.[4] Research on TGase dates back to 1957 when mammalian TGase has been discovered and extensively studied. Mammalian TGase is mainly isolated from guinea pig liver and other animal sources.[5] However, the application of this TGase has been limited on a large industrial scale due to the calcium-dependent transamidation activity, lack of source, and high production cost.[6] To optimize the processing cost and mass production of TGase for food industries, many attempts have been made by screening microorganisms. Microbial transglutaminase (mTGase) was first isolated by Ando et al. in 1989 from *Streptomyces mobaraensis*.[7] Furthermore, Gottmann and Sprössler in 1992 reported the application of mTGase in food processing for the first time.[8] Contrary to mammalian TGases, mTGase is highly stable and has a broader substrate specificity.[9] In addition, calcium-independent cross-linking activity and ease of production by fermentation make mTGase more favorable for commercial use.[7,10] Besides the widespread use of mTGase in food manufacturing, it has now become a useful and versatile tool in the biomedical field.[11] Using random and rational mutagenesis techniques, several generations of more and more thermoresistant mTGases have been generated.[12–14] These thermoresistant enzymes allow modification of (therapeutic) proteins at temperatures close to or above the transition temperature.

During past decades, the development of protein-based therapeutics has drawn interest in biotechnology and medicine. However, there are many challenges inherent to therapeutic proteins such as physicochemical and enzymatic instabilities, rapid body clearance, and immunogenicity.[15] An innovative technology to improve the clinical profiles of protein therapeutics is the conjugation of proteins to polymers. In general, many conventional chemical approaches have been employed for the conjugation of polymers to the protein surfaces. Several drawbacks such as heterogeneity, unwanted reactivity, and poor stability of the products have limited the applications of these strategies[16] even though, these chemical procedures have the potential to provide a highly efficient conjugation.[17] To address the aforementioned issues, site-specific, enzyme-based conjugations have been developed due to the high selectivity of enzymes under mild reaction conditions. Rashidian et al. summarized a wide range of enzymes that have been utilized for site-specific modification of proteins.[18]

R. Hore, R. Alaneed, J. Kressler
Department of Chemistry
Martin Luther University Halle-Wittenberg
Von-Danckelmann-Platz 4, D-06099 Halle/Saale, Germany
E-mail: joerg.kressler@chemie.uni-halle.de

R. Alaneed, M. Pietzsch
Department of Pharmacy
Martin Luther University Halle-Wittenberg
Weinbergweg 22, D-06120 Halle/Saale, Germany
E-mail: markus.pietzsch@pharmazie.uni-halle.de

DOI: 10.1002/star.202200034

Among them, mTGase is of great potential because of its sequence specificity. For example, the mTGase-catalyzed PEGylation of recombinant granulocyte colony-stimulating factor,[19] human growth factor,[20] and recombinant human interleukin-2.[21] Apart from PEG, a wide range of carbohydrate-based natural polysaccharides and synthetic polymers have been investigated for protein modification.[22–25] Among these polymers, hydroxyethyl starch (HES) has received increasing interest due to its biodegradability, biocompatibility, water solubility, and lack of immunogenicity.[26] HES is a semisynthetic derivative of the natural polysaccharide amylopectin and is widely used as a first-line plasma volume expander (PVE).[27] However, concerns regarding HES have been raised due to possible side effects mainly related to kidney injury.[28,29] It is worth mentioning that upon using HES as a carrier for protein therapeutics at lower concentrations than that of PVE applications, hence, such safety issues could be avoided.[28] Accordingly, several approaches have been reported for the conjugation of HES to proteins[30] as well as to therapeutic proteins such as erythropoietin (EPO). EPO is a glycoprotein hormone produced in the kidney and stimulates the production of red blood cells. It is essential for the treatment of patients with chronic renal failure and chemotherapy-related anemia. Because EPO has a relatively short serum half-life, the conjugation with HES via chemical strategies has been explored as an approach to increase its bioavailabilty.[31–34] Besides, the site-specific conjugation of EPO with PEG at the level of Gln or lysine residues using TGases has been patented in order to improve its pharmacokinetics.[35] Recently, our group has reported a successful conjugation of rHuEPO with a sugar-based amine-grafted poly(D-sorbitol adipate) at the level of Gln residues using a highly thermoresistant variant of mTGase, TG^{16}, at the transition temperature T_m of rHuEPO (54.3°C).[36]

Herein, we investigated the mTGase-catalyzed conjugation of recombinant human erythropoietin (rHuEPO) with amine-modified HES (HES-*g*-NH_2) to obtain an enzymatically synthesized carrier for rHuEPO delivery. Initially, we describe the synthesis of HES-*g*-NH_2 to obtain a potential substrate for mTGase by a one-step reaction of HES with hexamethylenediamine (HMDA) in the presence of 1,1′-carbonyldiimidazole (CDI). HES and HES-*g*-NH_2 were characterized by ^{1}H NMR, 2D ^{1}H–^{1}H homonuclear correlation spectroscopy (COSY), ^{13}C–^{1}H heteronuclear single quantum coherence (HSQC) spectroscopy, and Fourier transform infrared (FTIR) spectroscopy. Afterward, the free amine groups of HES-*g*-NH_2 were used for the partial labeling with rhodamine-B-isothiocyanate and the successful labeling was confirmed by ^{1}H NMR spectroscopy. Finally, both HES-*g*-NH_2 and rhodamine B-labeled HES-*g*-NH_2 (HES-*g*-NH_2-R) were applied for the conjugation reaction with rHuEPO catalyzed by a thermoresistant variant mTGase, TG^{16}. All conjugates were analyzed by SDS-PAGE before and after treatment with peptide-*N*-glycosidase F (PNGase F) and observed by fluorescence analysis and silver staining.

2. Experimantal Section

2.1. Materials

Glycosylated rHuEPO (Chinese hamster ovary [CHO] cell-derived, ≥90% purity) was obtained from PeproTech GmbH (Hamburg, Germany). Peptide-*N*-glycosidase F (PNGase F) with a concentration of 500, 000 U mL^{-1}, glycoprotein denaturing buffer, glycol buffer, and Nonidet P-40 (NP-40) were obtained from New England Biolabs GmbH (Frankfurt am Main, Germany). HES with a molar mass of 70, 000 g mol^{-1} and molar substitution (MS) of 0.5 was a gift from Serumwerk Bernburg (Bernburg, Germany). CDI (≥97.0%), HMDA (98%), monodansyl cadaverine (MDC, ≥97%), and rhodamine B-isothiocyanate were obtained from Sigma–Aldrich (Steinheim, Germany). Tris (tris(hydroxymethyl)aminomethane, ≥99,9%), sodium chloride (NaCl, >99,5%), dimethyl sulfoxide (DMSO, anhydrous), dialysis membranes with a cut-off molar mass of 1000 g mol^{-1}, acetic acid (CH_3COOH, 100%), formaldehyde aqueous solution (≥37%), silver nitrate ($AgNO_3$, ≥99.9%), ethanol (Et-OH, >99.8%), methanol (Me-OH, >99.8%), L-glutathione (reduced form, ≥98%), trichloroacetic acid (TCA, >99%), hydrochloric acid (HCl, 37%), sodium thiosulphate pentahydrate ($Na_2S_2O_3{\cdot}5H_2O$, ≥99%), and sodium carbonate (Na_2CO_3, ≥99.5%) were purchased from Carl Roth (Karlsruhe, Germany). Deuterium oxide (D_2O, 99.9%), and *N*,*N*-dimethylformamide-d_7 (DMF-d_7, 99.5%) were purchased from Armar Chemicals (Döttingen, Switzerland). Hydroxylammoniumchloride (NH_3(OH)Cl, >99%) and iron (III) chloride ($FeCl_3$, >99) were obtained from Merck KGaA (Darmstadt, Germany). Carbobenzoxy glutamine glycine (CBZ-Gln-Gly) was purchased from Bachem AG (Bubendorf, Switzerland). Protein molecular weight marker was obtained from Fermentas Life Sciences (St. Leon-Rot, Germany). PageRule Prestained Protein Ladder was obtained from Thermo Fisher Scientific (Schwerte, Germany). HPLC grade tetrahydrofuran (THF) was purchased from Carl Roth (Karlsruhe, Germany).

2.2. Methods

2.2.1. NMR Spectroscopy

The NMR spectra were recorded on a VNMRS spectrometer (Agilent Technologies) at 400 MHz for ^{1}H NMR and 100 MHz for ^{13}C NMR. 2D NMR measurements namely, ^{1}H–^{1}H COSY and ^{13}C-^{1}H HSQC spectroscopy, were performed to obtain detailed structural information. Thirty milligrams of polymer samples were dissolved in 0.7 mL of deuterated solvents (DMF-d_7 and D_2O) and the analysis was carried out at 27°C, using tetramethylsilane as an internal standard. The NMR spectral data were interpreted using MestRec (v.4.9.9.6) software (Mestrelab Research, Santiago de Compostela, Spain).

2.2.2. Fourier Transform Infrared Spectroscopy (FTIR)

FTIR experiments were performed with a BRUKER Vector 22 (Bruker Optik GmbH, Germany) spectrometer at room temperature with 64 scans using KBr pellets for sample preparation. All FTIR spectra were recorded in the wavenumber range of 4000–400 cm^{-1}. The data were interpreted using OMNIC 7.2 Spectra Software.

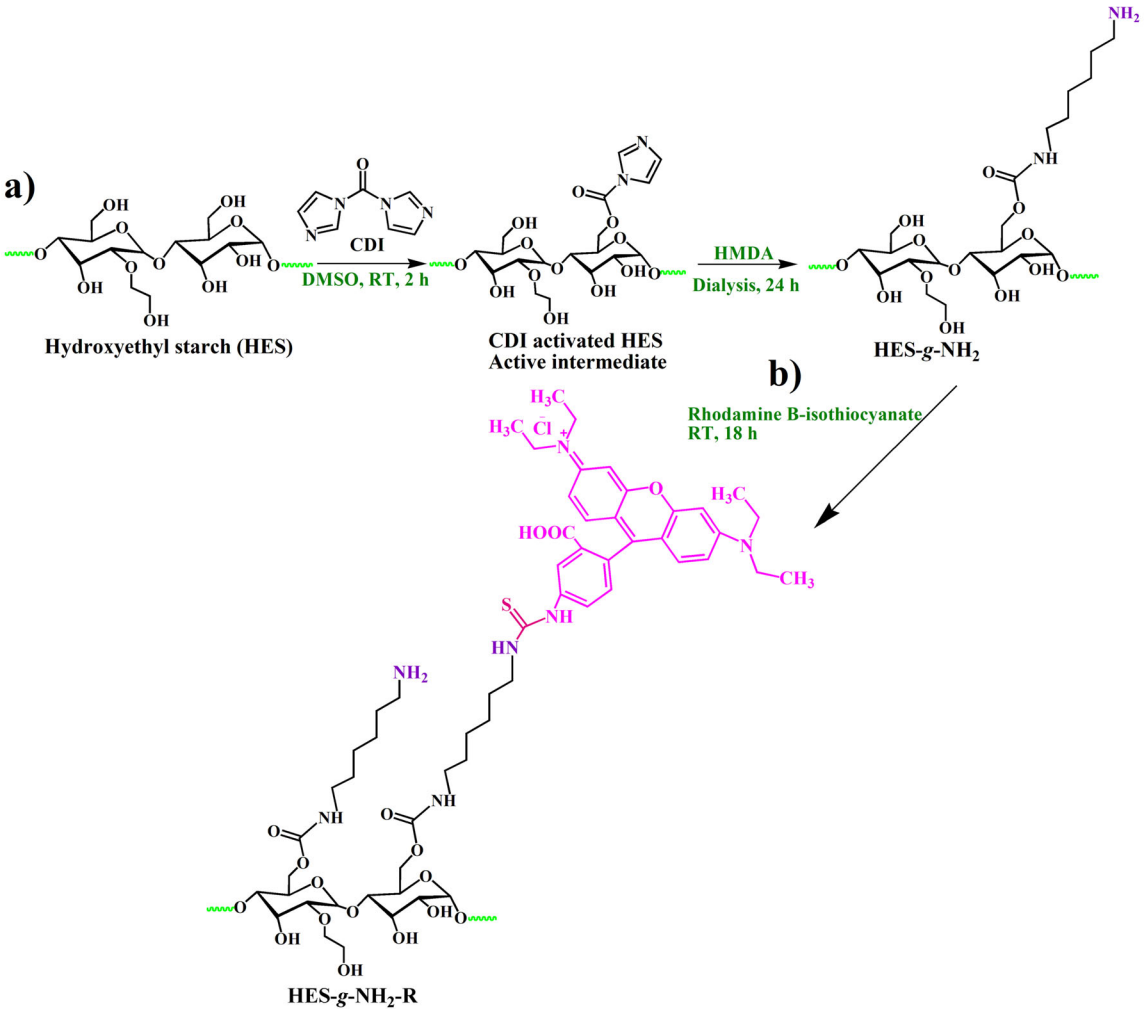

Scheme 1. Synthetic pathways for a) HES-*g*-NH_2 and b) partial labeling of HES-*g*-NH_2 with rhodamine B-isothiocyanate to obtain HES-*g*-NH_2-R. HES, hydroxyethyl starch; HES-*g*-NH_2, amine-modified HES; HES-*g*-NH_2-R, rhodamine B-labeled HES-*g*-NH_2.

2.2.3. Sodium Dodecyl Sulfate-Polyacrylamide Gel Electrophoresis (SDS-PAGE)

All SDS-PAGE experiments were conducted under reducing conditions according to the procedure described previously.[37] All protein samples were mixed with SDS sample buffer in equimolar ratio, denaturated at 95°C for 3–5 min, and then loaded on a 12.5% w/v poly(acrylamide) resolving gel with a 4.5% w/v poly(acrylamide) stacking gel. Ten microliters of protein ladder and 10 μL of protein sample were loaded into the wells of the stacking gel. This was followed by the first electrophoresis run (200 V, 100 mA, 8 min) and the second run (200 V, 60 mA, 45 min). After separation, the fluorescent bands were visualized under UV light and then the gels were silver stained following the same procedure reported by Blum et al.[38]

2.2.4. Synthesis of HES-g-NH_2

Synthesis of HES-*g*-NH_2 was performed in a single step according to Camacho et al.[39] and Besheer et al.[30] with a slight modification (see **Scheme 1**a). Briefly, HES 70, 000/0.5 (1 g, 5.4 mmol of anhydrous glucose unit [AGU]) was dried at 110°C for 2 h and then dissolved in 20 mL anhydrous DMSO in a 100 mL round-bottom flask. The OH groups of HES were activated by the reaction with CDI (0.088 g, 0.54 mmol) for 2 h, followed by the addition of an excess amount of HMDA under constant stirring. After 24 h, the solution was dialyzed against water and THF using a membrane with a cut-off molar mass of 1000 g mol^{-1} and then dried under continuous nitrogen flow.

2.2.5. Labeling of HES-g-NH_2 with Rhodamine B-Isothiocyanate

Rhodamine B-isothiocyanate was subsequently used to partially label HES-*g*-NH_2 according to the procedure described elsewhere[40] as illustrated in Scheme 1b. Briefly, the dye was dissolved in 5 mL anhydrous DMSO and then added dropwise to the polymer solution in DMSO with constant stirring. The reaction was allowed to proceed at room temperature for approximately 18 h. After that, the reaction solution was purified by dialysis against distilled water using a membrane with a cut-off molar

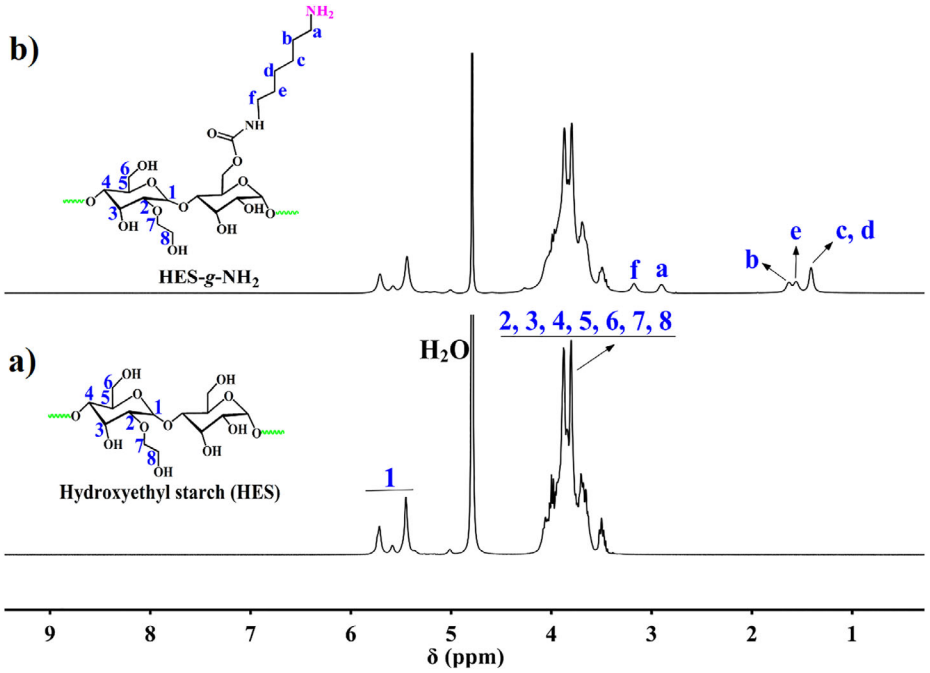

Figure 1. ^{1}H NMR spectra of a) HES and b) HES-*g*-NH_2, recorded at 27°C, 400 MHz, using D_2O as solvent. HES, hydroxyethyl starch; HES-*g*-NH_2, amine NMR, nuclear magnetic resonance.

mass of 1000 g mol^{-1} over a period of 72 h and finally dried by freeze dryer yielding HES-*g*-NH_2-R.

2.2.6. Enzymatic Conjugation of rHuEPO with HES-g-NH$_2$ and HES-g-NH$_2$-R

For this purpose, a high thermoresistant variant mTGase, TG^{16}, was obtained following the previously reported procedure,[12,13] and then applied with an activity of 60 U mL^{-1}.

Reactions were performed at a final protein concentration of 500 μg mL^{-1} in 50 mM Tris buffer and 300 mM NaCl at pH 8. A 10-fold molar excess of HES-*g*-NH_2 and HES-*g*-NH_2-R with respect to the Gln residues of rHuEPO was applied for both reactions.

Initially, each polymer was dissolved separately in the same buffer (final concentration 6 mg/total reaction volume) and then added to the stock solution of rHuEPO. Before enzyme addition, an aliquot of each reaction mixture was collected. This was followed by the addition of TG^{16} stock solution to start the reaction. Both conjugation reactions of rHuEPO with HES-*g*-NH_2 and HES-*g*-NH_2-R were incubated at 54°C for 90 min. An excess amount of TG^{16} (same stock solution with an activity of 60 U mL^{-1}) was added after 60 min reaction time. For the conjugation reaction with HES-*g*-NH_2, aliquots were taken at 0, 30, 60, and 90 min, boiled with SDS buffer at 95°C for 5 min, analyzed by SDS-PAGE, and finally visualized by silver staining. For the conjugation reaction with HES-*g*-NH_2-R, aliquots were also collected at different time intervals, boiled with SDS buffer, analyzed by SDS-PAGE, visualized by UV light, and then stained with silver nitrate. Additionally, HES-*g*-NH_2-R was incubated with TG^{16} at 54°C for 60 min as a negative control. The rHuEPO-HES conjugates were further enzymatically *N*-deglycosylated using PNGase F. Besides, *N*-deglycosylated rHuEPO was incubated with MDC at 37°C in the presence of less thermoresistant variant of mTGase, S2P,[41] having an activity of 38 U mL^{-1}. The reaction was carried out at a final protein concentration of 90 μg mL^{-1} in 50 mM Tris buffer and 300 mM NaCl at pH 8. A 10-fold molar excess of MDC with respect to the Gln residues of rHuEPO was applied. At the same time, some control experiments were performed at 37°C using mTGase-S2P, that is, i) MDC was incubated with mTGase-S2P, ii) MDC was incubated with *N*-deglygosylated rHuEPO, and iii) *N*-deglygosylated rHuEPO was incubated with mTGase-S2P. Aliquots were taken at different time intervals, boiled with SDS buffer, and finally analyzed by SDS-PAGE.

3. Results and Discussion

3.1. Synthesis of HES-g-NH$_2$ and HES-g-NH$_2$-R

The mTGase-reactive substrate was prepared based on HES having a molar mass of 70, 000 g mol^{-1} and a molar substitution of 0.5. Primary amine containing side chains were introduced to the HES backbone by CDI-mediated coupling reaction as shown in Scheme 1a.

^{1}H NMR spectroscopy was used for the structural determination of HES before and after modification as well as to calculate the number of side chains attached to 100 AGU, that is, percent MS. ^{1}H NMR spectra of HES and HES-*g*-NH_2 are shown in **Figure 1**. All peaks in Figure 1a can be assigned to the structure of HES, that is, the peaks (1) between 5.30 and 5.80 ppm belong to the H1 proton of the AGU.[30] All other protons from the polymer backbone coalesced into a broad peak (2–8) between 3.35 and 4.25 ppm. After modification (Figure 1b), the peak

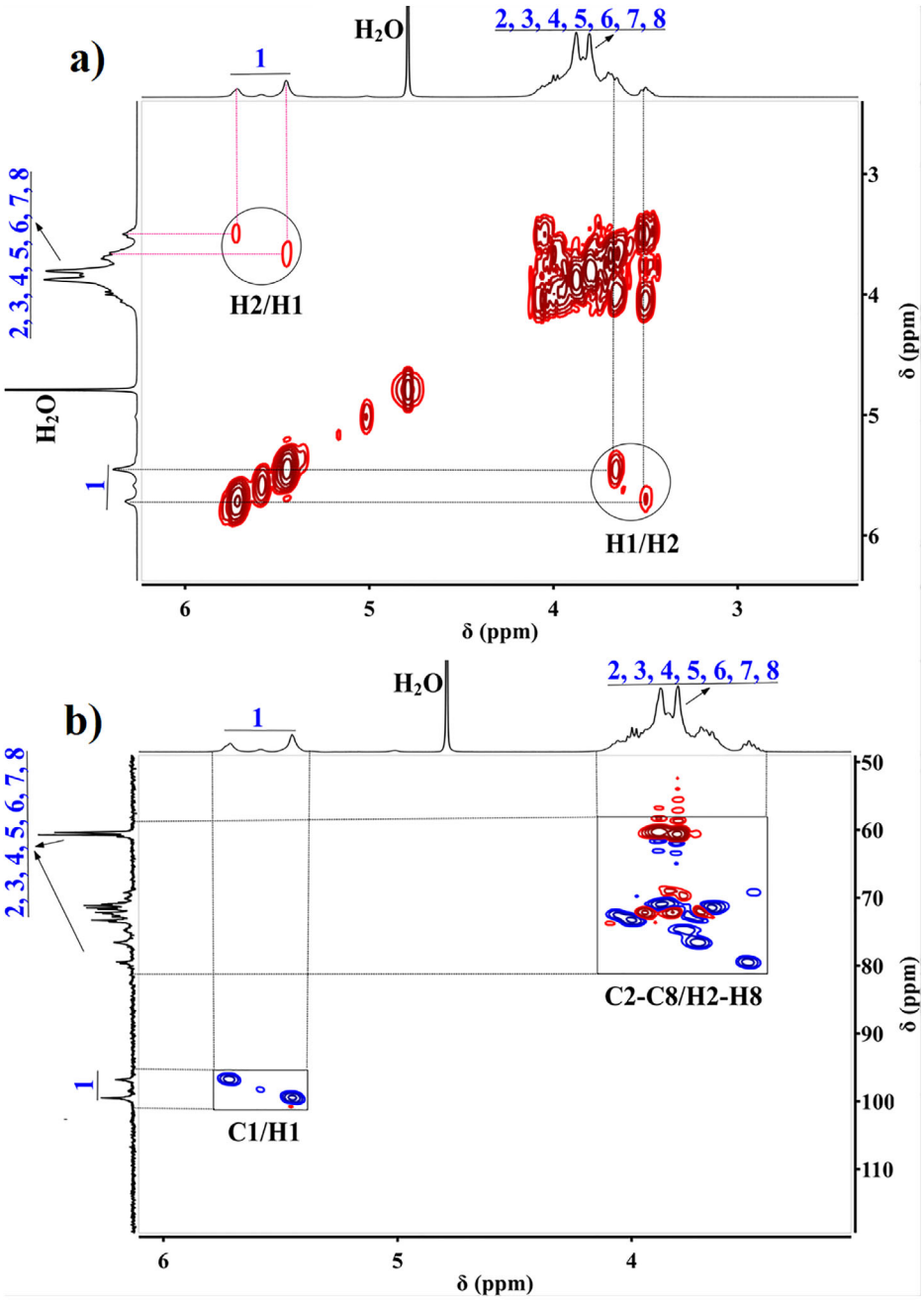

Figure 2. a) COSY and b) HSQC NMR spectra of HES, recorded at 27°C using D_2O as solvent. The structure of HES is given in Figure 1a. COSY, correlation spectroscopy; HES, hydroxyethyl starch; D_2O, deuterium oxide; HSQC, heteronuclear single quantum coherence; NMR, nuclear magnetic resonance.

(f) at 3.16 ppm corresponds to the methylene group beside the carbamate linkage and the peak (a) at 2.90 ppm is related to the methylene protons adjacent to the primary amine group of side chains. Two ^{1}H NMR chemical shifts are observed at 1.62 and 1.55 ppm corresponding to peak b and c. The other methylene groups (c) and (d) from the side chains show resonances at 1.40 ppm. The MS of HES-*g*-NH_2 is calculated as 7.5 mol% based on the integration values of peaks (1) and peak (a). As a result, around 28 primary NH_2 groups per polymer chain could be reactive sites for mTGase-catalyzed conjugation reaction.

All the assignments were further confirmed by 2D NMR experiments namely, COSY and HSQC spectroscopy. In the COSY spectrum, coupling between the adjacent protons can be observed as cross-peaks situated on either side of the diagonal while the HSQC spectrum describes the correlation between each carbon with its directly attached protons. In **Figure 2**a, the correlation signal at δ_H/δ_H 5.30–5.80/3.65–3.50 ppm indicates that

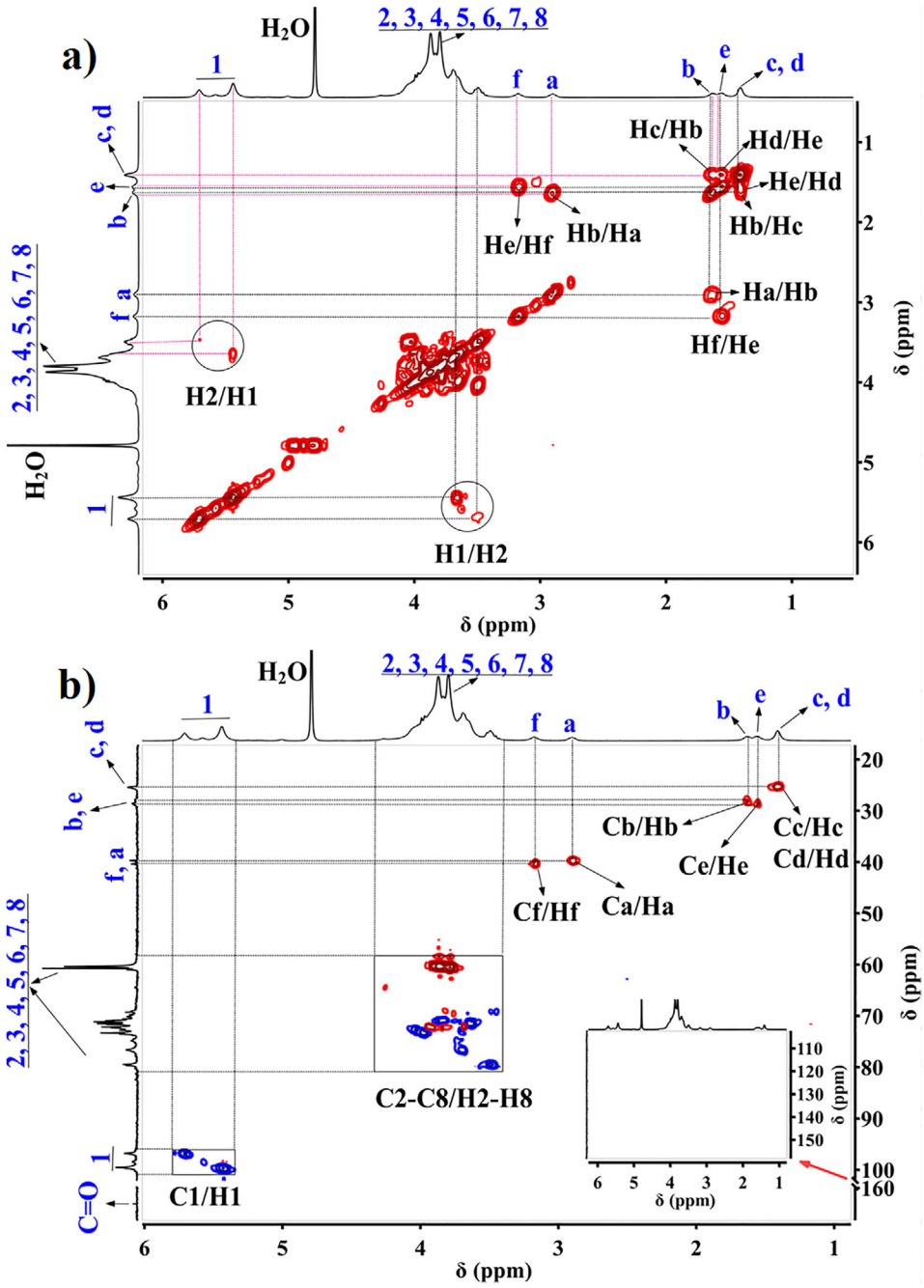

Figure 3. a) COSY and b) HSQC NMR spectra of HES-*g*-NH_2, recorded at 27°C using D_2O as solvent. The structure of HES-*g*-NH_2 is given in Figure 1b. The inset in Figure 3b shows the HSQC NMR spectrum of HES-*g*-NH_2 in the range of 1–6 ppm and 100–160 ppm for ^{1}H and ^{13}C NMR chemical shifts, respectively. No additional correlation signals are observed in this region. COSY, correlation spectroscopy; HES, hydroxyethyl starch; HES-*g*-NH_2, amine-modified HES; D_2O, deuterium oxide; HSQC, heteronuclear single quantum coherence; NMR, nuclear magnetic resonance.

the H1 proton of HES may couple with the adjacent proton H2. Additionally, the correlation signals (δ_C/δ_H) of HES were also recorded through the HSQC NMR spectrum (Figure 2b). The signal values at δ_C/δ_H 95.64–100.83/5.80–5.30 ppm are attributed to C1/H1 of the AGU. Although it is not possible to resolve the spectra completely (Figure 2a,b) due to signals overlapping raised from H2–H8 and C2–C8 of the HES backbone. The H1 proton of HES was well resolved that is useful for calculating the MS after modification with amine containing side chains. Furthermore, HES-*g*-NH_2 was well characterized by 2D NMR spectroscopy (COSY and HSQC). In **Figure 3**a, the correlation signals at δ_H/δ_H 3.16/1.55 ppm and δ_H/δ_H 2.90/1.62 ppm represent the coupling between the Hf/He and Ha/Hb protons, respectively. Other cross-peaks at δ_H/δ_H 1.62/1.40 ppm and δ_H/δ_H

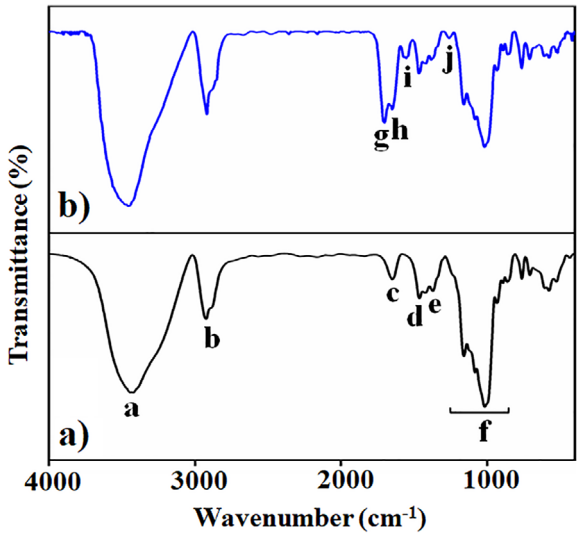

Figure 4. FTIR spectra of a) HES and b) HES-*g*-NH_2 at RT. FTIR, Fourier transform infrared spectroscopy; HES, hydroxyethyl starch; HES-*g*-NH_2, amine-modified HES.

1.55/1.40 ppm are assigned as the coupling between the protons of Hb/Hc and He/Hd, respectively. However, the signals from Hc and Hd are not distinguishable. These results were further confirmed by HSQC NMR spectroscopy. In Figure 3b, the correlation signals at δ_C/δ_H 40.29/3.16, 39.80/2.90, 28.13/1.62, and 28.50/1.55 correspond to Cf/Hf, Ca/Ha, Cb/Hb, and Ce/He of the amine containing side chain, respectively. At the same time, the correlation signal at δ_C/δ_H 25.34/1.40 ppm is assigned to Cc/Hc and Cd/Hd even though, these signals could not be unambiguously identified. A ^{13}C chemical shift is observed at 163.10 ppm with no additional correlation signal in the HSQC spectrum, which is assigned as the carbonyl carbon of the carbamate group.

The chemical structures of HES and HES-*g*-NH_2 were further analyzed by FTIR spectroscopy as shown in **Figure 4**. The IR spectrum of HES (Figure 4a) represents a wide strong band (a) at 3436 cm^{-1} and a second band (c) at 1650 cm^{-1} which indicate the stretching and in-plane vibrations of O–H, respectively. Another characteristic band (b) at 2926 cm^{-1} corresponding to the asymmetrical stretching of C–H is followed by the C–O–H bending (d) at 1465 cm^{-1} and C–H deformation (e) at 1367 cm^{-1}. A strong complex band system (f) between 1160 and 862 cm^{-1} belongs to the asymmetrical C–O–C vibration, symmetrical C–O vibration, C–O stretching, and C–O–C valence vibration.[42] In Figure 4b, a new band (h) at 1647 cm^{-1} is observed and assigned as N-H bending of the primary amine groups. Three new bands are observed, (g) at 1700 cm^{-1} belong to the stretching vibration of carbonyl in the carbamate groups (amide I), (i) at 1554 cm^{-1} related to amide II due to vibrations in plane N–H bending and C–N stretching, (j) at 1261 cm^{-1} corresponding to vibrations in plane of amide III due to C–N stretching and N–H deformation.[43] The appearance of new bands indicates the successful

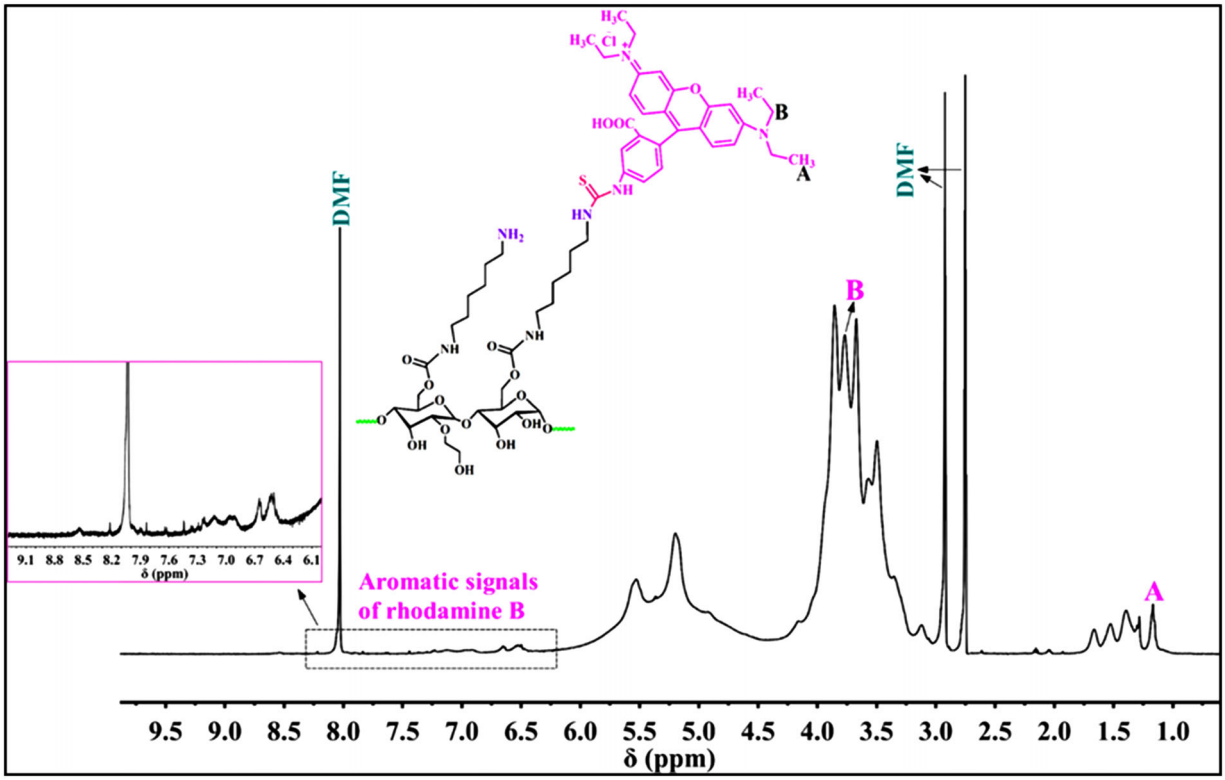

Figure 5. ^1H NMR spectrum of HES-*g*-NH_2-R, recorded at 27°C, 400 MHz, using DMF-d_7 as solvent. The inset shows the aromatic signals of rhodamine B between 6 and 9 ppm. DMF-d_7, *N,N*-dimethylformamide-d_7; HES, hydroxyethyl starch; HES-*g*-NH_2, amine-modified HES; HES-*g*-NH_2 NMR, nuclear magnetic resonance.

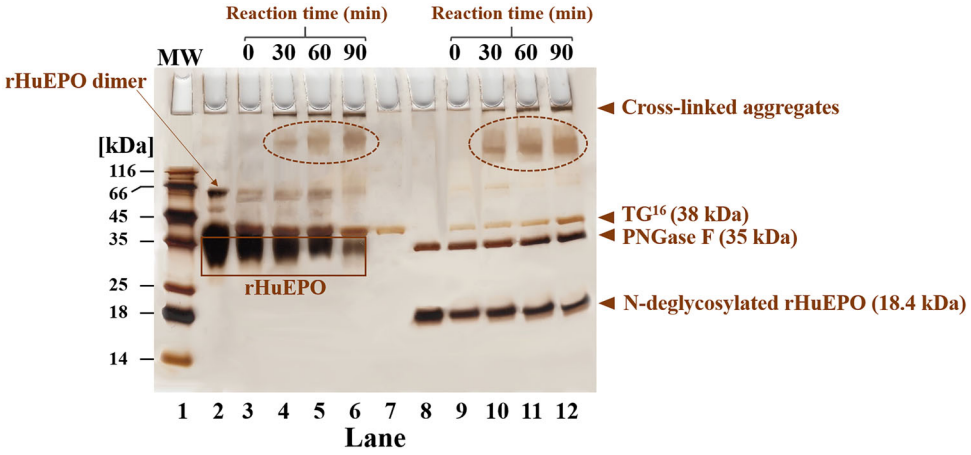

Figure 6. Image of the SDS-PAGE for the conjugation of rHuEPO with HES-*g*-NH_2 at 54°C. Lane 1: molecular weight marker, Lane 2: rHuEPO + HES-*g*-NH_2, lane 3–6: rHuEPO + HES-*g*-NH_2 + TG^{16} at 0, 30, 60, and 90 min, respectively, lane 7: TG^{16} (at higher concentration), lane 8: rHuEPO + HES-*g*-NH_2 after *N*-deglycosylation of rHuEPO, lane 9–12: rHuEPO + HES-*g*-NH_2 + TG^{16} incubated at 0, 30, 60, and 90 min, respectively, after the respective time enzymatic *N*-deglycosylation of rHuEPO was performed. A dimer band of rHuEPO appears at 66 kDa. The dashed ellipsoids indicate the formation of rHuEPO-HES conjugates. High molar mass bands (cross-linked aggregates) are visible in the stacking gel. HES, hydroxyethyl starch; HES-*g*-NH_2, amine-modified HES; rHuEPO, recombinant human erythropoietin; SDS-PAGE, sodium dodecyl sulfate-polyacrylamide gel electrophoresis.

modification of HES and the formation of HES-*g*-NH_2 in the presence of CDI.

In the second synthesis step, HES-*g*-NH_2 was partially labeled (approximately seven primary NH_2 groups per polymer chain) with an amine-reactive fluorescent dye, rhodamine B-isothiocyanate, by the reaction between the free amine groups of HES-*g*-NH_2 and the isothiocyanate group of the dye (Scheme 1b). HES-*g*-NH_2-R is characterized by ^{1}H NMR spectroscopy in DMF-d_7 as shown in **Figure 5**. The ^{1}H NMR spectrum reveals the appearance of peaks belonging to rhodamine B, that is, the signal (A) at 1.17 ppm corresponds to the methyl protons and the signal (B) at 3.72 ppm corresponds to the methylene protons in addition to the aromatic resonances in the region between 6 and 9 ppm.

3.2. TG^{16}-Mediated Conjugation of rHuEPO to HES-*g*-NH_2 and HES-*g*-NH_2-R

Since Gln residues recognized by mTGase are embedded in the unfolded region of the protein,[44] we recently demonstrated the TG^{16}-catalyzed conjugation of rHuEPO with a biodegradable polyester at the transition temperature T_m of rHuEPO, that is, the temperature at which half of the protein is in the unfolded state. T_m of rHuEPO was determined as 54.3°C by nano-differential scanning fluorimetry (nanoDSF).[36] In order to expand the application of this enzymatic method, we further tested the reactivity of rHuEPO toward TG^{16} using HES-*g*-NH_2. It should be noted that the conjugation reaction of *N*-deglygosylated rHuEPO with the well-known fluorescent substrate of mTGase, MDC, was carried out at 37°C using mTGase-S2P and the SDS-PAGE results (see Figure S1 in the Supporting Information) show that no conjugation reaction took place at 37°C since the acceptance of rHuEPO as a substrate requires partial unfolding of the 3D-structure. Here, the use of *N*-deglygosylated rHuEPO was necessary to increase to probability of conjugation since rHuEPO is in the folded state at 37°C and the presence of glycans can further hinder the accessibility of mTGase toward the Gln residues on rHuEPO. Further, a series of control experiments were performed at 37°C (see Figure S2 in the Supporting Information), that is, (i) MDC was incubated with mTGase-S2P and the SDS-PAGE results confirm the absence of fluorescent bands at the molar mass of mTGase-S2P, (ii) MDC was incubated with *N*-deglygosylated rHuEPO and no adsorption of MDC on rHuEPO is observed in the absence of mTGase-S2P, (iii) *N*-deglygosylated rHuEPO was incubated with mTGase-S2P and no significant conjugates or aggregates are observed.

In order to conduct the conjugation reaction at the T_m of rHuEPO, the more thermoresistant variant of mTGase, TG^{16}, was applied. HES-*g*-NH_2 was applied in excess for the conjugation reaction with rHuEPO in the presence of TG^{16} as a catalyst and the formed conjugates were analyzed by SDS-PAGE (**Figure 6**). At the start of the reaction (time 0), no new band appears over the pure band of rHuEPO (Figure 6, lane 3). With increasing reaction time, a consistent reduction in the band intensity of pure rHuEPO is noticed. After 30 min reaction, a new band for the rHuEPO-HES conjugates is observed as a high molar mass band with a broad distribution over 116 kDa (Figure 6, lane 4) that increases in intensity with time (Figure 6, lanes 5 and 6). The high distribution on the gel can be explained by the high polydispersity of HES and the heterogeneity of the glycan moieties of rHuEPO.[45,46] In addition to these conjugates, high molar mass aggregates on the top of the stacking gel are also observed. This is due to the fact that both HES-*g*-NH_2 and rHuEPO have multiple reactive sites for modification by TG^{16}. As a control, HES-*g*-NH_2 was incubated with rHuEPO and the results support that no conjugation reaction took place in the absence of TG^{16} (see lane 2 of Figure 6). An additional band for dimer species appears at 66 kDa which are probably resistant under reducing conditions. This is due to the fact that intermolecular disulfide cross-linking between protein molecules can occur at alkaline pH after loading on SDS-PAGE.[47,48] It is clearly noticeable that the band intensity of rHuEPO dimer is decreased after incubation

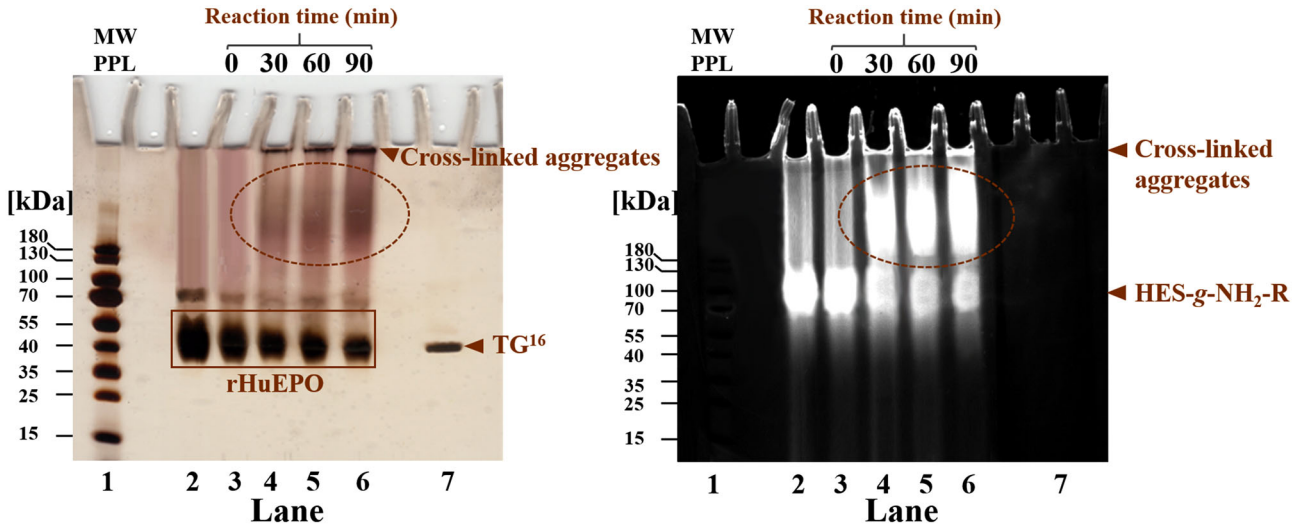

Figure 7. Silver stained images of the SDS-PAGE (left panel) and its fluorescent image (right panel) for the conjugation of rHuEPO with HES-*g*-NH_2-R at 54°C in the presence of TG^{16}. Lane 1: prestained marker, lane 2: rHuEPO + HES-*g*-NH_2-R, lane 3–6: rHuEPO + HES-*g*-NH_2-R + TG^{16} at 0, 30, 60, and 90 min, respectively, lane 7: TG^{16} (at higher concentration). The dashed ellipsoids indicate the formation of rHuEPO conjugates with HES-*g*-NH_2-R. HES, hydroxyethyl starch; HES-*g*-NH_2, amine-modified HES; HES-*g*-NH_2 rHuEPO, recombinant human erythropoietin; SDS-PAGE, sodium dodecyl sulfate-polyacrylamide gel electrophoresis.

(Figure 6, lane 3–6) as the concentration is reduced after addition of TG^{16}.

Thereafter, these conjugates were mixed with PNGase F and analyzed by SDS-PAGE in order to confirm that HES-*g*-NH_2 was conjugated with the polypeptide backbone and not with the glycans of rHuEPO. Following *N*-deglycosylation, the rHuEPO backbone migrates at a molar mass of ~18.4 kDa as shown in Figure 6, lanes 8–12. Moreover, the results show similar behavior of the conjugates before and after *N*-deglycosylation on the gel with the more intense band (Figure 6, lanes 10–12). Due to the fact that TG^{16} exhibits a half-life of 38 min at 60°C, a fresh amount of TG^{16} was added to the conjugation reaction. It is worth noting here that the most intense band is observed after 90 min reaction (Figure 6, lanes 6 and 12).

Conjugation experiments were further carried out with HES-*g*-NH_2-R and then analyzed by SDS-PAGE separation. **Figure 7** shows that no reaction occurred at time 0 (lane 3). After 30 min incubation at 54°C, rHuEPO-HES conjugates above 180 kDa together with aggregates on the top of the stacking gel (Figure 7 [left panel], lanes 4, 5, and 6) are observed. These are evidenced by the presence of high molar mass fluorescent band with a broad distribution (Figure 7 [right panel]). Furthermore, the fluorescent image indicates that the HES-*g*-NH_2-R band decreases with the reaction time. Together, these results confirm the successful conjugation reaction. Additionally, control experiment was carried out, where rHuEPO was incubated with HES-*g*-NH_2-R in the absence of TG^{16} (Figure 7 [left and right panel], lane 2) and the SDS-PAGE results reveal that no conjugation happened.

These conjugates were further treated with PNGase F and analyzed by SDS-PAGE as shown in **Figure 8**. From SDS-PAGE analysis, the conjugated species display a higher mobility and less distribution. A negative control investigated the possibility of HES-*g*-NH_2-R conjugation with TG^{16} in the absence of rHuEPO. As shown in Figure 8 (left and right panel, lane 7), some cross-linked aggregates are observed in the stacking gel which suggest that HES-*g*-NH_2-R can form aggregates with rHuEPO as well as with TG^{16}. The reaction is, however, much less pronounced than for rHuEPO since bands on the same height as rHuEPO conjugates with HES-*g*-NH_2-R (dashed ellipsoids in lanes 4–6) are absent in lane 7.

Overall, the detection of protein conjugates and aggregates at higher molar masses detected by SDS-PAGE was an indication of a successful protein-HES conjugation. The broad bandwidth is due to the molar mass distribution of HES and the multi-reactive sites (NH_2) along the polymer backbone.

4. Conclusions

An amine-functionalized HES was designed as an acyl acceptor substrate for the mTGase-catalyzed reaction with rHuEPO. Primary amine groups were initially introduced at the HES backbone via one step CDI coupling reaction giving HES-*g*-NH_2 (MS 7.5 mol%). The reaction of rHuEPO with HES-*g*-NH_2 using a thermoresistant TG^{16} results in the formation of high molar mass rHuEPO-HES conjugates and aggregates even in the presence of glycans. To proof these findings, some primary amine groups along the HES-*g*-NH_2 backbone were labeled with a fluorescent dye and then applied for the enzymatic conjugation reaction with rHuEPO. SDS-PAGE analysis revealed the presence of high molar mass fluorescent conjugates as well as crossed-linked aggregates. The presented mTGase variant TG^{16} can be regarded as a promising tool for the development of rHuEPO conjugates based on a fully biodegradable and water soluble polysaccharide, HES. HES conjugation with rHuEPO may positively impact its pharmacokinetics since the conjugation of HES with protein drugs generally leads to improved half-life in vivo.[49] However, in vitro and in vivo studies are still needed to verify the activity and immunogenicity of these conjugates.

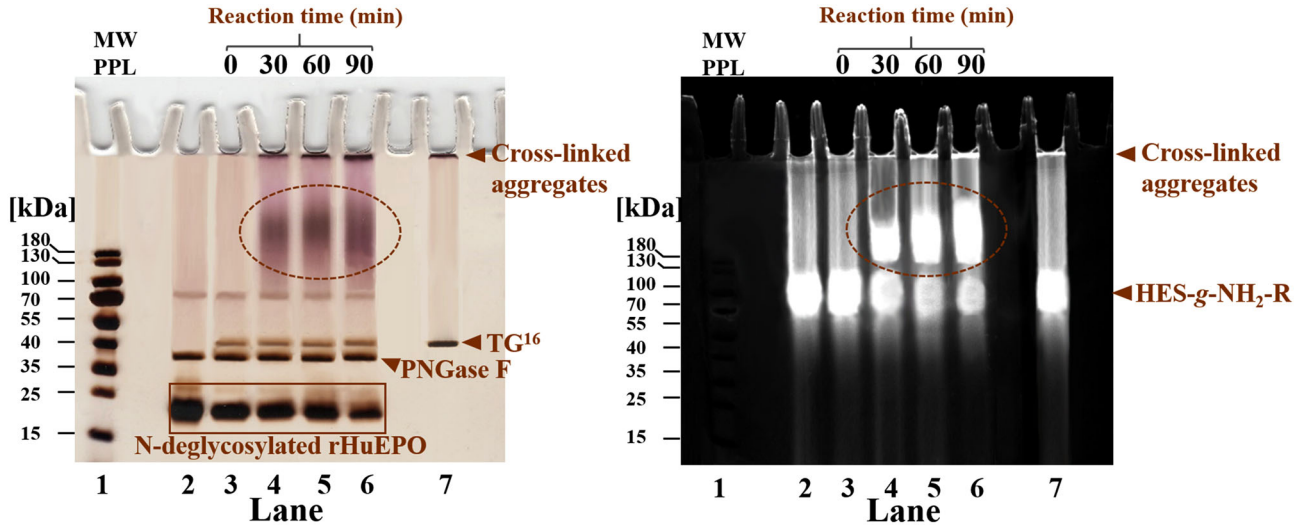

Figure 8. Silver stained images of the SDS-PAGE (left panel) and its fluorescent image (right panel) for the conjugation of rHuEPO with HES-*g*-NH_2-R at 54°C in the presence of TG^{16} after *N*-deglycosylation. Lane 1: prestained marker, lane 2: rHuEPO + HES-*g*-NH_2-R, lane 3–6: rHuEPO + HES-*g*-NH_2-R + TG^{16} at 0, 30, 60, and 90 min, respectively, Lane 7: HES-*g*-NH_2-R + TG^{16} incubated for 60 min. The dashed ellipsoids indicate the formation of rHuEPO conjugates with HES-*g*-NH_2-R. HES, hydroxyethyl starch; HES-*g*-NH_2, amine-modified HES; HES-*g*-NH_2-R, rhodamine B-labeled HES-*g*-NH_2; rHuEPO, recombinant human erythropoietin; SDS-PAGE, sodium dodecyl sulfate-polyacrylamide gel electrophoresis.

Supporting Information

Supporting Information is available from the Wiley Online Library or from the author.

Acknowledgements

R.H. and R.A. contributed equally to this work. This work was done in the frame of the International Graduate School AGRIPOLY supported by the European Social Fund (ESF) and the Federal State Saxony-Anhalt and Deutscher Akademischer Austauschdienst (DAAD) under a Research Grants – Doctoral Programs in Germany, 2017/18 (57299294).

Conflict of Interest

The authors declare no conflict of interest.

Data Availability Statement

The data that support the findings of this study are available from the corresponding author upon reasonable request.

Keywords

amine-modified hydroxyethyl starch, HES-g-NH_2-R, recombinant human erythropoietin, rHuEPO-HES conjugates, variant microbial transglutaminase

Received: February 1, 2022
Revised: May 3, 2022
Published online: July 11, 2022

[1] L. Lorand, S. M. Conrad, *Mol. Cell. Biochem.* **1984**, *58*, 9.
[2] L. Mariniello, R. Porta, *Prog. Exp. Tumor Res.* **2005**, *38*, 174.
[3] T. Ohtsuka, A. Sawa, R. Kawabata, N. Nio, M. Motoki, *J. Agric. Food Chem.* **2000**, *48*, 6230.
[4] L. Duarte, C. R. Matte, C. V. Bizarro, M. A. Z. Ayub, *World J. Microbiol. Biotechnol.* **2020**, *36*, 1.
[5] N. K. Sarkar, D. D. Clarke, H. Waelsch, *Biochim. Biophys. Acta* **1957**, *25*, 451.
[6] N. Doti, A. Caporale, A. Monti, A. Sandomenico, F. Selis, M. Ruvo, *World J. Microbiol. Biotechnol.* **2020**, *36*, 53.
[7] H. Ando, M. Adachi, K. Umeda, A. Matsuura, M. Nonaka, R. Uchio, H. Tanaka, M. Motoki, *Agric. Biol. Chem.* **1989**, *53*, 2613.
[8] K. Gottmann, B. Sprössler, (Röhm GMBH), *EP Patent 0492406*, **1992**.
[9] L. Deweid, O. Avrutina, H. Kolmar, *Biol. Chem.* **2019**, *400*, 257.
[10] V. Nagy, G. Szakacs, *Lett. Appl. Microbiol.* **2008**, *47*, 122.
[11] P. Strop, *Bioconjugate. Chem.* **2014**, *25*, 855.
[12] B. Böhme, B. Moritz, J. Wendler, T. C. Hertel, C. Ihling, W. Brandt, M. Pietzsch, *Amino Acids* **2020**, *52*, 313.
[13] K. Buettner, T. C. Hertel, M. Pietzsch, *Amino Acids* **2012**, *42*, 987.
[14] C. K. Marx, T. C. Hertel, M. Pietzsch, *J. Biotechnol.* **2008**, *136*, 156.
[15] K. Maso, A. Grigoletto, G. Pasut, *Adv. Protein Chem. Struct. Biol.* **2018**, *112*, 123.
[16] W. Steffen, F. C. Ko, J. Patel, V. Lyamichev, T. J. Albert, J. Benz, M. G. Rudolph, F. Bergmann, T. Streidl, P. Kratzsch, M. Boenitz-Dulat, T. Oelschlaegel, M. Schraeml, *J. Biol. Chem.* **2017**, *292*, 15622.
[17] C. D. Spicer, B. G. Davis, *Nat. Commun.* **2014**, *5*, 4740.
[18] M. Rashidian, J. K. Dozier, M. D. Distefano, *Bioconjugate. Chem.* **2013**, *24*, 1277.
[19] C. Maullu, D. Raimondo, F. Caboi, A. Giorgetti, M. Sergi, M. Valentini, G. Tonon, A. Tramontano, *FEBS J.* **2009**, *276*, 6741.
[20] A. Mero, B. Spolaore, F. M. Veronese, A. Fontana, *Bioconjugate. Chem.* **2009**, *20*, 384.
[21] H. Sato, E. Hayashi, N. Yamada, M. Yatagai, Y. Takahara, *Bioconjugate. Chem.* **2001**, *12*, 701.
[22] G. Gregoriadis, S. Jain, I. Papaioannou, P. Laing, *Int. J. Pharm.* **2005**, *300*, 125.
[23] A. Mero, M. Campisi, M. Caputo, C. Cuppari, A. Rosato, O. Schiavon, G. Pasut, *Curr. Drug Targets* **2015**, *16*, 1503.

[24] J. Hardwicke, E. L. Ferguson, R. Moseley, P. Stephens, D. W. Thomas, R. Duncan, *J. Control. Release* **2008**, *130*, 275.
[25] A. Mero, G. Pasut, L. D. Via, M. W. M. Fijten, U. S. Schubert, R. Hoogenboom, F. M. Veronese, *J. Control. Release* **2008**, *125*, 87.
[26] M. E. Brecher, H. G. Owen, N. Bandarenko, *J. Clin. Apher.* **1997**, *12*, 146.
[27] A. Besheer, G. Hause, J. Kressler, K. Mäder, *Biomacromolecules* **2007**, *8*, 359.
[28] C. M. Paleos, Z. Sideratou, D. Tsiourvas, *Bioconjugate. Chem.* **2017**, *28*, 1611.
[29] E. L. Ferguson, M. Varache, J. Stokniene, D. W. Thomas, in *Polymer-Protein Conjugates: From Pegylation and Beyond*, vol. *19* (Eds: G. Pasut, S. Zalipsky), Elsevier, New York, USA **2020**.
[30] A. Besheer, T. C. Hertel, J. Kressler, K. Mäder, M. Pietzsch, *J. Pharm. Sci.* **2009**, *98*, 4420.
[31] K. Sommermeyer, W. Eichner, S. Frie, C. Jungheinrich, R. Scharpf, K. Lutterbeck, (Fresenius Kabi Deutschland GMBH), *WO patent 02/080979*, **2002**.
[32] K. Sommermeyer, (Supramol Parenteral Colloid GMBH), *US patent 2009/0281296*, **2009**.
[33] A. Greindl, C. Kessler, B. Breuer, U. Haberl, A. Rybka, M. Emgenbroich, A. J. G. Pötgens, H. G. Frank, *Open Hematol. J.* **2010**, *4*, 1.
[34] H. S. Conradt, E. Grabenhorst, M. Nimtz, N. Zander, R. Frank, W. Eichner, (Fresenius Kabi Deutschland GMBH), *WO patent 2004/024761*, **2004**.
[35] C. Pool, (Janssen Biotech Inc), *US patent 2006/0116322*, **2006**.
[36] R. Alaneed, M. Naumann, M. Pietzsch, J. Kressler, *J. Biotechnol.* **2022**, *346*, 1.
[37] U. K. Laemmli, *Nature* **1970**, *227*, 680.
[38] H. Blum, H. Beier, H. J. Gross, *Electrophoresis* **1987**, *8*, 93.
[39] K. M. Camacho, S. Menegatti, S. Mitragotri, *Nanomedicine* **2016**, *11*, 1139.
[40] A. Paolini, L. Leoni, I. Giannicchi, Z. Abbaszadeh, V. D'Oria, F. Mura, A. D. Cort, A. Masotti, *Sci. Rep.* **2018**, *8*, 1.
[41] R. Alaneed, T. Hauenschild, K. Mäder, M. Pietzsch, J. Kressler, *J. Pharm. Sci.* **2020**, *109*, 981.
[42] A. Silva, E. Sousa, A. Palmeira, P. Amorim, P. G. De Pinho, D. A. Ferreira, *J. Biomol. Struct. Dyn.* **2014**, *32*, 1864.
[43] M. Weißl, M. A. Hobisch, L. S. Johansson, K. Hettrich, E. Kontturi, B. Volkert, S. Spirk, *Cellulose* **2019**, *26*, 7399.
[44] B. Spolaore, S. Raboni, A. A. Satwekar, A. Grigoletto, A. Mero, I. M. Montagner, A. Rosato, G. Pasut, A. Fontana, *Bioconjugate. Chem.* **2016**, *27*, 2695.
[45] W. Eichner, K. Lutterbeck, N. Zander, R. Frank, H. Knoller, H. Conradt, (Fresenius Kabi Deutschland GMBH), *WO patent 2005/092369*, **2005**.
[46] A. Santoso, Y. Rubiyana, W. Sk, N. Herawati, A. Wardiana, R. A. Ningrum, *Int. J. Pharma Bio Sci.* **2013**, *4*, 187.
[47] M. Manning, W. Colón, *Biochemistry* **2004**, *43*, 11248.
[48] T. K. Suresh Kumar, K. Gopalakrishna, V. V. H. Prasad, M. W. Pandit, *Anal. Biochem.* **1993**, *213*, 226.
[49] H. Wang, H. Hu, H. Yang, Z. Li, *R. Soc. Chem. Adv.* **2021**, *11*, 3226.

Enzymatic HES conjugation with recombinant human erythropoietin *via* variant microbial transglutaminase TG[16]

Rana Hore[1,†], Razan Alaneed[1,2,†], Markus Pietzsch[2,*] and Jörg Kressler[1,*]

[1] Department of Chemistry, Martin Luther University Halle-Wittenberg, Von-Danckelmann-Platz 4, D-06099 Halle/Saale, Germany

[2] Department of Pharmacy, Martin Luther University Halle-Wittenberg, Weinbergweg 22, D-06120, Halle/Saale, Germany

† These authors contributed equally to this study.

*Correspondence: markus.pietzsch@pharmazie.uni-halle.de; joerg.kressler@chemie.uni-halle.de

Supporting Information

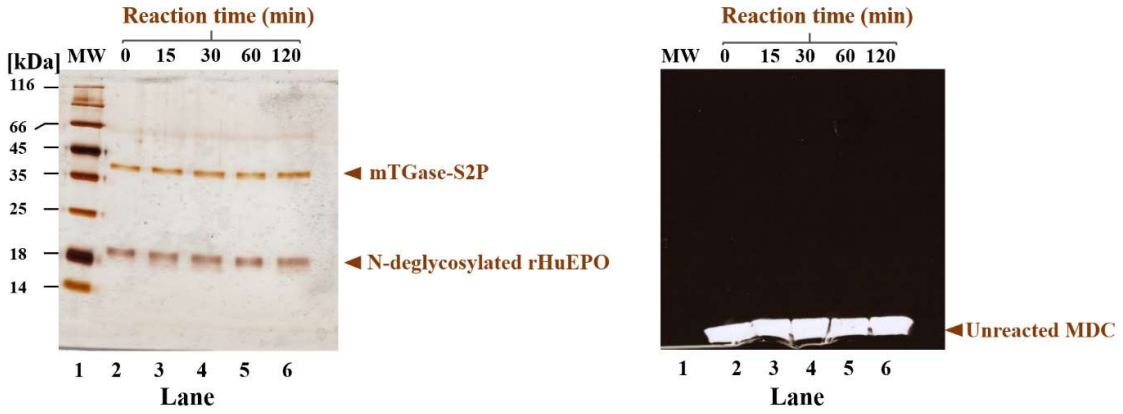

Fig. S1. Silver stained images of the SDS-PAGE (left panel) and its fluorescent image (right panel) for the reaction of rHuEPO with MDC at 37 °C in the presence of mTGase-S2P. Lane 1: molecular weight marker, Lane 2-6: N-deglycosylated rHuEPO + MDC + mTGase-S2P at 0, 15, 30, 60, and 120 min, respectively. The fluorescent image (right panel) shows no fluorescent bands at the molar mass of N-deglygosylated rHuEPO.

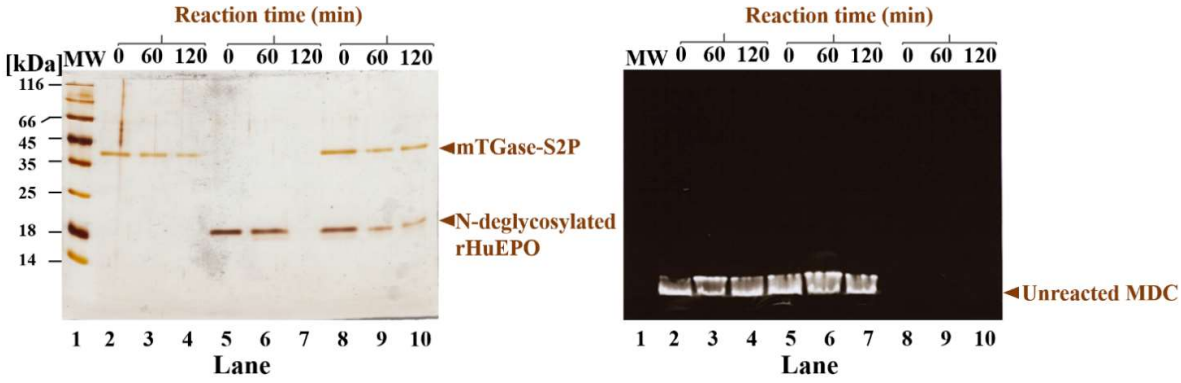

Fig. S2. Silver stained images of the SDS-PAGE (left panel) and its fluorescent image (right panel) for the reaction of MDC-mTGase-S2P, MDC-N-deglygosylated rHuEPO, and N-deglygosylated rHuEPO-

mTGase-S2P as control experiments at 37 °C. Lane 1: molecular weight marker, Lane 2-4: MDC + mTGase-S2P at 0, 60, and 120 min, respectively, Lane 5-7: MDC + N-deglygosylated rHuEPO at 0, 60, and 120 min, respectively, Lane 8-10: N-deglygosylated rHuEPO + mTGase-S2P at 0, 60, and 120 min, respectively.

3.1.2. Paper II: Synthesis and characterization of self-assembled highly stearate grafted hydroxyethyl starch conjugates

Polysaccharide-based nanotechnology in drug delivery leverages the natural properties of polysaccharides, offering a versatile and biocompatible platform for the effective delivery of therapeutic agents. To date, many natural and semisynthetic polysaccharides have been increasingly investigated as a drug delivery carrier for pharmaceutical applications. Among several polysaccharides, hydroxyethyl starch (HES) has attracted substantial interest for its excellent physiochemical and functional characteristics in the field of designing and synthesizing carriers for drug delivery systems.

To this aim, this publication focused on the development and characterization of polysaccharide-based nanocarrier, specifically using HES modified with stearic acid (SA) to achieve an enhanced hydrophobic inner core to entrap highly hydrophobic drugs. Two different hydrophobized stearate-HES (St-HES) conjugates were synthesized by varying the grafting ratio of SA to HES. Detailed structural characterization of HES and synthesized St-HES conjugates were investigated by ^{1}H, 2D HSQC, and HMBC NMR spectroscopy. Quantitative information on the degree of grafting of the St-HES conjugates was determined from ^{1}H NMR spectroscopy. The thermal and crystalline behavior of native HES and St-HES conjugates were investigated by DSC and WAXS. Furthermore, the ability and morphology of the conjugates to self-assemble into nanoparticles in aqueous media were characterized by DLS and SEM, respectively. Overall, the synthesized St-HES conjugates demonstrate promising carriers for various therapeutic applications within nanomedicine. These conjugates could potentially be applied to encapsulate hydrophobic drugs and bioactive compounds with improved encapsulation efficiency and loading capacity, thereby contributing new possibilities for the design and development of polysaccharide-based bio-nanocarrier for drug delivery systems.

The author's contributions to the following article are: R. Hore designed the research, conceptualized the work, performed the experiments and analyze the data, wrote the original draft, and made the finalization of the manuscript. H. Rashid and F. Syrowatka carried out the SEM experiment and analyzed the data. J. Kressler conceptualized the work, supervised, and discussed the results, reviewed them, and finalized the manuscript.

Title

Synthesis and Characterization of Self-Assembled Highly Stearate-Grafted Hydroxyethyl Starch Conjugates

Authors

Rana Hore, Haroon Rashid, Frank Syrowatka, and Jörg Kressler*

Bibliographic Details

Polysaccharides
Volume 5, Issue 2, Pages 142-157
Published 5 June 2024
DOI: 10.3390/polysaccharides5020011

∗: Corresponding Author

Source (Polysaccharide; https://doi.org/10.3390/polysaccharides5020011). The link to the article on the publisher's website is: https://www.mdpi.com/2673-4176/5/2/11.

polysaccharides

MDPI

Article

Synthesis and Characterization of Self-Assembled Highly Stearate-Grafted Hydroxyethyl Starch Conjugates

Rana Hore [1], Haroon Rashid [1,2], Frank Syrowatka [3] and Jörg Kressler [1,*]

[1] Department of Chemistry, Martin Luther University Halle-Wittenberg, Von-Danckelmann-Platz 4, D-06099 Halle/Saale, Germany; rana.hore@chemie.uni-halle.de (R.H.); haroon.rashid@student.uni-halle.de (H.R.)
[2] Department of Pharmacy, Martin Luther University Halle-Wittenberg, Weinbergweg 22, D-06120 Halle/Saale, Germany
[3] Interdisciplinary Center of Materials Science, Martin Luther University Halle-Wittenberg, Heinrich-Damerow-Str. 4, D-06120 Halle/Saale, Germany; frank.syrowatka@cmat.uni-halle.de
* Correspondence: joerg.kressler@chemie.uni-halle.de

Abstract: Polysaccharide-based nanoformulations with tailored hydrophobic properties have become a frontier in nanomedicine applications. Herein, highly hydrophobicized hydroxyethyl starch (HES) conjugates were synthesized by grafting stearic acid (SA) with HES via a carbodiimide-mediated reaction. A detailed NMR characterization of HES and the conjugates was studied to obtain structural information. The grafting ratio of the stearate-HES (St-HES) conjugates was determined from ^{1}H NMR spectra as 29.4% (St-HES29.4) and 60.3% (St-HES60.3). Thermal analyses and X-ray diffractograms suggested an entire transition from amorphous HES to a semicrystalline (St-HES60.3) character upon increasing the degree of grafting. Both conjugates, St-HES29.4 and St-HES60.3, were able to form self-assembled particles with a diameter of 130.7 nm and 152.5 nm, respectively. SEM images showed that the self-aggregates were mostly spherical in shape. These conjugates can be employed to entrap highly hydrophobic drugs with an increased encapsulation efficiency and loading capacity.

Keywords: polysaccharide; 1D and 2D NMR spectroscopy; hydrophobicized hydroxyethyl starch; St-HES; self-aggregates

Citation: Hore, R.; Rashid, H.; Syrowatka, F.; Kressler, J. Synthesis and Characterization of Self-Assembled Highly Stearate-Grafted Hydroxyethyl Starch Conjugates. *Polysaccharides* **2024**, *5*, 142–157. https://doi.org/10.3390/polysaccharides5020011

Academic Editor: Karin Stana Kleinschek

Received: 26 March 2024
Revised: 24 April 2024
Accepted: 31 May 2024
Published: 5 June 2024

1. Introduction

During the past decades, polymeric amphiphiles have received extensive attention owing to their distinctive properties and potential applications in the pharmaceutical and biomedical fields [1]. Such amphiphilic polymers have a unique supramolecular core–shell-like structure that can self-assemble in an aqueous environment to form polymeric nanoparticles or micelles, a promising drug delivery system to enhance bioavailability, and deliver hydrophobic bioactive materials with a better solubility profile [2]. The hydrophobic inner compartment serves as a microdomain for encapsulating various hydrophobic drugs and the outer hydrophilic corona provides steric stabilization, which can enhance the blood circulation time of the micelles and preserve active ingredients from rapid degradation [3–5]. The critical micelle concentration (CMC) is an important parameter to access the behavior of micelles. Amphiphilic molecules form micelles when concentration is at or above CMC. However, when administered in vivo, conventional micellar systems may encounter dilution effects below CMC in the bloodstream which may lead to the dissociation of micelles and premature drug release [6]. Several crosslinking and non-crosslinking approaches have been utilized to lower CMC and improve the stability of polymeric micelles. One of the strategies to lower the CMC is to increase the hydrophobic block and alter the crystallinity of the hydrophobic core of the micelles. Increasing the hydrophobic segments may enhance the hydrophobic interactions and the crystallization process may serve as an additional driving force for micelle assembly, consequently leading to a decreased CMC value [6,7].

Generally, the self-aggregates or micelles can be fabricated from macromolecular self-assembly using both synthetic and natural polymers. Biodegradability and biocompatibility are the most essential properties for the development of nanoparticulated polymer-based drug delivery systems [8]. Numerous polymeric amphiphiles have been studied as potential carriers for drug delivery systems and some of them are already available for commercial use [9]. Among them, synthetic polymers have played an essential role in the design and development of carrier systems for drug delivery. However, there are safety issues regarding their immunogenicity, non-biodegradability, and non-renewable sources [10]. Hence, natural biopolymers and their derivatives have gained particular research interest due to their versatility, unique properties, and available natural resources [11]. Polysaccharides, one of the most important and diverse classes of natural biopolymers, have been widely recognized and applied in biotechnology and biomedical applications. Moreover, natural polysaccharides have been notably studied as drug carriers due to their versatile characteristics such as wide accessibility, biocompatibility, biodegradability, and structural diversity [12]. In order to impart amphiphilicity, molecular modification is necessary to tailor their structures that can construct self-assembled nanocarriers for drug delivery [13]. Over the years, several polysaccharides and their derivatives have been investigated and studied as a potent carrier for drugs [14].

Hydroxyethyl starch (HES) is a semisynthetic derivative of starch utilized globally as a plasma volume expander [15]. In addition, HES attracts considerable interest as a designed nanocarrier in the form of nanomedicines due to its excellent properties such as biocompatibility, biodegradability, and low immunogenicity [16,17]. Moreover, introducing hydroxyethyl groups to the starch backbone in HES increases the water solubility of starch and improves stability to hydrolysis in vivo [18,19] making it one of the most favorable alternatives to fabricate nanocarriers in the pharmaceutical field. HESylation® is an excellent half-life extension (HLE) strategy to improve pharmacokinetic and pharmacodynamic properties based on the conjugation of HES with biopharmaceuticals [20,21]. However, several studies revealed an increased risk of kidney injury or renal dysfunction when HES is administered particularly to critically ill patients with sepsis requiring fluid resuscitation [22]. It is noteworthy that HES is used in substantially lower concentrations for nanoparticle preparation compared to fluid resuscitation therapy, therefore, safety concerns associated with HES are significantly reduced. Accordingly, various HES-based prodrugs, bioconjugates, nanocarriers, and hydrogels have been studied for the delivery of drugs and biomacromolecules [23]. For example, recently we reported an enzymatic approach for the conjugation of HES with recombinant human erythropoietin (HES-rHuEPO) via thermoresistant variant microbial transglutaminase, TG^{16} [24]. Accordingly, long-chain fatty acids have been used to obtain hydrophobically modified HES which can form self-assembled nanoparticles in aqueous media. Among them, HES modified with a low degree of grafting formed stable nanodispersions [25,26]. Stearic acid (SA) is a naturally occurring long-chain fatty acid widely used as a pharmaceutical excipient. Furthermore, SA has been explored in the field of polymeric nanoparticle formulations for drug delivery due to its better biocompatibility with low toxicity [27]. It was observed that a higher grafting ratio of SA may lead to an increased amount of drug loading [28].

Based on these considerations, highly grafted fatty acid esters of HES have been investigated by introducing stearate side chains for the preparation of polymeric self-aggregates to attain high encapsulation efficiency and sustained release of drugs or therapeutics. Initially, SA was covalently attached to HES via an esterification reaction to synthesize stearate-HES (St-HES) conjugates. Detailed structural and physicochemical characteristics of the native HES and two different grafted St-HES conjugates were thoroughly investigated by ^{1}H NMR, 2D heteronuclear single quantum coherence (HSQC), and heteronuclear multiple bond correlation (HMBC) spectroscopy, differential scanning calorimetry (DSC) and wide-angle X-ray scattering (WAXS). Afterwards, the synthesized conjugates were used to prepare self-assembled micelles in an aqueous phase. The particle size and mor-

phology of the micelles were characterized by dynamic light scattering (DLS) and scanning electron microscopy (SEM).

2. Materials and Methods

2.1. Materials

Hydroxyethyl starch (HES) with a weight average molar mass (M_w) of 70 kDa and molar substitution (the number of hydroxyethyl residues per glucose subunit) of 0.5 was a gift from Serumwerk Bernburg, Germany. Stearic acid was obtained from Sigma-Aldrich (Steinheim, Germany). N,N-dimethylformamide (DMF, extra dry, 99.8%) was purchased from Acros Organics (Schwerte, Germany). Tetrahydrofuran (THF), 4-(dimethylamino)pyridine (DMAP), 1-ethyl-3-(3-dimethylaminopropyl)carbodiimide hydrochloride (EDC·HCl), dimethyl sulfoxide (DMSO), and dialysis membrane (having a cut-off molar mass of 3000 g/mol) were purchased from Carl Roth (Karlsruhe, Germany). N,N-dimethylformamide-d_7 (DMF-d_7, 99.5%), dimethyl sulfoxide-d_6 (DMSO-d_6, 99.8%), and deuterium oxide (D_2O, 99.9%) were purchased from Armar Chemicals (Döttingen, Switzerland). Ethanol and diethyl ether were reagent grade and used as received.

2.2. Methods

2.2.1. Nuclear Magnetic Resonance (NMR) Spectroscopy

The NMR spectra were acquired on a VNMRS spectrometer (Agilent Technologies, Santa Clara, CA, USA) at 500 MHz for ^{1}H and 125 MHz for ^{13}C and the attached proton test (APT) ^{13}C NMR measurements. Two-dimensional (2D) NMR measurements, namely, HSQC and HMBC spectroscopy, were performed for complete structural characterization. For native HES, 20 mg of samples were dissolved in 0.6 mL of deuterated solvents and the measurements were carried out at 27 °C using tetramethylsilane (TMS) as an internal standard. For synthesized St-HES conjugates, 2–10 mg of samples were dissolved in 0.6 mL of deuterated solvents at 50 °C for complete dissolution and the measurements were carried out at 50 °C using TMS standard. The residual solvent signals were set for DMSO-d_6 at δ_H 2.50 ppm and δ_C 39.52 ppm, for D_2O at δ_H 4.79 ppm, and for DMF-d_7 at δ_H 2.75, 2.92 and 8.03 ppm. An intense residual HDO peak was observed in the NMR spectra, which may be due to the hygroscopic nature of both NMR solvents and HES. The NMR spectral data were interpreted using MestRec (v.4.9.9.6) software (Mestrelab Research, Santiago de Compostela, Spain).

2.2.2. Differential Scanning Calorimetry (DSC)

DSC measurements were carried out using a Mettler Toledo DSC 822^e (Schwerzenbach, Switzerland) instrument. A total of 4–5 mg of the samples was poured into 40 µL aluminium pans and then sealed. The experiments were run in a temperature range from −60 °C to 120 °C with a heating and cooling rate of 1 K/min, a holding time of 10 min, and a continuous nitrogen flow of 10 mL/min. All DSC data were taken from the second heating curve.

2.2.3. Wide-Angle X-ray Scattering (WAXS)

The wide-angle X-ray diffraction patterns were recorded with a PANalytical Empyrean Diffractometer. The instrument was equipped with a position-sensitive PIXcel-3D detector in Bragg–Brentano geometry. The samples were measured on a silicon zero-background substrate in a TTK 450 temperature chamber (Anton Paar) with Ni-filtered CuK_α (λ = 0.15418 nm) radiation. The measurements were performed under a constant nitrogen flow. The diffractograms were recorded with a scattering angle of 2θ in the range of 6° to 60° with a step size of 2θ = 0.053° and a counting time of 93 s per step. The samples were initially heated to 100 °C and then cooled to T = −30 °C with a cooling rate of 10 K/min. All the WAXS diffractograms were recorded at T = −30 °C, except SA, which was recorded at room temperature.

2.2.4. Determination of Particle Size by Dynamic Light Scattering (DLS)

The particle size and intensity-weighted size distribution of the self-aggregates were determined by DLS using a Litesizer 500 device (Anton Paar GmbH, Graz, Austria) at 25 °C. The sample concentration of 0.1 mg/mL in water was taken in 70 µL micro cuvettes and measured at a light wavelength of 658 nm and a detection angle of 175°. Hydrodynamic diameter (D_h) and the broadness of the intensity size distribution, polydispersity index (PDI), were obtained from the intensity curve fitting by applying the autocorrelation function using an integrated Kalliope Ver. 2.16.0 software (Anton Paar GmbH).

2.2.5. Scanning Electron Microscopy (SEM)

The morphology of the particles was characterized by GeminiSEM 500 (Carl-Zeiss Microscopy GmbH, Jena, Germany) at an acceleration voltage of 1 kV. A total of 0.01–0.1 mg/mL of samples were taken in a Hamilton syringe and applied on the CO_2 snow jet-cleaned silicon plate at a volume of 5 to 10 µL followed by air-drying. The average particle size of each sample was determined by fitting the size distribution histogram to the log-normal distribution function.

2.2.6. Synthesis of Stearate-Hydroxyethyl Starch (St-HES) Conjugates

The synthesis of modified HES was carried out via a simple Steglich esterification reaction [26,29] with small modifications. Briefly, 1 g (5.45 mmol) of HES was dried at 110 °C for 2 h before dissolving in 20 mL of anhydrous DMF in a round bottom flask. Either 0.52 g (1.83 mmol) or 1.03 g (3.63 mmol) of SA were added to that solution and left under stirring with a speed of 400 rpm at 40 °C until it turned into a clear solution. Afterwards, EDC·HCl (3 eq.) and DMAP (0.3 eq.) were added to the solution and the flask was tightly sealed and stirred for 24 h at 40 °C. Then, the reactant mixture was cooled down to room temperature and precipitated in an ethanol:diethyl ether (1:1) solvent mixture and kept at 4 °C until the precipitate completely settled down. The solvent was decanted, and the procedure was repeated three times with the same solvent mixture. Finally, the precipitate was dialyzed against distilled water for three days and then lyophilized.

2.2.7. Preparation of Self-Assembled Nanoparticles of St-HES Conjugates

Self-assembled nanoparticles were prepared according to the nanoprecipitation method [30]. A total of 10 mg of each conjugate was dissolved in 1 mL of DMSO or THF into a small vial under magnetic stirring at 60 °C. After complete dissolution, the solution was slowly injected using a syringe pump into 10 mL of distilled water previously equilibrated at 60 °C under rapid magnetic stirring. Afterwards, the dispersion was poured into an ice-cooled empty vial under magnetic stirring to attain rapid solidification and kept stirring for 3 h to homogenize the system. Then, the dispersion was dialyzed against distilled water for three days and finally, part of the water was removed by rotary evaporator to obtain a 0.1 mg/mL dispersion.

3. Results and Discussion

3.1. Characterization of HES

HES, a derivative of natural starch, was selected for the synthesis of highly grafted hydrophobicized HES conjugates due to its abundance of hydroxyl groups, allowing easy modifications according to the desired properties and designing programmable self-assembled nanocarriers with multiple functionalities [31]. Previously, Kulicke et al. reported the chemical characterization of HES by 1D NMR spectroscopy [32]. However, it is worthwhile to investigate a detailed 2D NMR analysis of the native HES to provide precise information regarding ^{1}H and ^{13}C assignments and subsequently the calculation of the degree of grafting. Thus, a comprehensive structural characterization of native HES was performed by utilizing ^{1}H NMR including labile proton exchange phenomena, 2D HSQC, and HMBC spectroscopy. Here, the –OH substitutions by the hydroxyethyl groups and

branching points are denoted as (s) and (b), respectively. Figure 1 shows the ^{1}H NMR spectrum of HES in DMSO-d_6 including the chemical structure and the signal assignments.

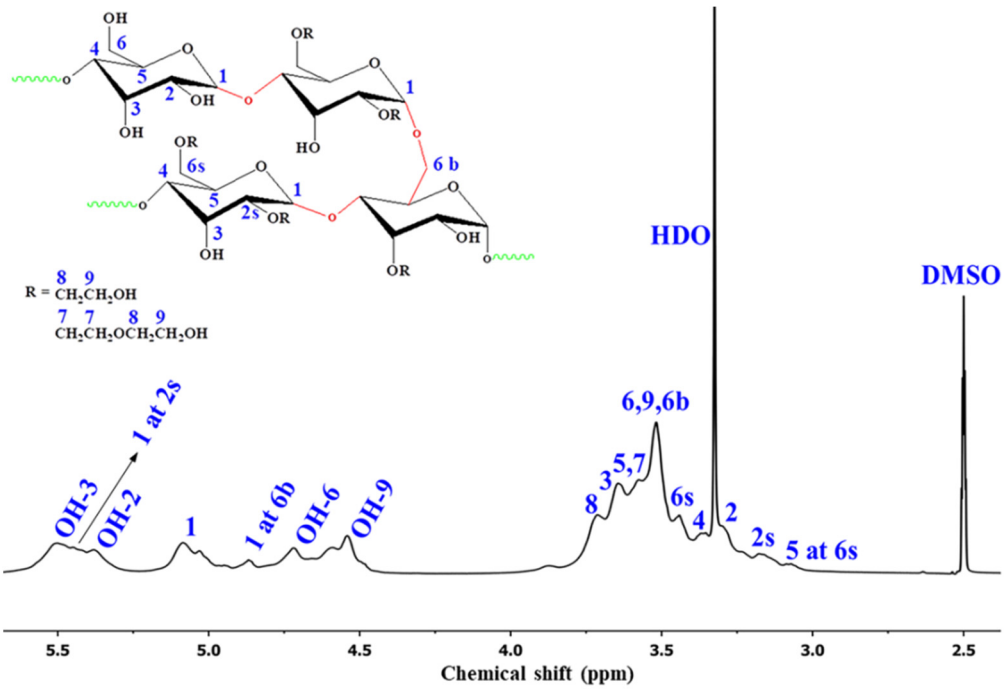

Figure 1. ^{1}H NMR spectrum of HES in DMSO-d_6 at 27 °C. The inset shows the structure of HES with peak assignments.

In Figure 1, significant peak overlapping is observed, making it challenging to identify and assign all the peaks in the spectrum [33–36]. The anomeric proton resonances of H-1 at α-1,4 unsubstituted (peak 1), H-1 at α-1,4 substituted at C-2 position by hydroxyethyl group (peak 1 at (2s)), and H-1 at α-1,6 branching points (peak 1 at (6b)) are also difficult to resolve due to signal overlapping with the hydroxyl group (–OH) peaks from the anhydroglucose unit (AGU) of HES in the region of δ_H 4.44−5.70 ppm. To determine the peaks raised from anomeric protons, ^{1}H NMR measurements (Figure 2) were carried out in D_2O and D_2O/DMSO-d_6 mixture 1:9 ratio so that the protons of the hydroxyl groups of HES can rapidly exchange with labile deuterium.

As shown in Figure 2A,C, due to deuterium exchange only the anomeric protons are observed in the range of δ_H 4.44–5.70 ppm. By comparing Figure 2A–C, the ^{1}H NMR chemical shift at 5.45 ppm, 5.08 ppm, and 4.86 ppm can be identified as the anomeric protons labeled as peak 1, peak 1 at (2s), and peak 1 at (6b) [32,37–41]. All other ring protons of the HES backbone coalesced into a broad peak 2–9 between δ_H 3.02 and 3.92 ppm. Based on the ^{1}H and ^{13}C NMR peak assignment of starch, and its derivatives, it is possible to assign the proton resonance signals raised from the AGU of HES denoted as peaks 2 to 9 in the region of δ_H 3.02–3.92 [32,37–39,41,42]. For complete characterization of the native HES, 2D NMR experiments, namely ^{1}H-^{13}C HSQC and ^{1}H-^{13}C HMBC spectroscopy were performed. Figure 3 represents the HSQC and HMBC NMR spectra of HES. The ^{1}H and the APT ^{13}C spectra are depicted on the x- and y-axis, respectively. In Figure 3A the HSQC NMR spectrum, the correlation signals of AGU at δ_C/δ_H 100.23/5.08, 71.72/3.29, 73.28/3.64, 79.01/3.36, 71.15/3.57, 60.49/3.51, 72.40/3.57, and 72.40/3.71 correspond to C1/H1, C2/H2, C3/H3, C4/H4, C5/H5, C6/H6 and C9/H9, C7/H7, and C8/H8, respectively. In addition, other correlation signals are also observed due to branching and –OH substitution by the hydroxyethyl group. The correlation peaks at δ_C/δ_H 80.15/3.17, 72.18/3.44, 70.13/3.06, 96.43/5.45, and 69.14/3.52 are attributed to C2s/H2s, C6s/H6s, C5 at (6s)/H5 at (6s), C1 at (2s)/H1 at (2s), and C6b/H6b, respectively.

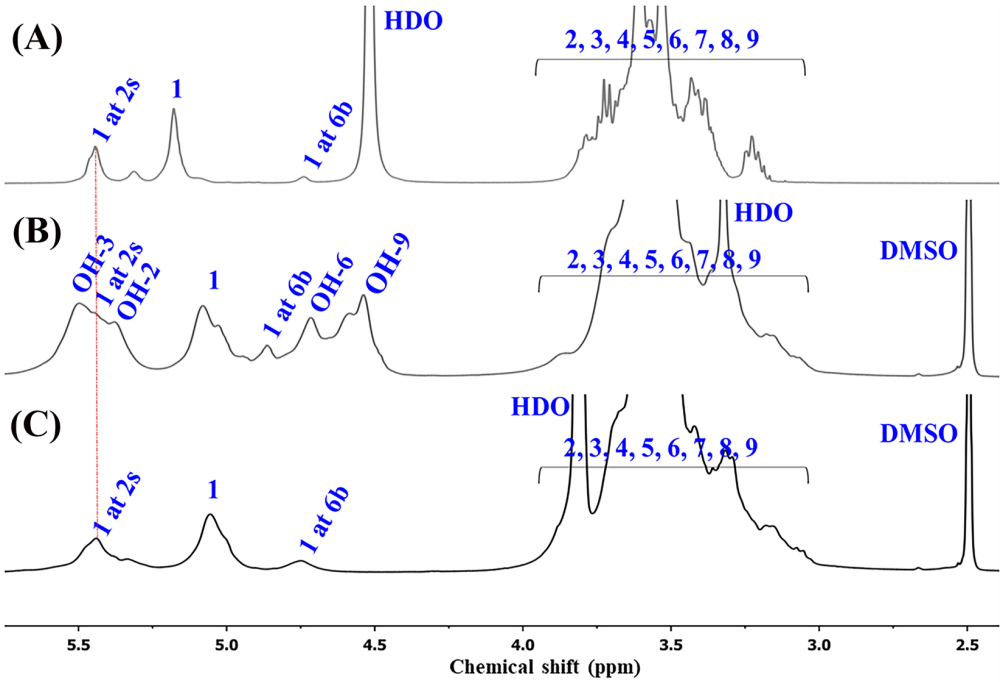

Figure 2. ^{1}H NMR spectra of HES in (**A**) D_2O, (**B**) DMSO-d_6, and (**C**) D_2O/DMSO-d_6 (1:9) at 27 °C. The structure of HES is given in the inset of Figure 1.

However, the HSQC NMR spectrum depicts only the correlation signal between each carbon with its directly attached protons. Because of this phenomenon, the signal for OH-2, 3, 6, and 9 could not be detected as these protons are not directly attached to the carbon atom of the HES molecule. To identify the proton shift in the hydroxyl groups and other protons, the 2D HMBC experiment was recorded which reveals the correlation between carbon and protons in the long range ($^{2}J_{C\text{-}H}$ or more). Figure 3B represents the HMBC spectrum of HES. In Figure 3B, the correlation signals at δ_C/δ_H 60.49/4.72, 70.13/4.86, 73.28/4.86, 71.15/4.72, 60.49/4.54, 72.40/4.54, 60.49/3.71, 80.15/3.71, 60.49/3.57, 72.40/3.51, 60.49/3.44, and 70.13/3.44 correspond to C6/OH-6, C5 at (6s)/H1 at (6b), C3/H1 at (6b), C5/OH-6, C9/OH-9, C8/OH-9, C6/H8, C2s/H8, C6/H5, C8/H9, C9/H6s, and C5 at (6s)/H6s, respectively. By combining HSQC and HMBC spectra, all the resonance signals that arise from the HES backbone are readily assigned except OH-2 and OH-3. However, the ^{1}H chemical shift of OH-2 and OH-3 can be assigned at 5.40 ppm and 5.50 ppm, respectively, based on other reports [38,39,43,44].

3.2. Synthesis and NMR Characterization of St-HES Conjugates

St-HES conjugates were synthesized by the formation of ester linkage via a simple esterification reaction between the carboxylic group of SA and the hydroxyl groups of HES. The synthesis scheme of the St-HES conjugates is shown in Scheme 1.

Two different highly grafted hydrophobicized St-HES conjugates were synthesized by controlling the grafting ratio of SA to HES. The two conjugates were defined as St-HES with degrees of grafting at 29.4% (St-HES29.4) and 60.3% (St-HES60.3). The structure of St-HES conjugates was verified by ^{1}H, 2D HSQC, and HMBC NMR spectroscopy. The ^{1}H NMR spectra of St-HES29.4, St-HES60.3, and SA are shown in Figure 4A–C. By comparing Figures 1 and 4A–C, it is noticeable that the proton signals arising from the grafted stearate side chain are completely distinguishable from the polymer backbone. The characteristic proton signals of HES were observed between 3.01 ppm and 5.70 ppm. After modification, the new peak b at 0.80 ppm appeared, which corresponds to the methyl protons of the esterified stearate side chain. Two ^{1}H NMR signals are observed at 1.08–1.28 ppm (peak c, d, and e) and the 1.46 ppm (peak f) is attributed to the methylene protons of stearate. The

methylene protons attached to the carbonyl group of the ester linkage give a resonance signal at 2.24 ppm (peak g) [26].

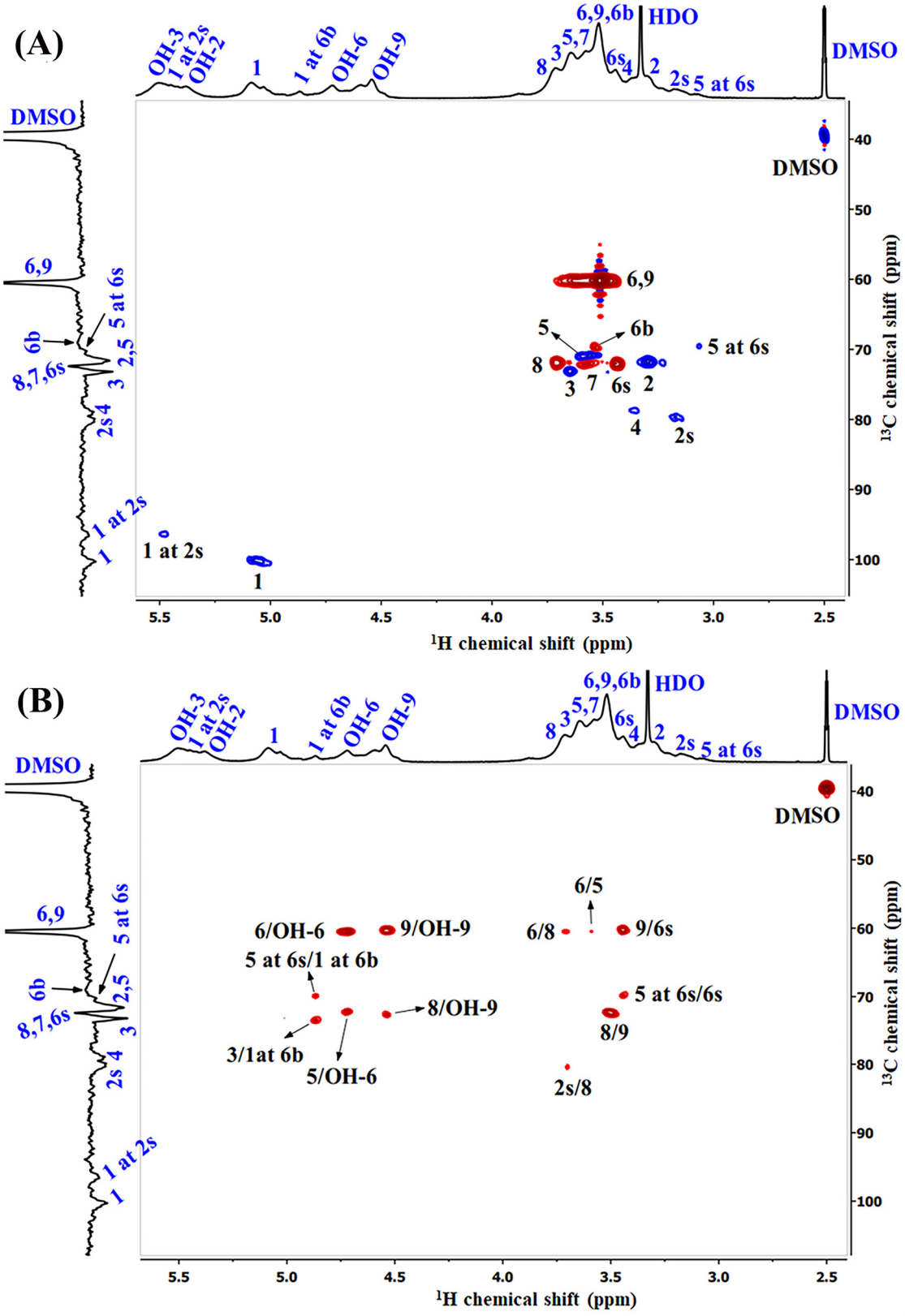

Figure 3. (**A**) HSQC and (**B**) HMBC NMR spectra of HES in DMSO-d_6 at 27 °C. The structure of HES is given in the inset of Figure 1.

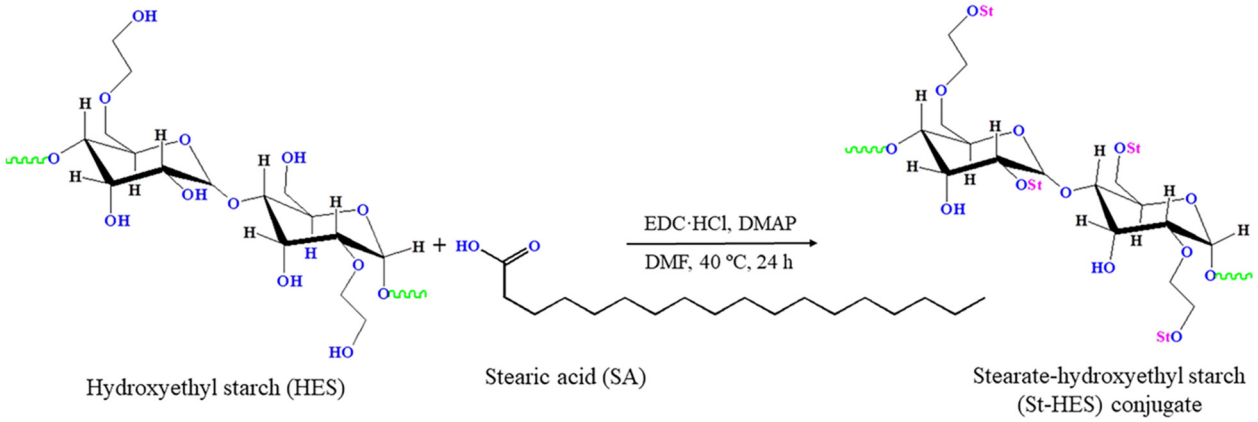

Scheme 1. Synthetic pathway for stearate-hydroxyethyl starch (St-HES) conjugates.

The complete disappearance of the proton signal of the carboxyl group of SA at 11.93 ppm, is an indication of HES conjugation with SA. The chemical structure of St-HES conjugates was further characterized by HSQC and HMBC NMR spectroscopy. As both St-HES29.4 and St-HES60.3 have similar structures except for variation in the degree of grafting, only the 2D NMR spectra for St-HES29.4 are shown in Figure 5. The ^{1}H and ^{13}C spectra are presented along the x- and y-axis, respectively. In Figure 5A the HSQC NMR spectrum, a cross-peak at δ_C/δ_H 13.81/0.80 belongs to the Cb/Hb signal, which represents the methyl group of stearates. The correlation signals at 22.02/1.08–1.28, 31.32/1.08–1.28, and 29.09/1.08–1.28 are attributed to the methylene groups of grafted chain denoted as Cc/Hc, Cd/Hd, and Ce/He. The cross-peak Cf/Hf (δ_C/δ_H 24.41/1.46) is related to the methylene group adjacent to the carbonyl group and the cross-peak Cg/Hg (δ_C/δ_H 33.45/2.24) is assigned as the methylene group directly attached to the carbonyl group. Figure 5B represents the HMBC spectrum of St-HES29.4. The correlation signals at δ_C/δ_H 22.02/0.80, 31.32/0.80, 22.02/1.08–1.28, 29.09/1.08–1.28, and 31.32/1.08–1.28 are attributed to the Cc/Hb, Cd/Hb, Cc/Hd, Ce/Hd, and Cd/Hf or He, respectively. A new ^{13}C chemical shift is observed at 175.16 ppm, with no corresponding cross-peak in the HSQC and HMBC NMR spectra (Figure 5A,B) assigned as the carbonyl signal from the newly formed ester linkage (–COO). This is a clear indication of the efficient conjugation of St-HES. The degree of grafting is defined as the number of stearate chains attached to 100 AGUs. The degree of grafting is determined as 29.4% (St-HES29.4) and 60.3% (St-HES60.3) from the integration peak a and peak b shown in the ^{1}H NMR spectra (Figure 4A,B), using Equation (1).

$$Degree\ of\ grafting = \left(\frac{\frac{I_b}{3}}{\frac{I_a + \frac{I_b}{3}}{4}} \right) \quad (1)$$

Here, I_b is the integral value of three methyl protons from the stearate side chains and I_a is the integral of the four protons, particularly the anomeric proton and the three protons from the hydroxyl groups of the AGU.

3.3. DSC and WAXS Analysis

The thermal and crystalline behavior of native HES, St-HES29.4, and St-HES60.3 were investigated by DSC and WAXS, respectively (Figure 6). Figure 6A represents the DSC thermograms of HES, St-HES29.4, and St-HES60.3 in the temperature range between −60 °C and 120 °C at a heating rate of 1 K/min. All the DSC thermograms shown here are taken from the second heating curve. The DSC curve (Figure 6A) of native HES shows that this polymer is fully amorphous in the temperature range studied. Consequently, the DSC thermogram of St-HES29.4, containing 29.4% stearate side chains, does not show any melting endotherm and behaves like an amorphous polymer. This demonstrates that the grafted stearate chains on HES form non-crystalline structures with no distinct

ordered arrangement of the chains. One reason is that the amorphous HES prevents the crystallization of side chains, thus no characteristic endothermal peak is observed during the heating cycle [45]. With increasing the grafting ratio from 29.4% (St-HES29.4) to 60.3% (St-HES60.3), a melting transition appeared in the DSC thermogram (Figure 6A). Since HES is an amorphous polymer, the endothermal transition arises from the stearate side chains, which indicates a semi-crystalline behavior of St-HES60.3 [46]. This can be explained by the differences in the grafting ratio of St-HES29.4 and St-HES60.3. When the grafting ratio increased from 29.4% to 60.3%, the stearate chains on the HES backbone were sufficient to form a regular arrangement of the side chains and pack into an ordered crystal structure [47]. St-HES60.3 shows a broad melting range of −7 °C to 29 °C, with a melting point (T_m) of 21.2 °C taken as the maximum of the DSC heating curve (Figure 6A). In addition, the DSC thermogram of St-HES60.3 shows that grafting SA with amorphous HES at around 60% causes the melting point depression of SA (T_m of SA is 69.3 °C [48]) and is close to the T_m of octadecane (28–30 °C) [46]. One possible explanation could be that the amorphous nature of HES and the random distribution of the stearate chains along the HES backbone might interfere with the highly ordered packing of the side chains, resulting in the formation of more imperfect crystals of varying sizes [49,50]. These results further confirmed that HES was successfully grafted with SA.

The WAXS patterns of SA, HES, St-HES29.4, and St-HES60.3 are presented in Figure 6B and were recorded (except SA measured at room temperature) at −30 °C. The Bragg reflections from the silicon substrate appeared below 2θ = 8° and at more than 30°. Hence, no interference was observed with the measured samples. SA exhibits sharp diffraction peaks at 2θ of 19.18°, 21.74°, and 24.43°, shown in Figure 6B, demonstrating the crystalline nature of SA at room temperature. The pure HES showed a broad amorphous halo in the range of 2θ = 13°–27° indicating that the sample is completely amorphous [51]. Furthermore, the WAXS profile of St-HES29.4 did not show any distinct Bragg reflections rather than a big halo, which is consistent with the DSC result. The absence of characteristic diffraction peaks of pure SA in the grafted St-HES29.4 indicates the complete disappearance of the crystalline nature of SA after conjugation. However, St-HES60.3 showed a strong reflection at 2θ = 21.84° together with an amorphous halo, which is in agreement with the DSC analysis (Figure 6A). This diffraction peak may be attributed to the intense Bragg reflection raised from the 110 plane of SA, which usually appeared at 2θ = 21.74° (Figure 6B) in pure SA. This result suggests that the partial crystalline nature of St-HES60.3 arises only from the grafted side chains.

3.4. Characterization of Self-Aggregated St-HES Conjugates

The St-HES conjugates could readily self-assemble in aqueous media and form micelles or self-aggregates due to intra- or intermolecular hydrophobic interactions [9]. The hydrophilic backbone of HES forms the outer shell of the micelles, and the hydrophobic stearate segments are oriented towards the core to achieve an energy-minimized spherical structure [52,53]. Figure 7 shows the size distribution of self-aggregates of St-HES29.4 and St-HES60.3 conjugates in distilled water as determined by DLS. In Figure 7A, the intensity size distribution of the St-HES29.4 conjugate shows a monomodal size distribution with a hydrodynamic diameter (D_h) of 130.7 nm and a polydispersity index (PDI) of 0.16. A similar self-assembled behavior was observed for the St-HES60.3 conjugate. The DLS histogram of the St-HES60.3 conjugate (Figure 7B) suggests a single Gaussian distribution (monomodal) of the sample with a D_h of 152.5 nm and a PDI of 0.21. The size of St-HES micelles increases from 130.7 nm to 152.5 nm, with an increase in the grafting ratio of stearate side chains from 29.4% (St-HES29.4) to 60.3% (St-HES60.3) possibly due to two factors. Firstly, two different solvents, DMSO for St-HES29.4 and THF for St-HES60.3, were used initially to dissolve the conjugates to formulate micelles in water, which could impact the average particle dimensions later [54]. Secondly, the higher degree of side chain grafting would lead to aggregating more St-HES chains close together in one particle. Consequently, more chain aggregation in one particle results in more repulsive forces between and within the hydrophobic stearate chains, which in turn contributes to the overall increase in particle size [8].

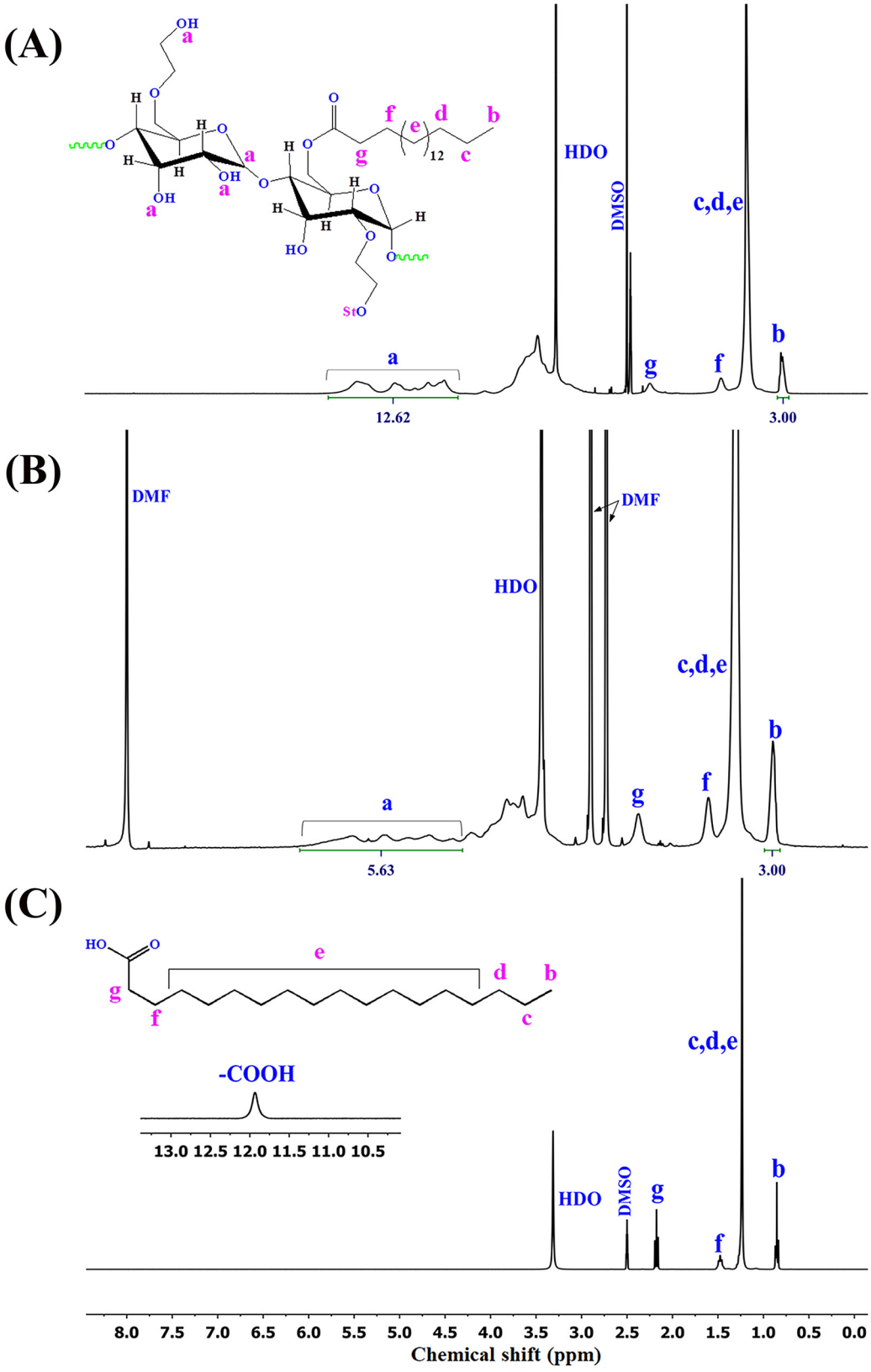

Figure 4. The ^{1}H NMR spectra of (**A**) St-HES29.4 and (**B**) St-HES60.3 were recorded at 50 °C using DMSO-d_6 and DMF-d_7 as solvents, respectively. The (**C**) ^{1}H NMR spectrum of SA was recorded at 27 °C using DMSO-d_6.

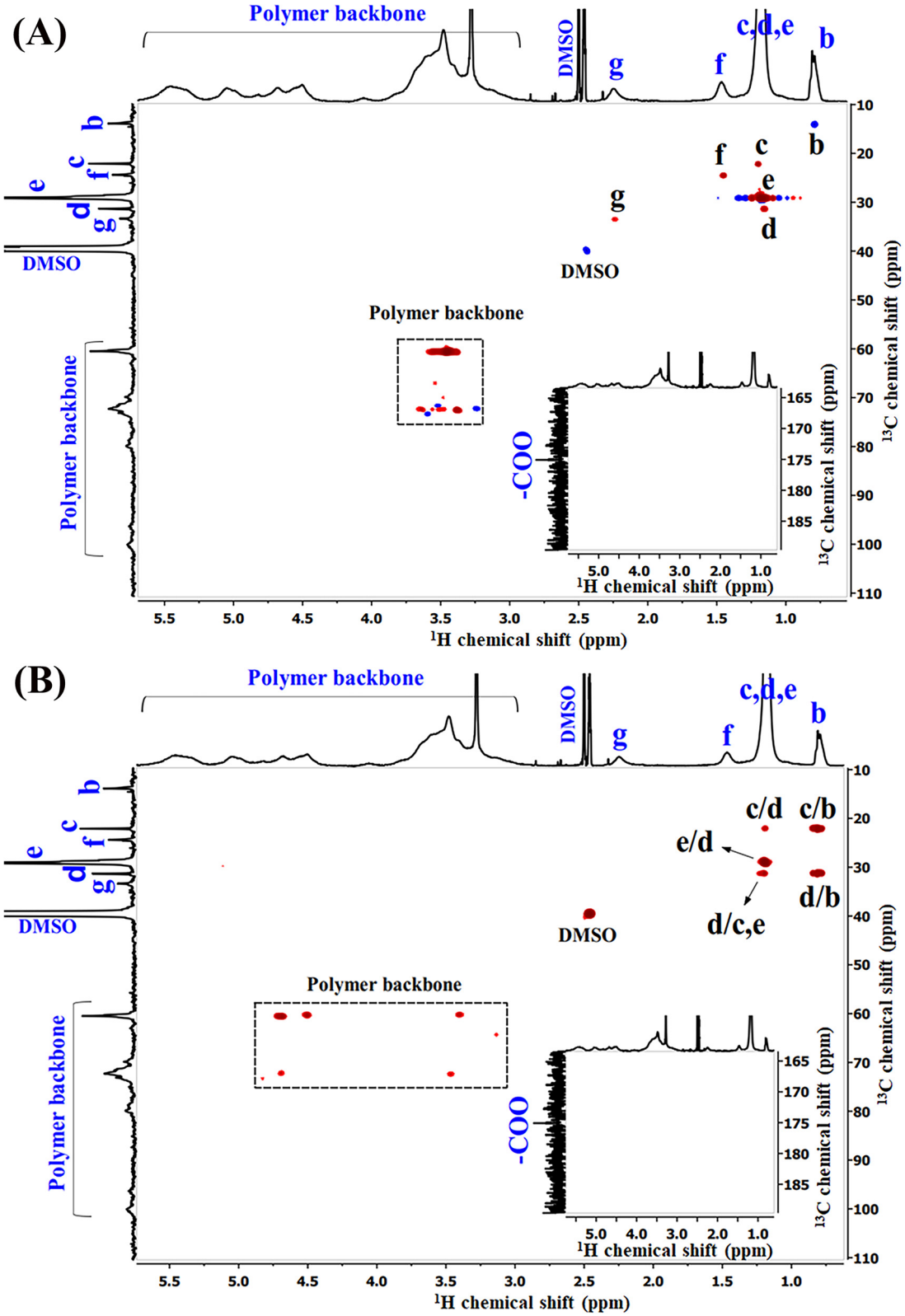

Figure 5. (**A**) HSQC and (**B**) HMBC NMR spectra of St-HES29.4 in DMSO-d_6 at 50 °C. The structure of St-HES is given in the inset of Figure 4(**A**). The insets show the range of 1−5.5 ppm and 165−185 ppm for ^{1}H and ^{13}C NMR chemical shifts, respectively. No additional correlation signals are observed for –COO.

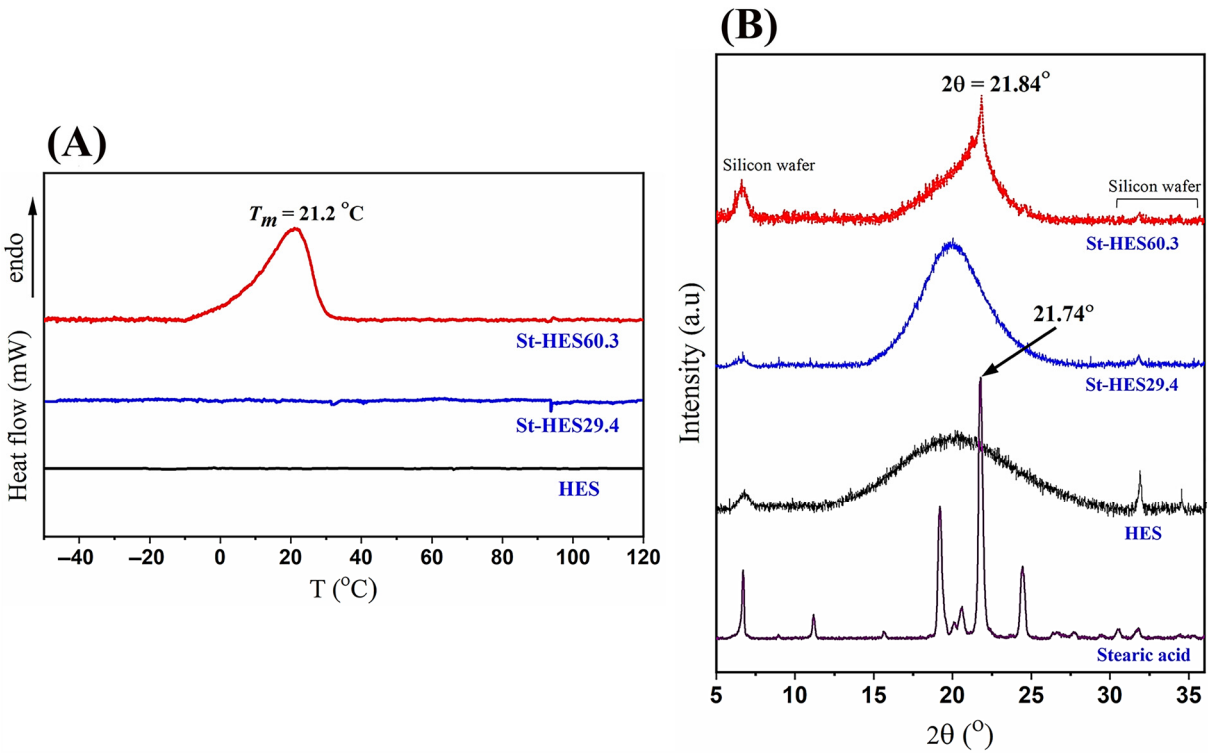

Figure 6. (**A**) DSC traces of HES, St-HES29.4, and St-HES60.3, with the respective melting temperature, T_m, recorded at a heating rate of 1 K/min. (**B**) WAXS diffraction patterns of SA, HES, St-HES29.4, and St-HES60.3 at T = −30 °C (except SA measured at room temperature).

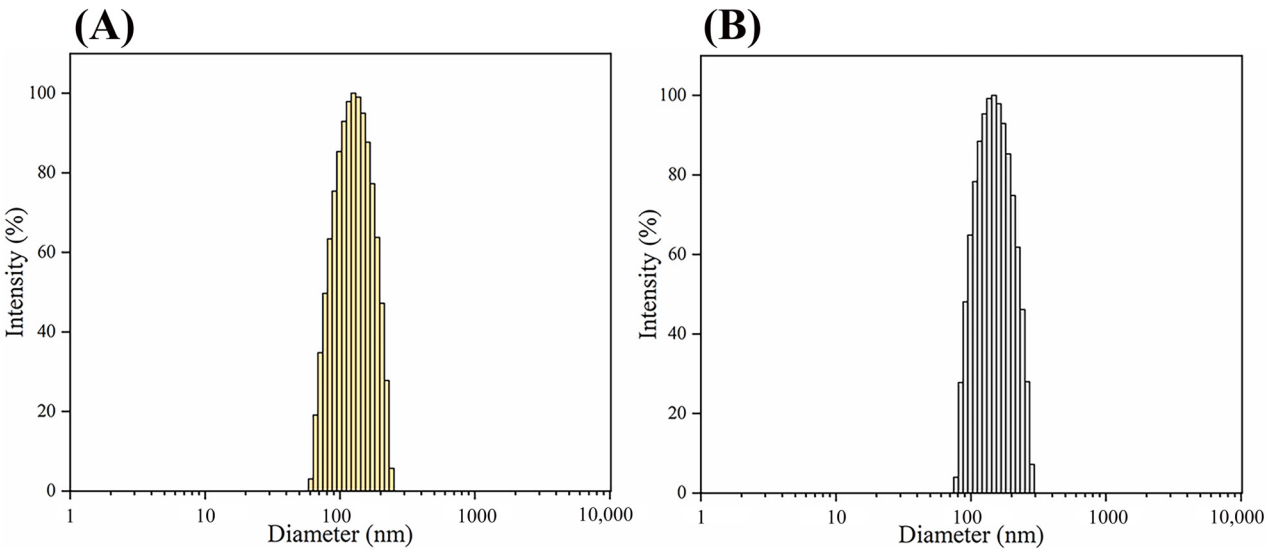

Figure 7. Intensity-weighted particle size distribution of (**A**) St-HES29.4 and (**B**) St-HES60.3 in distilled water measured by DLS at 25 °C.

To further examine the morphology of St-HES micelles, SEM was carried out by dispersing the prepared samples and drying them on the silicon substrate. Figure 8A–D represent the SEM images and size distribution of St-HES29.4 and St-HES60.3, respectively. The SEM microphages demonstrate that both samples are nearly spherical in shape and, to some extent, collapse structures are formed, as shown in Figure 8A–C.

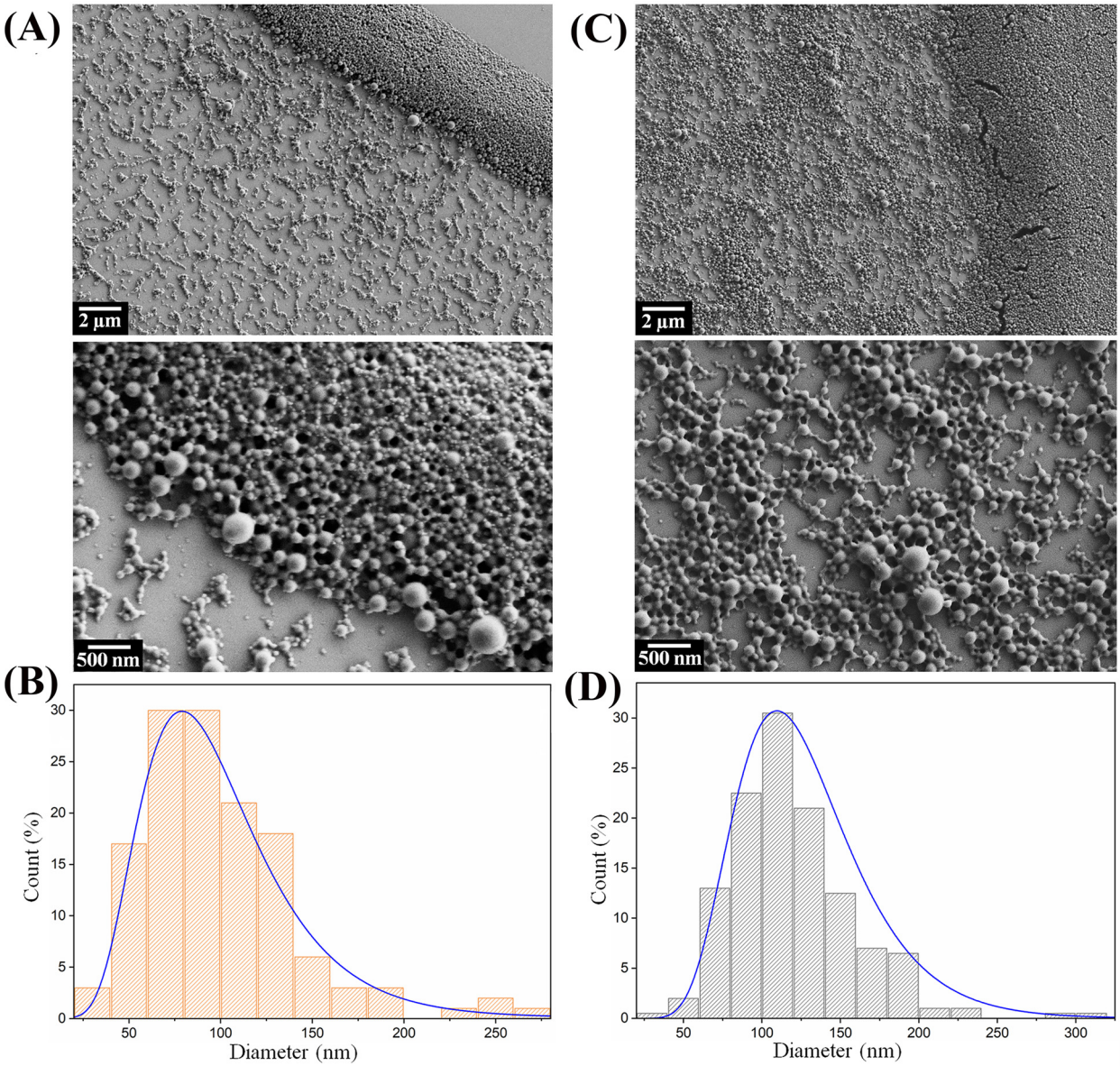

Figure 8. SEM images of (**A**) St-HES29.4 (left) and (**C**) St-HES60.3 (right) nanoparticles with the respective particle size distribution (**B**,**D**) obtained by fitting with a log-normal distribution function.

The mean diameter of St-HES29.4 and St-HES60.3 was 99.8 nm (Figure 8B) and 119.4 nm (Figure 8D), respectively, estimated by fitting the particle size distribution curve obtained from SEM images. However, the size of the micelles measured by SEM appeared to be smaller than the results obtained by DLS analysis. This may be due to the different states of the samples during measurements. The DLS method provides the size as D_h of the particles in the hydrated state, while SEM images are obtained from the dried state of the samples. Hence, during SEM sample preparation, the drying process induces particle collapse and causes shrinkage of the aggregates, leading to the formation of smaller particles than those obtained by the DLS method [55]. It is also noticeable that the size of the micelles increased when increasing the grafting ratio of St-HES from 29.4% to 60.3%, which is in good agreement with the DLS measurements.

4. Conclusions

In conclusion, the synthesis of stearate-substituted esters of HES is reported to obtain highly hydrophobic St-HES conjugates, St-HES29.4 and St-HES60.3. The structural and

physicochemical properties of the synthesized conjugates were investigated by NMR, DSC, and WAXS experiments. The ^{1}H and 2D NMR spectra of the St-HES conjugates revealed the successful conjugation via ester bond formation. In addition, thermal analyses and WAXS experiments showed a complete transition from fully amorphous HES to semicrystalline St-HES60.3. Both conjugates, St-HES29.4 and St-HES60.3, self-assembled in water and provided a monodispersive particle size distribution with a D_h of 130.7 nm and 152.5 nm, respectively. The SEM images of the self-aggregates showed the formation of nearly spherical particles. The mean diameter appeared to be smaller than obtained by DLS measurements due to the drying procedure of the SEM samples. However, the dependence of particle size on the grafting ratio was in good agreement with DLS. The synthesized nano-assembly could potentially be applied in the pharmaceutical field, i.e., to encapsulate poorly water-soluble drugs with a high-loading capacity and prolong the drug circulation time and oral delivery of labile bioactive agents to optimize drug stability in the gastrointestinal tract with improved absorption and complexation with protein therapeutics to resist denaturation and enhance thermal stability.

In addition, a complete structural characterization of native HES was analyzed utilizing labile proton exchange phenomena of the hydroxyl groups to determine the anomeric proton signals in ^{1}H NMR spectra. Furthermore, 2D NMR spectroscopy was performed to determine the other proton signals raised from the HES backbone and to verify the structure more precisely. Finally, it is demonstrated that 1D and 2D NMR spectroscopy provide a more detailed and clear structural analysis of HES and an exact determination of the degree of grafting of St-HES conjugates.

Author Contributions: Conceptualization, R.H. and J.K.; methodology, R.H. and J.K.; investigation, R.H., H.R., and F.S.; writing—original draft preparation, R.H.; writing—review and editing, R.H. and J.K.; supervision, J.K.; funding acquisition, J.K. All authors have read and agreed to the published version of the manuscript.

Funding: This work was conducted in the frame of the International Graduate School AGRIPOLY, supported by the European Social Fund (ESF) and the Federal State Saxony-Anhalt.

Institutional Review Board Statement: Not applicable.

Informed Consent Statement: Not applicable.

Data Availability Statement: The data presented in this article are available upon request. Samples of the compounds are available upon request from the authors.

Acknowledgments: We would like to thank Dieter Ströhl and Nazmul Hasan for their help during the NMR and WAXS measurements.

Conflicts of Interest: The authors declare no conflicts of interest.

References

1. Kashapov, R.; Gaynanova, G.; Gabdrakhmanov, D.; Kuznetsov, D.; Pavlov, R.; Petrov, K.; Zakharova, L.; Sinyashin, O. Self-Assembly of Amphiphilic Compounds as a Versatile Tool for Construction of Nanoscale Drug Carriers. *Int. J. Mol. Sci.* **2020**, *21*, 6961. [CrossRef]
2. Yang, J.; Gao, C.; Lü, S.; Zhang, X.; Yu, C.; Liu, M. Physicochemical Characterization of Amphiphilic Nanoparticles Based on the Novel Starch-Deoxycholic Acid Conjugates and Self-Aggregates. *Carbohydr. Polym.* **2014**, *102*, 838–845. [CrossRef]
3. Jones, M.C.; Leroux, J.C. Polymeric Micelles—A New Generation of Colloidal Drug Carriers. *Eur. J. Pharm. Biopharm.* **1999**, *48*, 101–111. [CrossRef]
4. Kesharwani, R.; Tripathy, S.; Patel, D.K.; Yadav, P.K.; Das, M.K. Multifunctional Micellar Nanomedicine for Cancer Therapy. *Multifunct. Theranostic Nanomed. Cancer* **2021**, *234*, 57–65.
5. Francis, M.F.; Cristea, M.; Winnik, F.M. Polymeric Micelles for Oral Drug Delivery: Why and How. *Pure Appl. Chem.* **2004**, *76*, 1321–1335. [CrossRef]
6. Li, Y.; Xiao, K.; Luo, J.; Xiao, W.; Lee, J.S.; Gonik, A.M.; Kato, J.; Dong, T.A.; Lam, K.S. Well-Defined, Reversible Disulfide Cross-Linked Micelles for on-Demand Paclitaxel Delivery. *Biomaterials* **2011**, *32*, 6633–6645. [CrossRef] [PubMed]
7. Lu, Y.; Zhang, E.; Yang, J.; Cao, Z. Strategies to Improve Micelle Stability for Drug Delivery. *Nano Res.* **2018**, *11*, 4985–4998. [CrossRef]

8. Zhou, H.; Yu, W.; Guo, X.; Liu, X.; Li, N.; Zhang, Y.; Ma, X. Synthesis and Characterization of Amphiphilic Glycidol-Chitosan-Deoxycholic Acid Nanoparticles as a Drug Carrier for Doxorubicin. *Biomacromolecules* **2010**, *11*, 3480–3486. [CrossRef]
9. Yadav, S.; Sharma, A.K.; Kumar, P. Nanoscale Self-Assembly for Therapeutic Delivery. *Front. Bioeng. Biotechnol.* **2020**, *8*, 127. [CrossRef]
10. Li, Y.; Gao, Q. Novel Self-Assembly Nano OSA Starch Micelles Controlled by Protonation in Aqueous Media. *Carbohydr. Polym.* **2023**, *299*, 120146. [CrossRef]
11. Sun, Y.; Bai, Y.; Yang, W.; Bu, K.; Tanveer, S.K.; Hai, J. Global Trends in Natural Biopolymers in the 21st Century: A Scientometric Review. *Front. Chem.* **2022**, *10*, 915648. [CrossRef] [PubMed]
12. Liu, Z.; Jiao, Y.; Wang, Y.; Zhou, C.; Zhang, Z. Polysaccharides-Based Nanoparticles as Drug Delivery Systems. *Adv. Drug Deliv. Rev.* **2008**, *60*, 1650–1662. [CrossRef] [PubMed]
13. Liu, J.; Li, J.; Ma, Y.; Chen, F.; Zhao, G. Synthesis, Characterization, and Aqueous Self-Assembly of Octenylsuccinate Oat β-Glucan. *J. Agric. Food Chem.* **2013**, *61*, 12683–12691. [CrossRef] [PubMed]
14. Fan, Y.; Liu, Y.; Wu, Y.; Dai, F.; Yuan, M.; Wang, F.; Bai, Y.; Deng, H. Natural Polysaccharides Based Self-Assembled Nanoparticles for Biomedical Applications—A Review. *Int. J. Biol. Macromol.* **2021**, *192*, 1240–1255. [CrossRef] [PubMed]
15. Hey, T.; Helmut, K.; Vorstheim, P. Half-life Extension through HESylation®. In *Therapeutic Proteins: Strategies to Modulate Their Plasma Half-Lives*; Kontermann, R., Ed.; Wiley-VCH Verlag Gmbh & Co. KGaA: Weinheim, Germany, 2012; pp. 117–140, ISBN 9780470411964.
16. Besheer, A.; Liebner, R.; Meyer, M.; Winter, G. Challenges for PEGylated Proteins and Alternative Half-Life Extension Technologies Based on Biodegradable Polymers. *ACS Symp. Ser.* **2013**, *1135*, 215–233.
17. Wang, H.; Hu, H.; Yang, H.; Li, Z. Hydroxyethyl Starch Based Smart Nanomedicine. *RSC Adv.* **2021**, *11*, 3226–3240. [CrossRef] [PubMed]
18. Treib, J.; Baron, J.F.; Grauer, M.T.; Strauss, R.G. An International View of Hydroxyethyl Starches. *Intensive Care Med.* **1999**, *25*, 258–268. [CrossRef] [PubMed]
19. Dumitriu, S. *Polysaccharides in Medicinal Applications*; Marcel Dekker Inc.: New York, NY, USA, 1996.
20. Liebner, R.; Mathaes, R.; Meyer, M.; Hey, T.; Winter, G.; Besheer, A. Protein HESylation for Half-Life Extension: Synthesis, Characterization and Pharmacokinetics of HESylated Anakinra. *Eur. J. Pharm. Biopharm.* **2014**, *87*, 378–385. [CrossRef]
21. Besheer, A.; Hertel, T.C.; Kressler, J.; Mäder, K.; Pietzsch, M. Enzymatically Catalyzed HES Conjugation Using Microbial Transglutaminase: Proof of Feasibility. *J. Pharm. Sci.* **2009**, *98*, 4420–4428. [CrossRef]
22. Xiao, C.; Hu, H.; Yang, H.; Li, S.; Zhou, H.; Ruan, J.; Zhu, Y.; Yang, X.; Li, Z. Colloidal Hydroxyethyl Starch for Tumor-Targeted Platinum Delivery. *Nanoscale Adv.* **2019**, *1*, 1002–1012. [CrossRef]
23. Paleos, C.M.; Sideratou, Z.; Tsiourvas, D. Drug Delivery Systems Based on Hydroxyethyl Starch. *Bioconjug. Chem.* **2017**, *28*, 1611–1624. [CrossRef] [PubMed]
24. Hore, R.; Alaneed, R.; Pietzsch, M.; Kressler, J. Enzymatic HES Conjugation with Recombinant Human Erythropoietin via Variant Microbial Transglutaminase TG^{16}. *Starch/Stärke* **2022**, *74*, 2200034. [CrossRef]
25. Tan, R.; Wan, Y.; Yang, X. Hydroxyethyl Starch and Its Derivatives as Nanocarriers for Delivery of Diagnostic and Therapeutic Agents towards Cancers. *Biomater. Transl.* **2020**, *1*, 46–57. [PubMed]
26. Besheer, A.; Hause, G.; Kressler, J.; Mäder, K. Hydrophobically Modified Hydroxyethyl Starch: Synthesis, Characterization, and Aqueous Self-Assembly into Nano-Sized Polymeric Micelles and Vesicles. *Biomacromolecules* **2007**, *8*, 359–367. [CrossRef] [PubMed]
27. Hu, F.Q.; Zhao, M.D.; Yuan, H.; You, J.; Du, Y.Z.; Zeng, S. A Novel Chitosan Oligosaccharide-Stearic Acid Micelles for Gene Delivery: Properties and in Vitro Transfection Studies. *Int. J. Pharm.* **2006**, *315*, 158–166. [CrossRef] [PubMed]
28. Shaki, H.; Vasheghani-Farahani, E.; Ganji, F.; Jafarzadeh-Holagh, S.; Taebnia, N.; Dolatshahi-Pirouz, A. A Self Assembled Dextran-Stearic Acid-Spermine Nanocarrier for Delivery of Rapamycin as a Hydrophobic Drug. *J. Drug Deliv. Sci. Technol.* **2021**, *66*, 102768. [CrossRef]
29. Neises, B.; Steglich, W. Simple Method for the Esterification of Carboxylic Acids. *Angew. Chem. Int. Ed. Engl.* **1978**, *17*, 522–524. [CrossRef]
30. Weiss, V.M.; Naolou, T.; Amado, E.; Busse, K.; Mäder, K.; Kressler, J. Formation of Structured Polygonal Nanoparticles by Phase-Separated Comb-like Polymers. *Macromol. Rapid Commun.* **2012**, *33*, 35–40. [CrossRef] [PubMed]
31. Labelle, M.A.; Ispas-Szabo, P.; Mateescu, M.A. Structure-Functions Relationship of Modified Starches for Pharmaceutical and Biomedical Applications. *Starch/Stärke* **2020**, *72*, 2000002. [CrossRef]
32. Kulicke, W.-M.; Roessner, D.; Kull, W. Characterization of Hydroxyethyl Starch by Polymer Analysis for Use as a Plasma Volume Expander. *Starch/Stärke* **1993**, *45*, 445–450. [CrossRef]
33. Sleightholm, R.; Yang, B.; Yu, F.; Xie, Y.; Oupický, D. Chloroquine-Modified Hydroxyethyl Starch as a Polymeric Drug for Cancer Therapy. *Biomacromolecules* **2017**, *18*, 2247–2257. [CrossRef] [PubMed]
34. Li, Y.; Hu, H.; Zhou, Q.; Ao, Y.; Xiao, C.; Wan, J.; Wan, Y.; Xu, H.; Li, Z.; Yang, X. α-Amylase- and Redox-Responsive Nanoparticles for Tumor-Targeted Drug Delivery. *ACS Appl. Mater. Interfaces* **2017**, *9*, 19215–19230. [CrossRef] [PubMed]
35. Xu, Z.; Yang, D.; Long, T.; Yuan, L.; Qiu, S.; Li, D.; Mu, C.; Ge, L. PH-Sensitive Nanoparticles Based on Amphiphilic Imidazole/Cholesterol Modified Hydroxyethyl Starch for Tumor Chemotherapy. *Carbohydr. Polym.* **2022**, *277*, 118827. [CrossRef] [PubMed]

36. Li, J.; Yang, Y.; Lu, L.; Ma, Q.; Zhang, J. Preparation, Characterization and Systemic Application of Self-Assembled Hydroxyethyl Starch Nanoparticles-Loaded Flavonoid Morin for Hyperuricemia Therapy. *Int. J. Nanomed.* **2018**, *13*, 2129–2141. [CrossRef] [PubMed]
37. Nilsson, G.S.; Bergquist, K.E.; Nilsson, U.; Gorton, L. Determination of the Degree of Branching in Normal and Amylopectin Type Potato Starch with 1H-NMR Spectroscopy: Improved Resolution and Two-Dimensional Spectroscopy. *Starch/Stärke* **1996**, *48*, 352–357. [CrossRef]
38. Gong, Q.; Wang, L.Q.; Tu, K. In Situ Polymerization of Starch with Lactic Acid in Aqueous Solution and the Microstructure Characterization. *Carbohydr. Polym.* **2006**, *64*, 501–509. [CrossRef]
39. Chi, H.; Xu, K.; Wu, X.; Chen, Q.; Xue, D.; Song, C.; Zhang, W.; Wang, P. Effect of Acetylation on the Properties of Corn Starch. *Food Chem.* **2008**, *106*, 923–928. [CrossRef]
40. Richardson, S.; Nilsson, G.S.; Bergquist, K.E.; Gorton, L.; Mischnick, P. Characterisation of the Substituent Distribution in Hydroxypropylated Potato Amylopectin Starch. *Carbohydr. Res.* **2000**, *328*, 365–373. [CrossRef] [PubMed]
41. Heins, D.; Kulicke, W.M.; Käuper, P.; Thielking, H. Characterization of Acetyl Starch by Means of NMR Spectroscopy and SEC/MALLS in Comparison with Hydroxyethyl Starch. *Starch/Stärke* **1998**, *50*, 431–437. [CrossRef]
42. Gagnaire, D.; Mancier, D.; Vincendon, M. Spectres RMN Des Polysaccharides et de Leurs Dérivés: Influence Des Substituants Sur Le Déplacement Chimique 13C. *Org. Magn. Reson.* **1978**, *11*, 344–349. [CrossRef]
43. Peng, Q.J.; Perlin, A.S. Observations on N.M.R. Spectra of Starches in Dimethyl Sulfoxide, Iodine-Complexing, and Solvation in Water-Di-Methyl Sulfoxide. *Carbohydr. Res.* **1987**, *160*, 57–72. [CrossRef]
44. Liu, J.; Wang, X.; Bai, R.; Zhang, N.; Kan, J.; Jin, C. Synthesis, Characterization, and Antioxidant Activity of Caffeic-Acid-Grafted Corn Starch. *Starch/Stärke* **2018**, *70*, 1700141. [CrossRef]
45. Luo, Q.; Wang, P.; Miao, Y.; He, H.; Tang, X. A Novel 5-Fluorouracil Prodrug Using Hydroxyethyl Starch as a Macromolecular Carrier for Sustained Release. *Carbohydr. Polym.* **2012**, *87*, 2642–2647. [CrossRef]
46. Aburto, J.; Alric, I.; Thiebaud, S.; Borredon, E.; Bikiaris, D.; Prinos, J.; Panayiotou, C. Synthesis, Characterization, and Biodegradability of Fatty-Acid Esters of Amylose and Starch. *J. Appl. Polym. Sci.* **1999**, *74*, 1440–1451. [CrossRef]
47. Huang, F.Y. Thermal Properties and Thermal Degradation of Cellulose Tri-Stearate (CTs). *Polymers* **2012**, *4*, 1012–1024. [CrossRef]
48. Lide, D.R. *CRC Handbook of Chemistry and Physics*; CRC Press: Boca Raton, FL, USA, 2005.
49. Feng, L.; Kama, M.R. Distributions of Crystal Size from DSC Melting Traces for Polyethylenes. *Can. J. Chem. Eng.* **2004**, *82*, 1239–1251. [CrossRef]
50. Rim, P.B.; Runt, J.P. Melting Point Depression in Crystalline/Compatible Polymer Blends. *Macromolecules* **1984**, *17*, 1520–1526. [CrossRef]
51. Nanaki, S.G.; Koutsidis, I.A.; Koutri, I.; Karavas, E.; Bikiaris, D. Miscibility Study of Chitosan/2-Hydroxyethyl Starch Blends and Evaluation of Their Effectiveness as Drug Sustained Release Hydrogels. *Carbohydr. Polym.* **2012**, *87*, 1286–1294. [CrossRef]
52. Tuncel, D.; Demir, H.V. Conjugated Polymer Nanoparticles. *Nanoscale* **2010**, *2*, 484–494. [CrossRef]
53. Lee, K.Y.; Jo, W.H.; Kwon, I.C.; Kim, Y.H.; Jeong, S.Y. Physicochemical Characteristics of Self-Aggregates of Hydrophobically Modified Chitosans. *Langmuir* **1998**, *14*, 2329–2332. [CrossRef]
54. Gökçe Kocabay, Ö.; İsmail, O. Preparation and Optimization of Biodegradable Self-Assembled PCL-PEG-PCL Nano-Sized Micelles for Drug Delivery Systems. *Int. J. Polym. Mater. Polym. Biomater.* **2021**, *70*, 328–337. [CrossRef]
55. Golding, C.G.; Lamboo, L.L.; Beniac, D.R.; Booth, T.F. The Scanning Electron Microscope in Microbiology and Diagnosis of Infectious Disease. *Sci. Rep.* **2016**, *6*, 26516. [CrossRef] [PubMed]

3.2. Part B – Lipid-based drug conjugates

3.2.1. Paper III: Synthesis and characterization of dimeric artesunate glycerol monocaprylate conjugate and formulation of nanoemulsion preconcentrate

Antimalarial drugs remain a critical endeavor in combating malaria, a disease that poses significant global health challenges worldwide, due to the emergence and spread of resistance against conventional antimalarial therapies among malaria parasites. The development of novel therapeutic strategies to enhance the efficacy and stability of these drugs can significantly improve treatment outcomes. Recent approaches in drug design have highlighted the use of advanced pharmaceutical techniques such as dimerization, which can potentially improve drug bioavailability, potency, and therapeutic efficacy. Additionally, the incorporation of these dimerized compounds into nanoemulsion formulations can further enhance the solubility, stability, and controlled release of the drugs.

To this aim, this publication focused on the integration of dimerization technique and nanoemulsion technology to develop a new artesunate-based antimalarial drug formulation that could overcome current challenges by optimizing drug performance, paving the way for more effective malaria treatment and improving global health outcomes. Artesunate (AS) was covalently conjugated with glycerol monocaprylate (GC) to synthesize a dimeric artesunate glycerol monocaprylate conjugate (D-AS-GC). Detailed structural characterization of AS, GC, and D-AS-GC conjugate was investigated by ^{1}H, attached proton test (APT) ^{13}C, 2D HSQC, and HMBC NMR spectroscopy. The molar mass of the conjugate was confirmed by ESI-TOF MS. Furthermore, a series of D-AS-GC loaded nanoemulsion preconcentrates were prepared to optimize a clear nanoemulsion formulation upon dilution with an aqueous phase (double distilled water). The particle size of the transparent formulation was determined by DLS and DOSY NMR spectroscopy. AFM was used to analyze the morphological structure of the optimized D-AS-GC loaded nanoemulsion.

The author's contributions to the following article are: R. Hore designed the research, conceptualized the work, performed the experiments and analyze the data, wrote the original draft, and made the finalization of the manuscript. N. hasan carried out the AFM experiment and analyzed the data. J. Kressler and K. Mäder conceptualized the work, supervised, and discussed the results, reviewed them, and finalized the manuscript.

Title

Synthesis and Characterization of Dimeric Artesunate Glycerol Monocaprylate Conjugate and Formulation of Nanoemulsion Preconcentrate

Authors

Rana Hore,Nazmul Hasan,Karsten Mäder, and Jörg Kressler*

Bibliographic Details

Molecules
Volume 28, Issue 13, Pages 5208
Published 4 July 2023
DOI: 10.3390/molecules28135208

∗: Corresponding Author

Source (Molecules; https://doi.org/10.3390/molecules28135208). The link to the article on the publisher's website is: https://www.mdpi.com/1420-3049/28/13/5208. Supporting information can be found at: https://www.mdpi.com/article/10.3390/molecules28135208/s1.

molecules

MDPI

Article

Synthesis and Characterization of Dimeric Artesunate Glycerol Monocaprylate Conjugate and Formulation of Nanoemulsion Preconcentrate

Rana Hore [1], Nazmul Hasan [1], Karsten Mäder [2] and Jörg Kressler [1,*]

[1] Department of Chemistry, Martin Luther University Halle-Wittenberg, Von-Danckelmann-Platz 4, D-06099 Halle (Saale), Germany
[2] Institute of Pharmacy, Martin Luther University Halle-Wittenberg, D-06099 Halle (Saale), Germany
* Correspondence: joerg.kressler@chemie.uni-halle.de

Abstract: Malaria is one of the major life-threatening health problems worldwide. Artesunate is the most potent antimalarial drug to combat severe malaria. However, development of drug resistance, short plasma half-life, and poor bioavailability limit the efficacy of this drug. Here, we applied the dimerization concept to synthesize dimeric artesunate glycerol monocaprylate conjugate (D-AS-GC) by conjugating artesunate (AS) with glycerol monocaprylate (GC) via esterification reaction. D-AS-GC conjugate, AS, and GC were well characterized by ^{1}H NMR, attached proton test (APT) ^{13}C NMR and 2D NMR spectroscopy. D-AS-GC conjugate was further analyzed by ESI-TOF MS. Finally, a series of nanoemulsion preconcentrate (F1–F6) of D-AS-GC was prepared by mixing different ratios of oil and surfactant/cosurfactant and evaluated after dilution with an aqueous phase. The optimized formulation (F6) exhibits a clear nanoemulsion and the hydrodynamic diameter of the dispersed phase was determined by DLS and DOSY NMR spectroscopy. The morphology of the nanoemulsion droplets of F6 was investigated by AFM, which revealed the formation of tiny nanoemulsion droplets on a hydrophilic mica substrate. Moreover, using a less polar silicon wafer led to the formation of larger droplets with a spherical core shell-like structure. Overall, the rational design of the dimeric artesunate-based nanoemulsion preconcentrate could potentially be used in more efficient drug delivery systems.

Keywords: malaria; dimerization; artesunate; glycerol monocaprylate; dimeric artesunate glycerol monocaprylate conjugate; nanoemulsion preconcentrate

Citation: Hore, R.; Hasan, N.; Mäder, K.; Kressler, J. Synthesis and Characterization of Dimeric Artesunate Glycerol Monocaprylate Conjugate and Formulation of Nanoemulsion Preconcentrate. *Molecules* **2023**, *28*, 5208. https://doi.org/10.3390/molecules28135208

Academic Editor: Maria Camilla Bergonzi

Received: 9 June 2023
Revised: 30 June 2023
Accepted: 1 July 2023
Published: 4 July 2023

1. Introduction

One of the significant challenges to the public health sector, especially in developing nations, is the prevalence of the malaria disease. Nearly half of the world's population is susceptible to the risk of malaria infection, establishing it as one of the most prominent health issues in humans [1]. According to the World Health Organization (WHO), approximately 241 million malaria incidences and 627,000 fatalities were reported worldwide in 2020 [2]. Antimalarial drugs are the main means to treat and fight malaria. However, the development and spread of resistance to the majority of traditional antimalarial drugs, such as quinoline derivatives and antifolates, which have been the mainstay over years, have limited the treatment of malaria [3,4]. Artemisinin and its derivatives, broadly known as Artemisinins (ARTs), a new class of compounds derived from the Chinese herbal plant Qinghao and discovered by Youyou Tu in the 1970s, have been the most potent and useful frontline drugs for the treatment of drug-resistant malaria available to date [5–7]. Chemically, ARTs are attributed to the sesquiterpene lactone class, having an endoperoxide bridge which is pharmacologically significant for anti-malarial activity [8]. Among the ART analogs, artesunate (AS) demonstrated the most versatile semisynthetic derivative due to its broader therapeutic potential, rapid action, and better water solubility [9–11].

Apart from its wide therapeutic use, AS exhibits a short plasma half-life and low bioavailability, which undermine the effectiveness of optimal therapeutic efficacy [12]. Moreover, AS monotherapy becomes less effective due to the emergence of parasite resistance [13]. Therefore, the WHO introduced artemisinin-based combination therapies (ACTs), in which fast-acting artesunate is administered together with slow-acting antimalarial drugs of different classes to combat resistance and improve the effectiveness of the treatment [10,14–17]. Nevertheless, recent studies demonstrated a high rate of ACT failure, which might be due to the substandard quality of drugs, inappropriate use of monotherapies, and prematurely stopping of ACT therapy. This leads often to parasite recrudescence in the Greater Mekong Subregion (GMS) [18].

Over the years, many studies have been conducted to find a way to increase the potency of antimalarial drugs [19]. One of the most promising concepts is the synthesis of new efficient artemisinin therapeutics through the dimerization technique [20]. This technique has gained great interest due to the increase in antimalarial potency and provides new strategies for drug discovery and development [21]. Dimerization refers to the process of combining two identical molecules, which may lead to the development of novel compounds with improved pharmacological properties compared to parent compounds [22]. Many ART dimers have been reported by several groups. Posner et al. introduced a series of artemisinin-derived dimers that possess potential antimalarial activity both in vitro and in vivo [23–25]. It was also reported that ART trioxane dimers showed complete parasitic clearance with a prolonged survival time of the malaria-infected mice model [26]. Reiter et al. prepared a series of ART dimers and trimers and assessed their efficiency against malarial 3d7 strains. The dimeric derivatives showed superior antimalarial activity compared to the trimer and parent compound [27]. Several ART triazine hybrids and hybrid dimers were synthesized by Cloete et al. which exhibit effectiveness against chloroquine-sensitive (CQS) and chloroquine-resistant (CQR) Dd2 strains of the malaria parasite [28].

Furthermore, other studies have been directed toward the field of nanotechnology to resolve the challenges of the conventional antimalarial dosage form such as poor water solubility, short half-life, low bioavailability, multiple drug dose, and high drug-related toxicity. Nanocarriers can play an essential role in the case management of malaria by altering the pharmacokinetics and pharmacodynamics of drugs [29]. In this respect, several ART-based drug delivery systems have been investigated, such as implants [30], liposomes, polymeric nanoparticles, lipid-based nanoparticles, metal-based nanoparticles, hybrid drugs, and nanoemulsion (NE) [31]. Among them, NE has been explored extensively as an appropriate carrier to improve the pharmacokinetics and to release the drug in a controlled manner [32]. The NE can protect the active ingredient from oxidative and hydrolytic degradation [33].

In the current work, two well-known strategies were combined into one system. Firstly, dimerization of the drug to develop a new dimeric entity, and, secondly, utilization of this new conjugate for the formulation of nanoemulsion preconcentrate. In short, we synthesized a dimeric artesunate glycerol monocaprylate conjugate (D-AS-GC) and designed a nanocarrier-based lipid NE. Initially, AS was conjugated with a linker molecule namely glycerol monocaprylate (GC) via simple esterification reaction to obtain a D-AS-GC conjugate. AS, GC, and D-AS-GC conjugate were characterized by ^{1}H NMR, attached proton test (APT) ^{13}C NMR, 2D NMR such as homonuclear correlation spectroscopy (COSY), heteronuclear single quantum coherence (HSQC), and heteronuclear multiple bond correlation (HMBC) spectroscopy. The molar mass of the conjugate was confirmed by electrospray ionization time-of-flight mass spectroscopy (ESI-TOF MS). Afterwards, different formulations of D-AS-GC loaded nanoemulsion preconcentrate were developed. The particle size of all formulations was measured by dynamic light scattering (DLS). Finally, the particle size of optimized nanoformulation was further characterized by diffusion-ordered spectroscopy (DOSY). Atomic force microscopy (AFM) was used to investigate the final morphology of drying emulsion droplets on different substrates.

2. Results and Discussion

2.1. Synthesis and Characterization of the D-AS-GC Conjugate

Generally, the synthesis of ART dimers can increase the selectivity for target binding, reduce toxicity, and overcome drug resistance, leading to the design of more effective and safer antimalarial agents [19]. Accordingly, dimeric artesunate glycerol monocaprylate conjugate (D-AS-GC) was achieved by the formation of the ester bond between artesunate (AS) and glycerol monocaprylate (GC) via a facile esterification reaction in the presence of EDC·HCl and DMAP as a coupling agent and a catalyst, respectively, as shown in Scheme 1. Here, the GC linker was chosen to conjugate artesunate dimer, which, in turn, results in an increase in compatibility with the formulation of lipid-based nanoemulsion preconcentrate [34].

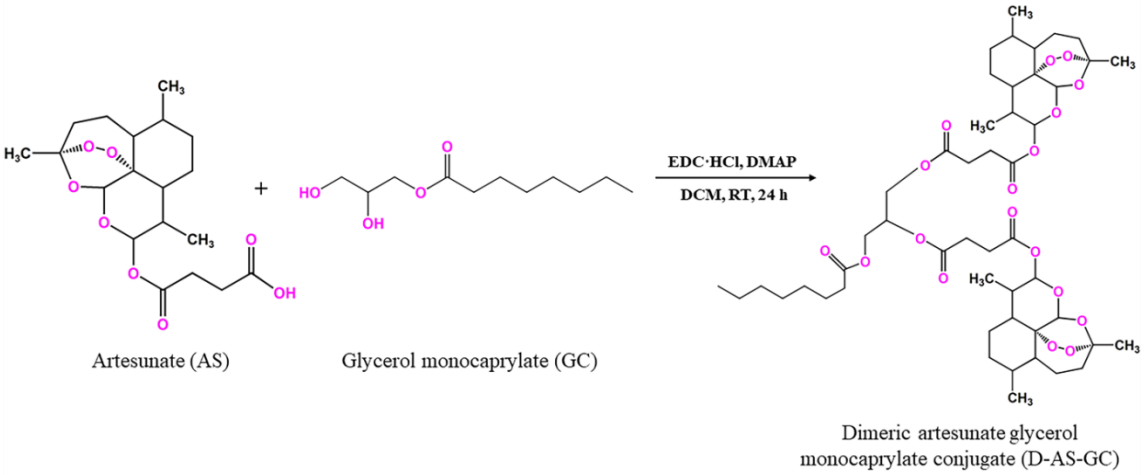

Scheme 1. Synthetic pathway for dimeric artesunate glycerol monocaprylate conjugate (D-AS-GC).

The conjugation product D-AS-GC was characterized by ^{1}H NMR, APT ^{13}C NMR, and 2D HSQC NMR spectroscopy. The ^{1}H NMR spectra of GC, AS, and D-AS-GC are shown in Figure 1a–c, respectively. The comparison between ^{1}H NMR spectra a and c in Figure 1 shows a significant downfield shift of the resonance signal (labeled as J) from 3.92–3.88 ppm to 5.28–5.23 ppm, which is attributed to the methine proton of GC, as well as a downfield shift of the proton resonances (labeled as K) from 3.69–3.55 ppm to a higher overlap signal at 4.32–4.09 ppm assigned as methylene protons of GC. Additionally, a complete disappearance of the proton signal of the hydroxyl groups (–OH) of GC is observed, which indicates the successful conjugation of AS with GC. Besides ^{1}H NMR, APT ^{13}C NMR spectra of GC, AS, and D-AS-GC are given in Figure 2a–c, respectively. Comparing APT ^{13}C NMR spectra a and c in Figure 2 reveals upfield shifts of carbon signals from 70.38 ppm to 69.37 ppm (peak J) and 63.52 ppm to 62.41–61.86 ppm (peak K), which belong to the methine and methylene carbons of GC. Further, no carbonyl signal (C=O) of the carboxylic acid group (peak 21) of AS is observed in Figure 2c in comparison with Figure 2b, thereby suggesting the efficient formation of D-AS-GC conjugate. Additionally, the chemical structure of AS, GC, and D-AS-GC conjugate was further confirmed by 2D NMR spectroscopy (given in the Supplementary Materials in Figures S1–S7 and Tables S1–S7).

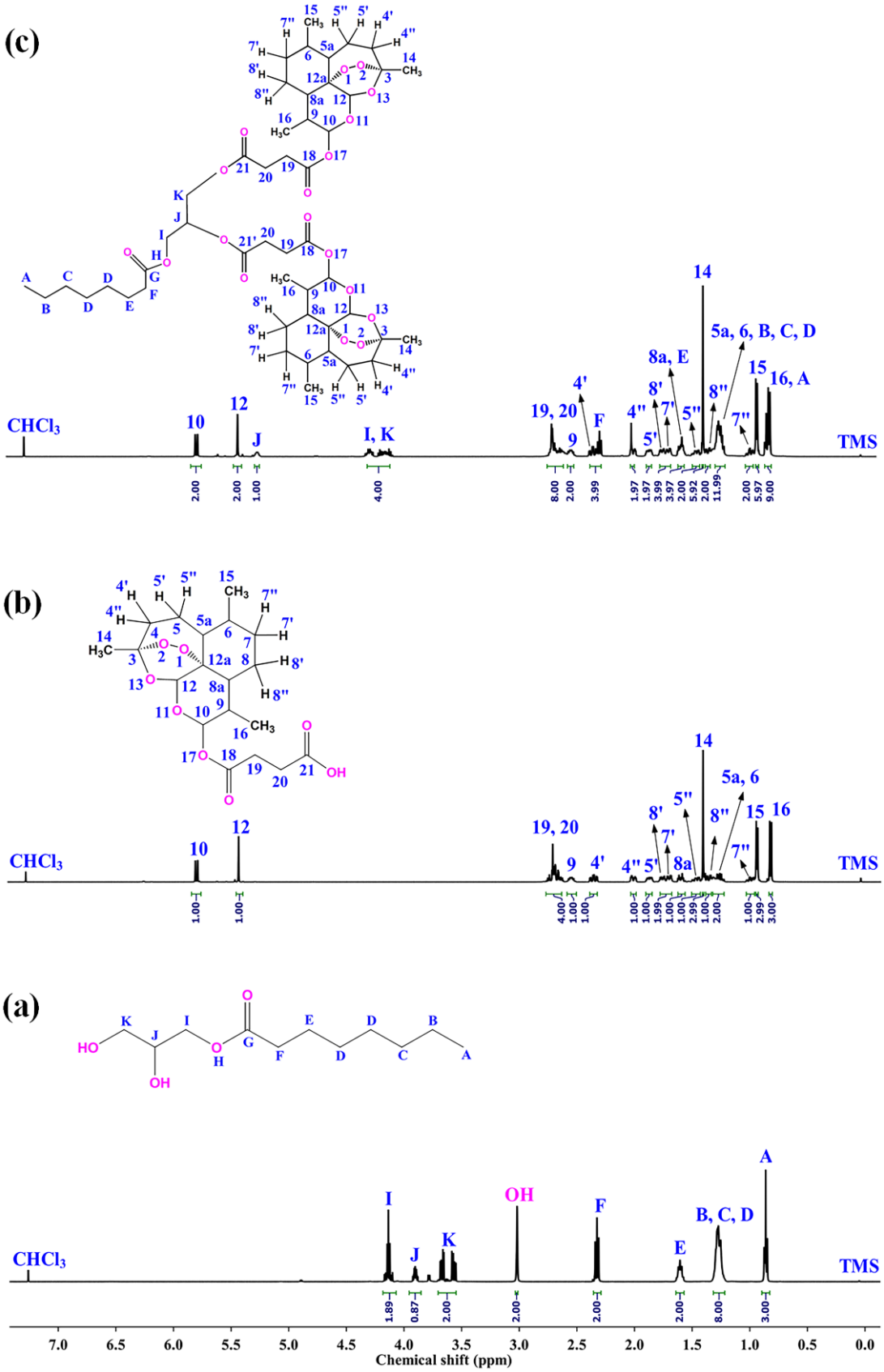

Figure 1. The ^{1}H NMR spectra of (**a**) GC, (**b**) AS, and (**c**) D-AS-GC were recorded at 27 °C, 500 MHz, using $CDCl_3$ as solvent.

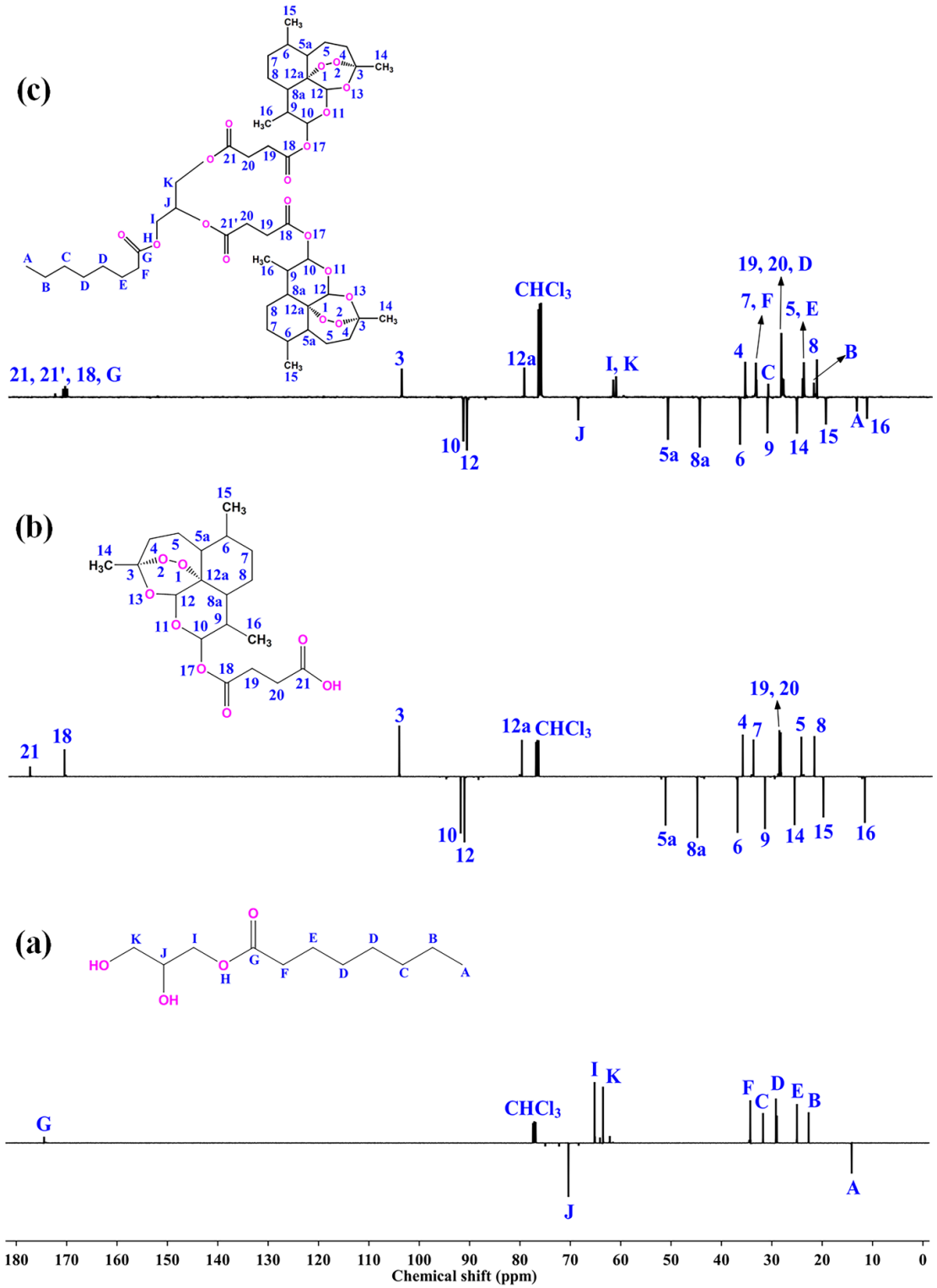

Figure 2. APT ^{13}C NMR spectra of (**a**) GC, (**b**) AS, and (**c**) D-AS-GC were recorded at 27 °C, 125 MHz, using $CDCl_3$ as solvent.

The molar mass of the D-AS-GC conjugate was determined by electrospray ionization time-of-flight mass spectroscopy (ESI-TOF MS), which is a soft ionization technique used for the precise determination of the molecular mass of organic molecules [35]. The ESI-TOF MS spectrum in Figure 3a shows a major molecular ion peak at m/z 973.4775 $(M+Na)^+$, which matches with the simulated isotopic patterns for the theoretically calculated value

m/*z* 973.4767. The neighboring mass peaks (Figure 3b) follow the natural isotope distribution (with binomial distributed 1.1% ^{13}C) as indicated by the simulated pattern (Figure 3c).

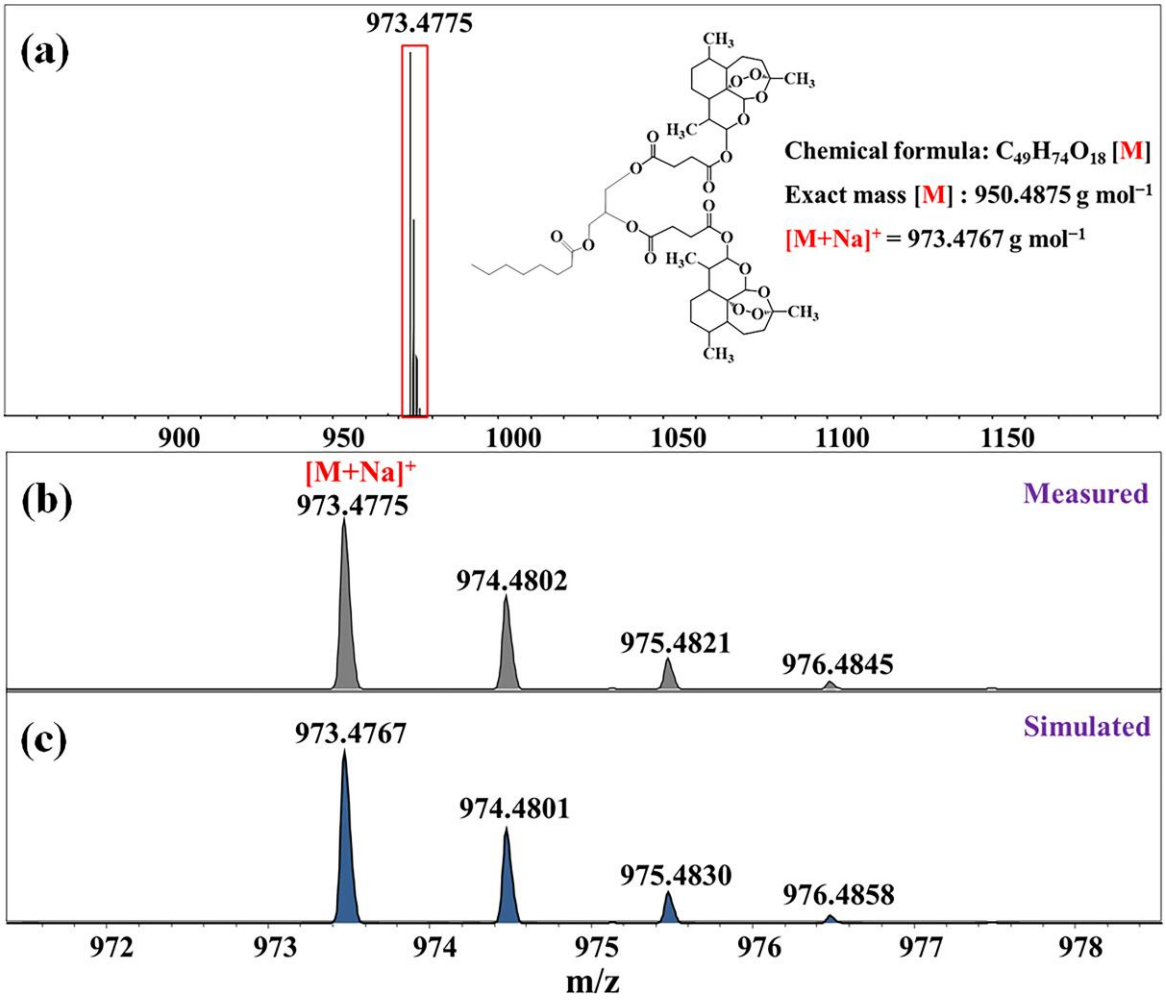

Figure 3. ESI-TOF MS spectra of D-AS-GC. (**a**) Full spectrum, (**b**) region of the main peak, and (**c**) simulated isotope signals of the marked section. Inset shows the structure of D-AS-GC with the respective molar mass.

2.2. Preparation and Characterization of Nanoemulsion

Nanoemulsion preconcentrate is a combination of drugs and lipophilic excipients as an oil phase with water-soluble surfactants and cosurfactants. It forms clear, stable small droplets of o/w nanoemulsion upon dilution by an aqueous phase [36]. All the excipients selected here are based on a saturated chemical structure because unsaturated compounds are very prone to undergo oxidative degradation [37]. Medium-chain triglyceride (MCT) was chosen as the oil phase due to its superior physical, pharmaceutical, and clinical attributes [38]. Kolliphor HS 15 and propylene glycol were selected as surfactant and cosurfactant, respectively. Kolliphor HS 15 is mainly designed for parenteral applications owing to its good safety margin [39]. The dimeric artesunate conjugates (D-AS-GC) were used to prepare in total six different formulations (see Table 1) namely, F1 (1:1:2), F2 (1:1:3), F3 (1:1:4), F4 (1:2:4), F5 (1:2:6), and F6 (1:2:8) by varying the mass ratios (w/w) of D-AS-GC to MCT to Kolliphor HS 15/propylene glycol, respectively, to optimize a transparent nanoemulsion upon dispersing into an aqueous phase. The Kolliphor HS 15/propylene glycol mass ratio of 2:1 (w/w) was kept unchanged for all formulations.

Table 1. Formulation composition ratios (*w*/*w*) of the different nanoemulsion preconcentrate.

Formulation Code	D-AS-GC (Drug)	MCT (Oil)	Kolliphor HS 15/Propylene Glycol (2:1) (Surfactant/Cosurfactant)
F1	1	1	2
F2	1	1	3
F3	1	1	4
F4	1	2	4
F5	1	2	6
F6	1	2	8

The visual observation of turbidity is a simple method to identify clear nanoemulsion formulation. In Figure 4a, it is observable that the optical appearance of the formulations changed from white (F1) to a transparent or slightly opalescent (F6) appearance. The shift of turbidity to clear transparency can be described in terms of thermodynamics and kinetic phenomena of nanoemulsions. Generally, nanoemulsion formation is a non-equilibrium and non-spontaneous process because the total Gibbs free energy required for the formation of nanoemulsion is positive [40]. A surfactant/cosurfactant assists the kinetic stability of nanoemulsion by reducing the interfacial tension between oil and water, leading to a decrease in Gibbs free energy [41]. Hence, an increase in the surfactant/cosurfactant amount leads to a decrease in droplet size by increasing the surface to volume ratio, which, in turn, reduces the scattering of the incident light and gives rise to visually clear nanoemulsions [42,43]. The opalescence is another indication of Rayleigh scattering that confirms the stable nanoemulsion formation. It occurs when the droplet size of the nanoemulsion is less than the wavelength of incident light. Since violet-blue light with a wavelength of 400 nm scatters more than red light, the nanoemulsion droplet size of less than 100 nm shows a blue tint in the formulation [44]. Overall, the change in turbidity is directly related to the droplet size of the formulations.

To make a relationship between turbidity with the particle size and polydispersity index, the DLS technique is used for all formulations (Figure 4b,d). In the case of formulation F1 to F3, the D-AS-GC to MCT ratio is constant at 1:1, but MCT to Kolliphor HS 15/propylene glycol ratios increase gradually from 1:2 (F1) to 1:3 (F2) and 1:4 (F4) (see Table 1), which produce a white to opaque appearance of the formulations. In addition, the hydrodynamic diameter (D_h) of the particles decreases from 157.8 nm (F1) to 74.8 nm (F3) while the polydispersity index (PDI) increases from 0.21 (F1) to 0.28 (F3) (Figure 4d). In formulations F4 to F6 (see Table 1), the D-AS-GC to MCT ratio is 1:2, and MCT to Kolliphor HS 15/propylene glycol ratios increase accordingly from 2:4 (F4) to 2:6 (F5) and 2:8 (F6). Formulations F4 to F6 appear translucent to clear. This indicates that the oil phase is sufficient to completely dissolve the drugs (D-AS-GC). Consequently, the D_h of formulation F4 to F6 (Figure 4d) decreases from 91.4 nm to 19.1 nm, and the PDI decreases from 0.29 to 0.13. The decrease in hydrodynamic diameter is due to the increase in surface to volume ratio with an increase in the surfactant/cosurfactant ratio in the formulations. It is known that Kolliphor HS 15 forms micelles with a diameter of about 12 nm [45]. The diameter of F6 is only slightly higher. This formulation could also be regarded as swollen micelles. With increasing loading of hydrophobic liquids, micelles transform into swollen micelles and finally into emulsions. The above observations demonstrate that oil and surfactant/cosurfactant ratios have a great influence on the solubility of D-AS-GC and the formation of a clear nanoemulsion. Though the particle size decreases with increasing surfactant/cosurfactant ratios to D-AS-GC and oil, the formulations (F1, F2, F3, F4, and F5) exhibit bimodal distributions in DLS measurements, which indicates the existence of two important populations of droplets (Figure 4b,d). The Table in Figure 4d represents the mean diameter of the droplets (F1–F6) and the peak numbering is based on the respective total area under each peak (peak 1 is the largest and peak 2 is the smallest area under the peaks). Only formulation F6 shows a monomodal particle size distribution with a very

narrow PDI of 0.13 (Figure 4b,d). Hence, formulation F6 (1:2:8) was selected as the best combination for nanoemulsion formulation.

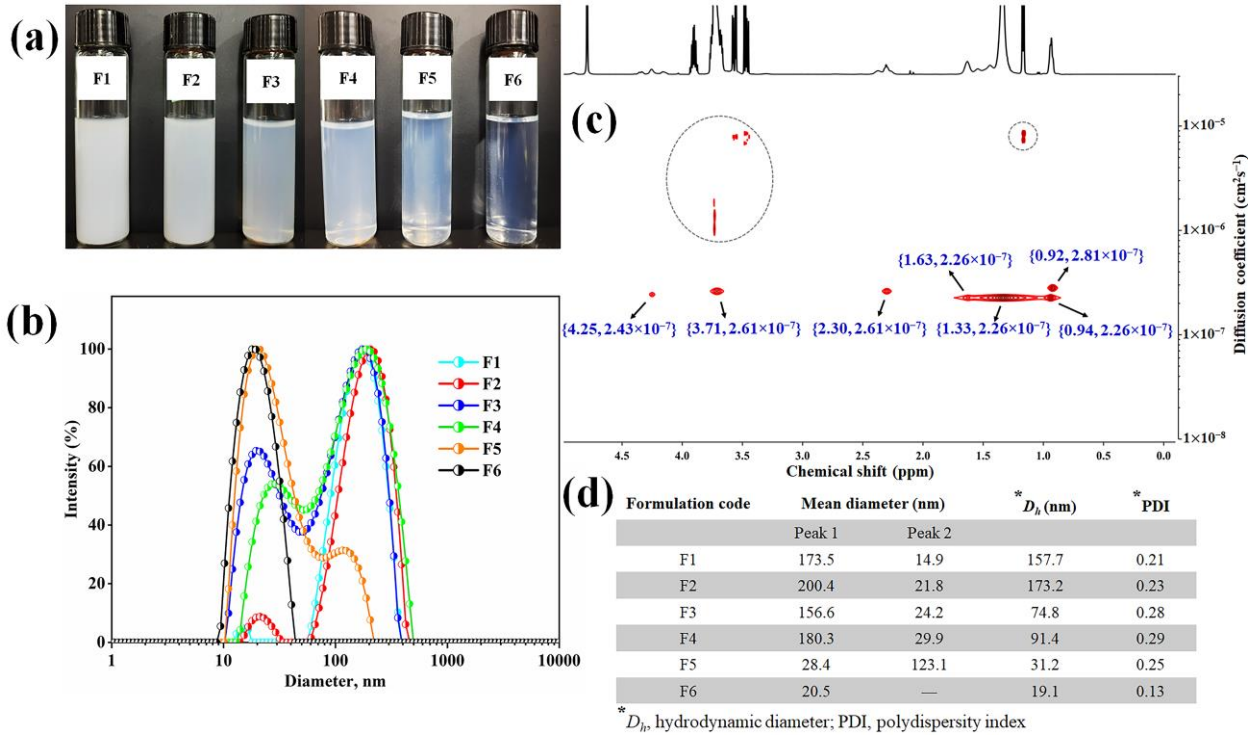

(d)

Formulation code	Mean diameter (nm)		*D_h (nm)	*PDI
	Peak 1	Peak 2		
F1	173.5	14.9	157.7	0.21
F2	200.4	21.8	173.2	0.23
F3	156.6	24.2	74.8	0.28
F4	180.3	29.9	91.4	0.29
F5	28.4	123.1	31.2	0.25
F6	20.5	—	19.1	0.13

*D_h, hydrodynamic diameter; PDI, polydispersity index

Figure 4. Characterization of D-AS-GC nanoemulsions. (**a**) The visual appearance and (**b**) DLS measurements of nanoemulsion formulations F1, F2, F3, F4, F5, and F6. (**c**) DOSY NMR of formulation F6 (Inset shows the ^{1}H chemical shift and diffusion coefficient). (**d**) Summary of the mean diameter, hydrodynamic diameter, and polydispersity index of different formulations (F1–F6) analyzed by DLS.

Two-dimensional diffusion-ordered nuclear magnetic resonance spectroscopy (DOSY NMR) was further used to determine the hydrodynamic diameter of droplets in the F6 formulation. DOSY NMR is a sensitive and noninvasive tool to determine the hydrodynamic diameter of the macromolecular complexes in the dispersion medium [46]. It provides a 2D NMR plot that represents a ^{1}H chemical shift along the x-axis and the diffusion coefficient along the y-axis. The cross peak in DOSY NMR indicates the diffusion coefficient of the molecule corresponding to the ^{1}H NMR shifts [47]. The hydrodynamic diameter is calculated from the Stokes–Einstein equation, $D_h = k_B T/3\pi\eta D$, where D_h is the hydrodynamic diameter (m), k_B is the Boltzmann constant (1.38×10^{-23} kgm^{2}s^{-2}K^{-1}), T is the absolute temperature (298.15 K), η is the viscosity of the continuous phase D_2O (0.00125 kgm^{-1}s^{-1} at 298.15 K), and D is the diffusion coefficient (cm^{2}s^{-1}). The DOSY NMR spectrum of the F6 formulation is shown in Figure 4c. From the ^{1}H NMR spectra of D-AS-GC (Figure 1c), MCT, Kolliphor HS 15, and propylene glycol (shown in Figure S8), it is confirmed that most of strong DOSY NMR signals correspond to MCT, Kolliphor HS 15, and propylene glycol. All the resonances allow us to calculate the diffusion coefficient of around 2.26–2.81 $\times$ 10^{-7} cm^{2}s^{-1}. Consequently, the hydrodynamic diameter was calculated from the Stokes–Einstein equation and ranged from around 13 nm to 16 nm. Small cross peaks in the DOSY NMR spectrum (dashed circle in Figure 4c) in the range of 1×10^{-5} to 1×10^{-6} cm^{2}s^{-1} represent the diffusion coefficient of propylene glycol or tiny aggregates present in the formulation. The measured oil droplet size (D_h) of 13–16 nm is close to the value of 19.1 nm obtained by DLS.

To examine the morphology of nanoemulsion (formulation F6), we dispersed the prepared sample of different concentrations on two different substrates, i.e., mica or silicon wafer, dried and checked by AFM. Figure 5 shows the morphology of F6 prepared with a

concentration of 0.01 mg/mL and dried on mica. The dark reddish color represents the mica surface, whereas the bright color depicts the morphology of the nanoemulsion droplets.

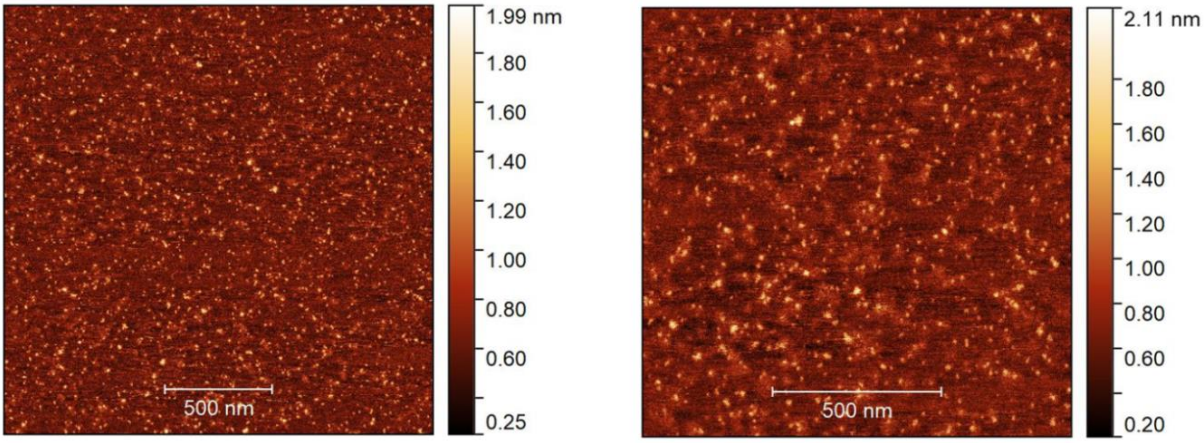

Figure 5. AFM height images in two different sizes, 2 × 2 μm (**left**) and 1.3 × 1.3 μm (**right**), with a sample (F6) concentration of 0.01 mg/mL dried on the mica substrate.

AFM reveals the presence of small droplets in the dried nanoemulsion with a dimension ranging from ~10 to 50 nm with an average height of ~2 nm. The actual morphology of the nanoemulsion is hard to resolve due to the soft or sticky nature of the droplets which generate artifacts and become deformed during imaging [48]. Hence, a typical core shell-like structure of o/w droplets was not observed in the height images or even in other imaging modes (e.g., adhesion or modulus). The droplet size obtained from DLS and DOSY NMR spectroscopy, however, was in quite good agreement with the AFM measurement. In the next step, we spread a slightly higher concentration (0.05 mg/mL) of the formulation F6 on a silicon wafer and dried it. Figure 6a visualizes the different images (left: height, right: adhesion) of the droplets. The AFM image of the F6 formulation shows a distinct spherical core (denoted by a white arrow) and shell (marked by a yellow arrow) morphology of the droplets. The dark color is observed in the inner cavity, which is composed of drug molecules (D-AS-GC), and a slightly bright color is observed around the core, which is the shell made of MCT (oil) and Kolliphor HS 15/propylene glycol (surfactant/cosurfactant). However, the dimensions of the droplets are in the range of ~200 nm to 2 μm with an average height of ~100 nm, which is much larger than the droplet size found on the mica surface. This is because the silicon wafer is a less polar substrate, and spreading a slightly higher concentration of the sample on the substrate, along with solvent evaporation, leads to the formation of large droplets due to the evaporation-induced coalescence of oil droplets [49]. A schematic diagram of the coalescence process of the oil droplets during drying on the substrate is shown in Figure 6b. The above findings provide evidence of the formation of nanoemulsion with a well-defined inner core of D-AS-GC surrounded by a spherical homogenous shell composed of oil and surfactant/cosurfactant.

The dimerization technique used to synthesize D-AS-GC conjugate may potentially improve the potency of the drug, increase bioavailability with a minimum dose of drug, reduce side effects, and overcome the drug resistance. Afterwards, the synthesized conjugate was used to develop D-AS-GC loaded nanoemulsion preconcentrate. Comparing with the previous reports, the advantages of nanoemulsions over the conventional drug delivery systems is that small droplets increase the kinetical stability of nanoemulsions. Moreover, a small droplet size of the nanoemulsions provides a large surface area, which enhances the penetration of active ingredients and increases the bioavailability of drugs. The utilization of nanoemulsions enables a reduction in the required drug dosage by enhancing bioavailability, extending retention time within the body, and minimizing drug

loss. Nanoemulsion could also increase chemical stability of drugs by protecting them from oxidation and hydrolysis.

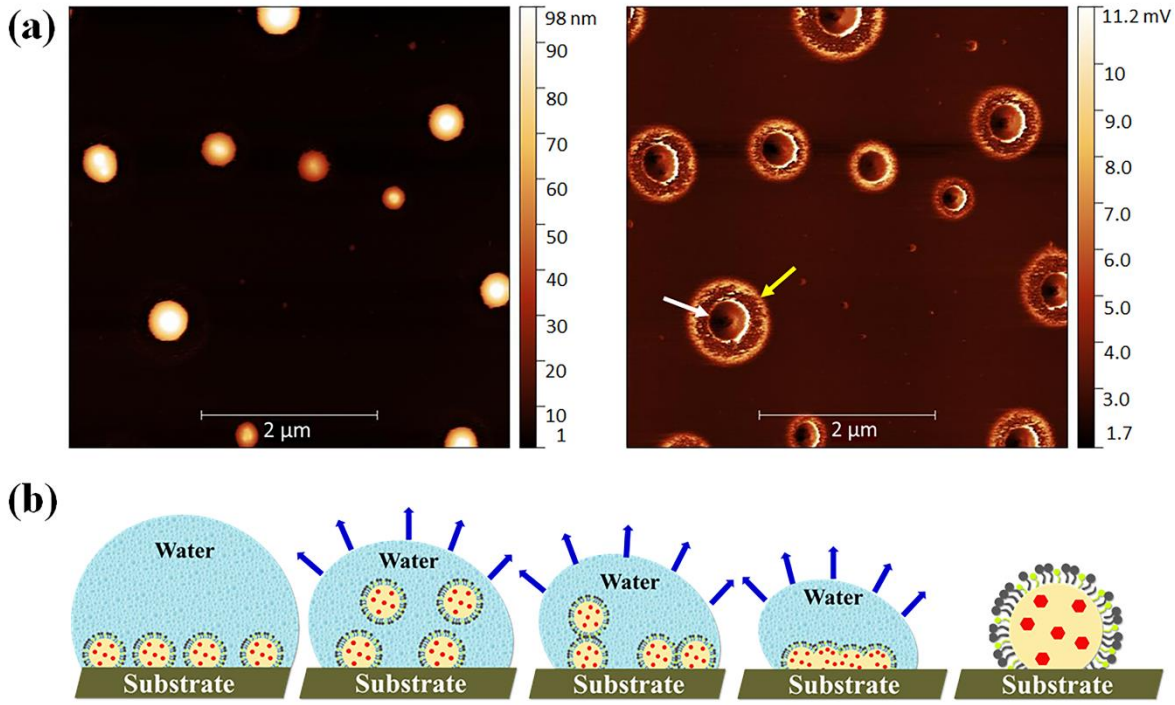

Figure 6. (**a**) AFM height (**left**) and adhesion (**right**) image with a size of 5 × 5 µm and with a sample (F6) concentration of 0.05 mg/mL dried on the silicon substrate, and (**b**) schematic presentation of the coalescence process of the oil droplets during drying on the substrate.

3. Materials and Methods

3.1. Materials

Artesunate (97%) was purchased from abcr GmbH (Karlsruhe, Germany). Glycerol monocaprylate (type II, IMWITOR® 308) and medium-chain triglycerides (MIGLYOL® 812 N) were purchased from IOI Oleo GmbH (Hamburg, Germany). 4-(dimethylamino)pyridine (DMAP), silica gel (SiO_2, 0.03–0.2 mm), 1-ethyl-3-(3-dimethylaminopropyl)carbodiimide hydrochloride (EDC·HCl), deuterium oxide (D_2O, 99.9%), deuterated chloroform ($CDCl_3$, 99.8%), HPLC grade *n*-hexane, and ethyl acetate were purchased from Carl Roth (Karlsruhe, Germany). Dichloromethane (DCM, anhydrous, 99.9%) was obtained from Acros Organics (Schwerte, Germany). Kolliphor® HS 15 (Polyoxyl (15) hydroxystearate) was obtained from BASF (Ludwigshafen, Germany). Propylene glycol (≥99.5%, GC grade) was purchased from Fluka Chemie AG (Buchs, Switzerland).

3.2. Methods

3.2.1. Nuclear Magnetic Resonance (NMR) Spectroscopy

The NMR spectra were recorded on a VNMRS spectrometer (Agilent Technologies, Santa Clara, CA, USA) at 500 MHz for ^{1}H NMR and 125 MHz for the attached proton test (APT) ^{13}C NMR. Two-dimensional NMR measurements, namely, homonuclear correlation spectroscopy (COSY), heteronuclear single quantum coherence (HSQC) spectroscopy, and heteronuclear multiple bond correlation (HMBC) spectroscopy, were performed to obtain detailed structural elucidation. A total of 20 mg of samples were dissolved in 0.6 mL of deuterated solvents ($CDCl_3$ and D_2O). The solvent residual signal for $CHCl_3$ was set at 7.26 ppm for ^{1}H, 77.0 ppm for the APT ^{13}C NMR spectra, and 4.79 ppm for HDO in the ^{1}H NMR spectrum. All measurements were carried out at 27 °C, using tetramethylsilane (TMS) as an internal standard. The NMR spectral data were interpreted using MestRec (v.4.9.9.6) software (Mestrelab Research, Santiago de Compostela, Spain).

3.2.2. Electrospray Ionization Time-of-Flight Mass Spectroscopy (ESI-TOF MS)

A Focus Micro TOF spectrometer from Bruker Daltonics (Billerica, MA, USA) was used to conduct ESI-TOF MS measurements. A total of 1 mg of the sample was dissolved in HPLC grade THF at a final concentration of 10 µL/mL. Then, 10 µL of sodium iodide (NaI) was added to the sample solution. The samples were injected with a flow rate of 180 µL/h. An acceleration voltage of 4.5 kV was used to record the spectra in positive mode. The measured data were interpreted using Data Analysis 4.2 software from Bruker Daltonics.

3.2.3. Thin-Layer Chromatography (TLC)

Detection of the conjugate formation was performed by thin-layer chromatography (TLC) using the precoated silica gel aluminum sheet (Merck silica gel 60) as the stationary phase. A total of 5–10 µL of the sample was spotted on the TLC plate and immersed in the mobile phase containing a mixture of solvents (ethyl acetate:*n*-hexane 4:10) in a way that the spot remained above the level of the mobile phase. Afterwards, the TLC plate was removed and dried. The spot of the new conjugate was visualized by iodine vapor.

3.2.4. Synthesis of Dimeric Artesunate Glycerol Monocaprylate Conjugate (D-AS-GC)

Dimeric artesunate glycerol monocaprylate conjugate (D-AS-GC) was synthesized via a simple one-step Steglich esterification reaction [50,51]. Briefly, 0.5 g (2.29 mmol) of glycerol monocaprylate (GC) was dissolved in 40 mL of ice-cooled anhydrous DCM in a 100 mL 3-neck round-bottom flask equipped with a magnetic stirrer. Afterwards, 2.64 g (6.86 mmol, 3 eq. of –OH groups) of artesunate (AS), 1.3 g of EDC·HCl (6.87 mmol, 3 eq.), and 0.084 g of DMAP (0.687 mmol, 0.3 eq.) were added to the solution. The reaction was carried out at 0 °C for 30 min followed by 24 h at room temperature under constant stirring. The whole reaction was performed under inert conditions. The synthesized product was purified by column chromatography using a mixture of ethyl acetate and n-hexane (4:10) as mobile phase. The desired product was separated and confirmed by TLC. The pure fractions were collected and dried under reduced pressure by rotary evaporator. The resultant product was kept under high vacuum to provide D-AS-GC conjugate as white solid. ESI-TOF MS (m/z): calculated for $C_{49}H_{74}O_{18}$, 950.4875 g mol^{-1} [M]; found, 973.4775 g mol^{-1} $[M+Na]^+$. The ^{1}H NMR (D-AS-GC, 500 MHz, $CDCl_3$): δ (ppm) 5.78–5.76 (2H, H-10), 5.43–5.40 (2H, H-12), 5.28–5.23 (1H, H-J), 4.32–4.09 (4H, H-I, K), 2.73–2.62 (8H, H-19, 20), 2.57–2.50 (2H, H-9), 2.39–2.29 (4H, H-4′, F), 2.04–1.99 (2H, H-4″), 1.90–1.86 (2H, H-5′), 1.78–1.69 (4H, H-8′, 7′), 1.62–1.58 (4H, H-8a, E), 1.50–1.45 (2H, H-5″), 1.42–1.39 (6H, H-14), 1.39–1.34 (2H, H-8″), 1.31–1.23 (12H, H-5a, 6, B, C, D), 1.04–0.97 (2H, H-7″), 0.96–0.93 (6H, H-15) and 0.88–0.83 (9H, H-16, A). APT ^{13}C NMR (D-AS-GC, 125 MHz, $CDCl_3$): δ (ppm) 173.24–171.66 (C-21, 21′, 18, G), 104.42 (C-3), 92.19 (C-10), 91.48 (C-12), 80.09 (C-12a), 69.37 (C-J), 62.41–61.86 (C-I, K), 51.57 (C-5a), 45.24 (C-8a), 37.25 (C-6), 36.22 (C-4), 34.10–33.98 (C-7, F), 31.80 (C-9), 31.63 (C-C), 29.04–28.62 (C-19, 20, D), 25.93 (C-14), 24.84–24.58 (C-5, E), 22.51(C-B), 21.98 (C-8), 20.19 (C-15), 14.05 (C-A) and 12.03 (C-16). The ^{1}H NMR (AS, 500 MHz, $CDCl_3$): δ (ppm) 5.78–5.76 (1H, H-10), 5.43–5.40 (1H, H-12), 2.73–2.62 (4H, H-19, 20), 2.57–2.50 (1H, H-9), 2.39–2.33 (1H, H-4′), 2.04–1.99 (1H, H-4″), 1.90–1.86 (1H, H-5′), 1.78–1.69 (2H, H-8′, 7′), 1.62–1.58 (1H, H-8a), 1.50–1.45 (1H, H-5″), 1.42–1.39 (3H, H-14), 1.39–1.34 (1H, H-8″), 1.31–1.23 (2H, H-5a, 6), 1.04–0.97 (1H, H-7″), 0.96–0.93 (3H, H-15) and 0.88–0.83 (3H, H-16). APT ^{13}C NMR (AS, 125 MHz, $CDCl_3$): δ (ppm) 177.94 (C-21), 171.10 (C-18), 104.42 (C-3), 92.39 (C-10), 91.63 (C-12), 80.22 (C-12a), 51.68 (C-5a), 45.36 (C-8a), 37.38 (C-6), 36.33 (C-4), 34.21 (C-7), 31.92 (C-9), 29.06–28.79 (C-19, 20), 26.04 (C-14), 24.69 (C-5), 22.10 (C-8), 20.31 (C-15) and 12.08 (C-16). The ^{1}H NMR (GC, 500 MHz, $CDCl_3$): δ (ppm) 4.17–4.10 (2H, H-I), 3.92–3.88 (1H, H-J), 3.69–3.55 (2H, H-K), 3.02 (–OH), 2.35–2.31 (2H, H-F), 1.64–1.58 (2H, H-E), 1.32–1.21 (8H, H-B, C, D) and 0.88–0.85 (3H, H-A). APT ^{13}C NMR (GC, 125 MHz, $CDCl_3$): δ (ppm) 174.49 (C-G), 70.38 (C-J), 65.20 (C-I), 63.52 (C-K), 34.27 (C-F), 31.74 (C-C), 29.19 (C-D), 25.00 (C-E), 22.69 (C-B) and 14.14 (C-A).

3.2.5. Formulation of Nanoemulsion Preconcentrate and Optimization

Nanoemulsion preconcentrate is an anhydrous system composed of drug, oil, surfactant, and cosurfactant. It spontaneously forms oil in water (o/w) nanoemulsion upon dispersing in an aqueous phase [52]. Accordingly, in this study, the nanoemulsion preconcentrates were prepared which were composed of D-AS-GC, medium-chain triglycerides (MCT), Kolliphor HS 15/propylene glycol as drug, oil, and surfactant/cosurfactant. The preconcentrates were prepared according to Yao-Xing Dou et al. with a slight modification [53]. The composition of different nanoemulsion preconcentrates is presented in Table 1, keeping the surfactant/cosurfactant ratio of 2:1 (w/w) constant for all formulations. Predetermined ratios of D-AS-GC, MCT and Kolliphor HS 15/propylene glycol were taken in a small vial and mixed under gentle magnetic stirring at 40 °C until a clear solution was obtained. Afterwards, the preconcentrate was cooled down to room temperature and kept in the air-tight vial and dispersed in double distilled water for nanoemulsion formulation. All the nanoemulsion preconcentrates were further examined visually and by dynamic light scattering (DLS) after being dispersed into the double distilled water to optimize a homogeneous and clear nanoemulsion formulation.

3.2.6. Visual Evaluation of the Formulations

The prepared nanoemulsion preconcentrates were diluted at 1:30 with double distilled water and gently mixed by a magnetic stirrer. The resulting mixtures were equilibrated for 30 min at room temperature and the appearance of the formulations was visually examined.

3.2.7. Determination of Droplet Size by Dynamic Light Scattering (DLS)

Hydrodynamic diameter (D_h) and intensity-weighted size distribution of the droplets in the formulations were analyzed by DLS using Litesizer 500 device (Anton Paar GmbH, Graz, Austria). The formulations were taken from the previous experiment and poured carefully into a quartz cell (Hellma Analytics, Müllheim, Germany) to avoid air bubbles. The measurements were performed at a light wavelength of 658 nm, a detection angle of 175° (backscattering), and the temperature was set to 25 °C. D_h and the broadness of the intensity size distribution, called the polydispersity index (PDI), were derived from the intensity curve fitting by applying the autocorrelation function using Kalliope Software (Anton Paar GmbH).

3.2.8. Droplet Size Measurement Using Diffusion-Ordered NMR Spectroscopy (DOSY NMR)

Based on the results of the visual evaluation and DLS measurements, the hydrodynamic diameter of the optimized sample was further analyzed by DOSY NMR spectroscopy. The DOSY NMR sample was prepared using D_2O in place of H_2O as the dispersing phase of the desired nanoemulsion preconcentrate. The DOSY NMR spectrum was recorded in an Agilent VNMR DD2 (500 MHz, version OpenVnmr 2.1) spectrometer. The measurement was obtained using the Agilent pulse program DgcsteSL_cc. The diffusion delay and relaxation delay were set at 300 ms and 2 s, respectively, with a diffusion gradient length of 3 ms and a total number of 16 scans. The experiment was performed at 27 °C and the solvent residual signal of HDO was set at 4.79 ppm in the ^{1}H NMR spectrum.

3.2.9. Morphological Analysis by Atomic Force Microscopy (AFM)

A Bruker MultiMode 8 AFM instrument was used to check the droplet dimensions in the nanoemulsions. The samples were prepared in two different concentrations, 0.01 and 0.05 mg/mL, and were applied at a volume of 10 to 20 µL using a Hamilton syringe on two different substrates, e.g., a freshly cleaved mica surface and a CO_2 snow jet cleaned silicon plate of 10 mm^2. After solvent evaporation, the substrates were carefully examined by optical microscopy, and the area of interest was scanned by AFM. Images were acquired in PeakForce Quantitative Nanomechanics (PF-QNM) tapping mode using a SCANSYST-AIR cantilever with a spring constant of 0.4 N m^{-1} and a resonance frequency of 70 kHz. The images were recorded with a cantilever oscillation of 2 kHz and a scan speed of 0.5 Hz.

The PF-QNM modes provide six different images simultaneously, such as height, peak force error, modulus, adhesion, deformation, and dissipation. Only height and adhesion images are presented here. The height image provides information about the height and lateral dimensions, whereas the adhesion image provides the adhesion properties of the sample relative to the cantilever, meaning that a strong contrast can be seen when the cantilever and sample have higher adhesion. This helps to identify various morphologies that cannot be resolved well in the height image. However, as the cantilever was not calibrated, the adhesion force in the image appears as volt rather than newton. Finally, the captured images were then processed by Gwyddion software (open source software, Czech Metrology Institute, Brno, Czech Republic).

4. Conclusions

In this paper, the dimerization technique and the nanoemulsion formulation were combined to comprise the properties of both approaches into a drug delivery system in order to increase the potency and efficacy of artesunate-based antimalarial treatment. Recently, an amphiphilic dimeric artesunate glycerophosphorylcholine (Di-ART-GPC) liposome was developed, which showed longer retention time and enhanced bioavailability in vivo compared to the parent drug [54,55]. Accordingly, we described the covalent conjugation of artesunate (AS) with a linker molecule glycerol monocaprylate (GC) to synthesize dimeric artesunate glycerol monocaprylate conjugate (D-AS-GC), which was characterized by ESI-TOF MS and 1D and 2D NMR spectroscopy. Later, different D-AS-GC loaded nanoemulsion preconcentrates were developed to optimize a transparent, stable nanoemulsion formulation upon dilution with an aqueous phase (double distilled water). Formulation F6 showed a clear nanoemulsion with a monomodal particle size distribution and a very narrow PDI of 0.13. The morphology of F6 was investigated by AFM using two different substrates to understand nanoemulsion characteristics and to visualize the internal structure of the nanoemulsion droplets. AFM results revealed the formation of nanodroplets close to DLS and DOSY NMR values with no observed defined structure on the mica surface. However, upon deposition of the formulation and drying on the silicon surface, an inner cavity surrounded by a spherical outer shell was observed, which confirmed the formation of a core shell-like structure composed of an inner core of drug molecules (D-AS-GC) with a distinct outer layer of MCT (oil) and Kolliphor HS 15/propylene glycol (surfactant/cosurfactant). In conclusion, we successfully synthesized dimeric artesunate glycerol monocaprylate conjugate (D-AS-GC) and developed a nanocarrier system for D-AS-GC delivery, thus creating a promising drug candidate for antimalarial treatment in combination with other drugs or as monotherapy. This strategy can further help to achieve an extended drug circulation time, increase bioavailability with a minimum dose of drugs, and control drug release over a long period of time. However, further research is necessary to verify the structure–activity relationship (SAR), pharmacokinetic and pharmacodynamic properties, and overall pharmacological and toxicological profile of the formulation.

Supplementary Materials: The following supporting information can be downloaded at: https://www.mdpi.com/article/10.3390/molecules28135208/s1, Figure S1: HSQC NMR spectrum of AS was recorded at 27 °C using $CDCl_3$ as solvent. The inset shows the HSQC NMR spectrum of AS in the range of 0–8 ppm and 90–180 ppm for ^{1}H and APT ^{13}C NMR chemical shifts, respectively. No additional correlation signals are observed in this region; Figure S2: COSY NMR spectrum of AS was recorded at 27 °C using $CDCl_3$ as solvent; Figure S3: HMBC NMR spectrum of AS was recorded at 27 °C using $CDCl_3$ as solvent; Figure S4: HSQC NMR spectrum of GC was recorded at 27 °C using $CDCl_3$ as solvent. The inset shows the HSQC NMR spectrum of GC in the range of 0–8 ppm and 160–190 ppm for ^{1}H and APT ^{13}C NMR chemical shifts, respectively. No additional correlation signals are observed in this region; Figure S5: COSY NMR spectrum of GC was recorded at 27 °C using $CDCl_3$ as solvent; Figure S6: HMBC NMR spectrum of GC was recorded at 27 °C using $CDCl_3$ as solvent; Figure S7: HSQC NMR spectrum of D-AS-GC was recorded at 27 °C using $CDCl_3$ as solvent. The inset shows the HSQC NMR spectrum of D-AS-GC in the range of 0–8 ppm and 90–170 ppm for ^{1}H and APT ^{13}C NMR shifts, respectively. No additional correlation signals are

observed in this region; Figure S8: ^{1}H NMR spectra of (a) propylene glycol, (b) Kolliphor HS 15 and (c) medium-chain triglycerides (MCT) were recorded at 27 °C using D_2O and $CDCl_3$ as solvent; Table S1: HSQC NMR assignment of AS; Table S2: COSY NMR assignment of AS; Table S3: HMBC NMR assignment of AS; Table S4: HSQC NMR assignment of GC; Table S5: COSY NMR assignment of GC; Table S6: HMBC NMR assignment of GC; Table S7: HSQC NMR assignment of D-AS-GC.

Author Contributions: Conceptualization, R.H., J.K. and K.M.; methodology, R.H., J.K. and K.M.; investigation, R.H. and N.H.; writing—original draft preparation, R.H.; writing—review and editing, R.H., N.H., J.K. and K.M; supervision, J.K.; funding acquisition, J.K. All authors have read and agreed to the published version of the manuscript.

Funding: This work was conducted in the frame of the International Graduate School AGRIPOLY supported by the European Social Fund (ESF) and the Federal State Saxony-Anhalt.

Institutional Review Board Statement: Not applicable.

Informed Consent Statement: Not applicable.

Data Availability Statement: The data presented in this article are available on request from the corresponding author.

Acknowledgments: The authors would like to thank Dieter Ströhl for the NMR measurements, Susanne Tanner for conducting the ESI measurement, and Christian Schwieger for the DLS measurements.

Conflicts of Interest: The authors declare no conflict of interest.

Sample Availability: Samples of the compounds are available from the authors.

References

1. Pinheiro, L.C.S.; Feitosa, L.M.; Da Silveira, F.F.; Boechat, N. Current antimalarial therapies and advances in the development of semi-synthetic artemisinin derivatives. *An. Acad. Bras. Cienc.* **2018**, *90*, 1251–1271. [CrossRef]
2. World Health Organization. *WHO Guidelines for Malaria—25 November 2022*; World Health Organization: Geneva, Switzerland, 2022.
3. O'Neill, P.M.; Barton, V.E.; Ward, S.A. The molecular mechanism of action of artemisinin-the debate continues. *Molecules* **2010**, *15*, 1705–1721. [CrossRef]
4. Travassos, M.A.; Laufer, M.K. Resistance to antimalarial drugs: Molecular, pharmacologic, and clinical considerations. *Pediatr. Res.* **2009**, *65*, 64–70. [CrossRef]
5. Tu, Y. The discovery of artemisinin (qinghaosu) and gifts from chinese medicine. *Nat. Med.* **2011**, *17*, 1217–1220. [CrossRef] [PubMed]
6. Khanal, P. Antimalarial and anticancer properties of artesunate and other artemisinins: Current development. *Mon. Für Chem.-Chem. Mon.* **2021**, *152*, 387–400. [CrossRef]
7. Zhang, J.-F. *A Detailed Chronological Record of Project 523 and the Discovery and Development of Qinghaosu (Artemisinin)*; Yang Cheng Evening News Publishing Company: Guangzhou, China, 2005.
8. Ma, N.; Zhang, Z.; Liao, F.; Jiang, T.; Tu, Y. The birth of artemisinin. *Pharmacol. Ther.* **2020**, *216*, 107658. [CrossRef]
9. Gashe, F.; Wynendaele, E.; De Spiegeleer, B.; Suleman, S. Degradation kinetics of artesunate for the development of an ex-tempore intravenous injection. *Malar. J.* **2022**, *21*, 256. [CrossRef]
10. Adebayo, J.O.; Tijjani, H.; Adegunloye, A.P.; Ishola, A.A.; Balogun, E.A.; Malomo, S.O. Enhancing the antimalarial activity of artesunate. *Parasitol. Res.* **2020**, *119*, 2749–2764. [CrossRef]
11. Chekem, L.; Wierucki, S. Extraction of artemisinin and synthesis of its derivates artesunate and artemether. *Med. Trop.* **2006**, *66*, 602–605.
12. Morris, C.A.; Duparc, S.; Borghini-Fuhrer, I.; Jung, D.; Shin, C.S.; Fleckenstein, L. Review of the clinical pharmacokinetics of artesunate and its active metabolite dihydroartemisinin following intravenous, intramuscular, oral or rectal administration. *Malar. J.* **2011**, *10*, 263. [CrossRef] [PubMed]
13. Sahr, F.; Willoughby, V.R.; Gbakima, A.A.; Bockarie, M.J. Apparent drug failure following artesunate treatment of plasmodium falciparum malaria in freetown, sierra leone: Four case reports. *Ann. Trop. Med. Parasitol.* **2001**, *95*, 445–449. [CrossRef] [PubMed]
14. Nigam, M.; Atanassova, M.; Mishra, A.P.; Pezzani, R.; Devkota, H.P.; Plygun, S.; Salehi, B.; Setzer, W.N.; Sharifi-Rad, J. Bioactive compounds and health benefits of artemisia species. *Nat. Prod. Commun.* **2019**, *14*, 1934578X19850354.
15. Mohammadi, S.; Jafari, B.; Asgharian, P.; Martorell, M.; Sharifi-Rad, J. Medicinal plants used in the treatment of malaria: A Key emphasis to artemisia, cinchona, cryptolepis, and tabebuia genera. *Phyther. Res.* **2020**, *34*, 1556–1569. [CrossRef] [PubMed]
16. World Health Organization. *WHO Calls for an Immediate Halt to Provision of Single-Drug Artemisinin Malaria Pills*; World Health Organization: Geneva, Switzerland, 2006.

17. World Health Organization. WHO Resolution WHA6018 Malaria, Including Proposal for Establishment of World Malaria Day. In *Sixtieth World Health Assembly, Geneva, Resolutions and Decisions, Annexes Geneva*; World Health Organization: Geneva, Switzerland, 2007.
18. World Health Organization. *Meeting on Addressing Urgent Issues Pertaining to Antimalarial Drug Management to Facilitate Accelerated Elimination of Malaria from the Greater Mekong Subregion Countries of the Western Pacific Region, Phnom Penh, Cambodia, 26–28 February 2018: Meeting Report*; World Health Organization: Geneva, Switzerland, 2018.
19. Çapcı, A.; Herrmann, L.; Sampath Kumar, H.M.; Fröhlich, T.; Tsogoeva, S.B. Artemisinin-derived dimers from a chemical perspective. *Med. Res. Rev.* **2021**, *41*, 2927–2970. [CrossRef] [PubMed]
20. Frohlich, T.; Karagöz, A.Ç.; Reiter, C.; Tsogoeva, S.B. Artemisinin-derived dimers: Potent antimalarial and anticancer agents. *J. Med. Chem.* **2016**, *59*, 7360–7388. [CrossRef] [PubMed]
21. Chaturvedi, D.; Goswami, A.; Saikia, P.P.; Barua, N.C.; Rao, P.G. Artemisinin and its derivatives: A novel class of anti-malarial and anti-cancer agents. *Chem. Soc. Rev.* **2010**, *39*, 435–454. [CrossRef]
22. Bradley, D. Dimeric malarial drugs for enhanced activity. *Drug Discov.Today* **2000**, *5*, 44–45. [CrossRef]
23. Posner, G.H.; Ploypradith, P.; Parker, M.H.; O'Dowd, H.; Woo, S.-H.; Northrop, J.; Krasavin, M.; Dolan, P.; Kensler, T.W.; Xie, S.; et al. Antimalarial, antiproliferative, and antitumor activities of artemisinin-derived, chemically robust, trioxane dimers. *J. Med. Chem.* **1995**, *42*, 4275–4280. [CrossRef]
24. Mott, B.T.; Tripathi, A.; Siegler, M.A.; Moore, C.D.; Sullivan, D.J.; Posner, G.H. Synthesis and antimalarial efficacy of two-carbon-linked, artemisinin-derived trioxane dimers in combination with known antimalarial drugs. *J. Med. Chem.* **2013**, *56*, 2630–2641. [CrossRef]
25. Posner, G.H.; Paik, I.; Sur, S.; Mcriner, A.J.; Borstnik, K.; Xie, S. Orally active, antimalarial, anticancer, artemisinin-derived trioxane dimers with high stability and efficacy. *J. Med. Chem.* **2003**, *46*, 1060–1065. [CrossRef]
26. Conyers, R.C.; Mazzone, J.R.; Tripathi, A.K.; Sullivan, D.J.; Posner, G.H. Antimalarial chemotherapy: Orally curative artemisinin-derived trioxane dimer esters. *Bioorganic Med. Chem. Lett.* **2015**, *25*, 245–248. [CrossRef]
27. Reiter, C.; Fröhlich, T.; Gruber, L.; Hutterer, C.; Marschall, M.; Voigtländer, C.; Friedrich, O.; Kappes, B.; Efferth, T.; Tsogoeva, S.B. Highly potent artemisinin-derived dimers and trimers: Synthesis and evaluation of their antimalarial, antileukemia and antiviral activities. *Bioorganic Med. Chem.* **2015**, *23*, 5452–5458. [CrossRef]
28. Cloete, T.T.; De Kock, C.; Smith, P.J.; N'Da, D.D. Synthesis, in vitro antiplasmodial activity and cytotoxicity of a series of artemisinin-triazine hybrids and hybrid-dimers. *Eur. J. Med. Chem.* **2014**, *76*, 470–481. [CrossRef]
29. Rajwar, T.K.; Pradhan, D.; Halder, J.; Rai, V.K.; Kar, B.; Ghosh, G.; Rath, G. Opportunity in nanomedicine to counter the challenges of current drug delivery approaches used for the treatment of malaria: A review. *J. Drug Target.* **2023**, *31*, 354–368. [CrossRef]
30. Esfahani, G.; Häusler, O.; Mäder, K. Controlled release starch-lipid implant for the therapy of severe malaria. *Int. J. Pharm.* **2022**, *622*, 121879. [CrossRef]
31. Alven, S.; Aderibigbe, B.A. Nanoparticles formulations of artemisinin and derivatives as potential therapeutics for the treatment of cancer, leishmaniasis and malaria. *Pharmaceutics* **2020**, *12*, 748. [CrossRef]
32. Khani, S.; Keyhanfar, F.; Amani, A. Design and evaluation of oral nanoemulsion drug delivery system of mebudipine. *Drug Deliv.* **2016**, *23*, 2035–2043. [CrossRef] [PubMed]
33. Zhang, Y.; Shang, Z.; Gao, C.; Du, M.; Xu, S.; Song, H.; Liu, T. Nanoemulsion for solubilization, stabilization, and in vitro release of pterostilbene for oral delivery. *AAPS PharmSciTech* **2014**, *15*, 1000–1008. [CrossRef] [PubMed]
34. Ansell, S.M.; Johnstone, S.A.; Tardi, P.G.; Lo, L.; Xie, S.; Shu, Y.; Harasym, T.O.; Harasym, N.L.; Williams, L.; Bermudes, D.; et al. Modulating the therapeutic activity of nanoparticle delivered paclitaxel by manipulating the hydrophobicity of prodrug conjugates. *J. Med. Chem.* **2008**, *51*, 3288–3296. [CrossRef] [PubMed]
35. Konermann, L.; Ahadi, E.; Rodriguez, A.D.; Vahidi, S. Unraveling the mechanism of electrospray ionization. *Anal. Chem.* **2013**, *85*, 2–9. [CrossRef] [PubMed]
36. Elsheikh, M.A.; Elnaggar, Y.S.R.; Gohar, E.Y.; Abdallah, O.Y. Nanoemulsion liquid preconcentrates for raloxifene hydrochloride: Optimization and in vivo appraisal. *Int. J. Nanomed.* **2012**, *7*, 3787–3802.
37. Zech, J.; Gold, D.; Salaymeh, N.; Sasson, N.C.; Rabinowitch, I.; Golenser, J.; Mäder, K. Oral administration of artemisone for the treatment of schistosomiasis: Formulation challenges and in vivo efficacy. *Pharmaceutics* **2020**, *12*, 509. [CrossRef] [PubMed]
38. Patel, K.; Pati, A.; Mehta, M.; Gota, V.; Vavia, P. Medium chain triglyceride (MCT) rich, paclitaxel loaded self nanoemulsifying preconcentrate (PSNP): A safe and efficacious alternative to taxol®. *J. Biomed. Nanotechnol.* **2013**, *9*, 1996–2006. [CrossRef]
39. Rowe, R.C.; Sheskey, P.J.; Owen, S.C. *Handbook of Pharmaceutical Excipients*, 5th ed.; Pharmaceutical Press: London, UK, 2006.
40. Tadros, T.; Izquierdo, P.; Esquena, J.; Solans, C. Formation and stability of nano-emulsions. *Adv. Colloid Interface Sci.* **2004**, *108–109*, 303–318. [CrossRef] [PubMed]
41. Sarheed, O.; Dibi, M.; Ramesh, K.V.R.N.S. Studies on the effect of oil and surfactant on the formation of alginate-based o/w lidocaine nanocarriers using nanoemulsion template. *Pharmaceutics* **2020**, *12*, 1223. [CrossRef]
42. McClements, D.J. Colloidal basis of emulsion color. *Curr. Opin. Colloid Interface Sci.* **2002**, *7*, 451–455. [CrossRef]
43. McClements, D.J. Theoretical prediction of emulsion color. *Adv. Colloid Interface Sci.* **2002**, *97*, 63–89. [CrossRef]
44. Giusto, K.; Patki, M.; Koya, J.; Ashby, C.R.; Munnangi, S.; Patel, K.; Reznik, S.E. A vaginal nanoformulation of a sphk inhibitor attenuates lipopolysaccharide-induced preterm birth in mice. *Nanomedicine* **2019**, *14*, 2835–2851. [CrossRef]

45. Kirchherr, A.K.; Briel, A.; Mäder, K. Stabilization of indocyanine green by encapsulation within micellar systems. *Mol. Pharm.* **2009**, *6*, 480–491. [CrossRef]
46. Petrochenko, P.E.; Pavurala, N.; Wu, Y.; Yee Wong, S.; Parhiz, H.; Chen, K.; Patil, S.M.; Qu, H.; Buoniconti, P.; Muhammad, A.; et al. Analytical considerations for measuring the globule size distribution of cyclosporine ophthalmic emulsions. *Int. J. Pharm.* **2018**, *550*, 229–239. [CrossRef]
47. Naoui, W.; Bolzinger, M.A.; Fenet, B.; Pelletier, J.; Valour, J.P.; Kalfat, R.; Chevalier, Y. Microemulsion microstructure influences the skin delivery of an hydrophilic drug. *Pharm. Res.* **2011**, *28*, 1683–1695. [CrossRef] [PubMed]
48. Hasan, N.; Nguyen, T.M.H.; Busse, K.; Kressler, J. Influence of tacticity on the structure formation of poly(methacrylic acid) in Langmuir/Langmuir–Blodgett and thin films. *Macromol. Chem. Phys.* **2023**, *224*, 2200428. [CrossRef]
49. Bittermann, M.R.; Deblais, A.; Lépinay, S.; Bonn, D.; Shahidzadeh, N. Deposits from evaporating emulsion drops. *Sci. Rep.* **2020**, *10*, 14863. [CrossRef]
50. Neises, B.; Steglich, W. Simple method for the esterification of carboxylic acids. *Angew. Chem. Int. Ed. Engl.* **1978**, *17*, 522–524. [CrossRef]
51. Alaneed, R.; Naumann, M.; Pietzsch, M.; Kressler, J. Microbial transglutaminase-mediated formation of erythropoietin-polyester conjugates. *J. Biotechnol.* **2022**, *346*, 1–10. [CrossRef] [PubMed]
52. Ahmad, J.; Mir, S.R.; Kohli, K.; Chuttani, K.; Mishra, A.K.; Panda, A.K.; Amin, S. Solid-nanoemulsion preconcentrate for oral delivery of paclitaxel: Formulation design, biodistribution, and γ scintigraphy imaging. *Biomed Res. Int.* **2014**, *2014*, 984756. [CrossRef]
53. Dou, Y.X.; Zhou, J.T.; Wang, T.T.; Huang, Y.F.; Chen, V.P.; Xie, Y.L.; Lin, Z.X.; Gao, J.S.; Su, Z.R.; Zeng, H.F. Self-nanoemulsifying drug delivery system of bruceine D: A new approach for anti-ulcerative colitis. *Int. J. Nanomed.* **2018**, *13*, 5887–5907. [CrossRef]
54. Ismail, M.; Ling, L.; Du, Y.; Yao, C.; Li, X. Liposomes of dimeric artesunate phospholipid: A combination of dimerization and self-assembly to combat malaria. *Biomaterials* **2018**, *163*, 76–87. [CrossRef]
55. Du, Y.; Giannangelo, C.; He, W.; Shami, G.J.; Zhou, W.; Yang, T.; Creek, D.J.; Dogovski, C.; Li, X.; Tilley, L. Dimeric artesunate glycerophosphocholine conjugate nano- assemblies as slow-release antimalarials to overcome kelch 13 mutant artemisinin resistance. *Antimicrob. Agents Chemother.* **2022**, *66*, e02065-21. [CrossRef]

Synthesis and Characterization of Dimeric Artesunate Glycerol Monocaprylate Conjugate and Formulation of Nanoemulsion Preconcentrate

Rana Hore[1], Nazmul Hasan[1], Karsten Mäder[2] and Jörg Kressler[1,*]

[1]Department of Chemistry, Martin Luther University Halle-Wittenberg, Von-Danckelmann-Platz 4, D-06099 Halle/Saale, Germany

[2]Institute of Pharmacy, Martin Luther University Halle-Wittenberg, D-06099, Halle (Saale), Germany

*Correspondence: joerg.kressler@chemie.uni-halle.de

Supplementary Materials

Table S7. HSQC NMR assignment of D-AS-GC

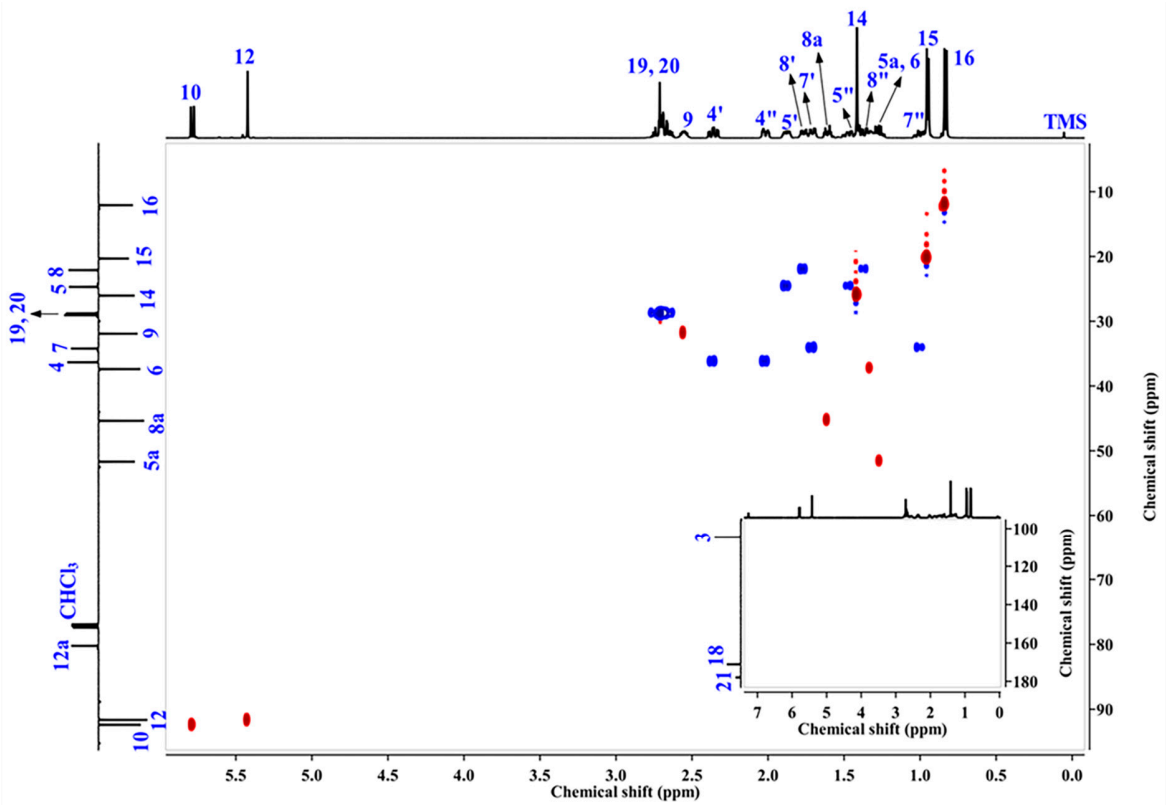

Figure S1. HSQC NMR spectrum of AS was recorded at 27 °C using $CDCl_3$ as solvent. The inset shows the HSQC NMR spectrum of AS in the range of 0–8 ppm and 90–180 ppm for ^{1}H and APT ^{13}C NMR chemical shifts, respectively. No additional correlation signals are observed in this region.

Table S1. HSQC NMR assignment of AS.

Chemical shift δ_H (ppm)	^{1}H peak assignment	Chemical shift δ_C (ppm)	APT ^{13}C peak assignment
5.78–5.76	10	92.39	10
5.43–5.40	12	91.63	12
2.73–2.62	19 and 20	29.06–28.79	19 and 20
2.57–2.50	9	31.92	9
2.39–2.33	4'	36.33	4'
2.04–1.99	4"	36.33	4"
1.90–1.86	5'	24.69	5'
1.78	8'	22.10	8'

1.67	7'	34.21	7'
1.62–1.58	8a	45.36	8a
1.50–1.45	5''	24.69	5''
1.42–1.39	14	26.04	14
1.39–1.34	8''	22.10	8''
1.33	6	37.38	6
1.27	5a	51.68	5a
1.04–0.97	7''	34.21	7''
0.96–0.93	15	20.31	15
0.88–0.83	16	12.08	16

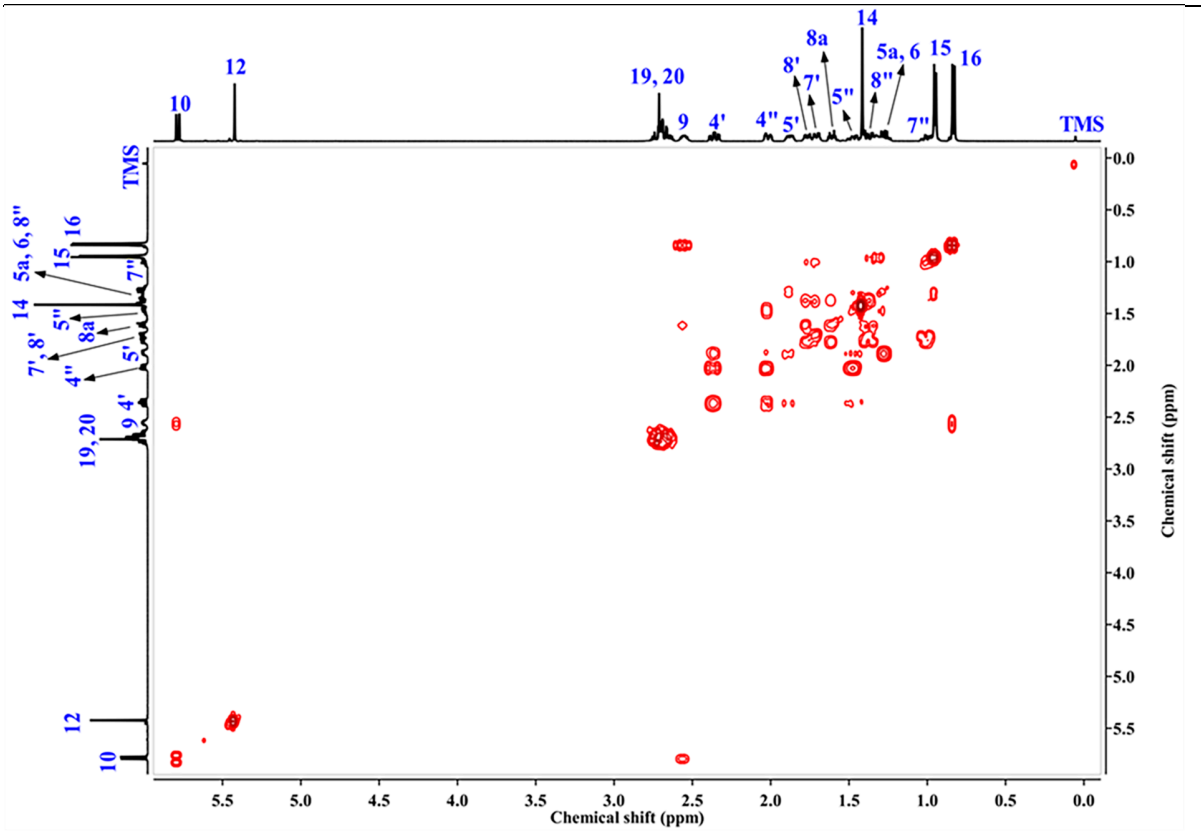

Figure S2. COSY NMR spectrum of AS was recorded at 27 °C using $CDCl_3$ as solvent.

Table S2. COSY NMR assignment of AS.

Chemical shift δ_H (ppm)	**Chemical shift δ_H (ppm)**	**COSY correlation assignment**
5.78–5.76	2.57–2.50	10-9
2.57–2.50	0.88-0.83	9-16
2.57–2.50	1.62–1.58	9-8a
2.39–2.33	1.90–1.86	4'-5'

2.39–2.33	2.04–1.99	4'-4"
2.04–1.99	1.50–1.45	4"-5"
2.04–1.99	1.90–1.86	4"-5'
1.90–1.86	1.27	5'-5a
1.78	1.04–0.97	8'-7"
1.67	1.04–0.97	7'-7"
1.67	1.39–1.34	7'-8"
1.78	1.39–1.34	8'-8"
1.78	1.62–1.58	8'-8a
1.62–1.58	1.39–1.34	8a-8"
1.50–1.45	1.27	5"-5a
1.33	0.96–0.93	6-15

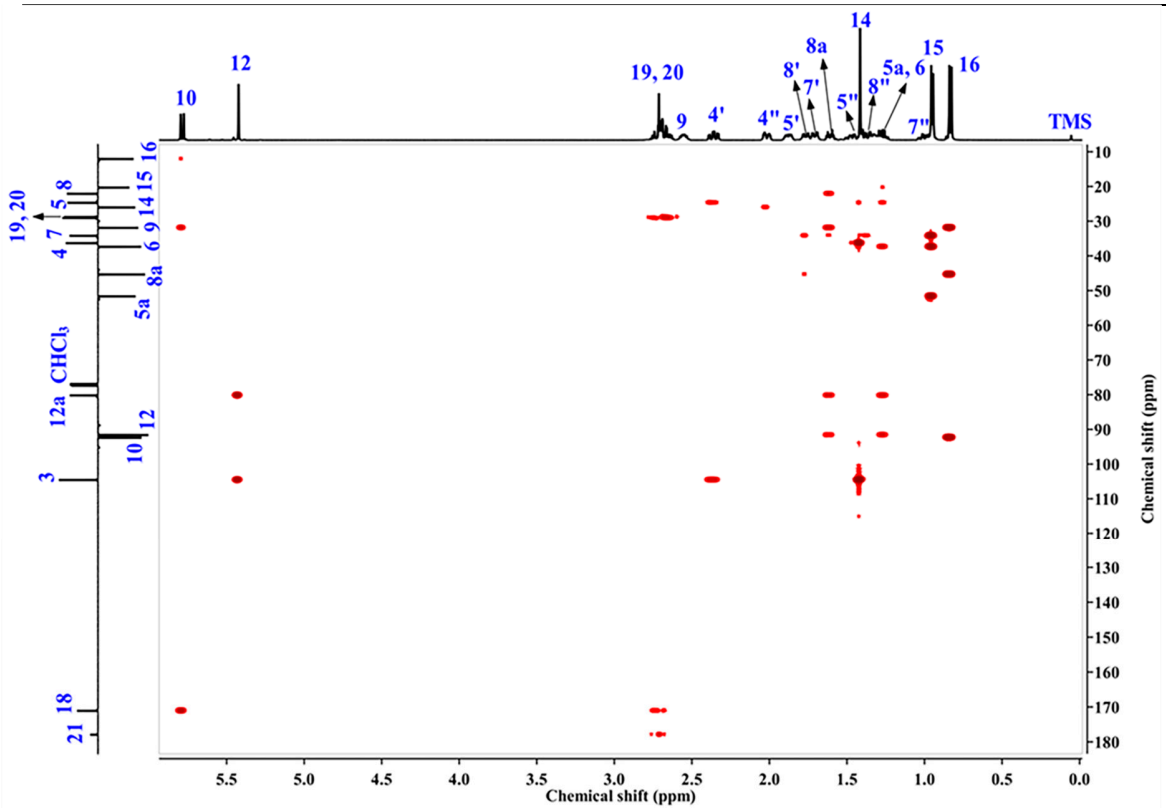

Figure S3. HMBC NMR spectrum of AS was recorded at 27 °C using $CDCl_3$ as solvent.

Table S3. HMBC NMR assignment of AS.

Chemical shift δ_H (ppm)	Chemical shift δ_C (ppm)	HMBC correlation assignment
5.78–5.76	12.08	10-16
5.78–5.76	31.92	10-9
5.78–5.76	171.10	10-18
5.43–5.40	80.22	12-12a

5.43–5.40	104.42	12-3
2.73–2.62	29.06–28.79	19-20 or 20-19
2.73–2.62	171.10	20-18
2.73–2.62	177.94	19-21
2.39–2.33	104.42	4'-3
2.39–2.33	24.69	4'-5
2.04–1.99	26.04	4"-14
1.78	34.21	8'-7
1.78	45.36	8'-8a
1.62–1.58	22.10	8a-8
1.62–1.58	31.92	8a-9
1.62–1.58	80.22	8a-12a
1.62–1.58	91.63	8a-12
1.42–1.39	36.33	14-4
1.42–1.39	104.59	14-3
1.27	24.69	5a-5
1.27	37.38	5a-6
1.27	80.22	5a -12a
1.27	91.63	5a-12
0.96–0.93	34.21	15-7
0.96–0.93	37.38	15-6
0.96–0.93	51.68	15-5a
0.88–0.83	31.92	16-9
0.88–0.83	45.36	16-8a
0.88–0.83	92.39	16-10

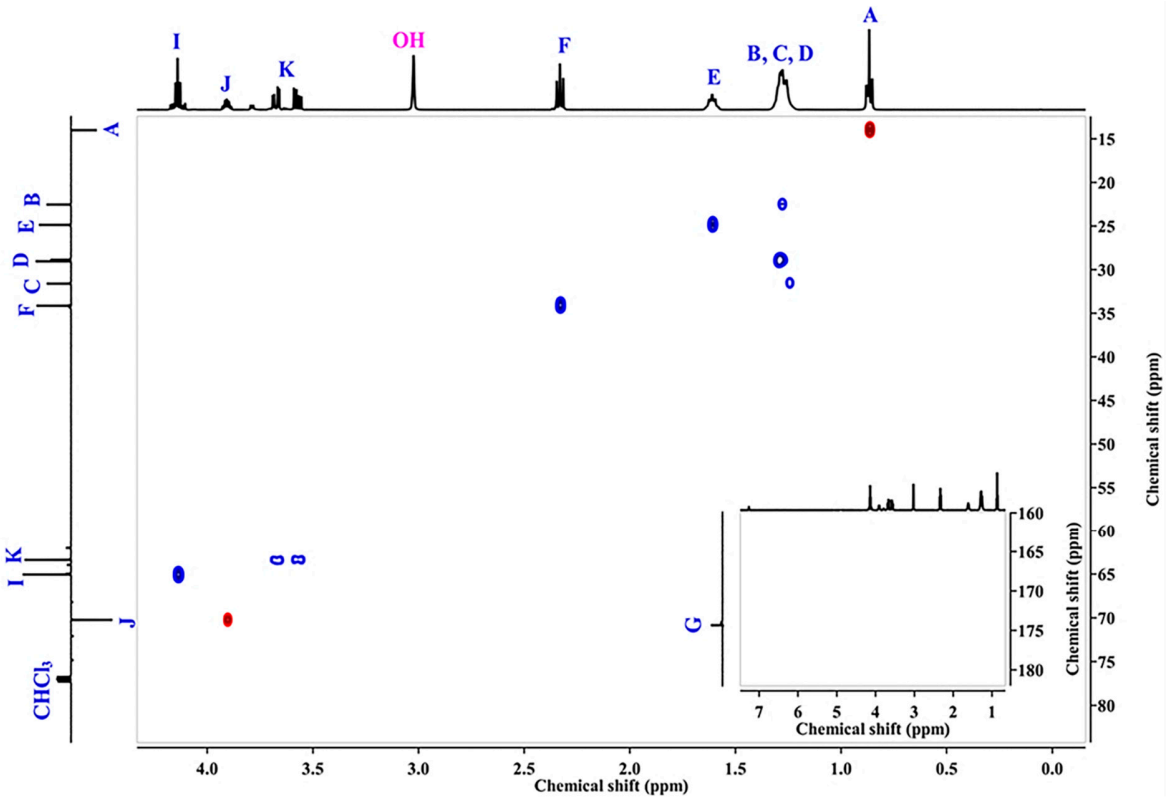

Figure S4. HSQC NMR spectrum of GC was recorded at 27 °C using $CDCl_3$ as solvent. The inset shows the HSQC NMR spectrum of GC in the range of 0–8 ppm and 160–190 ppm for ^{1}H and APT ^{13}C NMR chemical shifts, respectively. No additional correlation signals are observed in this region.

Table S4. HSQC NMR assignment of GC.

Chemical shift δ_H (ppm)	**^{1}H peak assignment**	**Chemical shift δ_C (ppm)**	**APT ^{13}C peak assignment**
4.17–4.10	I	65.20	I
3.92–3.88	J	70.38	J
3.69–3.55	K	63.52	K
2.35–2.31	F	34.27	F
1.64–1.58	E	25.00	E
1.32–1.21	B, C and D	22.69, 31.74 and 29.19	B, C and D
0.88–0.85	A	14.14	A

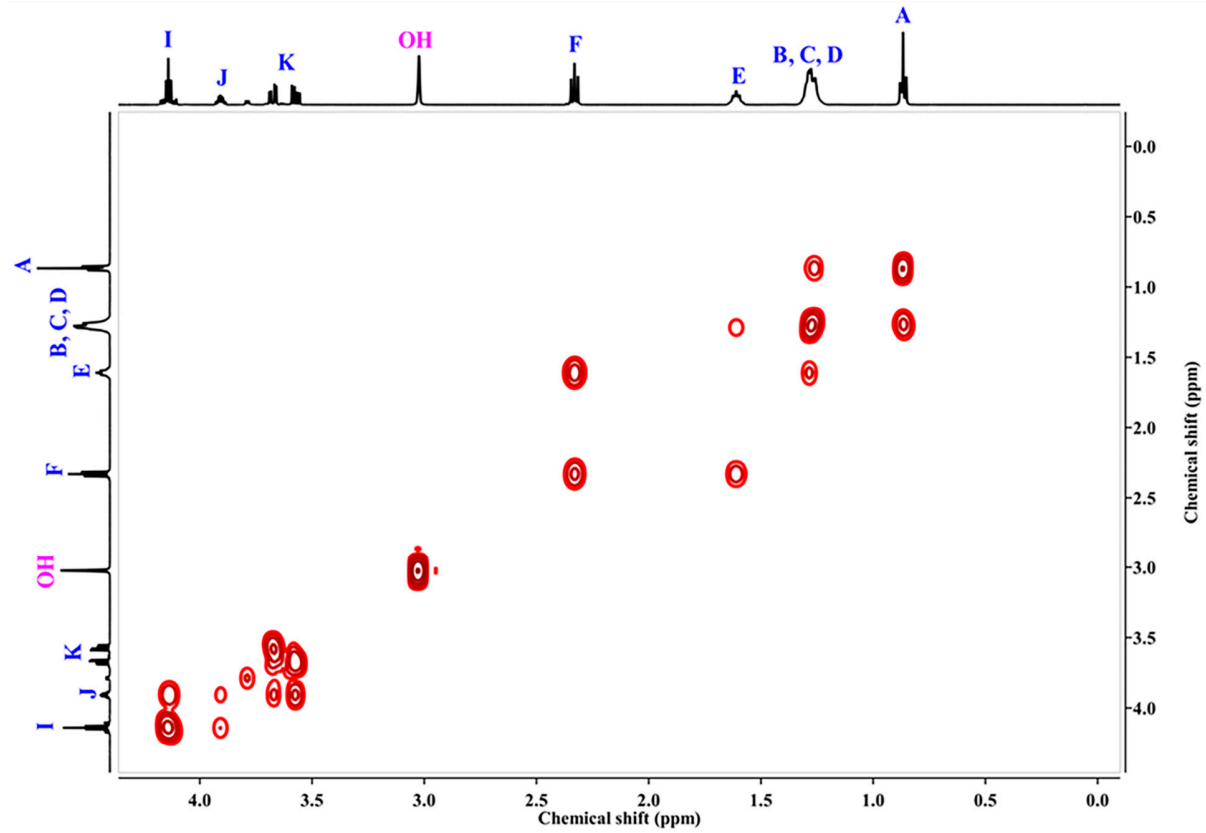

Figure S5. COSY NMR spectrum of GC was recorded at 27 °C using $CDCl_3$ as solvent.

Table S5. COSY NMR assignment of GC.

Chemical shift δ_H (ppm)	Chemical shift δ_H (ppm)	COSY correlation assignment
4.17–4.10	3.92–3.88	I-J
3.69–3.55	3.92–3.88	K-J
2.35–2.31	1.64–1.58	F-E
1.64–1.58	1.32–1.21	E-D
1.32–1.21	0.88–0.85	B-A

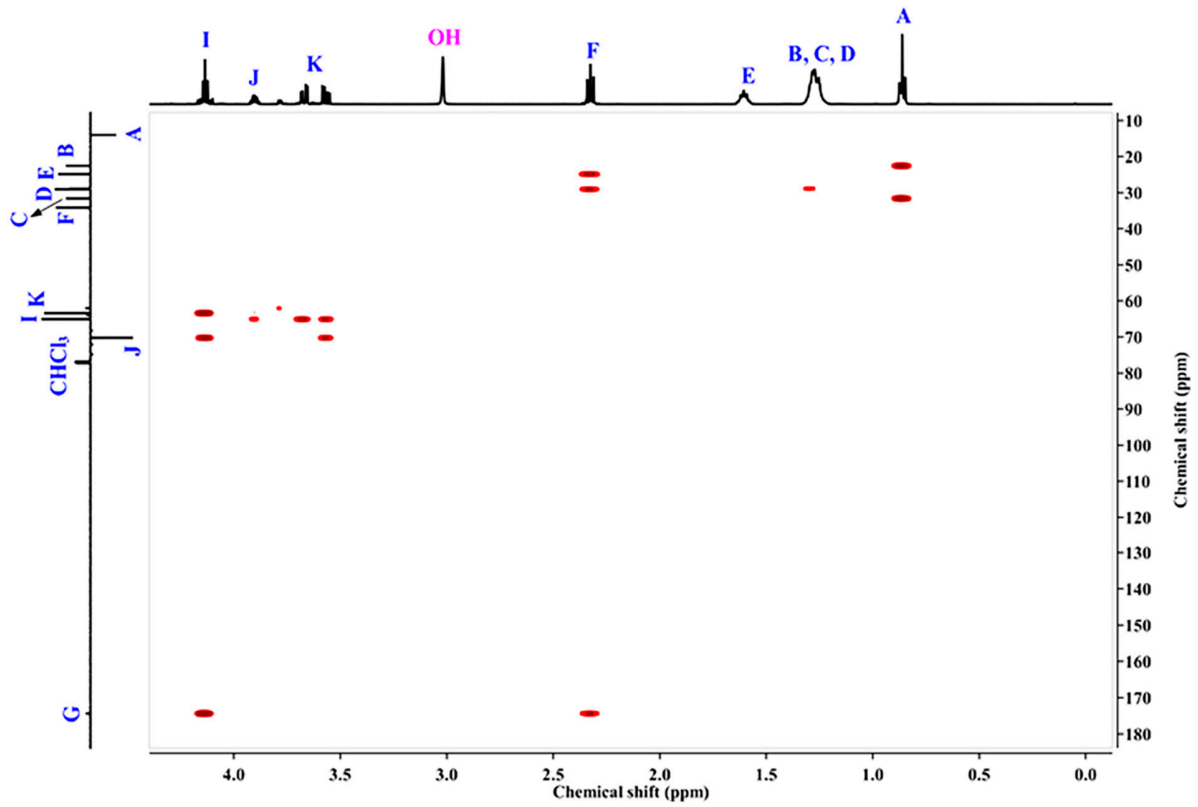

Figure S6. HMBC NMR spectrum of GC was recorded at 27 °C using $CDCl_3$ as solvent.

Table S6. HMBC NMR assignment of GC.

Chemical shift δ_H (ppm)	Chemical shift δ_C (ppm)	HMBC correlation assignment
4.17–4.10	63.52	I-K
4.17–4.10	70.38	I-J
4.17–4.10	174.49	I-G
3.92–3.88	65.20	J-I
3.69–3.55	65.20	K-I
3.69–3.55	70.38	K-J
2.35–2.31	25.00	F-E
2.35–2.31	29.19	F-D
2.35–2.31	174.49	F-G
1.32–1.21	29.19	B/C-D
0.88–0.85	22.69	A-B
0.88–0.85	31.74	A-C

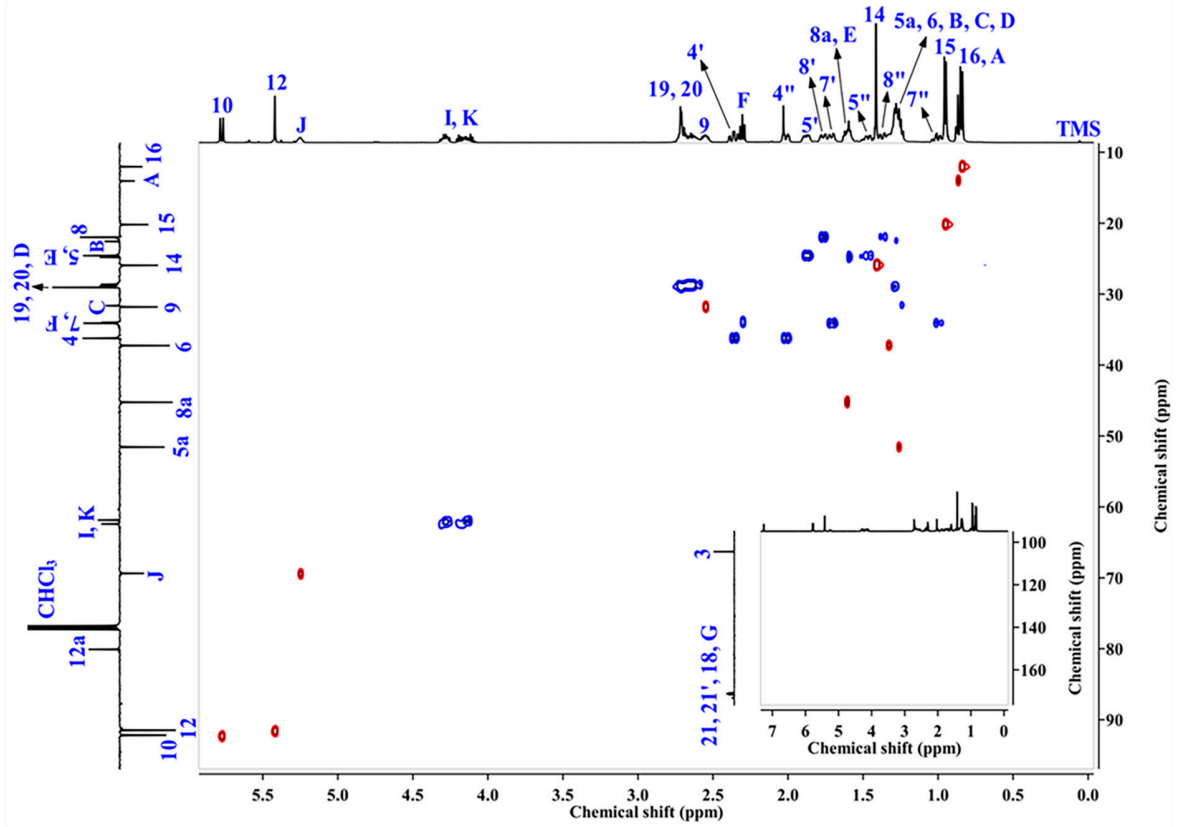

Figure S7. HSQC NMR spectrum of D-AS-GC was recorded at 27 °C using $CDCl_3$ as solvent. The inset shows the HSQC NMR spectrum of D-AS-GC in the range of 0–8 ppm and 90–170 ppm for ^{1}H and APT ^{13}C NMR shifts, respectively. No additional correlation signals are observed in this region.

Table S7. HSQC NMR assignment of D-AS-GC.

Chemical shift δ_H (ppm)	^{1}H peak assignment	Chemical shift δ_C (ppm)	APT ^{13}C peak assignment
5.78–5.76	10	92.19	10
5.43–5.40	12	91.48	12
5.28–5.23	J	69.37	J
4.32–4.09	I, K	62.41–61.86	I, K
2.73–2.62	19 and 20	29.04–28.62	19 and 20
2.57–2.50	9	31.80	9
2.39–2.29	4'	36.22	4
2.39–2.29	F	34.10–33.98	F
2.04–1.99	4''	36.22	4
1.90–1.86	5'	24.84–24.58	5
1.78–1.69	8'	21.98	8

1.78–1.69	7'	34.10–33.98	7
1.62–1.58	E	24.84–24.58	E
1.62–1.58	8a	45.24	8a
1.50–1.45	5''	24.84–24.58	5
1.42–1.39	14	25.93	14
1.39–1.34	8''	21.98	8
1.31–1.23	6	37.25	6
1.31–1.23	B	22.51	B
1.31–1.23	D	31.63	C
1.31–1.23	C	29.04–28.62	D
1.31–1.23	5a	51.57	5a
1.04–0.97	7''	34.10–33.98	7
0.96–0.93	15	20.19	15
0.88–0.83	A	14.05	A
0.88–0.83	16	12.03	16

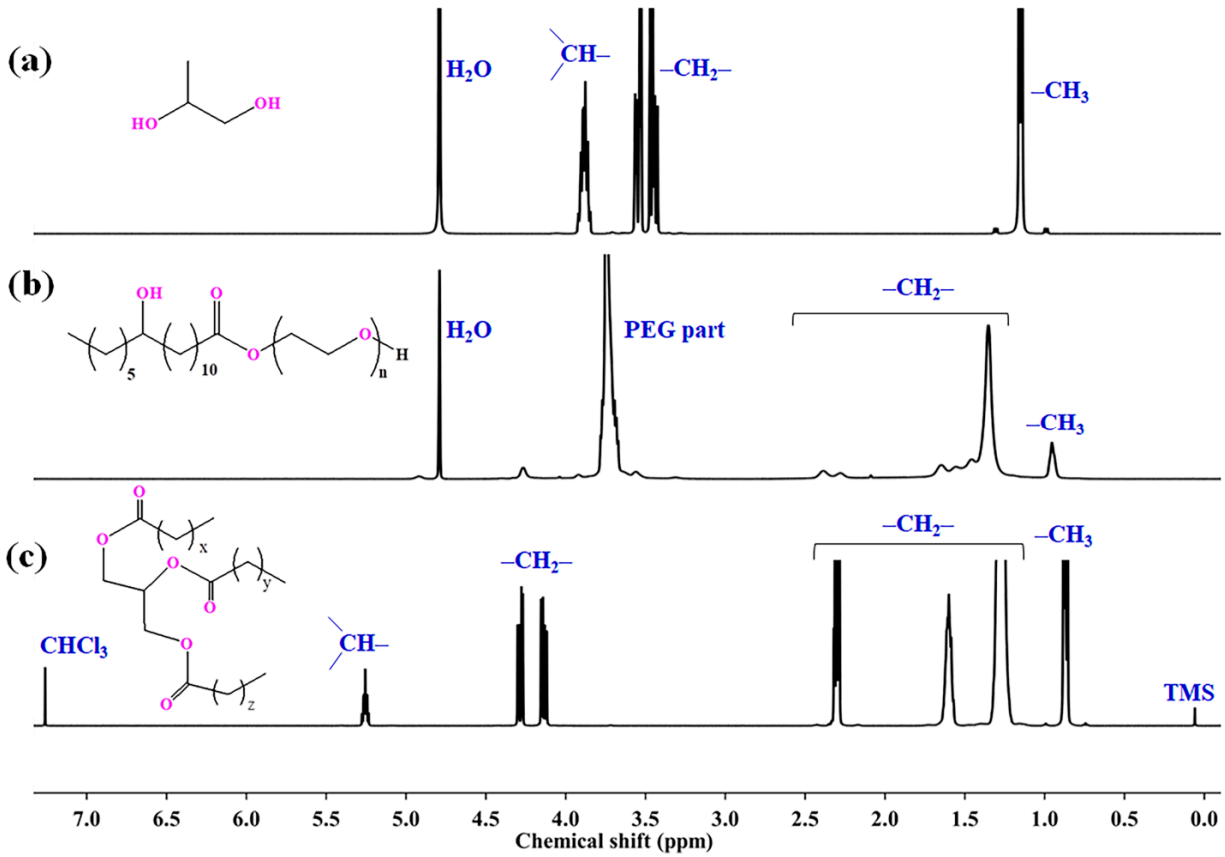

Figure S8. ^{1}H NMR spectra of (a) propylene glycol, (b) Kolliphor HS 15 and (c) medium-chain triglyceride (MCT) were recorded at 27 °C using D_2O and $CDCl_3$ as solvent.

4. Summary and outlook

Polymer and lipid-based nanocarriers have emerged as pivotal tools in the delivery of therapeutic agents, providing a range of benefits due to their distinct physicochemical properties. Based on this, the present thesis outlines three projects in two different subject areas focused on the design, synthesis, and structural characterization of carrier platforms for the delivery of therapeutics. The first part (Part A) of the thesis combines two projects focused on the development of HES-based therapeutic carriers and the second part (Part B) focuses on the designing of the lipid-based drug delivery system.

In the first project, HES was utilized for the development of enzymatically catalyzed polymer-protein conjugates as an effective carrier for the delivery of proteins. For this purpose, HES was modified with primary amine-containing side chains (HES-*g*-NH_2) by reacting with HMDA *via* a CDI-mediated coupling reaction. Detailed structural characterization of native HES before and after modification was investigated using ^{1}H NMR, 2D COSY and HSQC spectroscopy, and FTIR spectroscopy which validated the successful introduction of primary amines and the synthesis of HES-*g*-NH_2. The number of side chains attached to the HES backbone was calculated from the ^{1}H NMR as 7.5 mol% (approximately 28 primary amine groups per polymer chain). This amine-functionalized HES-*g*-NH_2 was later used as an acyl acceptor substrate for the mTGase-catalyzed reaction with rHuEPO. Further, HES-*g*-NH_2 was partially labeled with an amine-reactive fluorescent dye, rhodamine B isothiocyanate, to form rhodamine B tagged HES-*g*-NH_2-R and characterized by ^{1}H NMR spectroscopy. Both HES-*g*-NH_2 and HES-*g*-NH_2-R were subjected to the enzymatically catalyzed conjugation reaction with the rHuEPO at its transition temperature (T_m). Alaneed et al. determined the T_m of rHuEPO by nano differential scanning fluorimetry (nanoDSF) and demonstrated that half of the protein exists in its unfolded state at this temperature [288]. As a proof of study, a series of control experiments were carried out using N-deglycosylated rHuEPO with monodansyl cadaverine (MDC), a fluorescent substrate of mTGase, at 37 °C catalyzed by a variant mTGase-S2P. The results were analyzed SDS-PAGE and revealed that at 37 °C (a) no crosslinking reaction occurred between MDC and mTGase-S2P when MDC was incubated with mTGase-S2P, (b) no conjugation reaction took place between N-deglycosylated rHuEPO and MDC when MDC was incubated with N-deglycosylated

rHuEPO in absence of mTGase-S2P, (c) no notable conjugates or aggregates were detected when N-deglycosylated rHuEPO was incubated with mTGase-S2P and (d) no significant conjugation reaction happened between N-deglycosylated rHuEPO and MDC in the presence of mTGase-S2P. From the control experiments, it was clear that rHuEPO needs to be partially unfolded for further conjugation reaction as the Gln residues that are identified by mTGase are located within the protein's unfolded region. Hence, the conjugation reactions of HES-*g*-NH_2 and HES-*g*-NH_2-R with rHuEPO were carried out at 54 °C, using a thermoresistant variant mTGase TG[16] and investigated by SDS-PAGE. The SDS-PAGE analysis of the conjugation reaction between HES-*g*-NH_2 with rHuEPO in the presence of mTGase TG[16] clearly revealed the appearance of a high molar mass band represented the rHuEPO-HES conjugates over 116 kDa after silver staining, along with a consequent reduction of the pure rHuEPO band intensity. The high molar mass band appeared with a broad distribution on the gel that can be attributed to the high polydispersity of HES and the heterogeneity of the glycan moieties of rHuEPO. Cross-linked aggregates were also observed on the top of the stacking gel because both HES-*g*-NH_2 and rHuEPO possess multiple reactive sites that can be modified by mTGase TG[16]. Furthermore, SDS-PAGE investigations were conducted to assess the mTGase TG[16]-mediated conjugation reaction between HES-*g*-NH_2-R and rHuEPO, visualized under UV light followed by silver staining. The results showed an almost similar high molar mass fluorescent band of rhodamine B labeled rHuEPO-HES conjugates over 180 kDa together with cross-linked aggregates. It was observed that the fluorescent band intensity of HES-*g*-NH_2-R decreased with increasing reaction time, indicating the consumption of HES-*g*-NH_2-R for the formation of rHuEPO-HES conjugates under mTGase TG[16] catalysis. In addition, both conjugation reactions were further performed after the treatment with PNGase F to form N-deglycosylated rHuEPO and analyzed by SDS-PAGE. The results demonstrated that the conjugates exhibited similar behavior with more intense band intensity before and after N-deglycosylation. Together, these findings verified the successful conjugation of HES with rHuEPO and hence, developed a biodegradable HES-based enzymatically catalyzed polymer-protein conjugates for the delivery of rHuEPO which can improve the protein solubility, stability, and overall pharmacokinetics.

The second project involved the use of HES for the development of highly fatty acid-grafted HES nanocarriers, designed to improve the loading capacity and enhance drug delivery efficiency. To this aim, SA was grafted with HES through a Steglich esterification reaction. Two highly stearate-grafted HES conjugates (St-HES) were synthesized by differing the feeding ratio of SA to HES to obtain an improved hydrophobic inner core. Initially, a

thorough structural characterization of native HES was conducted to refine the structural verification by examining ^{1}H NMR and 2D NMR spectroscopy including labile proton exchange phenomena to identify the anomeric proton signals and other proton signals from the HES backbone, subsequently allowed for the precise determination of the grafting degree of St-HES conjugates. The St-HES conjugates were characterized by ^{1}H, 2D HSQC, and HMBC NMR spectroscopy. The degree of grafting of stearate side chains was determined from ^{1}H NMR spectroscopy as 29.4% (St-HES29.4) and 60.3% (St-HES60.3). Moreover, the thermal and crystalline properties of native HES, St-HES29.4, and St-HES60.3 were analyzed using DSC and WAXS techniques, respectively. The DSC thermogram of HES and St-HES29.4 did not exhibit any melting endotherm and behaved like an amorphous polymer while St-HES60.3 showed a melting transition with a broad melting range of –7 °C to 29 °C and a melting point of 21.2 °C. The DSC results were further confirmed by WAXS experiments. The WAXS diffractograms demonstrated that both HES and St-HES29.4 were entirely amorphous in nature, showing no distinct Bragg reflections but rather a broad amorphous halo. On the contrary, St-HES60.3 displayed a strong reflection at $2\theta = 21.84°$ along with an amorphous halo, indicating the semicrystalline nature of the conjugate. By comparing the WAXS diffractograms of SA and St-HES60.3, findings suggested that the partial crystalline nature of St-HES60.3 originates from the stearate grafted side chains. Afterwards, St-HES29.4 and St-HES60.3 were used to form self-assembled micelles in an aqueous phase, resulting in a monodisperse particle size distribution with hydrodynamic diameters (D_h) of 130.7 nm and 152.5 nm, respectively. The morphology of the self-assembled micelles St-HES29.4 and St-HES60.3 was investigated by SEM. The experiment showed that both samples were nearly spherical in shape with a diameter (obtained from SEM images) of 99.8 nm and 119.4 nm, respectively, with the presence of some collapsed structures. The size of the micelles observed in the SEM measurements appeared smaller than the results obtained from the DLS analysis. The collapse structures and the smaller particle size of the micelles were due to the drying process of the SEM samples. In short, these results confirmed the successful conjugation of SA to HES to synthesize St-HES29.4 and St-HES60.3 conjugates which were able to self-assemble in the aqueous phase. These conjugates could be used in pharmaceutical drug delivery as a nanocarrier to load hydrophobic drugs and labile bioactive compounds with enhanced encapsulation efficiency, drug stability, and prolonged circulation time.

The third project focused on the synthesis and development of lipid-based nanocarrier as a promising alternative to polymer-based delivery systems. To achieve this, two established

approaches were combined, firstly, the dimerization of the drug to create a new dimeric entity, and secondly, to design of nanoemulsion preconcentrate as a carrier for the delivery of this dimeric entity. Initially, a dimeric artesunate glycerol monocaprylate conjugate (D-AS-GC) was synthesized by conjugating the antimalarial drug artesunate (AS) with a dimeric linker, glycerol monocaprylate (GC), using a simple esterification reaction to produce lipidic D-AS-GC conjugates. The structure of the initial reactants and the formed D-AS-GC conjugate were thoroughly characterized by ^{1}H NMR, APT ^{13}C NMR, 2D NMR COSY, HSQC, and HMBC spectroscopy. The integration value from the ^{1}H NMR spectrum of D-AS-GC conjugate demonstrated that two molecules of AS were successfully conjugated with GC through ester linkages. The molar mass of the D-AS-GC conjugate was determined using electrospray ionization time-of-flight mass spectroscopy (ESI-TOF MS), showing a major molecular ion peak at *m/z* 973.4775 $(M+Na)^{+}$, which further confirmed the successful synthesis of dimeric D-AS-GC entity. Subsequently, a series of D-AS-GC loaded nanoemulsion preconcentrate (F1–F6) was prepared composed of MCT (oil), Kolliphor HS15 (surfactant), and propylene glycol (cosurfactant) by varying the mass ratios and then evaluated by DLS following dilution with an aqueous phase. All formulations, except for F6, exhibited bimodal distributions in the DLS measurements. Formulation F6 displayed a clear nanoemulsion and a monomodal particle size distribution with a D_h of 19.1 nm and a very narrow PDI of 0.13. Therefore, F6 was selected as the optimal combination for the nanoemulsion formulation. The droplet size of F6 was further determined by two-dimensional diffusion-ordered nuclear magnetic resonance spectroscopy (DOSY NMR) and showed D_h values between 13–16 nm, close to the value obtained by DLS. Finally, the morphology of F6 was examined by AFM using two different substrates mica and silicon wafer. AFM analysis on the mica substrate indicated the presence of small droplets with dimensions ranging from approximately 10 to 50 nm, however, these droplets were difficult to resolve due to their soft or sticky nature, which could lead to artifacts and deformation during imaging. Consequently, AFM assessment on a silicon wafer displayed a distinct core-shell-like structure consisting of an inner core of drug molecules (D-AS-GC) surrounded by a distinct outer layer of MCT and Kolliphor HS15/propylene glycol. The droplet size was around 200 nm, much larger than those on the mica surface, likely due to the less polar silicon wafer, resulting in the formation of larger droplets through the evaporation-induced coalescence process. In conclusion, an optimized nanoemulsion was developed to deliver the lipidic D-AS-GC conjugates which could effectively enhance the *in vivo* half-life, extend circulation time, protect against drug

degradation, combat drug resistance of the antimalarial drug artesunate, and improve treatment outcomes.

5. Bibliography

1. Muñoz-Écija, T.; Vargas-Quesada, B.; Chinchilla-Rodríguez, Z. Identification and Visualization of the Intellectual Structure and the Main Research Lines in Nanoscience and Nanotechnology at the Worldwide Level. *J. Nanoparticle Res.* **2017**, *19*, 62.

2. Anucha, C.B.; Guénin, E. Micro and Nanotechnology. In *Biomaterials and Tissue Engineering*; Springer, 2023; pp. 131–174.

3. Sao, P.; Nath, D.; Priyadharshini, V.J. *Introduction to Nanoscience and Nanotechnology*; AG Publishing House (AGPH Books), 2010.

4. Joudeh, N.; Linke, D. Nanoparticle Classification, Physicochemical Properties, Characterization, and Applications: A Comprehensive Review for Biologists. *J. Nanobiotechnol.* **2022**, *20*, 262.

5. Doll, T.A.P.F.; Raman, S.; Dey, R.; Burkhard, P. Nanoscale Assemblies and Their Biomedical Applications. *J. R. Soc. Interface* **2013**, *10*, 20120740.

6. Mu, Q.; Jiang, G.; Chen, L.; Zhou, H.; Fourches, D.; Tropsha, A.; Yan, B. Chemical Basis of Interactions between Engineered Nanoparticles and Biological Systems. *Chem. Rev.* **2014**, *114*, 7740–7781.

7. Mitchell, M.J.; Billingsley, M.M.; Haley, R.M.; Wechsler, M.E.; Peppas, N.A.; Langer, R. Engineering Precision Nanoparticles for Drug Delivery. *Nat. Rev. Drug Discov.* **2021**, *20*, 101–124.

8. Mahmud, M.Z.A. A Concise Review of Nanoparticles Utilized Energy Storage and Conservation. *J. Nanomater.* **2023**, *2023*, 5432099.

9. Dhahi, T.S.; Dafhalla, A.K.Y.; Tayfour, O.E.; Mubarakali, A.; Alqahtani, A.S.; Ahmed, A.E.T.; Elobaid, M.E.; Adam, T.; Gopinath, S.C.B. Advances in Nano Sensors for Monitoring and Optimal Performance Enhancement in Photovoltaic Cells. *iScience 27,* **2024**.

10. Astruc, D. Introduction: Nanoparticles in Catalysis. *Chem. Rev.* 2020, *120*, 461–463.

11. Willner, M.R.; Vikesland, P.J. Nanomaterial Enabled Sensors for Environmental Contaminants. *J. Nanobiotechnol.* **2018**, *16*, 1–16.

12. Asghar, N.; Hussain, A.; Nguyen, D.A.; Ali, S.; Hussain, I.; Junejo, A.; Ali, A. Advancement in Nanomaterials for Environmental Pollutants Remediation: A Systematic Review on Bibliometrics Analysis, Material Types, Synthesis Pathways, and Related Mechanisms. *J. Nanobiotechnol.* **2024**, *22*, 26.

13. Barber, D.J.; Freestone, I.C. An Investigation of the Origin of the Colour of the Lycurgus Cup by Analytical Transmission Electron Microscopy. *Archaeometry* **1990**, *32*, 33–45.

14. Freestone, I.; Meeks, N.; Sax, M.; Higgitt, C. The Lycurgus Cup–A Roman Nanotechnology. *Gold Bull.* **2007**, *40*, 270–277.

15. Sciau, P. Nanoparticles in Ancient Materials: The Metallic Lustre Decorations of Medieval Ceramics. In *The delivery of nanoparticles*; INTECH Open Access Publisher London, 2012; pp. 525–540.

16. Schaming, D.; Remita, H. Nanotechnology: From the Ancient Time to Nowadays. *Found. Chem.* **2015**, *17*, 187–205.

17. Pradell, T.; Climent-Font, A.; Molera, J.; Zucchiatti, A.; Ynsa, M.D.; Roura, P.; Crespo, D. Metallic and Nonmetallic Shine in Luster: An Elastic Ion Backscattering Study. *J. Appl. Phys.* **2007**, *101*.

18. Faraday, M. X. The Bakerian Lecture—Experimental Relations of Gold (and Other Metals) to Light. *Philos. Trans. R. Soc. London* **1857**, 145–181.

19. Kleebe, H.-J.; Lauterbach, S.; Müller, M. Transmission Electron Microscopy (TEM). *Bunsenmagazin* **2010**, 168.

20. von Ardenne, M. On the History of Scanning Electron Microscopy, of the Electron Microprobe, and of Early Contributions to Transmission Electron Microscopy. In *The beginnings of electron microscopy*; Academic Press Orlando, 1985; Vol. 16, pp. 1–21.

21. Binnig, G.; Rohrer, H.; Gerber, C.; Weibel, E. Tunneling through a Controllable Vacuum Gap. *Appl. Phys. Lett.* **1982**, *40*, 178–180.

22. Binning, G.; Rohrer, H.; Gerber, C.; Weibel, E. Surface Studies by Scanning Tunneling Microscopy. In *Scanning tunneling microscopy*; Springer, 1982; pp. 31–35.

23. Binning, G.; Quate, C.F.; Gerber, C. Atomic Force Microscope. *Phys. Rev. Lett.* **1986**, *56*, 930.

24. Quate, C.F. The AFM as a Tool for Surface Imaging. *Surf. Sci.* **1994**, *299*, 980–995.

25. Feynman, R. There's Plenty of Room at the Bottom. In *Feynman and computation*; CRC Press, 2018; pp. 63–76.

26. Taniguchi, N. On the Basic Concept of "Nano-Technology". In Proceedings of the *International Conference on Production Engineering*. Tokyo. Part II.; Japan Society of Precision Engineering, 1974.

27. Drexler, E. *Engines of Creation: The Coming Era of Nanotechnology*; Anchor Press, NY, USA, 1987.

28. Nunes, D.; Pimentel, A.; Santos, L.; Barquinha, P.; Pereira, L.; Fortunato, E.; Martins, R. *Metal Oxide Nanostructures: Synthesis, Properties and Applications*; Elsevier, 2019; pp. 1–19.

29. Deshmukh, K. Nanotechnology in Ancient Era. In *Biotechnology Products in Everyday Life*; EcoProduction Book Series; Khoobchandani, M., Saxena, A. (Eds.); Springer International Publishing: Cham, Switzerland, 2019; pp. 119– 129.

30. Omran, B.A. Fundamentals of Nanotechnology and Nanobiotechnology. In *Nanobiotechnology: A Multidisciplinary Field of Science. Nanotechnology in the Life Sciences;* Springer: Cham, Switzerland, 2020; pp.1–36.

31. Cooper, E.L. From Darwin and Metchnikoff to Burnet and Beyond. *Trends Innate Immun.* **2008**, *15*, 1–11.

32. Ehrlich, P. Address in Pathology, On Chemiotherapy: Delivered before the Seventeenth International Congress of Medicine. *Br. Med. J.* **1913**, *2*, 353–359.

33. Drexler, K.E.; Peterson, C.; Pergamit, G. *Unbounding the Future: The Nanotechnology Revolution*. William Morrow and Company, NY, USA, **1991**.

34. Freitas, R.A. *Nanomedicine, Volume I: Basic Capabilities*; Landes Bioscience

Georgetown, TX, USA, 1999.

35. *European Science Foundation Forward Look Nanomedicine: An EMRC Consensus Opinion 2005. [(Accessed on 20 September 2024)]*.

36. Mirza, A.Z.; Siddiqui, F.A. Nanomedicine and Drug Delivery: A Mini Review. *Int. Nano Lett.* **2014**, *4*, 1–7.

37. Patra, J.K.; Das, G.; Fraceto, L.F.; Campos, E.V.R.; Rodriguez-Torres, M. del P.; Acosta-Torres, L.S.; Diaz-Torres, L.A.; Grillo, R.; Swamy, M.K.; Sharma, S. Nano Based Drug Delivery Systems: Recent Developments and Future Prospects. *J. Nanobiotechnol.* **2018**, *16*, 1–33.

38. Pelaz, B.; Alexiou, C.; Alvarez-Puebla, R.A.; Alves, F.; Andrews, A.M.; Ashraf, S.; Balogh, L.P.; Ballerini, L.; Bestetti, A.; Brendel, C. Diverse Applications of Nanomedicine. *ACS Nano* **2017**, *11*, 2313–2381.

39. Bangham, A.D.; Standish, M.M.; Watkins, J.C. Diffusion of Univalent Ions across the Lamellae of Swollen Phospholipids. *J. Mol. Biol.* **1965**, *13*, 238–252.

40. Ringsdorf, H. Structure and Properties of Pharmacologically Active Polymers. In Proceedings of the *Journal of Polymer Science: Polymer Symposia*; Wiley Online Library, 1975; Vol. 51, pp. 135–153.

41. Cheng, X.; Xie, Q.; Sun, Y. Advances in Nanomaterial-Based Targeted Drug Delivery Systems. *Front. Bioeng. Biotechnol.* **2023**, *11*, 1177151.

42. Krammer, F. SARS-CoV-2 Vaccines in Development. *Nature* **2020**, *586*, 516–527.

43. Chung, Y.H.; Beiss, V.; Fiering, S.N.; Steinmetz, N.F. COVID-19 Vaccine Frontrunners and Their Nanotechnology Design. *ACS Nano* **2020**, *14*, 12522–12537.

44. Pires, P.C.; Mascarenhas-Melo, F.; Pedrosa, K.; Lopes, D.; Lopes, J.; Macário-Soares, A.; Peixoto, D.; Giram, P.S.; Veiga, F.; Paiva-Santos, A.C. Polymer-Based Biomaterials for Pharmaceutical and Biomedical Applications: A Focus on Topical Drug Administration. *Eur. Polym. J.* **2023**, *187*, 111868.

45. Díaz-Montes, E. Polysaccharides: Sources, Characteristics, Properties, and Their Application in Biodegradable Films. *Polysaccharides* **2022**, *3*, 480–501.

46. Gomez d'Ayala, G.; Malinconico, M.; Laurienzo, P. Marine Derived Polysaccharides for Biomedical Applications: Chemical Modification Approaches. *Molecules* **2008**, *13*, 2069–2106.

47. Hovgaard, L.; Brondsted, H. Current Applications of Polysaccharides in Colon Targeting. *Crit. Rev. Ther. Drug Carr. Syst.* **1996**, *13*.

48. Miao, T.; Wang, J.; Zeng, Y.; Liu, G.; Chen, X. Polysaccharide-based Controlled Release Systems for Therapeutics Delivery and Tissue Engineering: From Bench to Bedside. *Adv. Sci.* **2018**, *5*, 1700513.

49. Visan, A.I.; Cristescu, R. Polysaccharide-Based Coatings as Drug Delivery Systems. *Pharmaceutics* **2023**, *15*, 2227.

50. Jamroży, M.; Kudłacik-Kramarczyk, S.; Drabczyk, A.; Krzan, M. Advanced Drug Carriers: A Review of Selected Protein, Polysaccharide, and Lipid Drug Delivery Platforms. *Int. J. Mol. Sci.* **2024**, *25*, 786.

51. Barclay, T.G.; Day, C.M.; Petrovsky, N.; Garg, S. Review of Polysaccharide Particle-Based Functional Drug Delivery. *Carbohydr. Polym.* **2019**, *221*, 94–112.

52. Klein, S. Polysaccharides in Oral Drug Delivery—Recent Applications and Future Perspectives. In *ACS Symposium Series*; American Chemical Society, Washington, DC, USA, 2009; pp. 13–30.

53. Wen, Y.; Oh, J.K. Recent Strategies to Develop Polysaccharide-based Nanomaterials for Biomedical Applications. *Macromol. Rapid Commun.* **2014**, *35*, 1819–1832.

54. Ren, Y.; Bai, Y.; Zhang, Z.; Cai, W.; Del Rio Flores, A. The Preparation and Structure Analysis Methods of Natural Polysaccharides of Plants and Fungi: A Review of Recent Development. *Molecules* **2019**, *24*, 3122.

55. Hey, T.; Knoller, H.; Vorstheim, P. Half-Life Extension through HESylation®. In *Therapeutic Proteins: Strategies to Modulate Their Plasma Half-Lives;* Kontermann, R., (Ed.)*;* Wiley-VCH Verlag Gmbh & Co. KGaA, Weinheim, Germany, 2012; pp. 117–140.

56. Pérez, S.; Bertoft, E. The Molecular Structures of Starch Components and Their Contribution to the Architecture of Starch Granules: A Comprehensive Review. *Starch-*

Stärke **2010**, *62*, 389–420.

57. Sommermeyer, K.; Cech, F.; Weidler, B.; Henning, K. Hydroxylethylstarch (HES) as Plasma Expander and Process for Preparing HES, Fresenius Kabi Deutschland GmbH, US Patent 5218108, 1993.

58. Agreda-Vásquez, G.P.; Espinosa-Poblano, I.; Sánchez-Guerrero, S.A.; Crespo-Solís, E.; Cabrera-Vásquez, S.; López-Salmorán, J.; Barajas, J.; Peñaloza-Ramírez, P.; Tirado-Cárdenas, N.; Velázquez, A. Starch and Albumin Mixture as Replacement Fluid in Therapeutic Plasma Exchange Is Safe and Effective. *J. Clin. Apher.* **2008**, *23*, 163–167.

59. Dellacherie, E. Polysaccharides in Oxygen-Carrier Blood Substitutes. In *Polysaccharides in Medicinal Applications*; Marcel Dekker, NY, USA, 2017; pp. 525–544.

60. Kozek-Langenecker, S.A. Effects of Hydroxyethyl Starch Solutions on Hemostasis. *J. Am. Soc. Anesthesiol.* **2005**, *103*, 654–660.

61. Noga, M.; Edinger, D.; Kläger, R.; Wegner, S. V; Spatz, J.P.; Wagner, E.; Winter, G.; Besheer, A. The Effect of Molar Mass and Degree of Hydroxyethylation on the Controlled Shielding and Deshielding of Hydroxyethyl Starch-Coated Polyplexes. *Biomaterials* **2013**, *34*, 2530–2538.

62. Gosch, C.I.; Haase, T.; Wolf, B.A.; Kulicke, W. Molar Mass Distribution and Size of Hydroxyethyl Starch Fractions Obtained by Continuous Polymer Fractionation. *Starch-Stärke* **2002**, *54*, 375–384.

63. Panov, A. V.; Traven, V.F.; Panov, V.P. Studying Conformations of Hydroxyethylated Starch Macromolecules. *Pharm. Chem. J.* **2004**, *38*, 680–686.

64. Kulicke, W.; Roessner, D.; Kull, W. Characterization of Hydroxyethyl Starch by Polymer Analysis for Use as a Plasma Volume Expander. *Starch-Stärke* **1993**, *45*, 445–450.

65. Jenkins, P.J.; Cameron, R.E.; Donald, A.M. A Universal Feature in the Structure of Starch Granules from Different Botanical Sources. *Starch-Stärke* **1993**, *45*, 417–420.

66. Treib, J.; Haass, A.; Pindur, G.; Grauer, M.T.; Wenzel, E.; Schimrigk, K. All Medium

Starches Are Not the Same: Influence of the Degree of Hydroxyethyl Substitution of Hydroxyethyl Starch on Plasma Volume, Hemorrheologic Conditions, and Coagulation. *Transfusion* **1996**, *36*, 450–455.

67. Treib, J.; Haass, A.; Pindur, G.; Treib, W.; Wenzel, E.; Schimrigk, K. Influence of Intravascular Molecular Weight of Hydroxyethyl Starch on Platelets. *Eur. J. Haematol.* **1996**, *56*, 168–172.

68. Stump, D.C.; Strauss, R.G.; Henriksen, R.A.; Petersen, R.E.; Saunders, R. Effects of Hydroxyethyl Starch on Blood Coagulation, Particularly Factor VIII. *Transfusion* **1985**, *25*, 349–354.

69. Schortgen, F.; Lacherade, J.-C.; Bruneel, F.; Cattaneo, I.; Hemery, F.; Lemaire, F.; Brochard, L. Effects of Hydroxyethylstarch and Gelatin on Renal Function in Severe Sepsis: A Multicentre Randomised Study. *Lancet* **2001**, *357*, 911–916.

70. Winkelmayer, W.C.; Glynn, R..; Levin, R.; Avorn, J. Hydroxyethyl Starch and Change in Renal Function in Patients Undergoing Coronary Artery Bypass Graft Surgery. *Kidney Int.* **2003**, *64*, 1046–1049.

71. Deman, A.; Peeters, P.; Sennesael, J. Hydroxyethyl Starch Does Not Impair Immediate Renal Function in Kidney Transplant Recipients: A Retrospective, Multicentre Analysis. *Nephrol. Dial. Transplant.* **1999**, *14*, 1517–1520.

72. Dehne, M.G.; Mühling, J.; Sablotzki, A.; Dehne, K.; Sucke, N.; Hempelmann, G. Hydroxyethyl Starch (HES) Does Not Directly Affect Renal Function in Patients with No Prior Renal Impairment. *J. Clin. Anesth.* **2001**, *13*, 103–111.

73. Perner, A.; Haase, N.; Guttormsen, A.B.; Tenhunen, J.; Klemenzson, G.; Åneman, A.; Madsen, K.R.; Møller, M.H.; Elkjær, J.M.; Poulsen, L.M. Hydroxyethyl Starch 130/0.42 versus Ringer's Acetate in Severe Sepsis. *N. Engl. J. Med.* **2012**, *367*, 124–134.

74. Wang, H.; Hu, H.; Yang, H.; Li, Z. Hydroxyethyl Starch Based Smart Nanomedicine. *RSC Adv.* **2021**, *11*, 3226–3240.

75. Tan, R.; Wan, Y.; Yang, X. Hydroxyethyl Starch and Its Derivatives as Nanocarriers for Delivery of Diagnostic and Therapeutic Agents towards Cancers. *Biomater. Transl.* **2020**, *1*, 46.

76. Sleightholm, R.; Yang, B.; Yu, F.; Xie, Y.; Oupicky, D. Chloroquine-Modified Hydroxyethyl Starch as a Polymeric Drug for Cancer Therapy. *Biomacromolecules* **2017**, *18*, 2247–2257.

77. Hu, H.; Li, Y.; Zhou, Q.; Ao, Y.; Yu, C.; Wan, Y.; Xu, H.; Li, Z.; Yang, X. Redox-Sensitive Hydroxyethyl Starch–Doxorubicin Conjugate for Tumor Targeted Drug Delivery. *ACS Appl. Mater. Interfaces* **2016**, *8*, 30833–30844.

78. Besheer, A.; Hause, G.; Kressler, J.; Mäder, K. Hydrophobically Modified Hydroxyethyl Starch: Synthesis, Characterization, and Aqueous Self-Assembly into Nano-Sized Polymeric Micelles and Vesicles. *Biomacromolecules* **2007**, *8*, 359–367.

79. Hore, R.; Rashid, H.; Syrowatka, F.; Kressler, J. Synthesis and Characterization of Self-Assembled Highly Stearate Grafted Hydroxyethyl Starch Conjugates. *Polysaccharide* **2024**, *5*, 142–157.

80. Paleos, C.M.; Sideratou, Z.; Tsiourvas, D. Drug Delivery Systems Based on Hydroxyethyl Starch. *Bioconjug. Chem.* **2017**, *28*, 1611–1624.

81. Kessler, C.; Greindl, A.; Breuer, B.; Haberl, U.; Rybka, A.; Emgenbroich, M.; Frank, H.-G.; Pötgens, A.J.G. Erythropoietin Mimetic Compound AGEM400 (HES) Binds to the Same Receptor as Erythropoietin but Displays a Different Spectrum of Activities. *Cytokine* **2012**, *57*, 226–237.

82. Liebner, R.; Mathaes, R.; Meyer, M.; Hey, T.; Winter, G.; Besheer, A. Protein HESylation for Half-Life Extension: Synthesis, Characterization and Pharmacokinetics of HESylated Anakinra. *Eur. J. Pharm. Biopharm.* **2014**, *87*, 378–385.

83. Hore, R.; Alaneed, R.; Pietzsch, M.; Kressler, J. Enzymatic HES Conjugation with Recombinant Human Erythropoietin via Variant Microbial Transglutaminase TG^{16}. *Starch-Stärke* **2022**, *74*, 2200034.

84. Seo, Y.; Lim, H.; Park, H.; Yu, J.; An, J.; Yoo, H.Y.; Lee, T. Recent Progress of Lipid Nanoparticles-Based Lipophilic Drug Delivery: Focus on Surface Modifications. *Pharmaceutics* **2023**, *15*, 772.

85. Fahy, E.; Cotter, D.; Sud, M.; Subramaniam, S. Lipid Classification, Structures and Tools. *Biochim. Biophys. Acta* **2011**, *1811*, 637–647.

86. Battaglia, L.; Serpe, L.; Foglietta, F.; Muntoni, E.; Gallarate, M.; Del Pozo Rodriguez, A.; Solinis, M.A. Application of Lipid Nanoparticles to Ocular Drug Delivery. *Expert Opin. Drug Deliv.* **2016**, *13*, 1743–1757.

87. Shrivastava, P.; Gautam, L.; Jain, A.; Vishwakarma, N.; Vyas, S.; Vyas, S.P. Lipid Drug Conjugates for Improved Therapeutic Benefits. *Curr. Pharm. Des.* **2020**, *26*, 3187–3202.

88. Couvreur, P.; Reddy, L.H.; Mangenot, S.; Poupaert, J.H.; Desmaële, D.; Lepêtre-Mouelhi, S.; Pili, B.; Bourgaux, C.; Amenitsch, H.; Ollivon, M. Discovery of New Hexagonal Supramolecular Nanostructures Formed by Squalenoylation of an Anticancer Nucleoside Analogue. *Small* **2008**, *4*, 247–253.

89. Irby, D.; Du, C.; Li, F. Lipid–Drug Conjugate for Enhancing Drug Delivery. *Mol. Pharm.* **2017**, *14*, 1325–1338.

90. Date, T.; Paul, K.; Singh, N.; Jain, S. Drug–Lipid Conjugates for Enhanced Oral Drug Delivery. *AAPS Pharmscitech* **2019**, *20*, 41.

91. Sarheed, O.; Dibi, M.; Ramesh, K.V. Studies on the Effect of Oil and Surfactant on the Formation of Alginate-Based O/W Lidocaine Nanocarriers Using Nanoemulsion Template. *Pharmaceutics* **2020**, *12*, 1223.

92. Gabizon, A.; Amitay, Y.; Tzemach, D.; Gorin, J.; Shmeeda, H.; Zalipsky, S. Therapeutic Efficacy of a Lipid-Based Prodrug of Mitomycin C in Pegylated Liposomes: Studies with Human Gastro-Entero-Pancreatic Ectopic Tumor Models. *J. Control. Release* **2012**, *160*, 245–253.

93. Sarpietro, M.G.; Ottimo, S.; Paolino, D.; Ferrero, A.; Dosio, F.; Castelli, F. Squalenoyl Prodrug of Paclitaxel: Synthesis and Evaluation of Its Incorporation in Phospholipid Bilayers. *Int. J. Pharm.* **2012**, *436*, 135–140.

94. Hore, R.; Hasan, N.; Mäder, K.; Kressler, J. Synthesis and Characterization of Dimeric Artesunate Glycerol Monocaprylate Conjugate and Formulation of Nanoemulsion Preconcentrate. *Molecules* **2023**, *28*, 5208.

95. Alinezhad, H.; Yavari, H.; Salehian, F. Recent Advances in Reductive Amination Catalysis and Its Applications. *Curr. Org. Chem.* **2015**, *19*, 1021–1049.

96. Afanasyev, O.I.; Kuchuk, E.; Usanov, D.L.; Chusov, D. Reductive Amination in the Synthesis of Pharmaceuticals. *Chem. Rev.* **2019**, *119*, 11857–11911.

97. Smith, M.B. *March's Advanced Organic Chemistry: Reactions, Mechanisms, and Structure*; John Wiley & Sons, NJ, USA, 2007; pp. 518– 519.

98. Gusak, K.N.; Ignatovich, Z. V; Koroleva, E.V. New Potential of the Reductive Alkylation of Amines. *Russ. Chem. Rev.* **2015**, *84*, 288.

99. Tarasevich, V.A.; Kozlov, N.G. Reductive Amination of Oxygen-Containing Organic Compounds. *Russ. Chem. Rev.* **1999**, *68*, 55–72.

100. Abdel-Magid, A.F.; Carson, K.G.; Harris, B.D.; Maryanoff, C.A.; Shah, R.D. Reductive Amination of Aldehydes and Ketones with Sodium Triacetoxyborohydride. Studies on Direct and Indirect Reductive Amination Procedures[1]. *J. Org. Chem.* **1996**, *61*, 3849–3862.

101. Dalpathado, D.S.; Jiang, H.; Kater, M.A.; Desaire, H. Reductive Amination of Carbohydrates Using $NaBH(OAc)_3$. *Anal. Bioanal. Chem.* **2005**, *381*, 1130–1137.

102. Clemente, F.; Matassini, C.; Cardona, F. Reductive Amination Routes in the Synthesis of Piperidine Iminosugars. *European J. Org. Chem.* **2020**, *2020*, 4447–4462.

103. Ward, J.; Wohlgemuth, R. High-Yield Biocatalytic Amination Reactions in Organic Synthesis. *Curr. Org. Chem.* **2010**, *14*, 1914–1927.

104. Chen, X.; Zhu, Q.; Li, Z.; Yan, H.; Lin, Q. The Molecular Structure and Self-Assembly Behavior of Reductive Amination of Oxidized Alginate Derivative for Hydrophobic Drug Delivery. *Molecules* **2021**, *26*, 5821.

105. Jing, Z.-W.; Ma, Z.-W.; Li, C.; Jia, Y.-Y.; Luo, M.; Ma, X.-X.; Zhou, S.-Y.; Zhang, B.-L. Chitosan Cross-Linked with Poly(Ethylene Glycol) Dialdehyde via Reductive Amination as Effective Controlled Release Carriers for Oral Protein Drug Delivery. *Bioorg. Med. Chem. Lett.* **2017**, *27*, 1003–1006.

106. Xie, C.; Song, J.; Hua, M.; Hu, Y.; Huang, X.; Wu, H.; Yang, G.; Han, B. Ambient-Temperature Synthesis of Primary Amines via Reductive Amination of Carbonyl Compounds. *ACS Catal.* **2020**, *10*, 7763–7772.

107. He, J.; Chen, L.; Liu, S.; Song, K.; Yang, S.; Riisager, A. Sustainable Access to

Renewable N-Containing Chemicals from Reductive Amination of Biomass-Derived Platform Compounds. *Green Chem.* **2020**, *22*, 6714–6747.

108. Yan, L.; Wang, G.; Xiang, D.; Zhang, Y.; Deng, W. Reductive Amination of Bio-Platform Molecules to Nitrogen-Containing Chemicals. *Carb. Neutrality* **2024**, *3*, 24.

109. Martins, S.I.F.S.; Jongen, W.M.F.; Van Boekel, M.A.J.S. A Review of Maillard Reaction in Food and Implications to Kinetic Modelling. *Trends Food Sci. Technol.* **2000**, *11*, 364–373.

110. Vhangani, L.N.; Van Wyk, J. Antioxidant Activity of Maillard Reaction Products (MRPs) Derived from Fructose–Lysine and Ribose–Lysine Model Systems. *Food Chem.* **2013**, *137*, 92–98.

111. Di Lorenzo, C.; Colombo, F.; Biella, S.; Stockley, C.; Restani, P. Polyphenols and Human Health: The Role of Bioavailability. *Nutrients* **2021**, *13*, 273.

112. Bruhns, P.; Kanzler, C.; Degenhardt, A.G.; Koch, T.J.; Kroh, L.W. Basic Structure of Melanoidins Formed in the Maillard Reaction of 3-Deoxyglucosone and γ-Aminobutyric Acid. *J. Agric. Food Chem.* **2019**, *67*, 5197–5203.

113. Maillard, L.C. Reaction of Amino Acids on Sugars: Formation of Melanoidins by a Systematic Way. *Compt. Rend. Acad. Sci.* **1912**, *154*, 66–68.

114. Hodge, J.E. Dehydrated Foods, Chemistry of Browning Reactions in Model Systems. *J. Agric. Food Chem.* **1953**, *1*, 928–943.

115. Aalaei, K.; Rayner, M.; Sjöholm, I. Chemical Methods and Techniques to Monitor Early Maillard Reaction in Milk Products; A Review. *Crit. Rev. Food Sci. Nutr.* **2019**, *59*, 1829–1839.

116. Oliver, C.M.; Melton, L.D.; Stanley, R.A. Creating Proteins with Novel Functionality via the Maillard Reaction: A Review. *Crit. Rev. Food Sci. Nutr.* **2006**, *46*, 337–350.

117. Brands, C.M.J.; van Boekel, M.A.J.S. Kinetic Modeling of Reactions in Heated Monosaccharide− Casein Systems. *J. Agric. Food Chem.* **2002**, *50*, 6725–6739.

118. Coca, M.; García, M.T.; González, G.; Peña, M.; García, J.A. Study of Coloured Components Formed in Sugar Beet Processing. *Food Chem.* **2004**, *86*, 421–433.

119. Deng, W.; Li, J.; Yao, P.; He, F.; Huang, C. Green Preparation Process, Characterization and Antitumor Effects of Doxorubicin–BSA–Dextran Nanoparticles. *Macromol. Biosci.* **2010**, *10*, 1224–1234.

120. ALjahdali, N.; Carbonero, F. Impact of Maillard Reaction Products on Nutrition and Health: Current Knowledge and Need to Understand Their Fate in the Human Digestive System. *Crit. Rev. Food Sci. Nutr.* **2019**, *59*, 474–487.

121. Tamanna, N.; Mahmood, N. Food Processing and Maillard Reaction Products: Effect on Human Health and Nutrition. *Int. J. Food Sci.* **2015**, *2015*, 526762.

122. Al-Hakkak, J.; Al-Hakkak, F. Functional Egg White–Pectin Conjugates Prepared by Controlled Maillard Reaction. *J. Food Eng.* **2010**, *100*, 152–159.

123. Al-Hakkak, J.; Kavale, S. Improvement of Emulsification Properties of Sodium Caseinate by Conjugating to Pectin through the Maillard Reaction. In Proceedings of the *International Congress Series*; Elsevier, 2002; Vol. 1245, pp. 491–499.

124. Zhang, H.; Zhang, Y.; Bao, E.; Zhao, Y. Preparation, Characterization and Toxicology Properties of α-and β-Chitosan Maillard Reaction Products Nanoparticles. *Int. J. Biol. Macromol.* **2016**, *89*, 287–296.

125. Edelman, R.; Assaraf, Y.G.; Levitzky, I.; Shahar, T.; Livney, Y.D. Hyaluronic Acid-Serum Albumin Conjugate-Based Nanoparticles for Targeted Cancer Therapy. *Oncotarget* **2017**, *8*, 24337.

126. Wang, T.; Xue, J.; Hu, Q.; Zhou, M.; Chang, C.; Luo, Y. Synthetic Surfactant-and Cross-Linker-Free Preparation of Highly Stable Lipid-Polymer Hybrid Nanoparticles as Potential Oral Delivery Vehicles. *Sci. Rep.* **2017**, *7*, 2750.

127. Li, J.; Yao, P. Self-Assembly of Ibuprofen and Bovine Serum Albumin− Dextran Conjugates Leading to Effective Loading of the Drug. *Langmuir* **2009**, *25*, 6385–6391.

128. Khoder, M.; Gbormoi Sr, H.K.; Ryan, A.; Karam, A.; Alany, R.G. Potential Use of the Maillard Reaction for Pharmaceutical Applications: Gastric and Intestinal Controlled Release Alginate-Albumin Beads. *Pharmaceutics* **2019**, *11*, 83.

129. Feng, J.; Wu, S.; Wang, H.; Liu, S. Improved Bioavailability of Curcumin in Ovalbumin-Dextran Nanogels Prepared by Maillard Reaction. *J. Funct. Foods* **2016**,

27, 55–68.

130. Li, Z.; Gu, L. Fabrication of Self-Assembled (−)-Epigallocatechin Gallate (EGCG) Ovalbumin–Dextran Conjugate Nanoparticles and Their Transport across Monolayers of Human Intestinal Epithelial Caco-2 Cells. *J. Agric. Food Chem.* **2014**, *62*, 1301–1309.

131. Bertozzi, C.R. A Decade of Bioorthogonal Chemistry. *Acc. Chem. Res.* **2011**, *44*, 651–653.

132. Yoon, H.Y.; Koo, H.; Kim, K.; Kwon, I.C. Molecular Imaging Based on Metabolic Glycoengineering and Bioorthogonal Click Chemistry. *Biomaterials* **2017**, *132*, 28–36.

133. Kolb, H.C.; Finn, M.G.; Sharpless, K.B. Click Chemistry: Diverse Chemical Function from a Few Good Reactions. *Angew. Chemie Int. Ed.* **2001**, *40*, 2004–2021.

134. Kolb, H.C.; Sharpless, K.B. The Growing Impact of Click Chemistry on Drug Discovery. *Drug Discov. Today* **2003**, *8*, 1128–1137.

135. Lutz, J. 1, 3-Dipolar Cycloadditions of Azides and Alkynes: A Universal Ligation Tool in Polymer and Materials Science. *Angew. Chemie Int. Ed.* **2007**, *46*, 1018–1025.

136. Sahariah, P.; Sørensen, K.K.; Hjálmarsdóttir, M.A.; Sigurjónsson, Ó.E.; Jensen, K.J.; Másson, M.; Thygesen, M.B. Antimicrobial Peptide Shows Enhanced Activity and Reduced Toxicity upon Grafting to Chitosan Polymers. *Chem. Commun.* **2015**, *51*, 11611–11614.

137. Xiao, Y.; Chinoy, Z.S.; Pecastaings, G.; Bathany, K.; Garanger, E.; Lecommandoux, S. Design of Polysaccharide-b-Elastin-Like Polypeptide Bioconjugates and Their Thermoresponsive Self-Assembly. *Biomacromolecules* **2020**, *21*, 114–125.

138. Jiang, X.; Hao, X.; Jing, L.; Wu, G.; Kang, D.; Liu, X.; Zhan, P. Recent Applications of Click Chemistry in Drug Discovery. *Expert Opin. Drug Discov.* **2019**, *14*, 779–789.

139. García-Astrain, C.; Avérous, L. Synthesis and Evaluation of Functional Alginate Hydrogels Based on Click Chemistry for Drug Delivery Applications. *Carbohydr. Polym.* **2018**, *190*, 271–280.

140. Yi, G.; Son, J.; Yoo, J.; Park, C.; Koo, H. Application of Click Chemistry in Nanoparticle Modification and Its Targeted Delivery. *Biomater. Res.* **2018**, *22*, 1–8.

141. Rostovtsev, V. V.; Green, L.G.; Fokin, V. V.; Sharpless, K.B. A Stepwise Huisgen Cycloaddition Process: Copper(I)-Catalyzed Regioselective “Ligation” of Azides and Terminal Alkynes. *Angew. Chemie Int. Ed.* **2002**, *41*, 2596–2599.

142. Lallana, E.; Sousa-Herves, A.; Fernandez-Trillo, F.; Riguera, R.; Fernandez-Megia, E. Click Chemistry for Drug Delivery Nanosystems. *Pharm. Res.* **2012**, *29*, 1–34.

143. Sahyoun, T.; Arrault, A.; Schneider, R. Amidoximes and Oximes: Synthesis, Structure, and Their Key Role as No Donors. *Molecules* **2019**, *24*.

144. Schiff, H. Mittheilungen Aus Dem Universitätslaboratorium in Pisa: Eine Neue Reihe Organischer Basen. *Justus Liebigs Ann. Chem.* **1864**, *131*, 118–119.

145. Belowich, M.E.; Stoddart, J.F. Dynamic Imine Chemistry. *Chem. Soc. Rev.* **2012**, *41*, 2003–2024.

146. Sander, E.G.; Jencks, W.P. Equilibria for Additions to the Carbonyl Group. *J. Am. Chem. Soc.* **1968**, *90*, 6154–6162.

147. Jencks, W.P. Studies on the Mechanism of Oxime and Semicarbazone Formation. *J. Am. Chem. Soc.* **1959**, *81*, 475–481.

148. Gauthier, M.A.; Klok, H.-A. Peptide/Protein–Polymer Conjugates: Synthetic Strategies and Design Concepts. *Chem. Commun.* **2008**, 2591–2611.

149. Tinge, J.; Groothaert, M.; op het Veld, H.; Ritz, J.; Fuchs, H.; Kieczka, H.; Moran, W.C. *Ullmann’s Encyclopedia of Industrial Chemistry. Caprolactam*; Wiley-VCH Verlag Gmbh & Co. KGaA: Weinheim, Germany, 2018.

150. Mackenzie, K.J.; Francis, M.B. Recyclable Thermoresponsive Polymer–Cellulase Bioconjugates for Biomass Depolymerization. *J. Am. Chem. Soc.* **2013**, *135*, 293–300.

151. Venkatesan, N.; Kim, B.H. Peptide Conjugates of Oligonucleotides: Synthesis and Applications. *Chem. Rev.* **2006**, *106*, 3712–3761.

152. Singh, Y.; Murat, P.; Defrancq, E. Recent Developments in Oligonucleotide Conjugation. *Chem. Soc. Rev.* **2010**, *39*, 2054–2070.

153. Kochendoerfer, G.G.; Chen, S.-Y.; Mao, F.; Cressman, S.; Traviglia, S.; Shao, H.; Hunter, C.L.; Low, D.W.; Cagle, E.N.; Carnevali, M. Design and Chemical Synthesis

of a Homogeneous Polymer-Modified Erythropoiesis Protein. *Science* **2003**, *299*, 884–887.

154. Michael, A. On the Addition of Sodium Acetacetic Ether and Analogous Sodium Compounds to Unsaturated Organic Ethers. *Am. Chem. J.* **1887**, *9*, 115.

155. Bergmann, E.D.; Ginsburg, D.; Pappo, R. The Michael Reaction. *Org. React.* **1959**, *10*, 179–556.

156. Little, R.D.; Masjedizadeh, M.R.; Wallquist, O.; Mcloughlin, J.I. The Intramolecular Michael Reaction. *Org. React.* **2004**, *47*, 315–552.

157. Jung, M.E. Stabilized Nucleophiles with Electron Deficient Alkenes and Alkynes. *Compr. Org. Synth.* **1991**, 1–67.

158. Michael, A. Ueber Die Addition von Natriumacetessig-und Natriummalonsäureäthern Zu Den Aethern Ungesättigter Säuren. *J. für Prakt. Chemie* **1887**, *35*, 349–356.

159. Connor, R.; McClellan, W.R. The Michael Condensation. V. The Influence of the Experimental Conditions and the Structure of the Acceptor upon the Condensation. *J. Org. Chem.* **1939**, *3*, 570–577

160. Vernon, B.; Tirelli, N.; Bächi, T.; Haldimann, D.; Hubbell, J.A. Water-borne, *in Situ* Crosslinked Biomaterials from Phase-segregated Precursors. *J. Biomed. Mater. Res.* **2003**, *64A*, 447–456.

161. Mather, B.D.; Viswanathan, K.; Miller, K.M.; Long, T.E. Michael Addition Reactions in Macromolecular Design for Emerging Technologies. *Prog. Polym. Sci.* **2006**, *31*, 487–531.

162. Chen, J.; Ma, X.; Edgar, K.J. A Versatile Method for Preparing Polysaccharide Conjugates via Thiol-Michael Addition. *Polymers* **2021**, *13*, 1905.

163. Garcia, D.R.; Lavignac, N. Poly(Amidoamine)–BSA Conjugates Synthesised by Michael Addition Reaction Retained Enzymatic Activity. *Polym. Chem.* **2016**, *7*, 7223–7229.

164. Nair, D.P.; Podgorski, M.; Chatani, S.; Gong, T.; Xi, W.; Fenoli, C.R.; Bowman, C.N. The Thiol-Michael Addition Click Reaction: A Powerful and Widely Used Tool in Materials Chemistry. *Chem. Mater.* **2014**, *26*, 724–744.

165. Liu, X.; Gao, W. Precision Conjugation: An Emerging Tool for Generating Protein–Polymer Conjugates. *Angew. Chemie Int. Ed.* **2021**, *60*, 11024–11035.

166. Staudinger, H.; Meyer, J. Über Neue Organische Phosphorverbindungen III. Phosphinmethylenderivate Und Phosphinimine. *Helv. Chim. Acta* **1919**, *2*, 635–646.

167. Gololobov, Y.G.; Kasukhin, L.F. Recent Advances in the Staudinger Reaction. *Tetrahedron* **1992**, *48*, 1353–1406.

168. Leffler, J.E.; Temple, R.D. Staudinger Reaction between Triarylphosphines and Azides. Mechanism. *J. Am. Chem. Soc.* **1967**, *89*, 5235–5246.

169. Sletten, E.M.; Bertozzi, C.R. From Mechanism to Mouse: A Tale of Two Bioorthogonal Reactions. *Acc. Chem. Res.* **2011**, *44*, 666–676.

170. Saxon, E.; Bertozzi, C.R. Cell Surface Engineering by a Modified Staudinger Reaction. *Science* **2000**, *287*, 2007–2010.

171. Bednarek, C.; Wehl, I.; Jung, N.; Schepers, U.; Bräse, S. The Staudinger Ligation. *Chem. Rev.* **2020**, *120*, 4301–4354.

172. Prescher, J.A.; Dube, D.H.; Bertozzi, C.R. Chemical Remodelling of Cell Surfaces in Living Animals. *Nature* **2004**, *430*, 873–877.

173. Jacobs, C.L.; Goon, S.; Yarema, K.J.; Hinderlich, S.; Hang, H.C.; Chai, D.H.; Bertozzi, C.R. Substrate Specificity of the Sialic Acid Biosynthetic Pathway. *Biochemistry* **2001**, *40*, 12864–12874.

174. Dube, D.H.; Prescher, J.A.; Quang, C.N.; Bertozzi, C.R. Probing Mucin-Type O-Linked Glycosylation in Living Animals. *Proc. Natl. Acad. Sci.* **2006**, *103*, 4819–4824.

175. Nguyen, U.T.T.; Cramer, J.; Gomis, J.; Reents, R.; Gutierrez-Rodriguez, M.; Goody, R.S.; Alexandrov, K.; Waldmann, H. Exploiting the Substrate Tolerance of Farnesyltransferase for Site-selective Protein Derivatization. *ChemBioChem* **2007**, *8*, 408–423.

176. Kostiuk, M.A.; Corvi, M.M.; Keller, B.O.; Plummer, G.; Prescher, J.A.; Hangauer, M.J.; Bertozzi, C.R.; Rajaiah, G.; Falck, J.R.; Berthiaume, L.G. Identification of Palmitoylated Mitochondrial Proteins Using a Bio-Orthogonal Azido-Palmitate Analogue. *FASEB J.* **2008**, *22*, 721.

177. Hang, H.C.; Geutjes, E.-J.; Grotenbreg, G.; Pollington, A.M.; Bijlmakers, M.J.; Ploegh, H.L. Chemical Probes for the Rapid Detection of Fatty-Acylated Proteins in Mammalian Cells. *J. Am. Chem. Soc.* **2007**, *129*, 2744–2745.

178. Slavoff, S.A.; Chen, I.; Choi, Y.-A.; Ting, A.Y. Expanding the Substrate Tolerance of Biotin Ligase through Exploration of Enzymes from Diverse Species. *J. Am. Chem. Soc.* **2008**, *130*, 1160–1162.

179. Hosoya, T.; Hiramatsu, T.; Ikemoto, T.; Aoyama, H.; Ohmae, T.; Endo, M.; Suzuki, M. Design of Dantrolene-Derived Probes for Radioisotope-Free Photoaffinity Labeling of Proteins Involved in the Physiological Ca^{2+} Release from Sarcoplasmic Reticulum of Skeletal Muscle. *Bioorg. Med. Chem. Lett.* **2005**, *15*, 1289–1294.

180. Verdoes, M.; Florea, B.I.; Hillaert, U.; Willems, L.I.; Van Der Linden, W.A.; Sae-Heng, M.; Filippov, D. V; Kisselev, A.F.; Van Der Marel, G.A.; Overkleeft, H.S. Azido-BODIPY Acid Reveals Quantitative Staudinger–Bertozzi Ligation in Two-Step Activity-Based Proteasome Profiling. *Chembiochem* **2008**, *9*, 1735.

181. Winz, M.-L.; Linder, E.C.; André, T.; Becker, J.; Jäschke, A. Nucleotidyl Transferase Assisted DNA Labeling with Different Click Chemistries. *Nucleic Acids Res.* **2015**, *43*, e110.

182. Wu, C.; Kurinomaru, T. Development of the Bioluminescent Immunoassay for the Detection of 5-Hydroxymethylcytosine in Dinoflagellate. *Anal. Sci.* **2019**, *35*, 301–305.

183. Weisbrod, S.H.; Baccaro, A.; Marx, A. DNA Conjugation by Staudinger Ligation. *Nucleic Acids Symp. Ser.* **2008**, *52*, 383–384.

184. Andersen, K.A.; Raines, R.T. Creating Site-Specific Isopeptide Linkages between Proteins with the Traceless Staudinger Ligation. *Pept. Libr. Methods Protoc.* **2015**, *1248*, 55–65.

185. Serwa, R.; Wilkening, I.; Del Signore, G.; Mühlberg, M.; Claußnitzer, I.; Weise, C.; Gerrits, M.; Hackenberger, C.P.R. Chemoselective Staudinger-phosphite Reaction of Azides for the Phosphorylation of Proteins. *Angew. Chemie Int. Ed.* **2009**, *48*, 8234–8239.

186. Nilsson, B.L.; Kiessling, L.L.; Raines, R.T. Staudinger Ligation: A Peptide from a Thioester and Azide. *Org. Lett.* **2000**, *2*, 1939–1941.

187. Schilling, C.I.; Jung, N.; Biskup, M.; Schepers, U.; Bräse, S. Bioconjugation via Azide–Staudinger Ligation: An Overview. *Chem. Soc. Rev.* **2011**, *40*, 4840–4871.

188. Köhn, M.; Wacker, R.; Peters, C.; Schröder, H.; Soulère, L.; Breinbauer, R.; Niemeyer, C.M.; Waldmann, H. Staudinger Ligation: A New Immobilization Strategy for the Preparation of Small-molecule Arrays. *Angew. Chemie Int. Ed.* **2003**, *42*, 5830–5834.

189. Köhn, M. Immobilization Strategies for Small Molecule, Peptide and Protein Microarrays. *J. Pept. Sci.* **2009**, *15*, 393–397.

190. Stabler, C.L.; Sun, X.-L.; Cui, W.; Wilson, J.T.; Haller, C.A.; Chaikof, E.L. Surface Re-Engineering of Pancreatic Islets with Recombinant Azido-Thrombomodulin. *Bioconjug. Chem.* **2007**, *18*, 1713–1715.

191. Kalia, J.; Abbott, N.L.; Raines, R.T. General Method for Site-Specific Protein Immobilization by Staudinger Ligation. *Bioconjug. Chem.* **2007**, *18*, 1064–1069.

192. Yanagisawa, T.; Ishii, R.; Fukunaga, R.; Kobayashi, T.; Sakamoto, K.; Yokoyama, S. Multistep Engineering of Pyrrolysyl-TRNA Synthetase to Genetically Encode N^{ε}-(o-Azidobenzyloxycarbonyl) Lysine for Site-Specific Protein Modification. *Chem. Biol.* **2008**, *15*, 1187–1197.

193. Azoulay, M.; Tuffin, G.; Sallem, W.; Florent, J.-C. A New Drug-Release Method Using the Staudinger Ligation. *Bioorg. Med. Chem. Lett.* **2006**, *16*, 3147–3149.

194. Parkhouse, S.M.; Garnett, M.C.; Chan, W.C. Targeting of Polyamidoamine–DNA Nanoparticles Using the Staudinger Ligation: Attachment of an RGD Motif Either before or after Complexation. *Bioorg. Med. Chem.* **2008**, *16*, 6641–6650.

195. Miyaura, N.; Suzuki, A. Palladium-Catalyzed Cross-Coupling Reactions of Organoboron Compounds. *Chem. Rev.* **1995**, *95*, 2457–2483.

196. Miyaura, N.; Yamada, K.; Suzuki, A. A New Stereospecific Cross-Coupling by the Palladium-Catalyzed Reaction of 1-Alkenylboranes with 1-Alkenyl or 1-Alkynyl Halides. *Tetrahedron Lett.* **1979**, *20*, 3437–3440.

197. Miyaura, N.; Buchwald, S.L. *Cross-Coupling Reactions: A Practical Guide*; Springer, Berlin, Germany, 2002.

198. Tsuji, J.; Williams, J. *Palladium Reagents and Catalysts*. Wiley, Chichester, UK, 2004.

199. Meijere, A. de; Diederich, F. *Metal-Catalyzed Cross-Coupling Reactions*. Wiley-VCH, Weinheim, Germany, 2004.

200. Negishi, E. *Handbook of Organopalladium Chemistry for Organic Synthesis*. Wiley-VCH, Weinheim, Germany, 2002.

201. Willemse, T.; Schepens, W.; van Vlijmen, H.W.T.; Maes, B.U.W.; Ballet, S. The Suzuki–Miyaura Cross-Coupling as a Versatile Tool for Peptide Diversification and Cyclization. *Catalysts* **2017**, *7*, 74.

202. Gruß, H.; Sewald, N. Late-stage Diversification of Tryptophan-derived Biomolecules. *Chem. Eur. J.* **2020**, *26*, 5328–5340.

203. Roy, A.D.; Goss, R.J.M.; Wagner, G.K.; Winn, M. Development of Fluorescent Aryltryptophans by Pd Mediated Cross-Coupling of Unprotected Halotryptophans in Water. *Chem. Commun.* **2008**, *39*, 4831–4833.

204. Chalker, J.M.; Wood, C.S.C.; Davis, B.G. A Convenient Catalyst for Aqueous and Protein Suzuki− Miyaura Cross-Coupling. *J. Am. Chem. Soc.* **2009**, *131*, 16346–16347.

205. Sabadasch, V.; Dachwitz, S.; Hannappel, Y.; Hellweg, T.; Sewald, N. Acrylamide-Based Pd-Nanoparticle Carriers as Smart Catalysts for the Suzuki–Miyaura Cross-Coupling of Amino Acids. *Synthesis* **2022**, *54*, 3180–3192.

206. Hooshmand, S.E.; Heidari, B.; Sedghi, R.; Varma, R.S. Recent Advances in the Suzuki–Miyaura Cross-Coupling Reaction Using Efficient Catalysts in Eco-Friendly Media. *Green Chem.* **2019**, *21*, 381–405.

207. Dumas, A.; Spicer, C.D.; Gao, Z.; Takehana, T.; Lin, Y.A.; Yasukohchi, T.; Davis, B.G. Self-Liganded Suzuki-Miyaura Coupling for Site-Selective Protein PEGylation. *Angew. Chemie Int. Ed.* **2013**, *52*, 3916–3921.

208. Buskes, M.J.; Blanco, M.-J. Impact of Cross-Coupling Reactions in Drug Discovery and Development. *Molecules* **2020**, *25*, 3493.

209. Munawar, S.; Zahoor, A.F.; Hussain, S.M.; Ahmad, S.; Mansha, A.; Parveen, B.; Ali, K.G.; Irfan, A. Steglich Esterification: A Versatile Synthetic Approach toward the Synthesis of Natural Products, Their Analogues/Derivatives. *Heliyon* **2024**, *10*, e23416.

210. Hermanson, G.T. *Bioconjugate Techniques*; 3rd ed.; Academic Press, Boston, USA

2013.

211. Bauminger, S.; Wilchek, M. The Use of Carbodiimides in the Preparation of Immunizing Conjugates. *Methods Enzymol.* **1980**, 70, 151–159.

212. Sheehan, J.; Cruickshank, P.; Boshart, G. A Convenient Synthesis of Water-Soluble Carbodiimides. *J. Org. Chem.* **1961**, *26*, 2525–2528.

213. Chapelle, C.; David, G.; Caillol, S.; Negrell, C.; Desroches Le Foll, M. Advances in Chitooligosaccharides Chemical Modifications. *Biopolymers* **2021**, *112*, e23461.

214. Javia, A.; Vanza, J.; Bardoliwala, D.; Ghosh, S.; Misra, L.A.; Patel, M.; Thakkar, H. Polymer-Drug Conjugates: Design Principles, Emerging Synthetic Strategies and Clinical Overview. *Int. J. Pharm.* **2022**, *623*, 121863.

215. Cammarata, C.R.; Hughes, M.E.; Ofner, C.M. Carbodiimide Induced Cross-Linking, Ligand Addition, and Degradation in Gelatin. *Mol. Pharm.* **2015**, *12*, 783–793.

216. Dallmann, H.G.; Flynn, T.G.; Dunn, S.D. Determination of the 1-Ethyl-3-[(3-Dimethylamino) Propyl]-Carbodiimide-Induced Cross-Link between the Beta and Epsilon Subunits of Escherichia Coli F1-ATPase. *J. Biol. Chem.* **1992**, *267*, 18953–18960.

217. Gao, Y.; Kyratzis, I. Covalent Immobilization of Proteins on Carbon Nanotubes Using the Cross-Linker 1-Ethyl-3-(3-Dimethylaminopropyl)Carbodiimide—A Critical Assessment. *Bioconjug. Chem.* 2008, *19*, 1945–1950.

218. Camacho, K.M.; Menegatti, S.; Mitragotri, S. Low-Molecular-Weight Polymer–Drug Conjugates for Synergistic Anticancer Activity of Camptothecin and Doxorubicin Combinations. *Nanomedicine* **2016**, *11*, 1139–1151.

219. Liu, Y.; Liu, K.; Li, X.; Xiao, S.; Zheng, D.; Zhu, P.; Li, C.; Liu, J.; He, J.; Lei, J. A Novel Self-Assembled Nanoparticle Platform Based on Pectin-Eight-Arm Polyethylene Glycol-Drug Conjugates for Co-Delivery of Anticancer Drugs. *Mater. Sci. Eng. C* **2018**, *86*, 28–41.

220. Steiner, J.; Alaneed, R.; Kressler, J.; Mäder, K. Fatty Acid-Modified Poly(Glycerol Adipate) Microparticles for Controlled Drug Delivery. *J. Drug Deliv. Sci. Technol.* **2021**, *61*, 102206.

221. Shen, H.; Jawaid, A.M.; Snee, P.T. Poly(Ethylene Glycol) Carbodiimide Coupling Reagents for the Biological and Chemical Functionalization of Water-Soluble Nanoparticles. *ACS Nano* **2009**, *3*, 915–923.

222. Bartczak, D.; Kanaras, A.G. Preparation of Peptide-Functionalized Gold Nanoparticles Using One Pot EDC/Sulfo-NHS Coupling. *Langmuir* **2011**, *27*, 10119–10123.

223. Talebzadeh, S.; Queffélec, C.; Knight, D.A. Surface Modification of Plasmonic Noble Metal–Metal Oxide Core–Shell Nanoparticles. *Nanoscale Adv.* **2019**, *1*, 4578–4591.

224. Booth, M.A.; Kannappan, K.; Hosseini, A.; Partridge, A. In-Depth Electrochemical Investigation of Surface Attachment Chemistry via Carbodiimide Coupling. *Langmuir* **2015**, *31*, 8033–8041.

225. Armstrong, A.; Li, W. N,N'-Carbonyldiimidazole. In *Encyclopedia of Reagents for Organic Synthesis*; John Wiley & Sons, Chichester, UK, 2007.

226. Staab, H.A. Reaktionsfähige Heterocyclische Diamide Der Kohlensäure. *Justus Liebigs Ann. Chem.* **1957**, *609*, 75–83.

227. Staab, H.A. Reaktionsfähige N-Carbonsäureester Und N-Carbonsäureamide Des Imidazols Und Triazols. *Justus Liebigs Ann. Chem.* **1957**, *609*, 83–88.

228. Staab, H.A. New Methods of Preparative Organic Chemistry IV. Syntheses Using Heterocyclic Amides (Azolides). *Angew. Chemie Int. Ed.* **1962**, *1*, 351–367.

229. Lanzillotto, M.; Konnert, L.; Lamaty, F.; Martinez, J.; Colacino, E. Mechanochemical 1, 1′-Carbonyldiimidazole-Mediated Synthesis of Carbamates. *ACS Sustain. Chem. Eng.* **2015**, *3*, 2882–2889.

230. Woodman, E.K.; Chaffey, J.G.K.; Hopes, P.A.; Hose, D.R.J.; Gilday, J.P. N, N′-Carbonyldiimidazole-Mediated Amide Coupling: Significant Rate Enhancement Achieved by Acid Catalysis with Imidazole·HCl. *Org. Process Res. Dev.* **2009**, *13*, 106–113.

231. Anderson, G.W.; Paul, R. N,N'-Carbonyldiimidazole, a New Reagent for Peptide Synthesis. *J. Am. Chem. Soc.* **1958**, *80*, 4423.

232. Paul, R.; Anderson, G.W. N,N'-Carbonyldiimidazole, a New Peptide Forming Reagent1. *J. Am. Chem. Soc.* **1960**, *82*, 4596–4600.

233. Suppo, J.; Subra, G.; Bergès, M.; Marcia de Figueiredo, R.; Campagne, J. Inverse Peptide Synthesis via Activated A-Aminoesters. *Angew. Chemie Int. Ed.* **2014**, *53*, 5389–5393.

234. Saha, A.K.; Rapoport, H.; Schultz, P. 1,1'-Carbonylbis (3-Methylimidazolium) Triflate: An Efficient Reagent for Aminoacylations. *J. Am. Chem. Soc.* **1989**, *111*, 4856–4859.

235. Gante, J. Peptide Syntheses via N-(1-Imidazolylcarbonyl)- and N-(1-Imidazolylthiocarbonyl)-amino Esters. *Angew. Chemie Int. Ed.* **1966**, *5*, 315.

236. Austermuehle, B.J.; Collins, E.S.; Hamaker, C.G.; Hitchcock, S.R. Synthetic Preparation of N-Alkyl and N-Aryl Arenesulfinamides Using an Arenesulfinic Acid-CDI Driven Approach. *Synth. Commun.* **2021**, *51*, 3483–3491.

237. Baucom, K.D.; Jones, S.C.; Roberts, S.W. 1,1'-Carbonyldiimidazole (CDI) Mediated Coupling and Cyclization To Generate [1, 2, 4] Triazolo [4, 3-a] Pyridines. *Org. Lett.* **2016**, *18*, 560–563.

238. Hearn, M.T.W. 1, 1′-Carbonyldiimidazole-Mediated Immobilization of Enzymes and Affinity Ligands. *Methods Enzymol.* **1987**, 135, 102–117.

239. Hodneland, C.D.; Lee, Y.-S.; Min, D.-H.; Mrksich, M. Selective Immobilization of Proteins to Self-Assembled Monolayers Presenting Active Site-Directed Capture Ligands. *Proc. Natl. Acad. Sci.* **2002**, *99*, 5048–5052.

240. Tang, X.; Wen, Y.; Zhang, Z.; Zhu, J.; Song, X.; Li, J. Rationally Designed Multifunctional Nanoparticles as GSH-Responsive Anticancer Drug Delivery Systems Based on Host-Guest Polymers Derived from Dextran and β-Cyclodextrin. *Carbohydr. Polym.* **2023**, *320*, 121207.

241. Ho, J.; Al-Deen, F.M.N.; Al-Abboodi, A.; Selomulya, C.; Xiang, S.D.; Plebanski, M.; Forde, G.M. N,N'-Carbonyldiimidazole-Mediated Functionalization of Superparamagnetic Nanoparticles as Vaccine Carrier. *Colloids Surf. B Biointerf.* **2011**, *83*, 83–90.

242. Dale, D.J.; Draper, J.; Dunn, P.J.; Hughes, M.L.; Hussain, F.; Levett, P.C.; Ward, G.B.; Wood, A.S. The Process Development of a Scaleable Route to the PDE5 Inhibitor UK-357,903. *Org. Process Res. Dev.* **2002**, *6*, 767–772.

243. Dale, D.J.; Dunn, P.J.; Golightly, C.; Hughes, M.L.; Levett, P.C.; Pearce, A.K.; Searle, P.M.; Ward, G.; Wood, A.S. The Chemical Development of the Commercial Route to Sildenafil: A Case History. *Org. Process Res. Dev.* **2000**, *4*, 17–22.

244. Li, S.; Yang, X.; Yang, S.; Zhu, M.; Wang, X. Technology Prospecting on Enzymes: Application, Marketing and Engineering. *Comput. Struct. Biotechnol. J.* **2012**, *2*, e201209017.

245. Díaz-Rodríguez, A.; Davis, B.G. Chemical Modification in the Creation of Novel Biocatalysts. *Curr. Opin. Chem. Biol.* **2011**, *15*, 211–219.

246. Rashidian, M.; Dozier, J.K.; Distefano, M.D. Enzymatic Labeling of Proteins: Techniques and Approaches. *Bioconjug. Chem.* **2013**, *24*, 1277–1294.

247. Domeradzka, N.E.; Werten, M.W.T.; de Wolf, F.A.; de Vries, R. Protein Cross-Linking Tools for the Construction of Nanomaterials. *Curr. Opin. Biotechnol.* **2016**, *39*, 61–67.

248. Witus, L.S.; Francis, M.B. Using Synthetically Modified Proteins to Make New Materials. *Acc. Chem. Res.* **2011**, *44*, 774–783.

249. Minten, I.J.; Abello, N.; Schooneveld-Bergmans, M.E.F.; van den Berg, M.A. Post-Production Modification of Industrial Enzymes. *Appl. Microbiol. Biotechnol.* **2014**, *98*, 6215–6231.

250. Canalle, L.A.; Löwik, D.W.P.M.; van Hest, J.C.M. Polypeptide–Polymer Bioconjugates. *Chem. Soc. Rev.* **2010**, *39*, 329–353.

251. Broyer, R.M.; Grover, G.N.; Maynard, H.D. Emerging Synthetic Approaches for Protein–Polymer Conjugations. *Chem. Commun.* **2011**, *47*, 2212–2226.

252. Akkapeddi, P.; Azizi, S.-A.; Freedy, A.M.; Cal, P.M.S.D.; Gois, P.M.P.; Bernardes, G.J.L. Construction of Homogeneous Antibody–Drug Conjugates Using Site-Selective Protein Chemistry. *Chem. Sci.* **2016**, *7*, 2954–2963.

253. Szijj, P.A.; Bahou, C.; Chudasama, V. Minireview: Addressing the Retro-Michael Instability of Maleimide Bioconjugates. *Drug Discov. Today Technol.* **2018**, *30*, 27–34.

254. Shen, B.-Q.; Xu, K.; Liu, L.; Raab, H.; Bhakta, S.; Kenrick, M.; Parsons-Reponte, K.L.; Tien, J.; Yu, S.-F.; Mai, E. Conjugation Site Modulates the in Vivo Stability and Therapeutic Activity of Antibody-Drug Conjugates. *Nat. Biotechnol.* **2012**, *30*, 184–

189.

255. Bornscheuer, U.T.; Huisman, G.W.; Kazlauskas, R.J.; Lutz, S.; Moore, J.C.; Robins, K. Engineering the Third Wave of Biocatalysis. *Nature* **2012**, *485*, 185–194.

256. Zhang, Y.; Park, K.-Y.; Suazo, K.F.; Distefano, M.D. Recent Progress in Enzymatic Protein Labelling Techniques and Their Applications. *Chem. Soc. Rev.* **2018**, *47*, 9106–9136.

257. Milczek, E.M. Commercial Applications for Enzyme-Mediated Protein Conjugation: New Developments in Enzymatic Processes to Deliver Functionalized Proteins on the Commercial Scale. *Chem. Rev.* **2018**, *118*, 119–141.

258. Folk, J.E. Mechanism and Basis for Specificity of Transglutaminase-catalyzed ε-(γ-Glutamyl) Lysine Bond Formation. *Adv. Enzym. Relat. Areas Mol. Biol.* **1983**, *54*, 1–56.

259. Lorand, L.; Parameswaran, K.N.; Stenberg, P.; Tong, Y.S.; Velasco, P.T.; Jonsson, N.A.; Mikiver, L.; Moses, P. Specificity of Guinea Pig Liver Transglutaminase for Amine Substrates. *Biochemistry* **1979**, *18*, 1756–1765.

260. Lorand, L.; Conrad, S.M. Transglutaminases. *Mol. Cell. Biochem.* **1984**, *58*, 9–35.

261. Mariniello, L.; Porta, R. Transglutaminases as Biotechnological Tools. *Transglutaminases* **2005**, *38*, 174–191.

262. Duarte, L.; Matte, C.R.; Bizarro, C.V.; Ayub, M.A.Z. Transglutaminases: Part I—Origins, Sources, and Biotechnological Characteristics. *World J. Microbiol. Biotechnol.* **2020**, *36*, 1–18.

263. Neidle, A.; Sarkar N.K.; Waelsch, H. Metabolic Activity of Protein Amide Groups. *Arch. Biochem. Biophys.* **1957**, *71*, 277–279.

264. Doti, N.; Caporale, A.; Monti, A.; Sandomenico, A.; Selis, F.; Ruvo, M. A Recent Update on the Use of Microbial Transglutaminase for the Generation of Biotherapeutics. *World J. Microbiol. Biotechnol.* **2020**, *36*, 1–14.

265. Kieliszek, M.; Misiewicz, A. Microbial Transglutaminase and Its Application in the Food Industry. A Review. *Folia Microbiol.* **2014**, *59*, 241–250.

266. Ikura, K.; Nasu, T.; Yokota, H.; Tsuchiya, Y.; Sasaki, R.; Chiba, H. Amino Acid Sequence of Guinea Pig Liver Transglutaminase from Its CDNA Sequence. *Biochemistry* **1988**, *27*, 2898–2905.

267. Bishop, P.D.; Teller, D.C.; Smith, R.A.; Lasser, G.W.; Gilbert, T.; Seale, R.L. Expression, Purification, and Characterization of Human Factor XIII in Saccharomyces Cerevisiae. *Biochemistry* **1990**, *29*, 1861–1869.

268. Takehana, S.; Washizu, K.; Ando, K.; Koikeda, S.; Takeuchi, K.; Matsui, H.; Motoki, M.; Takagi, H. Chemical Synthesis of the Gene for Microbial Transglutaminase from Streptoverticillium and Its Expression in Escherichia Coli. *Biosci. Biotechnol. Biochem.* **1994**, *58*, 88–92.

269. Washizu, K.; Ando, K.; Koikeda, S.; Hirose, S.; Matsuura, A.; Takagi, H.; Motoki, M.; Takeuchi, K. Molecular Cloning of the Gene for Microbial Transglutaminase from Streptoverticillium and Its Expression in Streptomyces Lividans. *Biosci. Biotechnol. Biochem.* **1994**, *58*, 82–87.

270. Ando, H.; Adachi, M.; Umeda, K.; Matsuura, A.; Nonaka, M.; Uchio, R.; Tanaka, H.; Motoki, M. Purification and Characteristics of a Novel Transglutaminase Derived from Microorganisms. *Agric. Biol. Chem.* **1989**, *53*, 2613–2617.

271. Nonaka, M.; Tanaka, H.; Okiyama, A.; Motoki, M.; Ando, H.; Umeda, K.; Matsuura, A. Polymerization of Several Proteins by Ca^{2+}-Independent Transglutaminase Derived from Microorganisms. *Agric. Biol. Chem.* **1989**, *53*, 2619–2623.

272. Gaspar, A.L.C.; de Góes-Favoni, S.P. Action of Microbial Transglutaminase (MTGase) in the Modification of Food Proteins: A Review. *Food Chem.* **2015**, *171*, 315–322.

273. Kashiwagi, T.; Yokoyama, K.; Ishikawa, K.; Ono, K.; Ejima, D.; Matsui, H.; Suzuki, E. Crystal Structure of Microbial Transglutaminase From Streptoverticillium Mobaraense. *J. Biol. Chem.* **2002**, *277*, 44252–44260.

274. Seguro, K.; Nio, N.; Motoki, M. Some Characteristics of a Microbial Protein Cross-Linking Enzyme: Transglutaminase; N. Parris, A. Kato, L.K. Creamer, J. Pearce (Eds.), In *Macromolecular Interactions in Food Technology*, ACS symposium series, Vol. 650, American Chemical Society, Washington, DC, USA 1996, pp. 271–280.

275. Wang, L.; Wang, Y. Transglutaminases from Microorganisms. In *Transglutaminase*;

Academic Press, Elsevier, 2024; pp. 1–19.

276. Motoki, M.; Seguro, K. Transglutaminase and Its Use for Food Processing. *Trends Food Sci. Technol.* **1998**, *9*, 204–210.

277. Malešević, M.; Migge, A.; Hertel, T.C.; Pietzsch, M. A Fluorescence-based Array Screen for Transglutaminase Substrates. *ChemBioChem* **2015**, *16*, 1169–1174.

278. Spolaore, B.; Damiano, N.; Raboni, S.; Fontana, A. Site-Specific Derivatization of Avidin Using Microbial Transglutaminase. *Bioconjug. Chem.* **2014**, *25*, 470–480.

279. Spolaore, B.; Raboni, S.; Satwekar, A.A.; Grigoletto, A.; Mero, A.; Montagner, I.M.; Rosato, A.; Pasut, G.; Fontana, A. Site-Specific Transglutaminase-Mediated Conjugation of Interferon α-2b at Glutamine or Lysine Residues. *Bioconjug. Chem.* **2016**, *27*, 2695–2706.

280. Marx, C.K.; Hertel, T.C.; Pietzsch, M. Random Mutagenesis of a Recombinant Microbial Transglutaminase for the Generation of Thermostable and Heat-Sensitive Variants. *J. Biotechnol.* **2008**, *136*, 156–162.

281. Jiang, Y.; Shang, Y.-P.; Li, H.; Zhang, C.; Pan, J.; Bai, Y.-P.; Li, C.-X.; Xu, J.-H. Enhancing Transglutaminase Production of Streptomyces Mobaraensis by Iterative Mutagenesis Breeding with Atmospheric and Room-Temperature Plasma (ARTP). *Bioresour. Bioprocess.* **2017**, *4*, 1–7.

282. Böhme, B.; Moritz, B.; Wendler, J.; Hertel, T.C.; Ihling, C.; Brandt, W.; Pietzsch, M. Enzymatic Activity and Thermoresistance of Improved Microbial Transglutaminase Variants. *Amino Acids* **2020**, *52*, 313–326.

283. Sato, H.; Hayashi, E.; Yamada, N.; Yatagai, M.; Takahara, Y. Further Studies on the Site-Specific Protein Modification by Microbial Transglutaminase. *Bioconjug. Chem.* **2001**, *12*, 701–710.

284. Scaramuzza, S.; Tonon, G.; Olianas, A.; Messana, I.; Schrepfer, R.; Orsini, G.; Caliceti, P. A New Site-Specific MonoPEGylated Filgrastim Derivative Prepared by Enzymatic Conjugation: Production and Physicochemical Characterization. *J. Control. Release* **2012**, *164*, 355–363.

285. da Silva Freitas, D.; Mero, A.; Pasut, G. Chemical and Enzymatic Site Specific

PEGylation of HGH. *Bioconjug. Chem.* **2013**, *24*, 456–463.

286. Besheer, A.; Hertel, T.C.; Kressler, J.; Mäder, K.; Pietzsch, M. Enzymatically Catalyzed HES Conjugation Using Microbial Transglutaminase: Proof of Feasibility. *J. Pharm. Sci.* **2009**, *98*, 4420–4428.

287. Alaneed, R.; Hauenschild, T.; Mäder, K.; Pietzsch, M.; Kressler, J. Conjugation of Amine-Functionalized Polyesters with Dimethylcasein Using Microbial Transglutaminase. *J. Pharm. Sci.* **2020**, *109*, 981–991.

288. Alaneed, R.; Naumann, M.; Pietzsch, M.; Kressler, J. Microbial Transglutaminase-Mediated Formation of Erythropoietin-Polyester Conjugates. *J. Biotechnol.* **2022**, *346*, 1–10.

289. Guo, H.; Mi, P. Polymer–Drug and Polymer–Protein Conjugated Nanocarriers: Design, Drug Delivery, Imaging, Therapy, and Clinical Applications. *Wiley Interdiscip. Rev. Nanomed. Nanobiotechnol.* **2024**, *16*, e1988.

290. Ekladious, I.; Colson, Y.L.; Grinstaff, M.W. Polymer–Drug Conjugate Therapeutics: Advances, Insights and Prospects. *Nat. Rev. Drug Discov.* **2019**, *18*, 273–294.

291. Wen, P.; Ke, W.; Dirisala, A.; Toh, K.; Tanaka, M.; Li, J. Stealth and Pseudo-Stealth Nanocarriers. *Adv. Drug Deliv. Rev.* **2023**, *198*, 114895.

292. Rideau, E.; Dimova, R.; Schwille, P.; Wurm, F.R.; Landfester, K. Liposomes and Polymersomes: A Comparative Review towards Cell Mimicking. *Chem. Soc. Rev.* **2018**, *47*, 8572–8610.

293. Wang, S.; Chen, Y.; Guo, J.; Huang, Q. Liposomes for Tumor Targeted Therapy: A Review. *Int. J. Mol. Sci.* **2023**, *24*, 2643.

294. Soppimath, K.S.; Aminabhavi, T.M.; Kulkarni, A.R.; Rudzinski, W.E. Biodegradable Polymeric Nanoparticles as Drug Delivery Devices. *J. Control. Release* **2001**, *70*, 1–20.

295. Hu, C.-M.J.; Aryal, S.; Zhang, L. Nanoparticle-Assisted Combination Therapies for Effective Cancer Treatment. *Ther. Deliv.* **2010**, *1*, 323–334.

296. Kumari, A.; Yadav, S.K.; Yadav, S.C. Biodegradable Polymeric Nanoparticles Based Drug Delivery Systems. *Colloids Surf. B Biointerf.* **2010**, *75*, 1–18.

297. Svenson, S. Carrier-Based Drug Delivery; Svenson, S. (Ed.); In *ACS Symposium Series*, American Chemical Society, Washington, DC, 2004; Vol. 879, pp 2– 23.

298. Mandal, A.; Bisht, R.; Rupenthal, I.D.; Mitra, A.K. Polymeric Micelles for Ocular Drug Delivery: From Structural Frameworks to Recent Preclinical Studies. *J. Control. Release* **2017**, *248*, 96–116.

299. Lovelyn, C.; Attama, A.A. Current State of Nanoemulsions in Drug Delivery. *J. Biomater. Nanobiotechnol.* **2011**, *2*, 626.

300. Üner, M.; Yener, G. Importance of Solid Lipid Nanoparticles (SLN) in Various Administration Routes and Future Perspectives. *Int. J. Nanomedicine* **2007**, *2*, 289–300.

301. Müller, R.H.; Radtke, M.; Wissing, S.A. Solid Lipid Nanoparticles (SLN) and Nanostructured Lipid Carriers (NLC) in Cosmetic and Dermatological Preparations. *Adv. Drug Deliv. Rev.* **2002**, *54*, S131–S155.

302. Müller, R.H.; Radtke, M.; Wissing, S. Nanostructured Lipid Matrices for Improved Microencapsulation of Drugs. *Int. J. Pharm.* **2002**, *242*, 121–128.

303. Müller, R.H.; Petersen, R.D.; Hommoss, A.; Pardeike, J. Nanostructured Lipid Carriers (NLC) in Cosmetic Dermal Products. *Adv. Drug Deliv. Rev.* **2007**, *59*, 522–530.

Erklärung

Hiermit versichere ich, die vorliegende Arbeit selbstständig und ohne fremde Hilfe verfasst und keine anderen als die von mir angegebenen Quellen und Hilfsmittel verwendet zu haben. Die den benutzten Werken wörtlich oder inhaltlich entnommenen Stellen habe ich als solche kenntlich gemacht.

Ich erkläre, keine anderweitigen Promotionsversuche unternommen und die vorliegende Dissertation weder in der jetzigen noch in einer anderen Fassung einer anderen wissenschaftlichen Einrichtung vorgelegt zu haben.

Halle (Saale), den Rana Hore

Acknowledgments

I feel indebted to the many people whom, without their help, cooperation, or guidance, this work would have never been completed in its present form.

First of all, I have to express my deep gratitude and appreciation to my academic supervisor, **Prof. Dr. Jörg Kressler**, Institute of Chemistry of the Martin-Luther-University Halle-Wittenberg, for his assistance at every stage of my research project.

Prof. Dr. Jörg Kressler for giving me the opportunity to carry out my research project under his guidance. I highly appreciated his continuous scientific support, advice, and inspiration, not only during this thesis work but also throughout all my master's and Ph.D. studies.

Special thanks to **Prof. Dr. Markus Pietzsch** for his fruitful cooperation and for giving me the opportunity to work in the field of enzymatic protein-polymer conjugation. I highly appreciated his support, motivation, and helpful discussions and suggestions.

I would like to extend my sincere thanks to **Prof. Dr. Karsten Mäder**, Institute of Pharmacy of the Martin-Luther-University Halle-Wittenberg, for our successful collaborative work, for giving me the ideas, and for the helpful discussions and suggestions.

I have to express my gratitude to **Dr. Razan Alaneed** for her invaluable help during the whole Ph.D time, continuous support for experimental result analysis, great scientific discussions, and insightful comments and suggestions.

Many thanks go to **Dr. Nazmul Hasan** for his support during experimental measurements, analysis, and useful scientific discussions and for the pleasant office atmosphere.

I have also to thank **Dr. Haroon and Frank Syrowatka** for their kind help and assistance with nanoparticle preparation and SEM measurements.

Many thanks go to **Dr. Karsten Busse** for his support and great scientific discussions.

My sincere thanks to **all members of Prof. Jörg Kressler's group** for the comfortable atmosphere at work as well as for their helpful comments and suggestions.

My sincere thanks go also to **Frau Susanne Tanner** and **Frau Julia Weichhold** for the ESI-TOF measurements.

I would like to offer my special thanks to **Dr. Dieter Ströhl** for the technical support in terms of NMR spectroscopy.

My endless gratitude goes to my elder brother **Newton Sen**. Without his support this Ph.D thesis would not be achieveable. He is the person who continuously supports me in every step of my life, in every decision, in every up and down, and in my difficult times when I lost myself. Words will never be enough to express you.

Lastly, my family deserves endless gratitude for their unconditional love, their never-ending support and encouragement over the years, and their appreciation for my work. You are always there for me!

I gratefully acknowledge the funding received towards my Ph.D. from International Graduate School AGRIPOLY supported by the European Social Fund (ESF) and the Federal State Saxony-Anhalt.

This dissertation would not have been possible without the support of all these wonderful people!

List of publications

1. **Hore, R.***; Alaneed, R.; Pietzsch, M.; Kressler, J. Enzymatic HES Conjugation with Recombinant Human Erythropoietin via Variant Microbial Transglutaminase TG^{16}. *Starch-Stärke* **2022**, *74*, 2200034.

2. **Hore, R.***; Rashid, H.; Syrowatka, F.; Kressler, J. Synthesis and Characterization of Self-Assembled Highly Stearate Grafted Hydroxyethyl Starch Conjugates. *Polysaccharide* **2024**, *5*, 142–157.

3. **Hore, R.***; Hasan, N.; Mäder, K.; Kressler, J. Synthesis and Characterization of Dimeric Artesunate Glycerol Monocaprylate Conjugate and Formulation of Nanoemulsion Preconcentrate. *Molecules* **2023**, *28*, 5208.

***First author.**

Curriculum vitae

Personal data

Name:	Rana Hore
Gender:	Male

Education

08/2019 – 05/2024	Doctoral studies Martin Luther Universität Halle-Wittenberg, Germany Institute of Chemistry Supervisor: Prof. Dr. Jörg Kressler
10/2016 – 07/2019	Master in Polymer Materials Science Martin Luther Universität Halle-Wittenberg, Germany Degree: Master of Science
01/2013 – 12/2014	Master in Pharmacy University of Science and Technology Chittagong (USTC), Bangladesh Degree: Master of Pharmacy
01/2007 – 12/2012	Bachelor in Pharmacy University of Science and Technology Chittagong (USTC), Bangladesh Degree: Bachelor of Pharmacy

Halle (Saale), den Rana Hore